

Doctoral thesis

Doctoral theses at NTNU, 2023:260

Jonas Lidal

Hybrid devices for protected quantum information processing

NTNU
Norwegian University of Science and Technology
Thesis for the Degree of
Philosophiae Doctor
Faculty of Natural Sciences
Department of Physics



Norwegian University of
Science and Technology

Jonas Lidal

Hybrid devices for protected quantum information processing

Thesis for the Degree of Philosophiae Doctor

Trondheim, September 2023

Norwegian University of Science and Technology
Faculty of Natural Sciences
Department of Physics



Norwegian University of
Science and Technology

NTNU

Norwegian University of Science and Technology

Thesis for the Degree of Philosophiae Doctor

Faculty of Natural Sciences

Department of Physics

© Jonas Lidal

ISBN 978-82-326-7220-2 (printed ver.)

ISBN 978-82-326-7219-6 (electronic ver.)

ISSN 1503-8181 (printed ver.)

ISSN 2703-8084 (online ver.)

Doctoral theses at NTNU, 2023:260

Printed by NTNU Grafisk senter

Abstract

Quantum information is very fragile, and it is clear that we need to develop better qubits and employ error correction, in order to make use of the full potential that quantum computation has. In this thesis we explore known error correction codes and promising platforms for topological quantum computation. Furthermore, we look at new ways of engineering states which are useful for error correction using hybrid devices, and investigate properties of superconductor-semiconductor hybrid devices which have gained much attention due to their many interesting properties, such as possibly hosting topological superconductivity.

In the first part of the thesis we explore the engineering of quantum states by the use of hybrid devices. First, we look at a qubit coupled to a microwave cavity. By driving the qubit through level crossings, we show that it is possible to create Schrödinger-cat states. After this, we look at a spin-qubit coupled to an anisotropic ferromagnet, which we show is a physical realization of the quantum Rabi model. Furthermore, we show that by expanding the hybrid device to include 3 qubits, we are able to drive all three qubits simultaneously, creating a GHZ state, in a way that is robust against qubit asymmetries.

In the second part of the thesis, we look at hybrid devices made from superconductors and semiconductors. We start by introducing concepts that are necessary to describe these systems, before looking at one of the possible applications of these systems, namely in topologically protected quantum computation. The detailed spin dynamics of these devices can, however, heavily depend on features such as the microscopic details of the device or strain. The two last chapters investigate the spin-dynamics of 1D and 2D hybrid devices. We first look at a nanowire superconductor-normal-superconductor (SNS) junction, with spin-orbit coupling and an external magnetic field, where we derive an analytical expression for the critical current of the junction. Lastly, we look at a 2D hole gas SNS junction, with spin-orbit coupling and an external magnetic field, where we also here derive (semi)-analytic expressions for the critical current in limiting cases.

Preface

This thesis is submitted to the Norwegian University of Science and Technology in partial fulfillment of the requirements for the philosophiae doctor degree. The research was supervised by Prof. Jeroen Danon and co-supervised by Prof. Arne Brataas. The doctoral program included 30 ECTS of coursework, and was carried out over four years, a part of which was a total of one year of undergraduate teaching duties. The thesis is written to supplement the three papers [I–III], included at the end of this thesis.

Acknowledgements

Most of my thoughts about how my PhD would turn out, were completely wrong, both in terms of highs and lows. Half a year into my PhD the COVID-19 pandemic hit, turning everything upside down, and two years later I moved from Trondheim to Oslo.

First of all, I want to thank my supervisor Jeroen Danon, who have met me with more understanding than could ever be expected, for being on board with me finishing the last year of my PhD remotely from Oslo, finding solutions which made it possible and productive, and not least for guidance and great advice throughout the research.

Thank you to the people at QuSpin for all the lunches, dinners, 4 o'clock breaks, drinks, and ice cream. In no particular order, thanks to Eirik, Atousa, Arnau, Martin, Even, Niels Henrik, Vemund, Christian, Kristian, Anna Cecilie, Henning, Jonas, Tancredi, Sol, and Karen-Elisabeth, and so many more... A special thanks to my office mates, Matthias and Payel, to my collaborators Akash and Ida, to the 4 o'clock squad, Lina, Bjørnulf, and Håvard, to Verena and Max for letting me stay with you on one of my many trips from Oslo, and to Jabir Ali for creating the template which this thesis is based on [1].

I would also like to thank Tarjei and Frida who have been my good friends since high school, and especially for providing me with good company and a bed, the times I have visited from Oslo. Also thank you to Peter for being my "designated friend" during the pandemic, and along with Bjørn and Gert for many fun evenings and days the last year. Along with Einar, the four of you have been a huge part of my life at university the last 9 years. Thank you for all the good times, late nights, and interesting discussions!

Thank you to my family as well, who have been very supportive, and are a large part of why I decided to do research.

Finally, a huge thanks to Helene for your patience and support, for all the time we have spent together, all the hiking trips, and for all the dinners we have had together. Thank you for looking out for me, and among other things, suggesting that getting some fresh air during home office might be a good idea¹. And thank you for lots of comfort, support, food, and snacks during the finishing of this thesis.

1. You were right!

Contents

Publications ix

1. Introduction	1
2. Quantum information	3
2.1. Qubits	3
2.2. Protected quantum information processing	5
I. Quantum state engineering	11
3. Generating Schrödinger cat states with qubit/boson system	13
3.1. Landau-Zener physics	17
3.2. Landau-Zener-Stückelberg engineering of cat states	23
4. Generation of GHZ states with spin-qubit/magnon system	33
4.1. Spin qubit coupled to magnonic cavity	34
4.2. Generating GHZ states in qubits using coupling to the magnon mode	39
4.3. Concluding remarks	46
II. Semi/super hybrid devices for topologically protected quantum computation	49
5. Semi/super hybrid devices for topological protected quantum computation	51
5.1. Superconductors	51
5.2. Majorana fermions	55
5.3. Outlook and contributions	62
6. The critical current in an NW SNS junction with a scatterer	63
6.1. Model	63
6.2. Critical current	73
6.3. Applications	75

7. Probing spin-orbit and Zeeman fields via the critical current in a 2DHG SNS junction	77
7.1. Properties of the 2DHG	77
7.2. Model	81
7.3. Linearization of the Hamiltonian and the semi-classical approximation	86
7.4. Critical current	88
7.5. Signatures of SOI and Zeeman in critical current	94
8. Conclusion	95
Bibliography	97

Publications

- I. **J. Lidal, J. Danon.**
Generation of Schrödinger-cat states through photon-assisted Landau-Zener-Stückelberg interferometry.
Phys. Rev. A 102, 043717 (4 Oct. 2020).
DOI: [10.1103/PhysRevA.102.043717](https://doi.org/10.1103/PhysRevA.102.043717)
- II. **I.C. Skogvoll, J. Lidal, J. Danon, A. Kamra.**
Tunable Anisotropic Quantum Rabi Model via a Magnon–Spin-Qubit Ensemble.
Phys. Rev. Appl. 16, 064008 (6 Dec. 2021).
DOI: [10.1103/PhysRevApplied.16.064008](https://doi.org/10.1103/PhysRevApplied.16.064008)
- III. **J. Lidal, J. Danon.**
Effects of spin-orbit coupling and in-plane Zeeman fields on the critical current in two-dimensional hole gas SNS junctions.
Phys. Rev. B 107, 085303 (8 Feb. 2023).
DOI: [10.1103/PhysRevB.107.085303](https://doi.org/10.1103/PhysRevB.107.085303)
- IV. **J. Lidal, J. Danon.**
Critical current of a one-dimensional nanowire: the interplay of Zeeman and spin–orbit fields.
Manuscript in preparation (2023).

Introduction

One of the greatest achievements of humankind has been the invention and development of the computer. It is what allows me to write this thesis, typeset it, print it, and distribute it, with the help of only a handful of people, mostly using automated machines and devices. However, even though most of the progress within computer science has come after the paradigm shift of quantum mechanics, most concepts used in creating and operating a computer can be explained using classical physics. There are some exceptions¹, but fundamentally there are no requirements of knowledge of quantum mechanics when creating a computer.

A question one might ask is: Can we gain any meaningful advantage over the classical computer by using the full quantum nature of particles? It turns out that for some types of problems, employing concepts such as entanglement and superposition *can* give a considerable advantage over a classical computer. The problem however, is that quantum states are very fragile.

To be able to do millions, if not billions, of operations like a classical computer, the quantum systems that make up a quantum computer have to be extremely well isolated, and at the same time be controllable. Even with the best efforts over the last few decades, the best quantum computer components we have, are still not close to do the millions of operations needed to do complex tasks without errors.

However, this comparison is not completely fair, classical computers and storage media also experience errors. As an example, a CD or DVD can easily get scratched, but as long as the degree of scratching is not too large, the device will still play. This is possible because we have redundantly encoded the information we want to store on the disk, so even when errors occur, the reader can figure out what error has occurred and compensate for it. The same concept applies to quantum computation, if we are able to keep the number of errors below a certain threshold, and by using clever ways of redundantly encoding the information, we can still decode the right information even when errors occur. What we need is less error-prone hardware

1. Quantum mechanics have made designing small and efficient components possible.

and clever ways of redundantly encoding our information such that we can correct for potential errors.

This thesis covers a few different topics, and it might seem sporadic at times. You should know that this is not at any fault of the reader. This thesis is the product of projects which are not very closely related, but the red line throughout the thesis is the protection of quantum information by the use of hybrid devices. We will first look at some general concepts within quantum information, and some concepts which allows for the protection of quantum information in chapter 2.

The rest of this thesis consists of two parts. The first part focuses on paper [I] and [II], where we discuss the engineering of certain quantum states, that can be used in protecting quantum information. In chapter 3 we look at the topics discussed in paper [I], where we propose a method for engineering a type of bosonic state, the cat state, with the use of a qubit. The cat state can be used for many things, one of which is the protection of quantum information. In chapter 4 we introduce concepts from paper [II], looking at a system of a qubit and an anisotropic ferromagnet, that is a physical realization of the quantum Rabi model with tunable coupling terms. We demonstrate how a version of this system, with 3 qubits, can be used to create the so-called GHZ state, which also has applications within protecting quantum information.

The second part focuses on semiconductor/superconductor hybrid devices, which are believed to be a possible platform for topologically protected quantum computation. The theoretical framework used in working with these systems as well as some context for why these systems are desirable is addressed in chapter 5. Chapter 6 is based on a manuscript in preparation where we look at a superconducting-normal-superconducting (SNS) junction made from a nanowire with spin-orbit coupling between two superconductors in the presence of a magnetic field. In chapter 6 we focus on paper [III], where we look at the effects of spin-orbit coupling and the Zeeman effect on the critical current of an SNS junction consisting of a 2D hole gas between two superconducting contacts.

Quantum information

2

Quantum computation is often portrayed as revolutionary, with bold promises of infinite parallelization and exponential speed-ups. The truth is likely a lot more modest, but a working quantum computer *can* do things no classical computer can. Currently, we only know of a few *very* specialized tasks, where the quantum computer is superior to the classical computer.

For one of these specialized tasks, the idea of doing the task fast, was though so improbable that it is used in protocols for keeping important messages private. That task is the factorization of large primes. The assumption that multiplying two primes is very easy, even for large numbers, while doing the inverse, prime number factorization, is very hard, is used to make a non-symmetric cryptographic scheme known as RSA cryptography [2]. Peter Shor showed in 1994 that prime number factorization is possible with a quantum computer in polynomial time¹, using what is now known as Shor's algorithm [3, 4]. And so no matter the future of quantum computers, it is going to have had a huge impact on the world, as we all transition to other cryptographic methods.

Another promising application was in fact one of the first proposals for a quantum computer [5]: Simulating quantum systems using quantum computers. It is intuitive enough that a quantum computer, essentially a controllable quantum system, is able to simulate quantum systems, a task which is hard for classical computers to do. What is not trivial is whether a digital quantum computer, made up of quantum bits (qubits), can simulate arbitrary quantum systems well. It turns out that it is indeed possible to simulate these systems efficiently, at least in the case where we consider local interaction, using a general purpose quantum computer [6, 7]. Specialization has also been done for use in quantum chemistry [8], as well as quantum field theory [9].

2.1. Qubits

Analogous to a classical computer which manipulates and stores bits, a quantum computer manipulates and stores qubits. These qubits can

1. Fast.

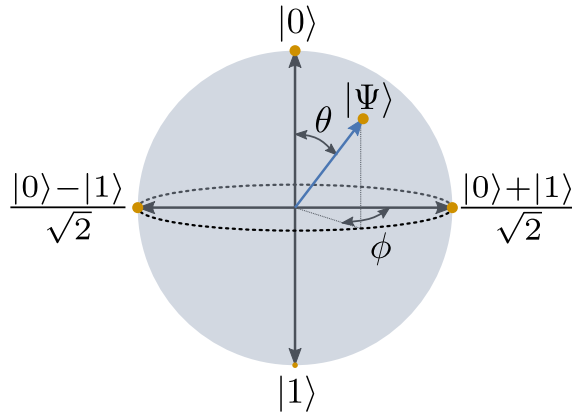


Figure 2.1.: A qubit state $|\Psi\rangle$ represented as a point on the Bloch sphere. The states $|0\rangle$ and $|1\rangle$ are the poles on the sphere, while the states which are equal superpositions of $|0\rangle$ and $|1\rangle$ are found along the equator.

in principle be any quantum system with two states we can encode information, which we will refer to as the $|0\rangle$ and $|1\rangle$ states, with sufficient control. A general qubit state is given by:

$$|\Psi\rangle = a|0\rangle + b|1\rangle, \quad (2.1)$$

where a and b are arbitrary complex numbers. However, we have a normalization constraint, the probability of the qubit being in either $|0\rangle$ or $|1\rangle$ has to add to 1, $|a|^2 + |b|^2 = 1$. Using this in combination with the fact that we are not able to measure the overall phase of the qubit, means that it is possible to describe the whole qubit with two real numbers, here with θ and ϕ :

$$|\Psi\rangle = \sin \frac{\theta}{2} |0\rangle + e^{i\phi} \cos \frac{\theta}{2} |1\rangle. \quad (2.2)$$

Because of this, it is common to imagine the qubit as a point on a sphere, the so-called Bloch sphere, as illustrated in figure 2.1.

Not every quantum system with two states is equally good for making a quantum computer, of course. In 2000 David DiVincenzo proposed a set criteria which are necessary in order to make a quantum computer [10]. They essentially boil down to being able to control the qubit well enough (initialize the qubit in known states, making it

possible to do the required operations on the qubits), having a way to read out the results, it being a scalable system, and long coherence times.

2.1.1. Current technology

There have been many suggested qubit platforms, which satisfy the DiVincenzo criteria to different degrees. Superconducting qubits, which have gained a lot of attention lately [11, 12], are superconducting circuits which utilize the nonlinear properties of Josephson junctions. These devices use the lowest two electromagnetic excitations of the device as a qubit [13]. There are many types of superconducting qubits, typically categorized into phase qubits [14], flux qubits [15], charge qubits [16]. Another popular avenue is qubits which leverage the decades long research into semiconductors. These qubits use the charge [17] and/or spin [18] degrees of freedom of electrons which can be trapped in quantum dots. There are countless other types of qubits, such as trapped-ion [19], neutral-atom qubits [20], NV centers in diamonds [21], and photon based qubits [22, 23] to name a few.

2.2. Protected quantum information processing

With the current state of qubits, it is possible to obtain gate fidelities, i.e. how well it is possible to do operations on the qubits, of up to 99.9% [24–26], which is quite remarkable. However, the fidelities required to do complex task, such as e.g. factorizing numbers which would be difficult to factorize on a classical computer, could require gate fidelities of up to 99.9999999% [27].

It is clear that none of the currently viable qubit platforms will reach the strictest requirements for general scalable quantum computers in the foreseeable future, but all hope is not lost. In this section we look at different methods of protecting the quantum information further, both intrinsically and extrinsically.

2.2.1. Extrinsic protection

By pooling multiple qubits together, using multiple qubits as one effective large qubit, we can in principle protect the quantum information. Looking at classical information theory, the easiest way of protecting

information is to use a repetition code. Imagine encoding a single logical bit, in three physical bits:

$$\bar{0} = 000, \tag{2.3}$$

$$\bar{1} = 111, \tag{2.4}$$

where the bar signifies that we are talking about a logical bit. This coding scheme, would allow for protection against a single error. A single error in a $\bar{0}$ bit would manifest as one of the following bit sequences: 001, 010, 100. Using a majority vote over the bits, we can recover the bit $\bar{0} = 000$. Two bit errors would lead to the wrong recovered qubit, and so we would have to expand the code to include more repetitions if we want it to be correctable for multiple errors. However, it would allow us to detect up to two errors, showing that the number of errors which are detectable by a code is not necessarily the same as it is able to correct. Adding bits to this code would make the code more resilient to errors, but this would become inconvenient for larger codes, but luckily more clever codes exist.

At first glance one might think that the same repetition code might work well for qubits as well [28]:

$$|\bar{0}\rangle = |000\rangle, \tag{2.5}$$

$$|\bar{1}\rangle = |111\rangle, \tag{2.6}$$

where $|000\rangle = |0\rangle \otimes |0\rangle \otimes |0\rangle$. We would not be able to do the majority vote that the classical code uses, because it would break any quantum superposition in the state by measuring the qubits, destroying the quantum information. We can however be a bit more clever, measuring the parity between neighboring bits:

$$\begin{array}{c} P_3 \\ \left. \begin{array}{c} | \\ \hline \sigma_1 \sigma_2 \sigma_3 \\ \hline | \end{array} \right\} \\ P_1 \quad P_2 \end{array}, \tag{2.7}$$

where $P_{1,2,3}$ are parity measurements over the two bits indicated by the brackets. This does not distinguish $|\bar{0}\rangle$ from $|\bar{1}\rangle$, since $P_i(0, 0) = P_i(1, 1) = 1$, but it would tell us if there is an error, and even the location of the error, so that we can correct for it.

This code would protect against a single bit flip error, and could detect up to two such errors. The problem is that in qubits, bit flip errors, going from north to south on the Bloch sphere, figure 2.1, are not the only errors that can occur. Phase errors, which rotates the state around the azimuthal angle, ϕ , on the Bloch sphere, figure 2.1, also has to be accounted for.

We can similarly create a repetition code which corrects a phase error (but not bit-flip errors) by rotating the qubit basis, or equivalently using parity measurements along the x -axis instead of the z -axis on the Bloch sphere.

The first full quantum error-correcting code was proposed by Shor [29], and was built by concatenating these two codes. This is done by starting with the phase error correctable code, where the three qubits are made up of the bit flip error correctable error code from above. Giving us a code consisting of 9 qubits which encodes one logical, error-correctable, qubit.

The Shor code, is an example of a larger class of codes, called CSS codes after Robert Calderbank, Peter Shor [27] and Andrew Stean [30], which again is a subset of so-called stabilizer codes. In the example above, we essentially have to do the two parity measurements for each of the 3 groups of 3 qubits, 6 parity measurements, and then do a x -oriented parity measurement on the two first groups and the two last groups of 3 qubits. These 8 parity measurements, P_i , are what is known as stabilizers for the Shor code, and they all have an eigenvalue of 1 if there is no error:

$$P_i |\psi\rangle = |\psi\rangle, \quad (2.8)$$

while if an error, bit-flip or sign-flip, has occurred, some stabilizers will have an eigenvalue of -1 :

$$P_i |\psi\rangle = -|\psi\rangle. \quad (2.9)$$

Which stabilizer shows errors can tell us where the error is and allow us to correct for it. A boson analog of the Shor code was first experimentally demonstrated using photons [31], and have also later been demonstrated in trapped-ion systems [32, 33]

Bosonic codes

Above we looked at encoding qubits in an ensemble of other two-level systems, qubits, which created a large dimensional Hilbert space, with some redundancy, which made error correction possible. A quantum harmonic oscillator, a bosonic system, gives us an infinite dimensional Hilbert space from the start to implement error correction codes.

One simple coding scheme is encoding the qubit in the number states of the harmonic oscillator, the so-called Fock states, $|n\rangle$, in the following way:

$$|\bar{0}\rangle = \frac{|0\rangle + |4\rangle}{\sqrt{2}}, \quad (2.10)$$

$$|\bar{1}\rangle = |2\rangle. \quad (2.11)$$

Since the main error channel in these types of systems typically is excitation loss [34], and the logical states are only made up of even excitation numbers, errors are easily detectable by measuring the parity of the state, which does not differentiate the two even logical states. If the oscillator has an odd number of excitations, $|1\rangle$ or $|3\rangle$, we know an error has occurred. This encoding, is an example of a binomial code [35, 36].

A very similar type of code, is built from the coherent states, which can make it more stable and be easier to make [37]. Superpositions of coherent states can make similar parity states as shown above. The coherent states can be thought of as the most classical state of the quantum harmonic oscillator. These superpositions of coherent states are called cat states, after Erwin Schrödinger's thought experiment, Schrödinger's cat. We will come back to these states in chapter 3.

2.2.2. Intrinsic protection

The repetition code mentioned above is essentially what makes hard disk drives work so well. The information is encoded in magnetic moments on a metallic disk. Each bit is many millions of magnetic moments, which because of the ferromagnetic order in the disk, tend to align. If an error occurs, i.e. one (or even thousands) of magnetic moments flip, the other millions of magnetic moments force them back in alignment with the majority, essentially doing the majority vote correction mentioned earlier fully automatically.

This concept of error correction by diffusion can be brought over to quantum error correction by using a system where errors send the state to an error space, which by passive or active coupling to the outside world, or some bath, decaying back into the logic space, and importantly, into the correct logical state. Methods based on this has been suggested for codes such as the cat code mentioned above [23, 38], where it can stabilize against both photon dephasing errors and photon loss errors.

Another different approach is to implement the qubit in a system which is in itself non-local, meaning that local perturbations cannot influence the logical information stored in the qubit. This is the basic idea behind topologically protected qubits. A theoretical proposal for such a topological quantum computer was made by Alexei Kitaev [39]. Kitaev proposed starting with a CSS code, the surface code, and looking at excitations in this model, which are treated like quasi-particles living in two dimensions called anyons. We will come back to anyons and how they can be used in quantum computation in chapter 5. However, the basic idea is that by exchanging the position of anyons, what is called braiding, we can change the state of the system, in a measurable way, equivalently to applying gates to qubits. And was in fact recently shown in practice by Google Quantum AI [12]. These topological quasi-particles have also been theorized (and maybe [40] found experimentally [41]) to appear in low dimensional solid state systems such as in 1D topological superconductors [42], which we also come back to in chapter 5.

An important feature of this computational scheme is that the anyons are a feature of the bulk material, as opposed to local degrees of freedom [43]. Additionally, the way quantum gates are applied, by braiding, is immune to microscopic deviations of the position of the particles. Applying a gate would entail moving a particle around other particles; the exact path is not important for the operation, only which particles move around which and in what order.

Part I.

Quantum state engineering

Generating Schrödinger cat states with qubit/boson system

The most famous thought experiment in quantum physics, if not in all of physics, Schrödinger's cat, was devised by Erwin Schrödinger in 1935 [44], to illustrate how the Copenhagen interpretation of quantum mechanics could be problematic. In the thought experiment, a very classical concept, a cat, is put in a quantum superposition of being alive and dead. This concept of putting something classical in a quantum superposition is the inspiration for the name of cat states which we will be looking at in this chapter. The "cat" in this analogy is the most classical state of the quantum harmonic oscillator, namely the coherent state:

$$|\alpha\rangle = e^{-\frac{|\alpha|^2}{2}} \sum_{n=0}^{\infty} \frac{\alpha^n}{\sqrt{n!}} |n\rangle, \quad (3.1)$$

where $|n\rangle$ are the excitation number eigenstates, the so-called Fock states, of the quantum Harmonic oscillators:

$$H = \hbar\omega \left(a^\dagger a + \frac{1}{2} \right), \quad (3.2)$$

where a^\dagger is the excitation creation operator, $a^\dagger |n\rangle = \sqrt{n+1} |n+1\rangle$ and ω is the angular frequency of the oscillator. We refer to $|\alpha|^2$ as the size of the state, because the average excitation number of the coherent state is given by $\langle n \rangle = |\alpha|^2$. This state is the most classical in the sense that it behaves the most like the classical harmonic oscillator, and it can be shown that for a large number of excitations this state recreates the behavior of the classical counterpart of the system [45].

Cat states are linear superpositions of coherent states with opposite phases:

$$|\Psi(\theta_S)\rangle = \frac{1}{\mathcal{N}(\theta_S)} \left(|\alpha\rangle + e^{-i\theta_S} |-\alpha\rangle \right), \quad (3.3)$$

where

$$\mathcal{N}(\theta_S) = \frac{1}{\sqrt{2[1 + \cos(\theta_S)e^{-2|\alpha|^2}]}}, \quad (3.4)$$

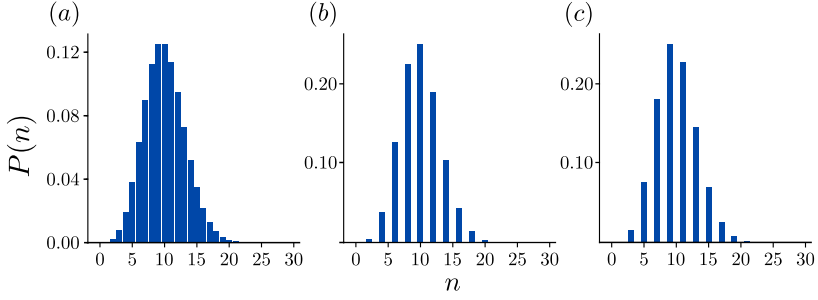


Figure 3.1.: A figure showing the occupation probability in the Fock basis, $P(n) = \langle n | \Phi | n \rangle$, of (a) a coherent state, (b) an even cat state, and (c) an odd cat state, with the average photon number, $\alpha^2 = 10$, for all three cases.

is a normalization factor. For the special cases of $\theta_S = 0$ and $\theta_S = \pi$ we get the states:

$$|\Psi(0)\rangle = |\Psi_{\text{even}}\rangle \propto \frac{\alpha^0}{\sqrt{0!}} |0\rangle + \frac{\alpha^2}{\sqrt{2!}} |2\rangle + \frac{\alpha^4}{\sqrt{4!}} |4\rangle + \dots \quad (3.5)$$

$$|\Psi(\pi)\rangle = |\Psi_{\text{odd}}\rangle \propto \frac{\alpha^1}{\sqrt{1!}} |1\rangle + \frac{\alpha^3}{\sqrt{3!}} |3\rangle + \frac{\alpha^5}{\sqrt{5!}} |5\rangle + \dots \quad (3.6)$$

These states are linear superpositions of only even or odd Fock states, which is why we will call these even and odd cat states. We can see an example of the occupation probability of three different states, a coherent state, an even cat state, and an odd cat state, in the Fock basis, $P(n) = \langle n | \Phi | n \rangle$, in figure 3.1.

From this figure we can see that, and which will become important when we want to engineer these states, even and odd cat states have the same shape of distribution envelope in the occupation probability as the coherent state (a Poisson distribution), but every other number state has zero probability, $P(n) = 0$.

Applications

The cat states are on the border between classical and quantum, which means that one possible application is using cat states in investigating the exact nature of this crossover [46]. Cat states have been proposed

for many other applications as well, including high-precision measurements [47–49], as a resource for quantum computation [50, 51], in quantum teleportation [52, 53], and quantum error correction [54, 55].

One aspect which makes these systems good for hosting error correctable quantum information is that we encode a qubit, a state in a 2D Hilbert space, in an infinite dimensional Hilbert space of the bosonic mode. As mentioned, this extra space is what allows us to redundantly encode the information in the qubit in a way that errors are possible to correct, without telling us which logical state the state is in.

Unlike in classical error correction, where we only have to protect against bit-flip errors, the code has to protect against phase errors as well to be fully protected. But phase errors and bit-flip errors do not necessarily occur with the same frequency. Photon cavities are generally very stable, and the main error channel is by far photon loss [34]. Hence, by designing a code where errors which are caused by photon loss are easy to correct for, we can protect the system well even though it can not correct for all types of errors.

One application of the cat states are namely this, to design a state which is very stable against photon loss errors, in the so-called *cat code*. Where the logical states are coded in the coherent states with opposite phase:

$$|0\rangle = |\alpha\rangle, \quad (3.7)$$

$$|1\rangle = |-\alpha\rangle, \quad (3.8)$$

where the $|+\rangle = \frac{|\alpha\rangle + |-\alpha\rangle}{\sqrt{2}}$ and $|-\rangle = \frac{|\alpha\rangle - |-\alpha\rangle}{\sqrt{2}}$ state of this code is then the even and odd cat states, $|\Psi_{\text{even}}\rangle$ and $|\Psi_{\text{odd}}\rangle$.

The logical states are far apart, in the sense that a photon loss event does not make one logical state similar to the other, $\langle 1|a|0\rangle \approx 0$. However, for the $|+\rangle$ and $|-\rangle$ states, we see that photon loss leads to odd number states transitioning to even number states, while the opposite is true for even number states (except for the $|0\rangle$ state). An even cat state, the $|+\rangle$ state, will turn into something similar to an odd cat state, the $|-\rangle$ state, in the event of a photon loss, $\langle -|a|+\rangle \gg 0$. Because of this, this cat code protects well against bit flip errors, but not phase errors in the qubit.

To get complete error correction, one can use the diffusive error correction mentioned in chapter 2 [23, 38], and/or by concatenating

the cat code with some other error correction code, e.g. the surface code [56]. However, the code we concatenate with the cat code should be tailored to use more resources in correcting for phase errors since the bit flip errors are to a great extent taken care of by the cat code. In the case of the surface code this can be done by using a more qubits in one dimension than the other [57]. We can obtain the ability to correct for phase errors as well with cat codes alone if we expand the code to a so-called four legged cat code.

Four legged cat code

If we imagine slightly different logical states of our code. Namely, two even states which are $\pi/2$ out of phase with each other:

$$|0\rangle = \frac{1}{\mathcal{N}(0)} (|\alpha\rangle + |-\alpha\rangle), \quad (3.9)$$

$$|1\rangle = \frac{1}{\mathcal{N}(0)} (i|\alpha\rangle + |-i\alpha\rangle). \quad (3.10)$$

Photon loss does not bring these states close to each other for the same reason as the coherent states; they are separated by the phase of the coherent state, rather than just photon number. The $|+\rangle$ and $|-\rangle$ states of this code, which are called four legged cat states since they are linear superpositions of four coherent states, are similar to the even and odd cat states of the original cat code, but instead of having a non-zero occupation probability, $P(n)$, for every other number state, $n \equiv 0 \pmod{2}$ and $n \equiv 1 \pmod{2}$, they have a non-zero occupation probability for every fourth number state, $n \equiv 0 \pmod{4}$ and $n \equiv 2 \pmod{4}$:

$$|+\rangle \propto \frac{\alpha^0}{\sqrt{0!}} |0\rangle + \frac{\alpha^4}{\sqrt{4!}} |4\rangle + \frac{\alpha^8}{\sqrt{8!}} |8\rangle + \dots \quad (3.11)$$

$$|-\rangle \propto \frac{\alpha^2}{\sqrt{2!}} |2\rangle + \frac{\alpha^6}{\sqrt{6!}} |6\rangle + \frac{\alpha^{10}}{\sqrt{10!}} |10\rangle + \dots \quad (3.12)$$

Photon loss makes all the states above transition to a common error space, which is spanned by odd number states, which does not overlap with the code space. A parity measurement qubit state can tell us whether a photon loss event has occurred or not, without giving information about the logical state and without the resulting state being a

part of the coding space, which allows us to perfectly correct for single photon loss events.

3.1. Landau-Zener physics

Focusing on the qubit, we now look at the transition dynamics of the two levels crossing. This is a very general problem with many applications, from collision between atoms [58] to quantum information which we will focus on here.

The Hamiltonian we consider is the general qubit Hamiltonian, with a time dependent qubit splitting and constant coupling:

$$H(t) = \Delta(t)\sigma_z + \delta\sigma_x. \quad (3.13)$$

Assuming that the level splitting varies linearly in time:

$$\Delta(t) = \nu_{LZ}t, \quad (3.14)$$

and that the coupling between the states is constant, the probability of diabatic transfer between the two basis states from the infinite past to the infinite future is given by the so called Landau-Zener formula.

To get some intuition, we can imagine how the system parameters might affect the transfer probability in two limits. If the crossing is very slow, we can use the adiabatic theorem, which makes it clear that the system will stay in its instantaneous eigenstates, which means fully transferring between basis states. On the other hand, if the crossing is very fast, we know that the system will stay in the initialized basis state by using the sudden approximation. Because of this, we know that the transfer probability will somehow depend on the “speed” of the crossing,

$$\nu_{LZ} = \frac{d\Delta(t)}{dt}, \quad (3.15)$$

i.e. how fast $\Delta(t)$ is changing. Fast and slow, however, must be compared to something, and it is only natural that this speed is somehow compared to the only other parameter of this model, the coupling, δ .

The Landau Zener formula, describing the probability of transfer between basis states, from a state prepared in the infinite past evolving to the infinite future, was derived in works published by Lev Landau

[59], Clarence Zener [60], Ernst Stückelberg [61], and Ettore Majorana [62] independently in 1932 and 1933:

$$P_{LZ} = e^{-2\pi \frac{2\delta^2}{\hbar v_{LZ}}}. \quad (3.16)$$

3.1.1. Landau-Zener-Stückelberg interferometry

We can now imagine that we drive the qubit periodically or in a more generalized way which leads to multiple level crossings. For periodic driving we can employ several theoretical approaches, such as Floquet theory or using the so-called dressed-state picture. For more general driving, we can employ a model called the adiabatic impulse model [63, 64]. Here we split the evolution of the system in an adiabatic region, far away from crossings, and non-adiabatic regions where we have level crossings. The adiabatic-impulse model is considered valid if the crossings are linear and well separated [64].

Adiabatic evolution

Far away from level crossings we assume that the system evolves adiabatically, meaning that there is no transfer between the instantaneous eigenstates, $\varphi_{\pm}(t)$, which are solutions to the time independent Schrödinger equation:

$$H(t)\varphi(t) = E(t)\varphi(t). \quad (3.17)$$

The wavefunction can generally be written in term on the adiabatic basis states as:

$$\psi(t) = \sum_{\pm} c_{\pm}(t)\varphi_{\pm}(t). \quad (3.18)$$

In the adiabatic approximation the occupation probability of the adiabatic basis states, are constant, while the phase evolves depending on the instantaneous eigenvalues, E_{\pm} between times t_i and t_f . This can be

described by the unitary matrix $U(t_i, t_f)$:

$$\begin{pmatrix} c_+(t_f) \\ c_-(t_f) \end{pmatrix} = U(t_i, t_f) \begin{pmatrix} c_+(t_i) \\ c_-(t_i) \end{pmatrix}, \quad (3.19)$$

$$U(t_i, t_f) = \begin{pmatrix} e^{-i\phi_+(t_i, t_f)} & 0 \\ 0 & e^{-i\phi_-(t_i, t_f)} \end{pmatrix}, \quad (3.20)$$

$$\hbar\phi_{\pm}(t_i, t_f) = \int_{t_i}^{t_f} E_{\pm}(t) dt. \quad (3.21)$$

Level crossing

We now have to treat the parts of the evolution where the levels cross. From the previous section, section 3.1, we know the probability of transfer between diabatic basis states for infinite-time propagation and linear crossings is given by the Landau-Zener formula. Assuming that the crossings are approximately linear, the questions still remain: Is this a good approximation for non-infinite crossings, and where do we say that this non-adiabatic region starts, and the adiabatic region from above ends?

It turns out that a good approximation is to consider the evolution to be adiabatic *everywhere* except the point of the crossing, where we imagine all the transfer between adiabatic basis state to happen in accordance with the Landau-Zener formula:

$$\psi(t_f) = \sum_{\pm} \left[\sqrt{1 - P_{LZ} c_{\pm}(t_f)} \varphi_{\pm}(t_f) + \sqrt{P_{LZ} c_{\mp}(t_f)} \varphi_{\mp}(t_f) \right]. \quad (3.22)$$

It has been shown that the scale of the duration of the transition can be estimated by the following [65]:

$$t_{LZ} \sim \frac{1}{\sqrt{2\hbar v_{LZ}}} \max\left(1, \frac{\delta}{\sqrt{2\hbar v_{LZ}}}\right), \quad (3.23)$$

which can be used to gauge whether the crossings are well separated.

The Landau-Zener formula, however, only gives the occupation probability after a level crossing. As we are interested in the effects of multiple level crossings, the phase of the occupation amplitude is important as well. We can keep track of the effects of the, now instantaneous, Landau-Zener transition by a unitary matrix, \hat{N} , still in

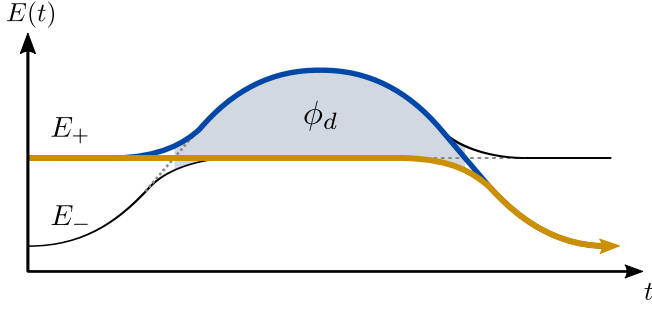


Figure 3.2.: Double level crossing. Adiabatic energy levels, E_{\pm} , as a function of time. The shaded area corresponds to the dynamical phase, ϕ_d . Path shown with arrows corresponding to the transfer from the adiabatic eigenstate φ_+ to the state φ_- .

the adiabatic basis, acting on the state vector:

$$\begin{pmatrix} c_+(t+\eta) \\ c_-(t+\eta) \end{pmatrix} = \hat{N} \begin{pmatrix} c_+(t-\eta) \\ c_-(t-\eta) \end{pmatrix}, \quad (3.24)$$

$$\hat{N} = \begin{pmatrix} \sqrt{1-P_{LZ}}e^{-i\phi_S} & -\sqrt{P_{LZ}} \\ \sqrt{P_{LZ}} & \sqrt{1-P_{LZ}}e^{i\phi_S} \end{pmatrix}, \quad (3.25)$$

$$\phi_S = -\frac{\pi}{4} + \frac{\delta^2}{2\hbar v_{LZ}} \left(\ln \frac{\delta^2}{2\hbar v_{LZ}} - 1 \right) + \arg \Gamma \left(1 - i \frac{\delta^2}{2\hbar v_{LZ}} \right), \quad (3.26)$$

for an infinitesimal time, η , before/after the transition, and where ϕ_S is a geometric phase, the so-called Stokes phase, and $\arg \Gamma$ is the argument of the gamma function [64].

Two crossings

We now have the tools to look at multiple crossings, and so we can look at the simplest possible case of two crossings, see figure 3.2. Starting with some initial state $\psi(t_0)$, written in the adiabatic basis, the state after two crossings is given by:

$$\psi(t_f) = \hat{N} \hat{U} \hat{N} \psi(t_0) \quad (3.27)$$

The probability of transferring from the φ_+ state to the φ_- state, the paths drawn by blue and orange arrows in figure 3.2, is given by:

$$P_{+\rightarrow-} = 2(1-P_{LZ})P_{LZ}(1+\cos(\phi_d+2\phi_S)), \quad (3.28)$$

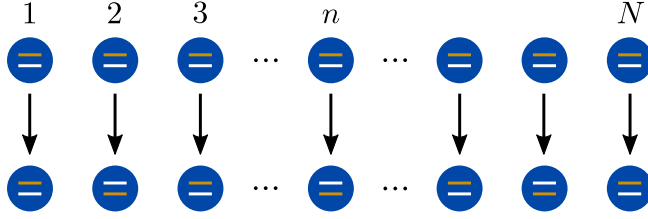


Figure 3.3.: Array of qubits, indexed from 1 to N . We want to transfer every second qubit from the $|1\rangle$ state to the $|0\rangle$ state. The qubits have the same x -coupling turned on, but they all have different qubit splittings, which is proportional to the qubit index.

where ϕ_d is the dynamical phase:

$$\hbar\phi_d = \int_{t_i}^{t_f} E_+(t)dt - \int_{t_i}^{t_f} E_-(t)dt, \quad (3.29)$$

which we can interpret as the area between the two instantaneous energy levels, E_{\pm} , in an energy-time diagram. This is illustrated as the shaded area in figure 3.2.

3.1.2. Landau-Zener-Stückelberg state engineering

In the next section we use a technique inspired by Landau-Zener-Stückelberg interferometry to engineer a cat state in a bosonic mode using a qubit. To get some intuition on how we are able to do this, we look at a slightly simpler example system, a set of N independent qubits, indexed from 1 to N .

The state we want to engineer is putting every second qubit in the $|0\rangle$ state, while keeping the other qubits in the $|1\rangle$ state, see figure 3.3. We are going to do this by initializing all the qubits in the $|1\rangle$ state, and then apply the same driving to all the qubits. All qubits have the same σ_x coupling, with amplitude δ , while the qubit splitting is depends on the qubit number. For simplicity, we work in units where $\hbar = 1$. The Hamiltonian of this system is the following:

$$H = \sum_{n=1}^N (\Delta_n \frac{\omega_0}{2} + \varepsilon(t))\sigma_z^{(n)} + \delta\sigma_x^{(n)}, \quad (3.30)$$

where $\sigma_{z/x}^{(n)}$ are the spin 1/2 operators for qubit n , $\Delta_n = n + \lambda$, and $\Delta_n\omega_0$ is the qubit splitting of qubit n , where ω_0 is the scale for the qubit

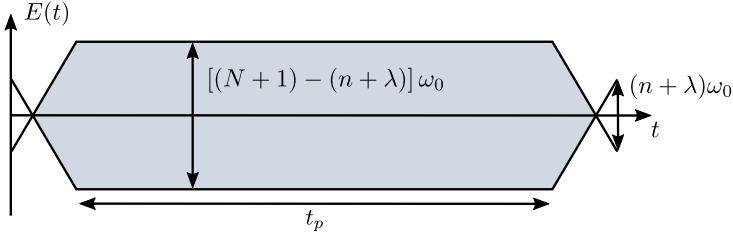


Figure 3.4.: Spectrum of qubit n during Landau-Zener-Stückelberg engineering.

splittings, and $\varepsilon(t)$ is the time dependent driving. The offset, λ , is for the time being a free parameter.

We apply driving to the qubits $\varepsilon(t)$ which drives the qubit splitting in such a way that all qubits experience two level crossings, with some waiting time in between, t_p . Explicitly, the driving we apply is the following:

$$\varepsilon(t) = \begin{cases} -vt, & t \leq t_1 \\ -(N + 1)\omega_0/2, & t_1 < t < t_1 + t_p \\ -(N + 1)\omega_0/2 + v[t - (t_1 + t_p)], & t_1 + t_p \leq t < 2t_1 + t_p \end{cases}$$

where v is the speed of driving during the level crossing, and $t_1 = [(N + 1)\omega_0/2] / v$ is the time the linear driving persists, t_p is the wait time that we later will tune to get the desired state. The driving is maximally $(N + 1)/\omega_0$ in amplitude, to make sure that all qubits experience level crossings. We set $v = \frac{\pi\delta^2}{\ln(2)}$ such that $P_{LZ} = 1/2$. The reason for this is that we essentially are making an interferometer, and this is required to achieve total constructive/destructive interference. The energy spectrum of one of the qubits, n , during the driving can be seen sketched in figure 3.4.

Every qubit is independent, so we focus on a general qubit with index n . We know the probability of transfer from the $|1\rangle$ state to the $|0\rangle$ state after two crossings from the previous section, equation (3.28):

$$P_{1 \rightarrow 0} = \frac{1}{2} [1 + \cos(\phi_d(n) + 2\phi_S)], \quad (3.31)$$

where the Stokes phase, $\phi_S \approx -1.08$ is constrained by the condition $P_{LZ} = 1/2$. The dynamical phase, $\phi_d(n)$, corresponds to the shaded area in figure 3.4.

If we for simplicity assume that coupling is very strong, the speed v becomes large because of the $P_{LZ} = 1/2$ condition. This means that the dynamical phase can be approximated by the dynamical phase gained in the region where the driving term is constant:

$$\phi_d(n) = [(N + 1) - (n + \lambda)] \omega_0 t_p. \quad (3.32)$$

With this, we see from equation (3.31), that one possible condition for engineering the desired state is the following:

$$[(N + 1) - (n + \lambda)] \omega_0 t_p + 2\phi_S = [(N + 1) - n] \pi. \quad (3.33)$$

The reasoning is that this means that qubits with even qubit indices will satisfy, $P_{1 \rightarrow 0} = 1$, which fully puts these in the $|0\rangle$ state, while the qubits with odd qubit indices satisfies $P_{1 \rightarrow 0} = 0$, which means that these stay in the $|1\rangle$ state.

After we set $\lambda = \frac{2\phi_S}{\omega_0 t_p}$ to compensate for the Stokes phase, the condition simplifies to give us the timing of the driving pulse, t_p :

$$t_p = \pi / \omega_0. \quad (3.34)$$

Notice that this is independent of the qubit index, n , and so setting $t_p = \pi / \omega_0$ puts all the qubits in the desired state, every even qubit is transferred from the initialized $|1\rangle$ state to the $|0\rangle$ state and every odd qubit stays $|1\rangle$ state.

3.2. Landau-Zener-Stückelberg engineering of cat states

We now have all the components needed in order to show the method we have proposed for engineering Schrödinger cat states in paper [1], and possibly more complicated states, such as multi legged cat states.

We will now combine the two systems previously discussed, a qubit and a bosonic mode. What we will describe here works for a general system, with a general qubit and a general boson cavity. To keep things concrete, we will for the rest of the discussion imagine a qubit (e.g. a semiconductor quantum dot qubit, or a superconducting qubit) which is coupled to a (superconducting) transmission line cavity, acting like

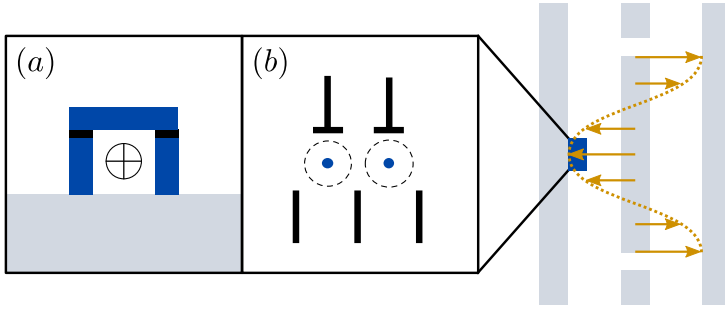


Figure 3.5.: Example hybrid system with transmission line and a qubit. The superconducting high is shown on right. the dotted line and the arrows show the magnitude of the electric field from the transmission line. In the inset to the left we see some possible qubit choices. (a) Schematic of a superconducting cooper pair box qubit, consisting of two josephson junctions, controlled by a magnetic flux penetrating the device. The black regions are isolators and the colored region is superconducting. (b) Schematic of a double quantum dot controlled by gates.

a harmonic oscillator, where the excitations are microwave photons, see figure 3.5.

We assume that we start with the microwave cavity in a coherent state. Motivated by the odd and even states from earlier, our goal is to design a driving pattern which “filters” out all the even/odd photon number occupation probabilities, which is accomplished by the Landau-Zener-Stückelberg engineering introduced earlier. This filtering leaves the system in an odd/even cat state.

The Hamiltonian of the system we look at is the tensor product of the qubit Hamiltonian and the photon cavity Hamiltonian, with some coupling between the systems:

$$H = \underbrace{\frac{\Delta(t)}{2}\sigma_z}_{H_{\text{qubit}}} + \underbrace{\hbar\omega a^\dagger a}_{H_{\text{photon}}} + \underbrace{\hbar A(a + a^\dagger)\sigma_x}_{H_{\text{coupling}}}, \quad (3.35)$$

where $\sigma_{z/x}$ are the z and x Pauli matrices, acting on the qubit subspace, a^\dagger is the creation operator in the cavity, $\Delta(t)$ is the time dependent qubit splitting, ω is the angular frequency of the cavity, and A is the

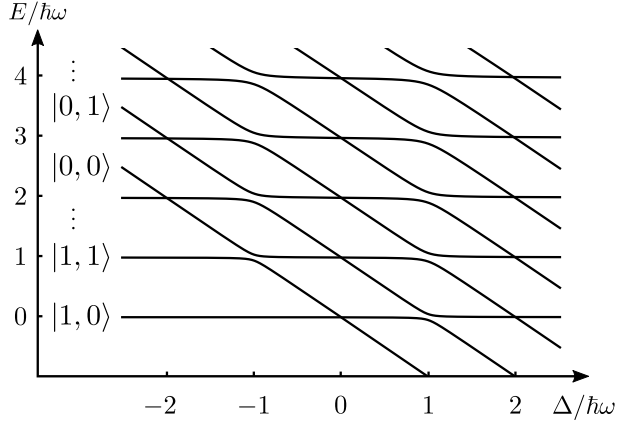


Figure 3.6.: Spectrum of the Hamiltonian, H , as a function of the qubit splitting, Δ , where $A/\omega = 0.05$. The labels $|i, n\rangle$ indicate the basis states the qubit in state $|i\rangle$ and n photons in the cavity, $|n\rangle$.

coupling strength between the cavity and the qubit. Unity matrices in spin space are implied for terms which do not contain Pauli matrices.

In figure 3.6 we can see a sketch of the spectrum of the Hamiltonian above, H , as a function of the qubit splitting, Δ . The labels $|i, n\rangle$ indicate the basis states $|i\rangle_{\text{qubit}} \otimes |n\rangle_{\text{photon}}$.

As expected from the coupling above, we see avoided level crossings when two states cross in energy which have a photon number n , which differ by one, $n \pm 1$. Additionally, it is worth noting that the avoided level crossings get larger for large photon numbers. This is because of the coupling being proportional to the creation/annihilation operators:

$$a|n\rangle = \sqrt{n}|n-1\rangle, \quad (3.36)$$

$$a^\dagger|n\rangle = \sqrt{n+1}|n+1\rangle. \quad (3.37)$$

In our proposal, we drive Δ in the region around the 1-photon resonance, close to $\Delta/\hbar\omega = -1$ in figure 3.6. In this regime, every state is coupled (approximately) only to one other state:

$$\langle 1, n|H|0, n+1\rangle = \hbar A\sqrt{n+1}. \quad (3.38)$$

Every other matrix element is assumed to be zero. This assumption is good as long as $2\omega \gg A\sqrt{n+1}$, essentially meaning that we are far away from the other avoided level crossing. This isolation of levels in

pairs, $|0, n\rangle$ and $|1, n + 1\rangle$ is equivalent to the so-called rotating wave approximation, which effectively gives us the Jaynes-Cummings model [66]:

$$H_{\text{JC}} = \frac{\Delta(t)}{2}\sigma_z + \hbar\omega a^\dagger a + \hbar A(a\sigma_+ + a^\dagger\sigma_-). \quad (3.39)$$

3.2.1. Connection to the toy model in section 3.1.2

Since we now have reduced the problem to pairs of levels it is simple to connect this to the toy model in section 3.1.2. Every pair of states, $|0, n\rangle$ and $|1, n + 1\rangle$, is essentially an isolated two-level system, analogous to the qubits of the toy system which do not interact with the other qubits. The individual pair of states, have the Hamiltonian:

$$H_{\text{pair}}^{(n)} = n + \frac{\Delta(t)}{2}\sigma_z + \hbar A\sqrt{n+1}\sigma_x. \quad (3.40)$$

We can see that similarly to the toy model all the qubit splittings are driven in the same way, given by $\Delta(t)$. Contrary to the toy model this model has the exact same qubit splitting for all “qubits”, and so if there is going to be a difference in dynamical phase, this must come from the qubit coupling, which is dependent on the index (the photon number, n) of the “qubit”.

3.2.2. Protocol for generating cat states from coherent states

The process which allows us to gain a different dynamical phase between each “qubit” is a fully adiabatic Landau-Zener transition. In figure 3.6 we saw that the “avoidedness” depends on the photon number, n , and so the dynamical phase acquired in the adiabatic evolution (the area under the curve in an energy-time diagram) through such a transition is n dependent.

We propose driving the system through three linear Landau-Zener transitions in the following way:

1. Drive the system through a single LZ transition, at a speed corresponding to $P_{\text{LZ}} = 1/2$.
2. Drive the system through a very slow, approximately adiabatic transition, $P_{\text{LZ}} = 1$.

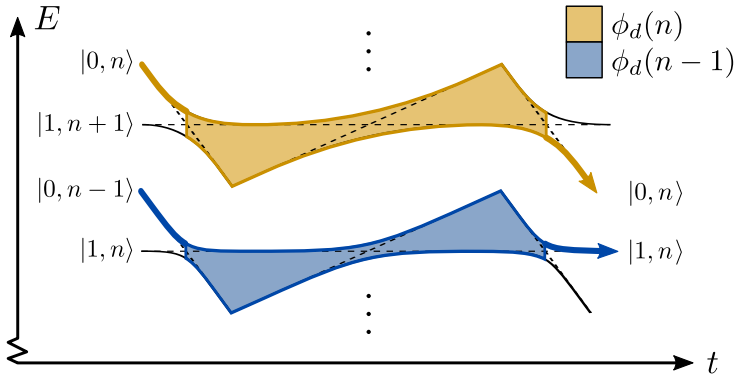


Figure 3.7.: Two pairs of coupled levels as a function of time through the driving proposed for cat state engineering. The n -dependent dynamical phase is indicated by the blue/orange shaded area. The blue/orange arrow and lines show the occupation probability of the respective states. Showing how the different dynamical phase, ends up giving different occupation probabilities.

3. Lastly, drive the system through a LZ transition, at a speed corresponding to $P_{LZ} = 1/2$.

The spectrum of the system under such driving is sketched in figure 3.7 for two adjacent independent level pairs. Due to the n -dependent coupling, the dynamical phase difference, ϕ_d , gained between the Landau-Zener transition at the beginning and end, is also n -dependent. The dynamical phase, ϕ_d , can be engineered in such a way that every other pair experiences a transfer between the two states in the pair, while the other pairs stay in the initial state, as shown by the arrows in figure 3.7. Because of this, the final step in the procedure is to filter out all the states which have transferred by projecting onto the $|0\rangle$ qubit state, which can be done by performing a measurement on the qubit, and requiring that the outcome of this measurement to be $|0\rangle$ in order for the procedure to be successful.

It is here worth noting that this post selection is done in order to make the best possible even and odd cat states. If the goal is simply to create even/odd parity states or that the fidelity of the state is less important than the success rate of the procedure, which would be $\approx 50\%$, the post selection can be dropped at the cost of fidelity. The

reason is that the process of transferring for a given pair, n , takes the state from $|0, n\rangle$ to $|1, n + 1\rangle$. This makes all even/odd states odd/even, while the states that are already odd/even, are left alone.

Just like in the toy example we get the desired engineered state by requiring that the phase gained between the two crossings, the dynamical phase ϕ_d and the geometric Stokes phase ϕ_S , differs by π from one pair, n , to the next, $n + 1$:

$$d(n) = [\phi_d(n + 1) + 2\phi_S(n + 1)] - [\phi_d(n) + 2\phi_S(n)] = \pi. \quad (3.41)$$

This condition makes it so that $\phi_d(n) = \phi_d(0) + n\pi$. The parity (even or odd) of the state can be tuned, by tuning $\phi_d(0)$, which can be done by tuning something that is the same for all states, such as at what energy the driving switch direction.

Unlike the toy model, this difference in phase difference, $d(n)$, is dependent on the photon number n . Which means that we have to choose a photon number to optimize for. To minimize the error, we naturally choose the peak of the coherent state $n = |\alpha|^2$.

Furthermore, it is worth noting that unlike the toy model the Stokes phase as well as the first and last Landau-Zener transitions, are also n dependent, since they depend on the coupling. However, the error which comes from these contributions get small for large coherent states, with $|\alpha|^2 \gg 1$. For the following we assume that these are n -independent.

With these assumptions the dynamical phase difference between adjacent pairs can be approximated by calculating the instantaneous energies. From the time independent Schrödinger equation assuming that we change sweep directions at $-\hbar\omega \pm \hbar k$, where $k < \omega$, see figure 3.7, we find the following expression for the phase difference between adjacent pairs:

$$d(n) = \frac{2\hbar A^2}{v^*} \left[\ln \left(\frac{k^2}{A^2 [n + 1]} \right) - \frac{1}{2 [n + 1]} \right], \quad (3.42)$$

assuming that $A^2 n \gg k^2$. Where we use an average over the fast driving speed, v_f , of the first and last crossing, and the slow driving speed, v_s of the middle crossing:

$$v^* = \frac{v_f + v_s}{v_f v_s}. \quad (3.43)$$

We can now see that we are able to satisfy condition from equation (3.41) for a given n close to the expectation value for the photon number of the state, $|\alpha|^2$.

We can furthermore use equation (3.42) to estimate contribution to the infidelity of the state due to the n -dependence of this phase difference. The details can be seen in paper [III], but it can be shown that this contribution to the infidelity does not decrease with rising $|\alpha|^2$ as the other errors mentioned above. However, the contribution to the infidelity approaches $\hbar A^2/v^*$ for large $|\alpha|^2$. One could in principle, therefore, tune $\hbar A^2/v^*$ as small as one would like, but due to additional constraints, such as the adiabaticity of the middle crossing, it could be inconvenient in practice.

3.2.3. Numerical simulations

To investigate the analytic results we found in the previous section, we can do numerical simulations of the proposed scheme. We here solve the Schrödinger equation using QuTiP, “Quantum toolbox in python” [67, 68]. We initialize the system in one qubit state, $|0\rangle$ or $|1\rangle$, and the bosonic mode in a coherent state, $|\alpha\rangle$. For simplicity, we here work in units where $\hbar = 1$. The Hilbert space of the bosonic mode is truncated at $n \geq 2|\alpha|^2 + 10$ in the simulations. The driving is done as in figure 3.7, and is explicitly given by:

$$\Delta(t) = \begin{cases} -\omega - k + v_f t, & 0 \leq t \leq \tau_1, \\ -\omega + k - v_s(t - \tau_1), & \tau_1 \leq t \leq \tau_2, \\ -\omega - k + v_f(t - \tau_2), & \tau_2 \leq t \leq \tau_3, \end{cases} \quad (3.44)$$

where $\tau_1 = 2k/v_f$, $\tau_2 = \tau_1 + 2k/v_s$, and $\tau_3 = \tau_2 + 2k/v_s$.

The numerical results presented in figure 3.8 are the occupation probability, $P(n)$, in the Fock basis (top) and the Wigner functions, $W(\alpha)$, (bottom) after a projection to the $|0\rangle$ qubit state. The Wigner function is a quasi probability function, which gives the right probability function by integrating out one of the conjugate variables, in this case photon number (radially) and phase (angle) [69]. The initial coherent state is of size $|\alpha|^2 = 10$, the coupling is set to $A = 0.003$, and where $v_f = 8.9741 \times 10^{-4}$ is set by demanding that $P(10) = 1/2$. The other parameters $v_s = 4.6965 \times 10^{-5}$ and $k = 0.50017$ are set by equation (3.42) and to tune $\phi_d(0)$ respectively.

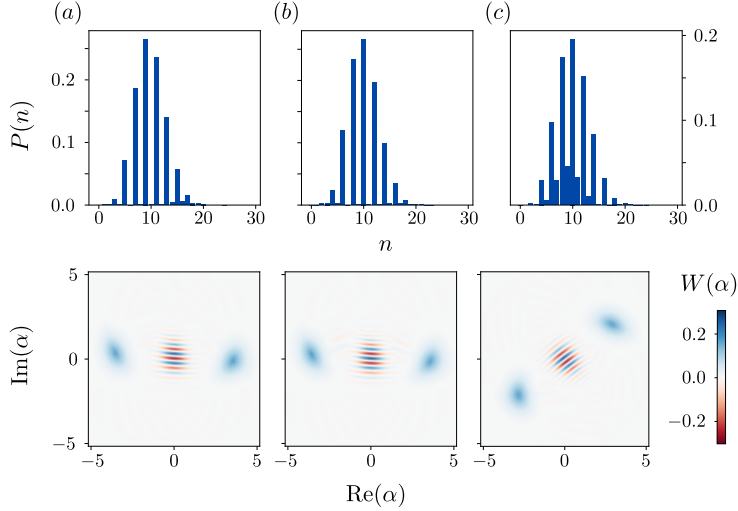


Figure 3.8.: Numerical simulations of the final boson mode states visualized by the occupation probability, $P(n)$, in the Fock basis (top) and the Wigner functions, $W(\alpha)$ (bottom) after a projection to the $|0\rangle$ qubit state. All the simulation above are initialized with the boson mode in a coherent state with $|\alpha|^2 = 10$ and a coupling of $A = 0.003$. The sweep speeds v_f and v_s is set by the conditions $P_{LZ}(10) = 1/2$ and $d(10) = \pi$. In (a,b) we fine tune $k = 0.50017$, which yields, (a) an odd cat state if the qubit is initialized in $|0\rangle$ giving a fidelity of $F = 0.986$, and (b) an even cat state if the qubit is initialized in $|1\rangle$ with fidelity $F = 0.989$. Not fine tuning k produces a more general cat state (c), in this case with $k = 0.49$ results in a cat state with $\theta_s = 0.713\pi$ (from equation (3.3)) with a fidelity of $F = 0.988$.

Visually we can see from both the Fock state occupation probabilities and the Wigner functions, that we have approximately created the desired even and odd states well, but to quantify exactly how well we have recreated the desired state we calculate the overlap of the final state, $|\Psi_F\rangle$, with the desired state, $|\Psi_D\rangle$, which we will call the fidelity of the state:

$$F = |\langle \Psi_f | \Psi_D \rangle|^2. \quad (3.45)$$

For all the examples in figure 3.8, we end up with a fidelity of $F \approx 0.99$.

3.2.4. Encoding qubit information in cat code

In figure 3.8 we saw that the boson mode could end up in either the odd or even cat state, depending on whether the qubit was initialized in the $|0\rangle$ or $|1\rangle$ states respectively. What this allows us to do, is to encode the qubit in a rotated cat code, where a general qubit state

$$|\Psi_{\text{qubit}}\rangle = a|0\rangle + b|1\rangle, \quad (3.46)$$

gets approximately encoded in the bosonic state:

$$|\Psi_{\text{cavity}}\rangle \approx a|\Psi_{\text{odd}}\rangle + e^{i\varphi}b|\Psi_{\text{even}}\rangle, \quad (3.47)$$

where the phase $\varphi \approx -1.08$ comes from taking a different path, and picking up a different geometric phase. This phase is however known and can be compensated for.

Multi legged cats

Additionally, one could produce multi legged cat states discussed earlier by repeating the procedure above m times, to create 2^m legged cat states. One could imagine making the four legged cat states discussed earlier by now starting with the cat state produced by the scheme proposed above, and tweaking the condition in equation (3.41), demanding that $d(n) = \pi/2$. This would make every fourth pair experience a transfer, instead of every second as discussed above.

In this case the post selection by a projective measurement to the $|0\rangle$ qubit state is essential to keep the parity of the initial state (keeping the state being made up of only even or odd Fock states). As a result, the success rate of creating higher order multi legged cat states using this method is exponentially suppressed the number of iterations, but linear in the number of legs.

Generation of GHZ states with spin-qubit/magnon system

The GHZ state was first studied by Daniel Greenberger, Michael Horne and Anton Zeilinger [70] as an example of an extremely non-classical state, in this case a four qubit state, where a classical theory cannot describe the correlations in the measurements of the qubits. This is a generalization of Bells theorem [71], where it can be shown that correlations between two entangled particles *can* be larger than any classical theory predicts. However, classical theory show the same results as quantum mechanics for certain measurement angles. The generalization in the GHZ case is to make definite predictions, for all measurement angles.

A Greenberger-Horne-Zeilinger (GHZ) state consists of at least 3 subsystems, qubits or qudits (generalized qubits with multiple levels). We here only consider the 3 qubit GHZ state, but what follows can be generalized to larger GHZ states. The 3 qubit GHZ state is defined as:

$$|\text{GHZ}\rangle = \frac{|000\rangle + |111\rangle}{\sqrt{2}}, \quad (4.1)$$

where $|\sigma_1\sigma_2\sigma_3\rangle = |\sigma\rangle_1 \otimes |\sigma\rangle_2 \otimes |\sigma\rangle_3$ for the qubits 1, 2 and 3, where $\sigma = \{0, 1\}$.

Many more applications have been found for these GHZ states, such as secret sharing between three people [72, 73], splitting quantum information by quantum teleportation to two people [72], and is used in a constant-time solution of the quantum version of the Byzantine agreement [74].

Quantum error correction also has applications for GHZ states. The simplest error correction scheme in section 2.2.1 which can correct for a single general error, Shor's error correction scheme [29], effectively creates three entangled qubits states made up of GHZ states. These are typically made by using the universal gates of a quantum computer using several pulses, however, they can be prepared outside the quantum computer and be used as a resource. In paper [11], we show a way of creating these GHZ states using a single pulse, using three spin qubits coupled via an exchange interaction to an anisotropic ferromagnet. The advantage of which is the robustness against qubit asymmetries,

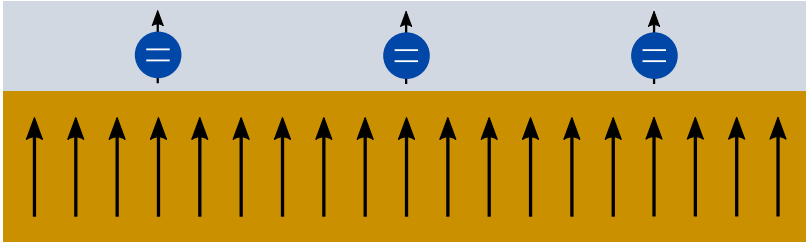


Figure 4.1.: Figure of the system, with a ferromagnet substrate (orange) and the three spin qubits coupling to the ferromagnet through an exchange interaction.

and that only a single timed pulse is needed in order to entangle the three qubits. In the following we explore this system and finally show how one can generate the GHZ state. The following is based on paper [11].

4.1. Spin qubit coupled to magnonic cavity

The system we are looking at in this chapter is that of a bosonic mode (magnons in a ferromagnet) interacting with two-level systems (spin qubits) through the exchange interaction. What we will show is that this system with a single spin qubit effectively is an ideal manifestation of the Jaynes-Cummings model [66] and that through the introduction of anisotropy in the ferromagnet the system effectively becomes a physical realization of the quantum Rabi model, with tunable interaction terms through the anisotropy. Introducing three spin qubits in this quantum Rabi model we show that we are able to excite all three qubits using a single control pulse, and that driving the qubits through half of such a transition creates the GHZ states.

The quantum Rabi model is used to understand the interaction between light and matter [75, 76], as it describes a bosonic mode that interacts with a single two-level system and which under the rotating wave approximation (an approximation which can be applied near resonance in the quantum Rabi model, where rapid oscillating terms are neglected) becomes the Jaynes-Cummings model [77]. Because of this, in addition to the application we propose, this system can be a

good platform in investigating both the Jaynes-Cummings model and the quantum Rabi model.

4.1.1. Magnon mode

We assume that we work with a thin film of an insulating ferromagnet that will act as the magnon cavity. With an applied magnetic field out of the plane of the thin film, $H_0 \hat{z}$, we can write the Hamiltonian of the ferromagnet as:

$$H_F = |\gamma| \mu_0 H_0 \sum_i S_{iz} - J \sum_{\langle i,j \rangle} \vec{S}_i \cdot \vec{S}_j, \quad (4.2)$$

where S_i is the spin operator at position i , J is the ferromagnetic coupling between nearest neighbors (where angled brackets signifies that the sum is over nearest neighbors), γ is the gyromagnetic ratio, μ_0 is the permeability of free space, and we use units where $\hbar = 1$.

We rewrite this Hamiltonian in what will become spin excitations, i.e. magnons, by first writing it in terms of the raising and lowering operators:

$$S_{j\pm} = S_{jx} \pm iS_{jy}. \quad (4.3)$$

These raising and lowering operators act like bosonic ladder operators, in that they raise and lower the spin. However, we have to make sure that the commutation relations are correct. We know that for a boson operator a , we have the following commutation relation, $[a_i^\dagger, a_j] = \delta_{ij}$, while the Spin operators should follow $[S_+, S_-] = 2S_z$. The result is the Holstein-Primakoff transformation[78]:

$$S_{j+} = \sqrt{2S - n_j} a_j^\dagger, \quad (4.4)$$

$$S_{j-} = \sqrt{2S - n_j} a_j, \quad (4.5)$$

$$S_{jz} = S - a_j^\dagger a_j, \quad (4.6)$$

where $n_j = a_j^\dagger a_j$ is the number operator for magnon excitations, and S is the spin magnitude. We can now see that we have written the Hamiltonian in terms of the number of spin excitations n away from the ground state where all the spins point along the z -axis and have a

spin projection of $S_{jz} = S$, and we can also see that the commutation relations of the spin operators still hold.

Further, we assume that we are in the low excitation number limit, $S \gg \langle n \rangle$, meaning that the Zeeman energy is relatively large compared to other energies, such as excitations and later anisotropies that we will introduce, meaning that the spins are mostly aligned in the z -direction. To lowest order in n we are left with the operators:

$$S_{j+} = \sqrt{2S} a_j^\dagger, \quad (4.7)$$

$$S_{j-} = \sqrt{2S} a_j, \quad (4.8)$$

$$S_{jz} = S - a_j^\dagger a_j. \quad (4.9)$$

We can now introduce this transformation in the Heisenberg Hamiltonian, and introducing the Fourier transform of the boson operators:

$$a_{\vec{k}} = \frac{1}{\sqrt{N}} \sum_i a_i e^{i\vec{k} \cdot \vec{r}_i}, \quad (4.10)$$

$$a_{\vec{k}}^\dagger = \frac{1}{\sqrt{N}} \sum_i a_i^\dagger e^{-i\vec{k} \cdot \vec{r}_i}, \quad (4.11)$$

where N is the number of spin sites. $a_{\vec{k}}$ is the annihilation operator for a magnon with the momentum \vec{k} . Discarding higher order terms in n , the Hamiltonian we are left is:

$$H_I = E_0 + \sum_{\vec{k}} \omega_{\vec{k}} a_{\vec{k}}^\dagger a_{\vec{k}}, \quad (4.12)$$

where

$$E_0 = -6NJS^2/2 - |\gamma|\mu_0 H_0 SN, \quad (4.13)$$

is the energy of the classical ground state, and the eigenfrequency of the mode is given by:

$$\omega_{\vec{k}} = -|\gamma|\mu_0 H_0 + 4JS(3 - (\cos(k_x a) + \cos(k_y a) + \cos(k_z a))), \quad (4.14)$$

where a is the lattice spacing.

Anisotropy

Next we assume that we have some source of anisotropy, this could come from dipolar interactions or magnetocrystalline single-ions, but the form in which we introduce the anisotropy is general:

$$H_A = \sum_i K_x(S_{ix})^2 + K_y(S_{iy})^2 + K_z(S_{iz})^2. \quad (4.15)$$

Applying the Hollstein-Primakoff transformation from equation (4.7), and the Fourier transform from equation (4.10) to the anisotropy term, H_A , we get the following full ferromagnet Hamiltonian, where we have left out the constant terms:

$$H_F = H_I + H_A = \sum_{\vec{k}} A_{\vec{k}} a_{\vec{k}}^\dagger a_{\vec{k}} + B_{\vec{k}} (a_{\vec{k}}^2 + a_{\vec{k}}^{\dagger 2}), \quad (4.16)$$

where

$$A_{\vec{k}} = -|\gamma|\mu_0 H_0 + K_x S + K_y S + 2K_z S + 4JS[3 - (\cos(k_x a) + \cos(k_y a) + \cos(k_z a))], \quad (4.17)$$

$$B_{\vec{k}} = (K_x S + K_y S) / 2. \quad (4.18)$$

For the rest of this discussion, we will focus on the $k = 0$ mode of the cavity. This can be justified by assuming a small magnet. In this case the higher modes are separated by energies of multiple times the qubit splittings (which is typically a few gigahertz).

We see that the anisotropy, specifically in the x - and y -direction, takes us away from the magnon being the eigenmode of the system. We can find the eigenmode of the system by introducing a final transformation. Assuming that the eigenmode of the system is some linear combination of the creation and annihilation operator of the magnon mode, we get the Bogoliubov transformation:

$$\alpha = ua + va^\dagger, \quad (4.19)$$

$$\alpha^\dagger = u^* a^\dagger + v^* a, \quad (4.20)$$

where the star signifies complex conjugation.

Using the fact that we still want this mode to follow bosonic statistics, we know that the commutation relations have to be equal to the magnon mode:

$$[\alpha, \alpha^\dagger] = (|u|^2 + |v|^2)[a, a^\dagger]. \quad (4.21)$$

Which leaves us with the constraint, $(|u|^2 + |v|^2) = 1$. By now requiring that the Hamiltonian is on the form:

$$H_F = \tilde{\omega}_0 \alpha^\dagger \alpha, \quad (4.22)$$

we obtain:

$$v = -2B/\sqrt{(A + \tilde{\omega}_0)^2 - 4B^2}, \quad (4.23)$$

$$u = \sqrt{1 - v^2}, \quad (4.24)$$

where the eigenmode energy is given by:

$$\tilde{\omega}_0 = \sqrt{A^2 - 4B^2} \quad (4.25)$$

The eigenmode, α , of the cavity is a slightly modified magnon, which we will refer to as squeezed magnons.

4.1.2. Spin qubit

The qubit we consider is a spin qubit, which for the purposes here can be thought of as a single confined electron. The spin up and down states of the electron correspond to the $|g\rangle$ and $|e\rangle$ states respectively¹. Full control of the qubit can be gained by applying external magnetic fields, but here we imagine only lifting the spin-degeneracy by applying a magnetic field along the z -direction, which gives us the spin-qubit Hamiltonian:

$$H_q = \frac{\omega_q}{2} \sigma_z, \quad (4.26)$$

where ω_q is the qubit splitting induced by the magnetic field.

4.1.3. Interaction between the magnon mode and the qubit

We assume that the main interaction between the two subsystems is an exchange interaction between the spin of the qubit and the spins of the ferromagnet. Since the electrons in the ferromagnet are in close proximity to the electrons in the qubit, there is an overlap in

1. We here use $|g\rangle$ and $|e\rangle$ to describe the two states of the qubit, and not $|0\rangle$ and $|1\rangle$, to avoid confusion with the 0 and 1 excitation states of the magnon mode and to be consistent with the notation in paper [11].

the wavefunctions of the two. Assuming there is an overlap of the wavefunction we get a non-zero exchange interaction parameter J_{int} :

$$H_{\text{int}} = J_{\text{int}} \sum_i \vec{S}_i \cdot \vec{s}_i, \quad (4.27)$$

where \vec{s}_i denotes the spin operator of the spin qubit at location i , and \vec{S}_i denotes the spin operator of the ferromagnet at spin. We note that such a transition is spin conserving, as opposed to a non-conserving interacting such as a dipolar interaction, meaning that spin is transferred between the qubit and the ferromagnet in a conserved manner. In terms of the qubit spin operators and the magnon operator this gives the following Hamiltonian:

$$H_{\text{int}} = g(a^\dagger \sigma_- + a \sigma_+), \quad (4.28)$$

where $\sigma_\pm = (\sigma_x \pm i\sigma_y)/2$ are the raising and lowering operators for the qubit, and g is the coupling amplitude. The qubit, the isotropic ferromagnet, and this interaction term is then a manifestation of the Jaynes-Cummings model:

$$H_{\text{JC}} = H_I + H_q + H_{\text{int}}. \quad (4.29)$$

Interaction in terms of squeezed magnons

Taking the interaction from above, H_{int} , and applying the Bogoliubov transformation we used to diagonalize the anisotropic ferromagnet Hamiltonian, H_F , we obtain the interaction in terms of the squeezed magnons:

$$H_{\text{int}} = g_R(\alpha^\dagger \sigma_- + \alpha \sigma_+) + g_{CR}(\alpha^\dagger \sigma_+ + \alpha \sigma_-), \quad (4.30)$$

where the amplitudes $g_R = gu$ and $g_{CR} = gv$. This is the interaction terms of the Rabi model, however, the rotating and counter rotating terms are usually equal in typical models. In this model they generally not equal and their relative magnitudes are even tunable via the squeezing, which is in term controlled by the anisotropy in the plane.

4.2. Generating GHZ states in qubits using coupling to the magnon mode

We are now going to show that we are able to prepare three qubits in the GHZ that we have talked about. The ingredients that we need is

the planar anisotropic ferromagnet, and three spin qubits, which are coupled to the ferromagnet via the exchange interaction between the qubits and the ferromagnet. We assume that the qubits are individually coupled to the same squeezed magnon mode. This gives us the Hamiltonian:

$$H = H_F + \sum_{n=1}^3 H_q^n + H_{\text{int}}^n, \quad (4.31)$$

where the superscript n labels the Hamiltonians of the three spin qubits and their interaction with the ferromagnet, which is given by equation (4.26) and equation (4.30) respectively. We are going to assume that the qubits are general, and so the method that we will present is robust against qubit asymmetries such as slightly different qubit splittings and couplings to the ferromagnet.

What we will show is that there is a coupling, g_{eff} , between the two states $|1, ggg\rangle$ and $|0, eee\rangle$, where the first index refers to the squeezed magnon number and the latter is the state of the three qubits, (e)xcited or in the (g)round state. By initializing in one of these two states, e.g. $|1, ggg\rangle$, and tuning the system close to the resonance between these two states, e.g. by tuning the qubit splitting such that $\omega_0 \approx 3\omega_q^2$, we can induce Rabi oscillations which make the system oscillate between the two states.

Tuning the system close to resonance, the system experiences Rabi oscillations, and evolve after a time t in the following way:

$$|\Psi\rangle(T) = \cos(g_{\text{eff}}t) |1, ggg\rangle + \sin(g_{\text{eff}}t) |0, eee\rangle. \quad (4.32)$$

Keeping the system at resonance for a time $t = \frac{\pi}{4}/g_{\text{eff}}$ leaves the system in the state:

$$|\Psi\rangle(\pi/g_{\text{eff}}) = \frac{|1, ggg\rangle + |0, eee\rangle}{\sqrt{2}}, \quad (4.33)$$

where the qubits are in a GHZ state.

The question is then whether $|1, ggg\rangle$ and $|0, eee\rangle$ are coupled. To show this and to gain analytically insight in the nature of the coupling we employ perturbation theory.

2. Or more generally $\omega_0 \approx \sum_{n=1}^3 \omega_q^n$.

4.2.1. Perturbation theory

To get some intuition about the two states $|1, ggg\rangle$ and $|0, eee\rangle$ are coupled, we turn to time independent perturbation theory. This is described in detail in any introductory book on quantum mechanics, but we will give a brief introduction here.

The premise of time independent perturbation theory is that we can write the Hamiltonian as an exactly solvable part, H_0 , with known eigenvalues E_0^n and eigenstates $|n\rangle_0$, in addition to a small perturbation, λH_{pert} :

$$H = H_0 + \lambda H_{\text{pert}}, \quad (4.34)$$

$$H_0 |n\rangle_0 = E_0^n |n\rangle_0, \quad (4.35)$$

where λ is dimensionless parameter, which we will assume to be small, $\lambda \ll 1$. Our goal is to write the exact eigenenergies, E_n , and the exact eigenstates, $|n\rangle$,

$$(H_0 + \lambda H_{\text{pert}}) |n\rangle = E^n |n\rangle, \quad (4.36)$$

in terms of the energy levels and eigenstates of the unperturbed Hamiltonian, H_0 , in a power series:

$$E^n = E_0^n + \lambda E_1^n + \lambda^2 E_2^n + \dots, \quad (4.37)$$

$$|n\rangle = |n\rangle_0 + \lambda |n\rangle_1 + \lambda^2 |n\rangle_2 + \dots. \quad (4.38)$$

Inserting these definitions in equation (4.36) we get:

$$(H_0 + \lambda H_{\text{pert}})(|n\rangle_0 + \lambda |n\rangle_1 + \dots) = (E_0^n + \lambda E_1^n + \dots)(|n\rangle_0 + \lambda |n\rangle_1 + \dots). \quad (4.39)$$

Separating this equation in terms with the same order of λ , gives us a set of equations which can be used to solve for the energy corrections E_i^n . As an example we can take a look the first order equation:

$$H_0 |n\rangle_1 + H_{\text{pert}} |n\rangle_0 = E_0^n |n\rangle_1 + E_1^n |n\rangle_0. \quad (4.40)$$

After multiplying with $\langle n|_0$ from the left, and assuming that $\langle n|_0 |n\rangle_1 = 0^3$, we get the first order correction to E^n :

$$E_1^n = \langle n|_0 H_{\text{pert}} |n\rangle_0. \quad (4.41)$$

3. This can be shown using that the state should be normalized to zeroth order as well as up to first order in λ

This can be inserted back in equation (4.40) to obtain the first order correction to the eigenstates:

$$|n\rangle_1 = \sum_{k \neq n} \frac{\langle k|_0 H_{\text{pert}} |n\rangle_0}{E_0^n - E_0^k} |k\rangle_0. \quad (4.42)$$

Effective coupling

We can of course continue this up to arbitrarily high orders, however, we are not interested in the full expansion of the state. Consequently, we make a simplification: We want to know the effective coupling between an initial state $|i\rangle$ and a final state $|f\rangle$, in our case this is $|1, ggg\rangle$ and $|0, eee\rangle$, and so we imagine expanding the exact eigenstate $|i\rangle$ to some order, $n - 1$, expressing that state in terms of a set of the unperturbed states, but only some of these will couple directly with $|f\rangle$ via H_{int} , and this matrix element is what we refer to the effective coupling:

$$g_{\text{eff}}^{(n)} = \langle f| H_{\text{int}} |i\rangle_{(n-1)}. \quad (4.43)$$

In the case where n is the lowest order to which $g_{\text{eff}}^{(n)}$ can be non-zero, the effective coupling between an initial state $|i\rangle$ and a final state $|f\rangle$ is given by [79]:

$$g_{\text{eff}}^{(n)} = \sum_{k_1, k_2 \dots k_{n-1}} \frac{\langle f| H_{\text{int}} |k_{n-1}\rangle \dots \langle k_2| H_{\text{int}} |k_1\rangle \langle k_1| H_{\text{int}} |i\rangle}{(E_i - E_{k_1})(E_i - E_{k_2}) \dots (E_i - E_{k_{n-1}})}, \quad (4.44)$$

where $|k_i\rangle$ are intermediary states, which are different from $|i\rangle$, and E_{k_i} are the energies of the states $|k_i\rangle$. The statement about n being the lowest order to which g_{eff} can be non-zero, is equivalent with all k_i are different, i.e. there are no loops, which is then a condition for this equation to hold.

A way of thinking of this is that as long as the initial state $|i\rangle$ and the final state $|f\rangle$ is coupled via intermediary states, we can calculate this coupling by multiplying the coupling between intermediary states, and divide by how far in energy these intermediary states are from the initial state, at least if there are no loops to consider. These intermediary states enable transitions between the initial state and the final state via virtual transition to the intermediary states.

Effective coupling up to third order in g

Because the coupling terms in the Hamiltonian, H_{int} , changes the magnon number and the qubit excitation number by one, it is possible to see that the lowest order terms which possibly could couple $|1, ggg\rangle$ and $|0, eee\rangle$, is third order in g , since all three qubits needs to be excited/relaxed in order to go from one to the other.

The special case from equation (4.44) can be used to third order to obtain the effective coupling:

$$g_{\text{eff}}^{(3)} = \sum_{k_1, k_2} \frac{\langle f | H_{\text{int}} | k_2 \rangle \langle k_2 | H_{\text{int}} | k_1 \rangle \langle k_1 | H_{\text{int}} | i \rangle}{(E_i - E_{k_1})(E_i - E_{k_2})}, \quad (4.45)$$

where k_1 and k_2 ranges over all possible states $|n, \sigma_1 \sigma_2 \sigma_3\rangle$, except $|1, ggg\rangle$. However, most of these matrix elements will be zero.

To get an understanding of which matrix elements are non-zero, and which terms to include in the effective coupling we can take a diagrammatic approach. We know that the interaction term, H_{int} , couples states where the excitation number in the qubits changes by one, as well as the magnon number changing by one. The so-called rotating terms, $\propto g_R$, conserve the number of total excitations, while the so-called counter-rotating terms, $\propto g_{CR}$ add or remove two total excitations.

We can draw the contributions to g_{eff} on a grid, see figure 4.2, where one axis represents the number of qubit excitations, and the other represents magnon excitations. The rotating terms connect squares on diagonals (parallel to bottom right to top left, or vice versa, drawn as full lines), while the counter rotating terms connect squares on anti-diagonals (parallel to bottom left to top right, or vice versa, drawn as dashed lines). To capture all relevant terms, we need to draw all possible paths in three steps from $|1, ggg\rangle$ to $|0, eee\rangle$.

The permutations of qubit excitations also has to be accounted for. There is essentially one diagram for each qubit permutation, but assuming that the qubits are symmetric, which for simplicity we will do here, the diagrams just get an additional factor corresponding to the number of possible qubit permutations, in this case $3! = 6$, since we have three qubits which gets excited in succession. The results where all permutations are considered separately, is covered in the Appendix B of paper [11].

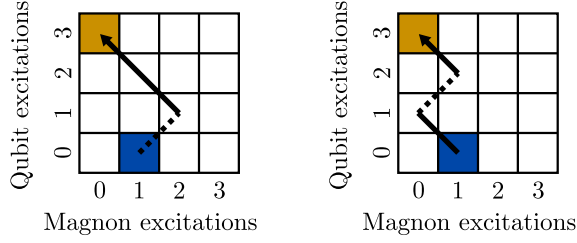


Figure 4.2.: Third order diagrams, connecting $|1, ggg\rangle$ (in blue) and $|0, eee\rangle$ (in orange), via virtual transitions. Rotating terms are represented by fully drawn lines, and counter-rotating terms are represented by dashed lines.

The effective coupling can then be written down from the diagrams as:

$$\begin{aligned}
 g_{\text{eff}}^{(3)} &= 3! \left(\frac{2g_{CR}g_R^2}{(\omega_m + \omega_q)2\omega_q} + \frac{g_{CR}g_R^2}{(\omega_q - \omega_m)2\omega_q} \right) \\
 &= 3g_R^2g_{CR} \frac{3\omega_q - \omega_m}{\omega_q(\omega_m^2 - \omega_q^2)}.
 \end{aligned} \tag{4.46}$$

It is worth noting that the factor 2 in the first term comes from the magnon raising/lowering operator going to and from the two magnon states, $|2, eeg/geg/gge\rangle$.

From equation (4.46) we can see that at resonance, $\omega_m = 3\omega_q$, the effective coupling is zero:

$$g_{\text{eff}}^{(3)}(\omega_m = 3\omega_q) = 0. \tag{4.47}$$

The two diagrams perfectly cancel each other out. Furthermore, it can be shown that they even cancel out if we introduce qubit asymmetries, see Appendix B in paper [11].

Effective coupling up to fifth order in g

Since the third order results where zero, we need to go to the next non-zero order. Drawing paths on the grid from the section above, it is fairly easy to convince one self that there are no fourth order contributions, and that the lowest possibly non-zero order is fifth order.

Calculating the fourth order correction to the states, as we did with the first order case is possible, but extremely time-consuming.

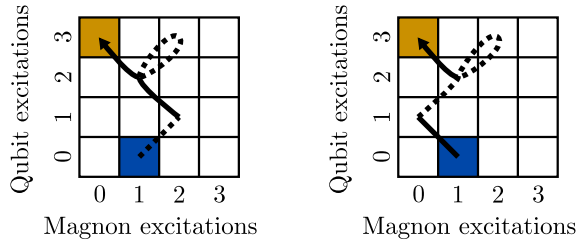


Figure 4.3.: Two fifth order diagrams which contain the two third order diagrams, with additional loops. We can use the third order results to show that the sum of these two diagrams must cancel. Counter rotating terms are shown as dashed lines.

Furthermore, the simplification we made to get to the third order effective coupling is not valid, since there are many ways of creating loops. There are however multiple diagrammatic ways to express higher order perturbation theory, one such method is detailed in [80], and is the one that we base the following discussion on.

Even though the third order results from above turned out to give zero contribution to the effective coupling, we are still able to use the results in making the calculation of the fifth order results easier. Fifth order diagrams which contain the third order diagrams can be matched up, and since we know that these cancel, we do not have to calculate these diagrams. Examples of two such diagrams which cancel is shown in figure 4.3.

Using the diagrammatic formulation of perturbation theory from Ref. [80], and the simplification of the canceling fifth order terms above, we can draw all the remaining contributions to the effective coupling in our own diagrammatic formulation, shown in figure 4.4. The effective coupling can then be written down from these diagrams.

Again, assuming that the qubits are symmetric, and now also that we are at resonance, $\omega_m = 3\omega_q$, we get the following non-zero contribution to the effective coupling:

$$g_{\text{eff}}^{(5)} = -\frac{9(3g_{CR}^3g_R^2 - 8g_{CR}g_R^4)}{32\omega_q^4}. \quad (4.48)$$

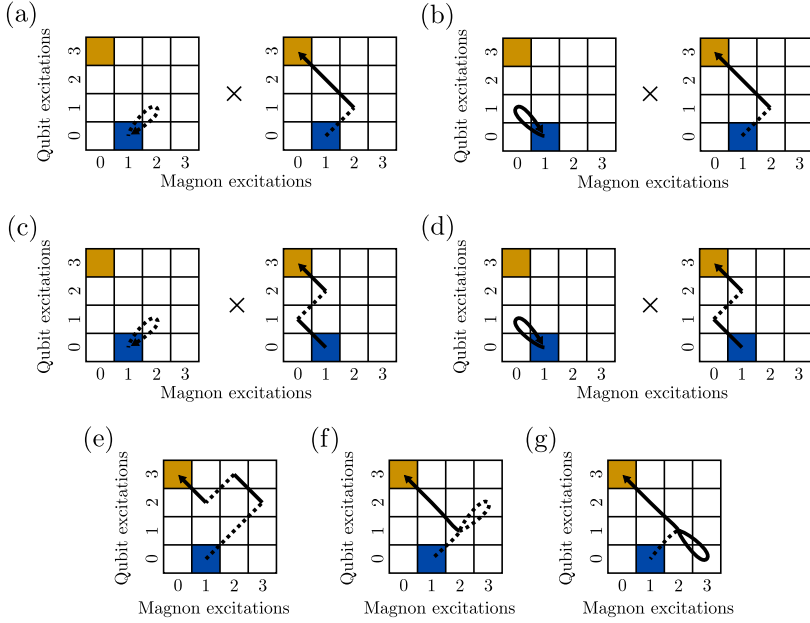


Figure 4.4.: All the fifth order diagrams contributing to the effective coupling $g_{\text{eff}}^{(5)}$.

4.3. Concluding remarks

What we have showed in this chapter is that the hybrid system of a ferromagnet acting as a magnon cavity and a spin qubit is a physical realization of the quantum Rabi model. Furthermore, by applying an anisotropy to the ferromagnet, we can obtain a controllable degree of squeezing of the magnon mode. This squeezing produces counter-rotating (non-spin conserving) terms in the coupling between the magnon cavity and the qubit. Hence, the squeezing allows for the control over the ratio of the amplitude of the rotating term and the counter-rotating coupling term.

We then showed that by introducing three spin qubits, the model couples the states where all three qubits are in the $|g\rangle$ state with states where all three qubits are inn the $|e\rangle$ state via virtual transitions. Since the results is fifth order in coupling, the low coupling limit discussed in the previous section is probably not applicable, but the above discussion

shows that there is a coupling between these two states. This allows us to excite all three qubits with a single pulse, and by driving the qubits halfway between $|g\rangle$ and $|e\rangle$ the qubits are left in the so-called GHZ state:

$$|\text{GHZ}\rangle = \frac{|ggg\rangle + |eee\rangle}{\sqrt{2}}. \quad (4.49)$$

Part II.

Semi/super hybrid devices for topologically protected quantum computation

Semi/super hybrid devices for topological protected quantum computation

5

In the previous chapters, we looked at hybrid devices which themselves are made up of devices, in chapter 3 with a microwave resonator and a spin qubit, or in chapter 4 a ferromagnet and again spin qubits. The hybrid nature of these devices allows us to combine advantageous features from the sub-devices.

Hybrid devices made of superconductors and semiconductors have gained a lot of attention recently because they allow us to combine material features no single material could have. The possibility of strong spin-orbit coupling in combination with superconductivity could possibly be used to engineer exotic properties such as topological superconductivity [81–84].

In this chapter, we introduce a few important concepts related to this as well as motivate why superconducting hybrid devices have gained so much attention lately. To do so we first have to have a grasp of how superconductors work, and build a theoretical framework which lets us describe systems which include superconductivity. We will then move on to discuss the engineering of topological states of matter and how this can be used in quantum computation.

5.1. Superconductors

The following is a quick introduction to a mean-field approach of a system that supports a superconducting phase. Here, we outline the main steps from refs. [85, 86], however, a more rigorous and formal derivation is found in many textbooks on the topic.

The starting point is a second quantization Hamiltonian describing a free electron with the addition of an attractive potential for the electrons:

$$H = \sum_{\sigma} \int d\vec{r} \psi_{\sigma}^{\dagger}(\vec{r}) H_0(r) \psi_{\sigma}(\vec{r}) - \frac{1}{2} \sum_{\sigma, \sigma'} \iint d\vec{r} d\vec{r}' V_{\sigma, \sigma'}(\vec{r}, \vec{r}') \psi_{\sigma}^{\dagger}(\vec{r}) \psi_{\sigma'}^{\dagger}(\vec{r}') \psi_{\sigma}(\vec{r}') \psi_{\sigma'}(\vec{r}), \quad (5.1)$$

where $\psi_\sigma^\dagger(\vec{r})$ and $\psi_\sigma(\vec{r})$ are the creation and annihilation operators for an electron with spin σ at \vec{r} , and $V_{\sigma,\sigma'}(\vec{r},\vec{r}')$ is the strength of the attraction between two electrons with spins σ and σ' at positions \vec{r} and \vec{r}' , $V_{\sigma,\sigma'}(\vec{r},\vec{r}')$ is chosen to be positive, hence the negative sign in the Hamiltonian. We will come back to more assumptions on $V_{\sigma,\sigma'}(\vec{r},\vec{r}')$ later in this section.

Next we employ a mean-field approximation of the second term of the Hamiltonian, which effectively assumes that we can neglect fluctuations, meaning that any of the following results is only valid in the low temperature limit. This allows us to use the following substitution:

$$\begin{aligned} \psi_\sigma^\dagger(\vec{r})\psi_{\sigma'}^\dagger(\vec{r}')\psi_\sigma(\vec{r}')\psi_{\sigma'}(\vec{r}) \rightarrow & \langle \psi_\sigma^\dagger(\vec{r})\psi_{\sigma'}^\dagger(\vec{r}') \rangle \psi_\sigma(\vec{r}')\psi_{\sigma'}(\vec{r}) \\ & + \psi_\sigma^\dagger(\vec{r})\psi_{\sigma'}^\dagger(\vec{r}') \langle \psi_\sigma(\vec{r}')\psi_{\sigma'}(\vec{r}) \rangle \\ & - \langle \psi_\sigma^\dagger(\vec{r})\psi_{\sigma'}^\dagger(\vec{r}') \rangle \langle \psi_\sigma(\vec{r}')\psi_{\sigma'}(\vec{r}) \rangle, \end{aligned} \quad (5.2)$$

where the angled brackets, $\langle \dots \rangle$, signify the thermodynamic average. There are additional terms which we have left out here, of the type $\propto \psi^\dagger\psi$ and $\propto \psi^\dagger\psi$, however these can be accounted for by absorbing them in the chemical potential of the free electron Hamiltonian. The mean field approximation Hamiltonian is then given by:

$$\begin{aligned} H_{MF} = & \sum_\sigma \int d\vec{r} \psi_\sigma^\dagger(\vec{r}) H_0(r) \psi_\sigma(\vec{r}) \\ & + \frac{1}{2} \sum_{\sigma,\sigma'} \iint d\vec{r} d\vec{r}' \left(\Delta_{\sigma,\sigma'}^*(\vec{r},\vec{r}') \psi_\sigma(\vec{r}') \psi_{\sigma'}(\vec{r}) \right. \\ & \qquad \qquad \qquad \left. + \Delta_{\sigma,\sigma'}(\vec{r}',\vec{r}) \psi_\sigma^\dagger(\vec{r}') \psi_{\sigma'}^\dagger(\vec{r}) \right) \\ & - \frac{1}{2} \sum_{\sigma,\sigma'} \frac{|\Delta_{\sigma,\sigma'}(\vec{r},\vec{r}')|^2}{V_{\sigma,\sigma'}(\vec{r},\vec{r}')}, \end{aligned} \quad (5.3)$$

where we define the pairing potential as:

$$\Delta_{\sigma,\sigma'}(\vec{r},\vec{r}') = -V_{\sigma,\sigma'}(\vec{r},\vec{r}') \langle \psi_\sigma(\vec{r}') \psi_{\sigma'}(\vec{r}) \rangle, \quad (5.4)$$

$$\Delta_{\sigma,\sigma'}^*(\vec{r},\vec{r}') = -V_{\sigma,\sigma'}(\vec{r},\vec{r}') \langle \psi_\sigma^\dagger(\vec{r}) \psi_{\sigma'}^\dagger(\vec{r}') \rangle. \quad (5.5)$$

The first term in equation (5.3) is the unchanged free electron Hamiltonian (except for the renormalized chemical potential), the second

term is the superconducting term which allows for the creation and annihilation of two electrons, reflecting that they are bound together in so-called Cooper pairs and can be absorbed by the superconducting condensate. The last term is a constant term, which will not be relevant for the purposes of this discussion.

Diagonalization and the BdG Hamiltonian

The Hamiltonian we are left with is now quadratic in electron creation/annihilation operators, but the second term in equation (5.3) makes diagonalizing the Hamiltonian non-trivial. To do this we are going to use a trick we used on the boson system in chapter 4, namely a Bogoliubov transformation. Where we previously introduced a boson field which was a linear combination of boson creation and annihilation operators, we now introduce fermionic operators γ_n which are the combination of fermionic creation and annihilation operators. The electron operators can inversely be written in terms of γ_n as:

$$\psi_\sigma = \sum_n u_\sigma^n \gamma_n - \sigma v_\sigma^{n*} \gamma_n^\dagger, \quad (5.6)$$

$$\psi_\sigma^\dagger = \sum_n u_\sigma^{n*} \gamma_n^\dagger - \sigma v_\sigma^n \gamma_n. \quad (5.7)$$

The coefficients u_σ^n and v_σ^n are determined by demanding that the Hamiltonian is diagonalized:

$$H_{MF} = E_g + \sum_n E_n \gamma_n^\dagger \gamma_n, \quad (5.8)$$

where E_g is the ground state energy, and E_n is the energy of the excited states. To obtain the coefficients and find the excited energies E_n we can slightly rewrite the Hamiltonian, using the Nambu spinor $\Psi(\vec{r}) = [\psi_\uparrow(\vec{r}), \psi_\downarrow(\vec{r}), \psi_\downarrow^\dagger(\vec{r}), -\psi_\uparrow^\dagger(\vec{r})]^\top$:

$$\begin{aligned} H_{MF} = & \frac{1}{2} \iint d\vec{r} d\vec{r}' \Psi(\vec{r})^\dagger \mathcal{H}_{\text{BdG}} \Psi(\vec{r}') \\ & + \frac{1}{2} \text{Tr} H_0 \\ & - \frac{1}{2} \sum_{\sigma, \sigma'} \frac{|\Delta_{\sigma, \sigma'}(\vec{r}, \vec{r}')|^2}{V_{\sigma, \sigma'}(\vec{r}, \vec{r}')}, \end{aligned} \quad (5.9)$$

where the so-called Bogoliubov-De Gennes (BdG) Hamiltonian is defined as:

$$\mathcal{H} = \begin{pmatrix} H_0(\vec{r}) & \hat{\Delta}(\vec{r}, \vec{r}') \\ \hat{\Delta}^\dagger(\vec{r}', \vec{r}) & -\mathcal{T}H_0\mathcal{T}^\dagger \end{pmatrix}, \quad (5.10)$$

where \mathcal{T} is the time reversal operator. The form which we have ended up in, over describes the system, having doubled the Hilbert space. This doubling of the Hilbert space is of course not physical, it is just an artifact of describing the system in terms of electrons and holes, which due to particle/hole symmetry is effectively describing the same dynamics. We can now solve for E_n and the coefficients u_σ^n and v_σ^n by the Bogoliubov-De Gennes equation:

$$\int d\vec{r}' \mathcal{H}_{\text{BdG}}(\vec{r}, \vec{r}') \psi^n(\vec{r}') = E_n \psi^n(\vec{r}), \quad (5.11)$$

with the eigenvectors $\psi^n(\vec{r}) = [u_\uparrow(\vec{r}), u_\downarrow(\vec{r}), v_\downarrow(\vec{r}), -v_\uparrow(\vec{r})]^\top$.

5.1.1. Andreev reflections and the proximity effect

It was early noticed that superconducting correlations could penetrate into normal metals placed in close proximity to superconductors [87]. This is known as the proximity effect, and is caused by Cooper pairs tunneling into the normal material. This can also equivalently be described by a single electron picture in the normal material, using what is known as Andreev reflection [88].

In this picture we look at what happens when an electron (hole) in the normal material scatters off the superconducting-normal (SN) surface. The superconductor is assumed to have a pairing potential of $\Delta = e^{i\phi} \Delta_0$. For simplicity we here consider a 1D example, where the particles have energies within the gap of the superconductor, $E < \Delta_0$. By matching the BdG wave function of the normal material with that of the exponentially decaying one in the superconductor [89] one can show that electrons with spin σ and momentum \vec{k} are reflected as holes with the opposite spin, $\bar{\sigma}$, and opposite momentum $-\vec{k}$ and vice versa:

$$\Psi_{\text{out}} = e^{-i \arccos E/\Delta_0} \begin{pmatrix} 0 & 0 & e^{i\phi} & 0 \\ 0 & 0 & 0 & e^{i\phi} \\ e^{-i\phi} & 0 & 0 & 0 \\ 0 & e^{-i\phi} & 0 & 0 \end{pmatrix} \Psi_{\text{in}}, \quad (5.12)$$

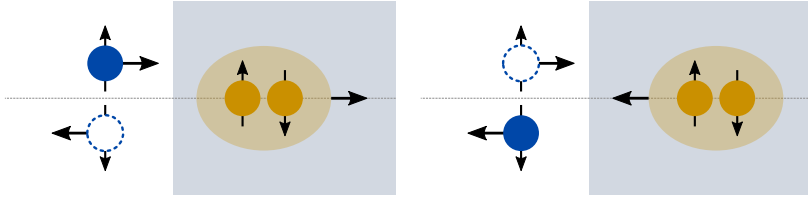


Figure 5.1.: Schematic of the process of Andreev reflection. In-coming electrons(holes) are reflected as holes(electrons) with opposite spin and momentum when scattered of the superconductor (gray shaded area). Electrons are shown as full circles, while the holes are shown as dotted circles, the vertical arrows signify the spin of the particle. A charge of $2e$ is carried between the normal material and the superconductor, which corresponds to a cooper pair. The incoming/outgoing cooper pairs are shown i orange.

where $\Psi_{\text{in/out}} = [\psi_{\uparrow}^{\text{in/out}}, \psi_{\downarrow}^{\text{in/out}}, \psi_{\downarrow}^{\text{in/out}}, -\psi_{\uparrow}^{\text{in/out}}]^T$, describes (in)coming electrons with a momentum pointing towards the surface, and (out)going electrons with momentum pointing away from the surface. The reflection of a hole, is essentially describing the inverse process. A schematic of the Andreev reflectio process can be seen in figure 5.1.

5.2. Majorana fermions

The notion of anti-particles came up as negative solutions to relativistic equations describing spin 1/2 particles by Paul Dirac [90]. The negative solutions was particles with the same mass, but with opposite charges, and is known as the anti-particle counterpart to the corresponding positive solution particle. The particle and the anti-particle of these fermions, known as Dirac fermions, are formally described by two different complex fields. One might ask if this has to be the case, or if a single field can describe both particles and antiparticles. This is exactly what Ettore Majorana questioned in his 1937 paper [91], and is wheree he put forth the idea that neutral fermions could be described by one single (real) field, making the particles its own anti-particle. Because of this, these fermions are called Majorana fermions.

Of the fundamental particles, there is only one neutrally charged fermion, namely the neutrino. Whether the neutrino is a Dirac or a

Majorana fermion is still not known, although huge¹ efforts have been made to answer the question. Answering this question could help answering fundamental questions of the universe such as why there is overwhelming asymmetry in the ratio between matter and anti-matter [93].

5.2.1. Majoranas in condensed matter systems

These concepts from particle physics can be carried over to condensed matter system, specifically to superconducting physics. Here, the particles are electrons and the anti-particles are holes. As we saw from eq. , the excitations within the superconducting gap can be written as superpositions of electrons and holes. The excitations in the gap can be described by the fermionic creation and annihilation operators $\gamma(E)$ and $\gamma^\dagger(E)$. Due to particle hole symmetry we know that:

$$\gamma(E) = \gamma^\dagger(-E), \quad (5.13)$$

which at the center of the gap, $E = 0$, gives:

$$\gamma(0) = \gamma^\dagger(0). \quad (5.14)$$

Which means that the excitations are their own anti-particles. These excitations which are their own anti-particles are indeed Majorana fermions, and due to their location at zero energy, they are named Majorana zero modes. These excitations do, however, come in pairs, and we would need to break spin-degeneracy to create unpaired Majorana fermions [94].

The first toy model showing, quite elegantly, unpaired Majorana fermions was made by Alexei Kitaev [42]. The model consist of a “simple” 1D spinless p-wave superconductor, where the “p-wave” refers to the momentum dependence of the pairing potential of the superconductor. The details of which we do not detail in this thesis, but can be looked up in reviews such as Ref. [95] or in the original paper, Ref. [42].

One way of recreating this toy model is to use a p-wave superconductor and in some way spin-polarize the system. The details of these

1. Litterally, 1000kg of isotopically enriched ⁷⁶Ge detectors have been proposed in the search for decay paths that would indicate that the neutrino is a Majorana fermion [92].

more exotic superconductors will not be looked at here, but many of the early proposal for creating Majorana fermions where based on this idea [96, 97]. One problem with these types of superconductors, is that they are very sensitive to disorder [94] as well as very few materials exhibiting this type of pairing. Since p-wave superconductors bring some problems, the question becomes: How can we get unpaired Majoranas without spin-less p-wave superconductors? Many approaches have been looked at, but one possible avenue is the approach of engineering spin polarized p-wave superconductivity without the need for intrinsic p-wave superconductors.

The main ingredients needed are deceivingly simple, namely proximitizing the superconductivity of a conventional s-wave superconductor into a material where we break time-reversal symmetry and some spin orbit interaction.

Nanowires

In 2010 there were two important works [83, 84] which laid the groundwork for a surprisingly simple model. By combining a 1D nanowire, with a strong spin-orbit interaction, and a conventional superconductor, one could engineer a topological phase by applying a small external magnetic field. We can see how this works by looking at the band structure of the conduction band of a 1D nanowire, see figure 5.2. What we see is that if the chemical potential is close to $E = 0$, there is only one band at the Fermi energy, this band is a mix of the spin up and spin down bands, but the spin mixing is one-to-one with the momentum, meaning that effectively there is no spin-degree of freedom.

In combination with the spin-orbit coupling mixing s-wave and p-wave superconductivity [95], means that we have all the ingredients needed for topological phases: An effective model with spinless p-wave superconductor. We will not look at the details here, but as we would expect from the arguments above, this model predicts that when the Zeeman splitting is larger than the induced superconducting gap a topological phase appears [83, 84, 98], assuming that we place the chemical potential at $E = 0$. Tuning the Fermi-level, by e.g. gate voltages, or the Zeeman splitting, by an external magnetic field, can be used to tune the system in and out of the topological phase.

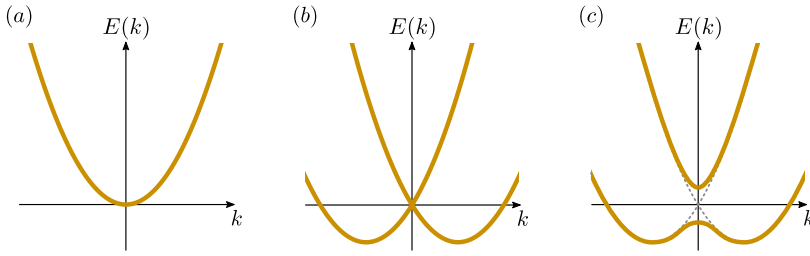


Figure 5.2.: The band structure of a 1D nanowire. With (a) just free electron, (b) free electron including spin-orbit interaction, (c) free electron with spin-orbit interaction and Zeeman splitting. We can see that if the chemical potential is close to $E = 0$, there is effectively only one band at the Fermi energy.

Additionally, it is worth noting that the sensitivity to disorder is decided by the degree to which time reversal symmetry is broken [95]. Time reversal symmetry is in the case described here broken by the external magnetic field, causing the Zeeman splitting in the material. One can gauge this grade of time-reversal symmetry breaking by comparing the Zeeman field to the spin orbit field, using the ratio of the Zeeman energy and the spin-orbit energy, E_Z/E_{so} [99, 100]. When this ratio is small, we are close to having a time-reversal symmetric system, and the impact of disorder is suppressed. When this ratio is large the opposite is the case and the impact of disorder can become substantial [95]. The ratio of the Zeeman energy and the spin-orbit energy is crucial in understanding the limitations of these systems. This is one motivation for investigating the details of the spin physics in these systems, and is what we will be looking at in the next chapters, chapters 6 and 7.

Other approaches to creating the desired topological state have been proposed, however, the basic ingredients are the same: Induced superconducting from a traditional s-wave superconductor, strong spin-orbit interaction, and breaking time-reversal symmetry. Two examples is the combination of a 2D topological insulator [101, 102], or a 3D topological insulator nanowire [103], materials with strong spin orbit interaction which are insulators, but due to topological

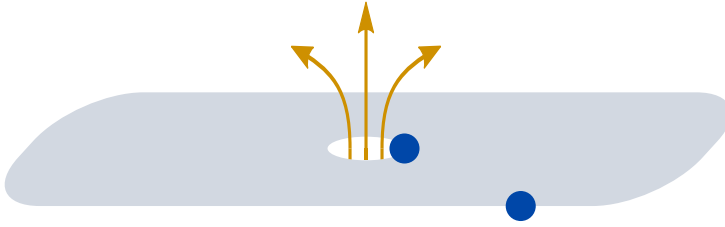


Figure 5.3.: Possible 2D platform for hosting Majorana zero modes. We see the effects of puncturing the topological state, changing the boundary conditions making unpaired Majorana zero modes on the inner boundaries.

effects have conducting surface states, with a conventional s-wave superconductors and magnetic fields.

2D Platforms

Similarly to the 1D case from above, the simplest example of a 2D material which can host topological Majorana fermions, is a 2D electron gas (2DEG) with $p_x + ip_y$ superconductivity [95], so called chiral p-wave superconductivity, which again refers to the momentum dependence of the pairing potential of the superconductor, $\Delta(\vec{k}) = i\Delta_0(k_x + ik_y)$, that is odd in momentum. The similarity to the 1D case is striking, and indeed, the same ingredients as before can again engineer the desired topological state: A 2DHG with spin-orbit interaction, an s-wave superconductor which proximitizes superconductivity in the 2DHG, and a Zeeman field. In this case, however, the Zeeman field has to come from an insulating ferromagnet instead of an external magnetic field [98]. The reason for this is that an out of plane magnetic field (perpendicular to the SOI which is in-plane) would easily break the superconductivity. Thus, the Zeeman coupling would need to come from the proximity effect from the ferromagnet [104] (electrons tunneling into the 2DHG) and not from the direct coupling between the external magnetic field from the ferromagnetic insulator and the electrons in the 2DHG.

The Majorana zero modes live at the boundary between the topological region and the normal region [105]. For a 2D surface, such as a disk, the two Majorana zero modes would live on the outer boundary of the

disk. This is however not desired since we want un-paired Majorana Fermions which are manipulated independently. A solution to this is to create a second boundary inside the disk, creating an annulus, such that the two Majorana zero modes can live independently on each surface, see figure 5.3. If more Majorana Zero modes are desired, more holes can be made, and while the Majorana zero modes on the outer ring pair up, the ones which live on the inner boundaries are unpaired.

Since magnetic fields can be used to control the topological phase, we can imagine what happens if we use a type II superconductor, and apply sufficiently strong magnetic fields perpendicular to the surface: The magnetic field penetrates the superconductor (and the 2DEG) in so-called vortices, this fairly localized magnetic field, breaks the topological phase in the 2DHG. By tuning how much flux goes through this vortex, it is possible to manipulate the boundary conditions in such a way that the two unpaired Majorana zero modes appear, where one Majorana zero mode is located at the vortex while the other is located at the outer edge [95].

Finally, we note that there are several other 2D platforms which are not directly relevant to the systems we will be looking at in this thesis, such as again using 3D topological insulators [101], or using intrinsic chiral p-wave superconductors, such as possibly Sr_2RuO_4 [106].

5.2.2. Quantum computation and braiding

The Majorana zero modes are clearly fascinating from a fundamental physics point of view, however, the main reason for their fame, is their quantum information applications. To see why we have to look at their exchange statistics.

For particles in 3D space there are essentially two options for what happens if we exchange two identical particles, either the wave function acquires an additional factor -1 (for fermions) or the wave function is unchanged, i.e., the wave function gains a factor $+1$ (for bosons). This essentially reflects the fact that we get back to the same indistinguishable state as we started in after exchanging particles twice. In two dimensions this is not necessarily the case, as first noted by Leinaas and Myrheim [107] in 1977. The essential difference is that in $3 + 1$ dimension, the world lines of the particles can be untangled without crossing paths, while in $2 + 1$ dimension this is not always possible,

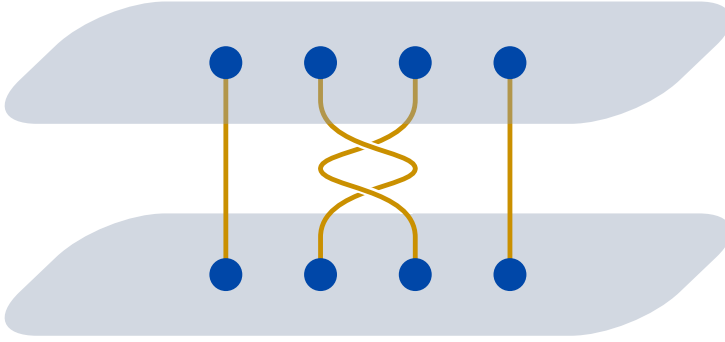


Figure 5.4.: In this figure we see the world lines of anyons through $2 + 1$ dimensions, from some time, t_1 , in the bottom to a later time, t_2 , on top. The world lines intertwine in such a way that there is no way of untangling them.

the states which experience exchange are topologically different from ones which has not experienced exchange, see figure 5.4. The result is that after two exchanges of two identical particles at position \vec{r}_1 and \vec{r}_2 , it is possible that we end up with something non-trivial:

$$\Psi(\vec{r}_1, \vec{r}_2) \rightarrow U\Psi(\vec{r}_1, \vec{r}_2), \quad (5.15)$$

Where U in general is a unitary matrix. The 2D particles that Leinaas and Myrheim thought up in the 70s had $U = e^{2i\phi}$, where ϕ could be any phase for a given particle, as opposed to fermions and bosons where $\phi = \pi, 0$ respectively. This lead to these particles being called anyons, since they could pick up *any* phase during exchange.

As noted, U can in principle be a unitary matrix [108], and unitary matrices do not necessarily commute. If we do multiple exchanges (with more particles), the order of the exchanges are important for the final wavefunction. The group of these matrices are so-called non-abelian, and the anyons which follows these exchange statistics are, therefore, called non-abelian anyons.

The Majorana zero modes we discussed earlier, turn out to be non-abelian anyons, and by exchanging the position of the Majorana zero modes, so-called braiding, the state of the system can change, see figure 5.4. Using four Majorana fermions it is possible to implement a qubit, a so-called Majorana box qubit, which is manipulated by braiding [105, 109]. This braiding can be used to implement a subset of the

gates needed for universal quantum computation, the Clifford gates. However, the remaining gates needed for universal quantum computation can still be implemented using these qubits, using operations which do not have the same topological protection or by using ancilla qubits [105]. It is also worth mentioning that actually performing the braiding is complicated, and a measurement based approach keeps the topological protection without the need for actually moving the Majorana fermions [110].

5.3. Outlook and contributions

As stated above the ingredients needed to create systems which can host Majorana zero modes are relatively simple. They have however been elusive and it turns out that the experimental side of things are much more complicated. The majorana zero mode has multiple features such as the so call zero bias peaks [111] and non local conductance [112]. However, it turns out that non-topological systems can recreate these signatures [40, 113], meaning that final proof of their existence is difficult to produce.

The ultimate proof is likely the actual braiding of the non-abelian anyons, but this is not currently within reach. In the mean time one important step is to know crucial properties of the materials/devices that make up these potentially topological systems. Some properties such as spin-orbit coupling is not just material specific, but device specific, and measuring these properties can be challenging. In the following chapters we look at two such hybrid devices, a 1D nanowire SNS junction, and a 2D hole gas SNS junction. We show that the analytic insight we get can be used to possibly measure properties such as the spin-orbit interaction of the normal material.

The critical current in an NW SNS junction with a scatterer

In this chapter we will be looking at a hybrid device composed of a semiconductor nanowire of length L connected to two superconducting contacts, known as an SNS junction, a superconducting-normal-superconducting junction. A sketch of the system we consider can be seen in figure 6.1. The nanowire is assumed to potentially have a significant spin-orbit coupling. We include an external magnetic field, pointing in a general direction. We also include disorder, which we model as a single scatterer in the middle of the wire, with a scattering amplitude, T .

The goal is to calculate the critical current of the junction. The supercurrent is naturally heavily dependent on the spin mixing in the normal material, and so we could potentially be able to extract information about the spin mixing parameters, the SOI field and the Zeeman field, from the critical current. Both the spin-orbit field and the Zeeman field, can depend heavily on parameters such as the microscopic geometry of the device and strain. By being able to describe an easily measured quantity, the critical current, we hope to bring useful insight into these devices. This chapter is based on a manuscript in preparation [IV].

6.1. Model

Since we are working with the proximity effect of the superconductor, we will phrase the Hamiltonian here in terms of the BdG Hamiltonian, \mathcal{H} , introduced in the previous chapter:

$$H = \frac{1}{2} \int dx \Psi^\dagger \mathcal{H} \Psi, \quad (6.1)$$

where $\Psi = [\psi_\uparrow(x), \psi_\downarrow(x), \psi_\downarrow^\dagger(x), -\psi_\uparrow^\dagger(x)]^\top$, with $\psi_\sigma(x)$ is the annihilation operator of an electron with spin $\sigma = \uparrow, \downarrow$. Furthermore, the BdG Hamiltonian is given by:

$$\mathcal{H} = \begin{pmatrix} H_0 & \hat{\Delta} \\ \hat{\Delta}^\dagger & -\mathcal{T} H_0 \mathcal{T}^\dagger \end{pmatrix}, \quad (6.2)$$

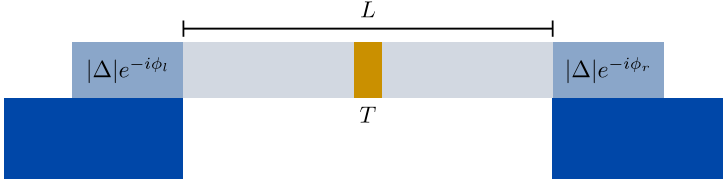


Figure 6.1.: Schematic of the NW SNS junction considered in this chapter. The device is made up of two superconducting regions, with phases $\phi_{l/r}$, proximitized from two superconductors (blue), connected with a semi-conducting nanowire of length L which has a scatterer in the middle (orange), which has a transparency amplitude T .

where \mathcal{T} is the time reversal operator, H_0 describes the physics of the electron sector, and the time reversed $-\mathcal{T}H_0\mathcal{T}^\dagger$ describes the physics of the hole sector, both of which are 2×2 matrices in spin space. We define the matrix H_0 in the following way:

$$H_0 = \underbrace{-\frac{\hbar^2 \partial_x^2}{2m} - \mu}_{\text{Free electron}} + \underbrace{V_0 \delta\left(x - \frac{1}{2}L\right)}_{\text{Scatterer}} + \underbrace{(\vec{B}_Z - i\partial_x \vec{\alpha}_{\text{so}}) \cdot \vec{\sigma}}_{\text{Zeeman effect and SOI}}, \quad (6.3)$$

where μ is the chemical potential, m is the electron mass, \hbar is the reduced Planck constant, $\delta(x)$ is the Dirac delta distribution, the potential V_0 parametrizes the strength of the scattering placed in the middle of the wire at position $x = L/2$, $\vec{B}_Z = (1/2)\mu_B g \vec{B}_m$ is the Zeeman field and $\vec{\alpha}_{\text{so}}$ is the spin-orbit field. The vector $\vec{\sigma} = [\sigma_x, \sigma_y, \sigma_z]$ is made from the three Pauli matrices. For the terms without matrices, the unit matrix I is implied, as usual.

The off-diagonal block of \mathcal{H} , which couples the electrons to the holes is diagonal in the basis which we have chosen, coupling electrons with holes of opposite spins, $\hat{\Delta}(x) = \Delta(x)\mathbb{1}$, where the amplitude is assumed to be:

$$\Delta(x) = \begin{cases} \Delta_0 e^{-i\phi_l}, & \text{for } x < 0, \\ \Delta_0 e^{-i\phi_r}, & \text{for } x > L, \\ 0, & \text{for } 0 \leq x \leq L, \end{cases} \quad (6.4)$$

i.e. , the pairing potential is non-zero only in the superconducting regions, with phases $\phi_{l/r}$ in the left and right superconductor regions respectively, with the same amplitude for both Δ_0 . The superconducting regions could be a superconducting material, or more realistically a region of the nanowire which obtains superconductivity because of the proximity effect, reflected in figure 6.1.

The goal is to find solutions to the BdG equation from chapter 5:

$$\int d\vec{r}' \mathcal{H}_{\text{BdG}}(\vec{r}, \vec{r}') \psi^n(\vec{r}') = E_n \psi^n(\vec{r}), \quad (6.5)$$

with the eigenvectors $\psi^n(\vec{r}') = [u_\uparrow(\vec{r}'), u_\downarrow(\vec{r}'), v_\downarrow(\vec{r}'), -v_\uparrow(\vec{r}')]^\top$. Assuming that we are in the short junction limit, i.e. , $L \ll \xi$, where ξ is the coherence length in the normal material, the zero-temperature supercurrent is given in terms of the energies E_n within the gap [89]:

$$I(\phi) = \frac{2e}{\hbar} \sum_n' \frac{dE_n}{d\phi}, \quad (6.6)$$

where the prime indicates that we are summing over the negative energies only.

6.1.1. Linearization and diagonalization

We assume that the pairing potential is much smaller than the chemical potential, $\Delta_0 \ll \mu$, and that we are interested in the physics within the gap, caused by the sub-gap states carrying the supercurrent as we just saw above. This means that we can linearize the Hamiltonian around the Fermi energy, since all the “important” physics is going on close to this. The Hamiltonian, to the left and right of the scatterer can then be written in terms of the wave vector k and the Fermi momentum k_F as:

$$H_{0\pm}^{L,R} = \pm \hbar v_F (k - k_F) + (\vec{B}_Z \pm \vec{B}_{so}) \cdot \vec{\sigma}, \quad (6.7)$$

Where the \pm indicates electron moving in the positive/negative x -direction, and where we have introduced the spin-orbit field, $\vec{B}_{so} = k_F \vec{\alpha}_{so}$.

We are of course able to freely choose the quantization axis for spins, and so we can align the z -axis along $(\vec{B}_Z + \vec{B}_{so})$. The positive momentum electrons get the diagonalized Hamiltonian:

$$H_{0+}^{L,R} = \hbar v_F (k - k_F) + B_e^+ \cdot \sigma_z, \quad (6.8)$$

where $B_e^+ = |\vec{B}_Z + \vec{B}_{so}|$ is the total field that the electrons moving in the positive direction sees.

We could of course have done the same for the electrons moving in the other direction, setting the quantization axis along $(\vec{B}_Z - \vec{B}_{so})$. And as long as there is no mixing between right and left moving electrons we are able to describe the full electron Hamiltonians as:

$$H_{0\pm}^{L,R} = \pm \hbar v_F (k - k_F) + B_e^\pm \sigma_z, \quad (6.9)$$

where $B_e^\pm = |\vec{B}_Z \pm \vec{B}_{so}|$. Where we describe the left moving and right moving electrons in two different bases.

We are similarly able to diagonalize the hole part of the BdG Hamiltonian, by noting that the effective fields are transformed by the time reversal operator as:

$$-\mathcal{T}(\vec{B}_Z \pm \vec{B}_{so}) \cdot \vec{\sigma} \mathcal{T}^\dagger = (\vec{B}_Z \mp \vec{B}_{so}) \cdot \vec{\sigma}, \quad (6.10)$$

and so the effective field the holes “feel” are that of the oppositely moving electrons, $B_e^\pm = B_h^\mp$. The hole sector Hamiltonian can then be written as:

$$-\mathcal{T} H_{0\pm}^{L,R} \mathcal{T}^\dagger = \pm \hbar v_F (k + k_F) + B_h^\pm \sigma_z. \quad (6.11)$$

Consequences of diagonalization

The way we diagonalized the Hamiltonians above, might seem a bit too good to be true, and it sort of is. The price we pay is that anything “simple” which scatters left moving electrons/holes to right moving electrons/holes, and vice versa, such as the scatterer, becomes more complicated because we have to take into account the change of basis between left moving and right moving electrons. Similarly, processes which scatter electrons to holes, such as the Andreev reflections, become more complicated, because electrons and holes are not expressed in the same spin basis.

We do not get rid of the spin mixing with this diagonalization, we just formulate it in such a way that all the spin mixing happens at the scattering events. However, this way of expressing the spin mixing makes the following discussion and calculation somewhat easier.

6.1.2. Scattering matrix

We now want to solve the BdG equation to find the bound state energies within the gap in order to calculate the supercurrent. To do this we are going to formulate the problem in terms of a scattering matrix [89]. A scattering matrix connects the amplitudes of an incoming wave with that of an outgoing one. For electrons moving to the right in the nanowire (i.e. with positive momentum), we can connect the amplitudes of the electrons just to the right of the left superconducting region, $x = 0$, with the amplitudes of electrons just to the left of the scatterer $x = L/2$ in the following way:

$$\begin{pmatrix} a_{\uparrow}^+(L/2) \\ a_{\downarrow}^+(L/2) \end{pmatrix} = t_e^+ \begin{pmatrix} a_{\uparrow}^+(0) \\ a_{\downarrow}^+(0) \end{pmatrix}, \quad (6.12)$$

where t_e^+ is the scattering matrix describing this process. The labeling \uparrow / \downarrow in the subscripts of the amplitudes above, is somewhat misleading. Since we are working with multiple spin bases, we cannot think of these as purely spin-up/spin-down, but rather as some more abstract pseudo-spin. However, this basis choice does make it simple to write transfer matrices, which, because there is no spin mixing, are diagonal:

$$t_e^+ = \begin{pmatrix} e^{i(\theta_{e^+} + k_F L)/2} & 0 \\ 0 & e^{i(-\theta_{h^-} + k_F L)/2} \end{pmatrix}, \quad (6.13)$$

where k_F is the Fermi momentum and where $\theta_{e^+} = (B_e^+ / \hbar v_F + k)L$ and $\theta_{h^-} = (B_h^- / \hbar v_F - k)L$. We consider the short junction limit where $kL \ll 1$, meaning that the θ s essentially are the phase gained by an electron due to the spin-orbit and Zeeman field. For electrons moving to the right on the right side of the scatterer, the same scattering matrix applies:

$$\begin{pmatrix} a_{\uparrow}^+(L) \\ a_{\downarrow}^+(L) \end{pmatrix} = t_e^+ \begin{pmatrix} a_{\uparrow}^+(L/2) \\ a_{\downarrow}^+(L/2) \end{pmatrix}. \quad (6.14)$$

The scattering matrix for the left moving electrons are however different, since these experience different fields, which generally do not point in the same direction as for the right moving electrons:

$$\begin{pmatrix} a_{\uparrow}^-(L/2) \\ a_{\downarrow}^-(L/2) \end{pmatrix} = t_e^- \begin{pmatrix} a_{\uparrow}^-(L) \\ a_{\downarrow}^-(L) \end{pmatrix}, \quad \begin{pmatrix} a_{\uparrow}^-(0) \\ a_{\downarrow}^-(0) \end{pmatrix} = t_e^- \begin{pmatrix} a_{\uparrow}^-(L/2) \\ a_{\downarrow}^-(L/2) \end{pmatrix}, \quad (6.15)$$

where the scattering matrix is given by:

$$t_e^- = \begin{pmatrix} e^{i(\theta_{e^-} - k_F L)/2} & 0 \\ 0 & e^{i(-\theta_{h^+} - k_F L)/2} \end{pmatrix}, \quad (6.16)$$

and where $\theta_{e^-} = (B_e^+ / \hbar v_F - k)L$ and $\theta_{h^+} = (B_h^+ / \hbar v_F + k)L$.

Similarly, we can define the transfer matrices for the holes:

$$\begin{aligned} \begin{pmatrix} b_{\uparrow}^+(L/2) \\ b_{\downarrow}^+(L/2) \end{pmatrix} &= t_h^+ \begin{pmatrix} b_{\uparrow}^+(0) \\ b_{\downarrow}^+(0) \end{pmatrix}, & \begin{pmatrix} b_{\uparrow}^+(L) \\ b_{\downarrow}^+(L) \end{pmatrix} &= t_h^+ \begin{pmatrix} b_{\uparrow}^+(L/2) \\ b_{\downarrow}^+(L/2) \end{pmatrix}, \\ \begin{pmatrix} b_{\uparrow}^-(L/2) \\ b_{\downarrow}^-(L/2) \end{pmatrix} &= t_h^- \begin{pmatrix} b_{\uparrow}^-(L) \\ b_{\downarrow}^-(L) \end{pmatrix}, & \begin{pmatrix} b_{\uparrow}^-(0) \\ b_{\downarrow}^-(0) \end{pmatrix} &= t_h^- \begin{pmatrix} b_{\uparrow}^-(L/2) \\ b_{\downarrow}^-(L/2) \end{pmatrix}, \end{aligned} \quad (6.17)$$

where the transfer matrices for positive/negative momentum holes are given by:

$$t_h^{\pm} = \begin{pmatrix} e^{i(\theta_{h^{\mp}} \pm k_F L)/2} & 0 \\ 0 & e^{i(-\theta_{e^{\pm}} \pm k_F L)/2} \end{pmatrix}. \quad (6.18)$$

Andreev reflection and the scatterer

As stated in the previous section, a consequence of diagonalizing the Hamiltonian in the way we have done, is that we would have to be careful when considering reflections which change the direction of the particles as well as when an electron is scattered as a hole and vice versa.

We previously looked at Andreev reflections, and saw that when scattered of the superconducting-normal surface, incoming electrons are scattered as outgoing holes with opposite spin, as well as picking up an energy dependent phase factor $e^{-i \arccos E/\Delta}$ and a phase corresponding to the phase of the superconducting region $\phi_{l/r}$. This would imply that we could describe the process of a left moving electron scattering to a right moving hole at the left SN surface with the following scattering matrix:

$$\begin{pmatrix} b_{\downarrow}^+(0) \\ -b_{\uparrow}^+(0) \end{pmatrix} = \underbrace{e^{-i \arccos E/\Delta} e^{i\phi_{l/r}}}_{r_A^I(0)} \begin{pmatrix} 1 & 0 \\ 0 & 1 \end{pmatrix} \begin{pmatrix} a_{\uparrow}^-(0) \\ a_{\downarrow}^-(0) \end{pmatrix}. \quad (6.19)$$

However, we have to account for the change of basis to be consistent with the scattering matrices above. Since the spin basis of the holes is rotated with respect to the electrons we have to apply a rotation matrix to the scattering matrix:

$$r_A^L(\theta) = e^{-i \arccos(E/\Delta)} e^{i\phi_l} \begin{pmatrix} \cos(\frac{\theta}{2}) & \sin(\frac{\theta}{2}) \\ -\sin(\frac{\theta}{2}) & \cos(\frac{\theta}{2}) \end{pmatrix}, \quad (6.20)$$

where θ is the angle between the effective fields for electrons and holes:

$$\theta(\vec{k}) = \arccos \left(\frac{\vec{B}_e(\vec{k}) \cdot \vec{B}_h(\vec{k})}{|\vec{B}_e(\vec{k})| |\vec{B}_h(\vec{k})|} \right). \quad (6.21)$$

The same can of course be done for the right surface, with the only change being picking up the phase from the right superconducting region ϕ_r :

$$r_A^R(\theta) = e^{-i \arccos(E/\Delta)} e^{i\phi_r} \begin{pmatrix} \cos(\frac{\theta}{2}) & \sin(\frac{\theta}{2}) \\ -\sin(\frac{\theta}{2}) & \cos(\frac{\theta}{2}) \end{pmatrix}. \quad (6.22)$$

The scattering matrix describing the inverse process (holes to electrons) can of course be found by applying the inverse rotation (by $-\theta$), and the phase picked up from the superconducting region is the opposite, because this is the time-reversed process:

$$r_A^{r/l*}(\theta) = e^{-i \arccos(E/\Delta)} e^{-i\phi_{r/l}} \begin{pmatrix} \cos(\frac{\theta}{2}) & -\sin(\frac{\theta}{2}) \\ \sin(\frac{\theta}{2}) & \cos(\frac{\theta}{2}) \end{pmatrix}. \quad (6.23)$$

Now the same basic idea can be applied to the case of the scatterer. The scattering matrix relating the amplitudes to the left and right of the scatterer is defined as:

$$\begin{pmatrix} a_{\uparrow}^+(L/2 + \eta) \\ a_{\downarrow}^+(L/2 + \eta) \\ a_{\uparrow}^-(L/2 - \eta) \\ a_{\downarrow}^-(L/2 - \eta) \end{pmatrix} = \begin{pmatrix} \hat{T} & -\hat{R} \\ \hat{R}^T & \hat{T} \end{pmatrix} \begin{pmatrix} a_{\uparrow}^+(L/2 + \eta) \\ a_{\downarrow}^+(L/2 + \eta) \\ a_{\uparrow}^-(L/2 - \eta) \\ a_{\downarrow}^-(L/2 - \eta) \end{pmatrix}, \quad (6.24)$$

where η is a small distance to the right and left of the scatterer, \hat{R} is a reflection matrix, \hat{R}^T is the transpose of the reflection matrix and \hat{T}

is the transfer matrix. The transfer matrix is proportional to the unit matrix:

$$\hat{T} = T \begin{pmatrix} 1 & 0 \\ 0 & 1 \end{pmatrix}, \quad (6.25)$$

and where T is the transfer amplitude. The reflection matrix, \hat{R} , gets the same rotation as the Andreev reflection matrix for the same reason, a rotation of the spin basis:

$$\hat{R} = \sqrt{1 - T^2} \begin{pmatrix} \cos(\frac{\theta}{2}) & \sin(\frac{\theta}{2}) \\ -\sin(\frac{\theta}{2}) & \cos(\frac{\theta}{2}) \end{pmatrix}. \quad (6.26)$$

Equation for the bound state energies

We now consider the amplitudes just to the right and left of the scatterer, which we label according to figure 6.2. Using the scattering matrices we have defined above we can relate the amplitudes of the positive momentum electrons on the right side of the scatterer, with the amplitudes of the negative momentum holes on the right side of the scatterer:

$$\begin{pmatrix} a_c^R \\ a_d^R \end{pmatrix} = M_1 \begin{pmatrix} a_a^R \\ a_b^R \end{pmatrix}, \quad (6.27)$$

where the scattering matrix, M_1 , consist of the piecewise scattering matrices:

$$M_1 = t_h^- r_A^R t_e^+. \quad (6.28)$$

On the left side of the scatterer we can do the same:

$$\begin{pmatrix} a_a^L \\ a_b^L \end{pmatrix} = M_2 \begin{pmatrix} a_c^L \\ a_d^L \end{pmatrix}, \quad (6.29)$$

$$M_2 = t_e^+ r_A^{L*} t_h^-. \quad (6.30)$$

From figure 6.2 we see that combining M_1 and M_2 makes a loop, which is how we are going to obtain the equation for the bound state energies. The scatterer does however make it so that we do not have

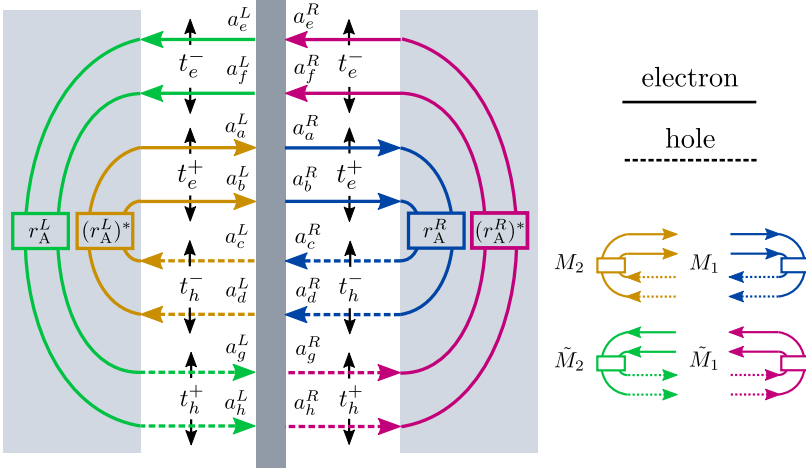


Figure 6.2.: Diagram showing the amplitudes labeling of the amplitudes to the right and left of the scatter in the 1D wire. The shaded region in the middle signifies the scatterer placed at $x = L/2$. The horizontal arrows represent the transfer matrices. The vertical arrows signify the pseudo-spin we introduced earlier, and should not be confused with the actual spin of the particle, unless there is no spin-orbit interaction. The mixing of the spin happens at the Andreev reflections and at the scatterer in the middle. Solid(dotted) lines signifies electrons(holes). The transfer matrices $M_{1,2}$ and $\tilde{M}_{1,2}$ are drawn in blue, orange, magenta and green respectively.

a closed loop quite yet. The scatterer can scatter electrons and holes into a different loop with the opposite direction. Hence, we do the same for the left moving electrons and right moving holes, obtaining:

$$\begin{pmatrix} a_e^R \\ a_f^R \end{pmatrix} = \tilde{M}_1 \begin{pmatrix} a_g^R \\ a_h^R \end{pmatrix}, \quad (6.31)$$

$$\begin{pmatrix} a_g^L \\ a_h^L \end{pmatrix} = \tilde{M}_2 \begin{pmatrix} a_e^L \\ a_f^L \end{pmatrix}, \quad (6.32)$$

where:

$$\tilde{M}_1 = t_e^- r_A^{R*} t_h^+, \quad (6.33)$$

$$\tilde{M}_2 = t_h^+ r_A^L t_e^-. \quad (6.34)$$

By using the scattering matrix for the scatterer, equation (6.24), and the M matrices from above, we can make the following relations for the amplitudes:

$$\begin{pmatrix} a_c^L \\ a_d^L \\ a_g^R \\ a_h^R \end{pmatrix} = \underbrace{\begin{pmatrix} \hat{T}M_1 & -\hat{R}\tilde{M}_2 \\ \hat{R}^T M_1 & \hat{T}\tilde{M}_2 \end{pmatrix}}_{M_A} \begin{pmatrix} a_a^R \\ a_b^R \\ a_e^L \\ a_f^L \end{pmatrix}, \quad (6.35)$$

and

$$\begin{pmatrix} a_a^R \\ a_b^R \\ a_e^L \\ a_f^L \end{pmatrix} = \underbrace{\begin{pmatrix} \hat{T}M_2 & \hat{R}^T \tilde{M}_1 \\ -\hat{R}M_2 & \hat{T}\tilde{M}_1 \end{pmatrix}}_{M_B} \begin{pmatrix} a_c^L \\ a_d^L \\ a_g^R \\ a_h^R \end{pmatrix}. \quad (6.36)$$

We now see that the vector on the right(left) side of equation (6.35) and the left(right) side of equation (6.36) are the same, meaning that we have a closed loop. This gives us the following eigenvalue problem:

$$\begin{pmatrix} a_a^R \\ a_b^R \\ a_e^L \\ a_f^L \end{pmatrix} = M_B M_A \begin{pmatrix} a_a^R \\ a_b^R \\ a_e^L \\ a_f^L \end{pmatrix}. \quad (6.37)$$

Which have solutions if the matrix $M_B M_A$ has an eigenvalue of 1. This is the case when:

$$\text{Det}[1 - M_B M_A] = 0, \quad (6.38)$$

which is an equation we can solve for the energy E of the bound states. Continuing to assuming that we are in the short junction limit we obtain the following expression for the bound state energies E :

$$E = \pm \Delta \sqrt{v \pm \sqrt{w}}, \quad (6.39)$$

where the two \pm are independent, and v and w are defined as:

$$v = \frac{1}{2}(1 + A - BR^2) - AT^2 \sin\left(\frac{\phi}{2}\right)^2, \quad (6.40)$$

$$w = (1 - A) \sin\left(\frac{\phi}{2}\right)^2 T^2 \times \left\{ (1 + A) \left[1 - \sin\left(\frac{\phi}{2}\right)^2 T^2 \right] - BR^2 \right\}, \quad (6.41)$$

where and $R^2 = 1 - T^2$, and using the notation:

$$A = \cos(\theta_{e+}) \cos(\theta_{h+}) - \cos(\theta) \sin(\theta_{e+}) \sin(\theta_{h+}), \quad (6.42)$$

$$B = 2 \sin(\theta)^2 \sin\left(\frac{\theta_{e+}}{2}\right)^2 \sin\left(\frac{\theta_{h+}}{2}\right)^2, \quad (6.43)$$

6.2. Critical current

From the bound state energies, equation (6.39), we are able to calculate the supercurrent using equation (6.6):

$$I(\phi) = \frac{2e}{\hbar} \sum_n' \frac{dE_n}{d\phi}, \quad (6.44)$$

A nice feature of the way we have expressed the energies is that we obtain two positive energies:

$$E_{\pm}^+ = \Delta \sqrt{v \pm \sqrt{w}}, \quad (6.45)$$

and two negative energies:

$$E_{\pm}^- = -\Delta \sqrt{v \pm \sqrt{w}}. \quad (6.46)$$

Which makes taking the sum over negative energies simple:

$$I_S(\phi) = \frac{2e}{\hbar} \sum_{\sigma=\pm} \frac{dE_{\sigma}^-}{d\phi}. \quad (6.47)$$

The expression for the supercurrent does, however, get quite involved, even with the notation introduced in the previous section. Because of this, we here look at a few parameter limits in some more detail.

Small-T limit

To obtain the supercurrent in the small-T limit we Taylor expand the energies from equation (6.46), keeping only terms up to $\mathcal{O}(T^2)$ and insert them into equation (6.47). This gives us the expression for the supercurrent in the small-T limit:

$$I_S(\phi) = \Delta \frac{2e}{\hbar} \frac{(A+1)T^2 \sin(\phi)}{2\sqrt{2A - BR^2 + 2}}. \quad (6.48)$$

As one would expect from a weakly coupled SNS junction, we get a sinusoidal critical current as a function of the phase difference between the two superconductors. Maximizing this with respect to the phase difference, ϕ , is as simple as setting $\sin(\phi) \rightarrow 1$, giving us the critical current in the small-T limit:

$$I_C(\phi) = \Delta \frac{2e}{\hbar} \frac{(A+1)T^2}{2\sqrt{2A - BR^2 + 2}}. \quad (6.49)$$

High-T limit

For the high-T limit we set the transmission amplitude to, $T \rightarrow 1$. Which after inserting the negative energies into equation (6.46) lets us write the supercurrent as:

$$I_S(\phi) = \Delta \frac{2e}{\hbar} \frac{1}{4} \left(\frac{\cos(\phi - \eta)}{\sqrt{\sin^2\left(\frac{1}{2}\left(-\eta + \phi - \frac{\pi}{2}\right)\right)}} - \frac{\cos(\eta + \phi)}{\sqrt{\cos^2\left(\frac{1}{2}\left(\eta + \phi - \frac{\pi}{2}\right)\right)}} \right), \quad (6.50)$$

Where η is the angle of the point $(\sqrt{1 - A^2}, A)$ ¹.

We can now, by using the symmetry of the supercurrent $I(\phi) = -I(-\phi)$ and the 2π periodicity of the critical current, focus on the region $\phi \in [0, \pi]$. Furthermore, using the fact that $-1 < A < 1$, which leads to $-\frac{\pi}{2} < \eta < \frac{\pi}{2}$, allows us to make the following simplification:

$$I_S(\phi) = \Delta \frac{2e}{\hbar} \begin{cases} \frac{\sin\left(\frac{\phi}{2}\right)\left(\sin\left(\frac{\eta}{2}\right) + \cos\left(\frac{\eta}{2}\right)\right)}{\sqrt{2}}, & \text{for } \phi < \eta + \frac{\pi}{2}, \\ \frac{\cos\left(\frac{\phi}{2}\right)\left(\sin\left(\frac{\eta}{2}\right) - \cos\left(\frac{\eta}{2}\right)\right)}{\sqrt{2}}, & \text{for } \phi > \eta + \frac{\pi}{2}. \end{cases} \quad (6.51)$$

1. This is essentially $\arctan(A/\sqrt{1 - A^2})$, but with an $\arctan(y/x)$ function which takes into account which quadrant the point (x, y) is in.

The absolute value of the first function above is monotonically increasing on the valid range $[0, \pi]$, while the absolute value of the second function is monotonically decreasing in the same region. This means that the critical current has to be at the point where we switch from one to the other at $\phi = \eta + \pi/2$:

$$\begin{aligned} I_c &= \Delta \frac{2e}{\hbar} \max \left[\left| \frac{1}{2} \{\sin(\eta) + 1\} \right|, \left| \frac{1}{2} \{\sin(\eta) - 1\} \right| \right] \\ &= \Delta \frac{e}{\hbar} [1 + \sin(|\eta|)], \end{aligned} \quad (6.52)$$

which after inserting the definition of η gives us the critical current for a transparent wire:

$$I_c = \Delta \frac{e}{\hbar} (1 + |A|), \quad (6.53)$$

which in terms of the electron and hole fields is:

$$I_c = \Delta \frac{e}{\hbar} [1 + |\cos(\theta_{e+}) \cos(\theta_{h+}) - \cos(\theta) \sin(\theta_{e+}) \sin(\theta_{h+})|]. \quad (6.54)$$

6.3. Applications

What we have obtained above is a model for the critical current in a nanowire with spin orbit interaction and Zeeman splitting. The critical current is written in terms of the effective field experienced by electrons and holes with positive momentum, the angle between these fields, and the transparency of the wire, T . Equivalently, by using the definition of the electron and hole field, we are able to express the critical current by the magnitude of the spin-orbit field and the Zeeman field, the angle between these, and again the transparency of the wire, T .

One application could be to measure the spin-orbit field in the nanowire. Assuming that the transparency of the wire and the g-factor can be found by other experiments, in principle the only unknown in the model is the spin orbit field². This model could possibly allow us to measure the spin-orbit coupling by using critical current measurements.

-
2. All angles between the Zeeman field and the spin-orbit field can be mapped out by critical current measurements for magnetic fields with different angles perpendicular to the wire, since we know the Rashba spin-orbit field is perpendicular to the wire.

A more general application is describing more complex devices such as devices made from multiple 1D SNS junctions [114]. Furthermore, the model can be used as a way of approximating the behavior of 2D SNS junctions. The current is not always carried uniformly through a 2D SNS junction [115], such as running along the edges of the junction. An approximate model for these systems could be one or more nanowires modeled in this chapter.

Probing spin–orbit and Zeeman fields via the critical current in a 2DHG SNS junction

Similarly to the previous chapter, we here look at the critical current of an SNS junction. The aim is also here to uncover details of the spin dynamics of the normal material. This time however, we look at a 2D hole gas (2DHG) SNS junction. This is motivated by the interest in recent years for devices made with 2DHGs [116–118], due to interesting properties such as anisotropic and tunable g -factors [119, 120], and strong and tunable spin-orbit interaction [121–124], all of which stem from the p-type orbital structure of the valence band [125]. Superconducting/2DHG devices have also gained attention lately due their applications within engineering topological superconductivity [126, 127].

The 2DHG SNS junction faces many of the same challenges as was brought up when discussing the NW SNS junction in the previous chapter, such as that microscopic geometric details of the junction, strain, carrier density and so on, can have a great impact on the both the effective spin orbit interaction and the g -factor of the material. However, these quantities are not trivial to measure. In the following, which is based on paper [III], we obtain analytical expressions for the critical current as a function of some of these parameters, and show that critical current measurements can tell us something about them.

7.1. Properties of the 2DHG

We imagine placing the chemical potential in the top of the valence band of a semiconductor, and are interested in the simplest model which describe the valence band. The valence band is p-orbital in the materials we consider, and hence has a total angular momentum of $3/2$ (electron spin, $1/2$, and the angular momentum from the orbital, 1). Because of this there are 6 sub-bands in the valence band: $|3/2, +3/2\rangle$, $|3/2, -3/2\rangle$, $|3/2, +1/2\rangle$, $|3/2, -1/2\rangle$, $|1/2, +1/2\rangle$, $|1/2, -1/2\rangle$. A sketch of the valence band and the conduction band can be seen in figure 7.1. Because of spin orbit interaction the $|1/2, +1/2\rangle$ and $|1/2, -1/2\rangle$ bands are split off from the rest. The energy which these bands are split off from the rest, Δ_{SO} , is assumed to be large, and so the top two bands,

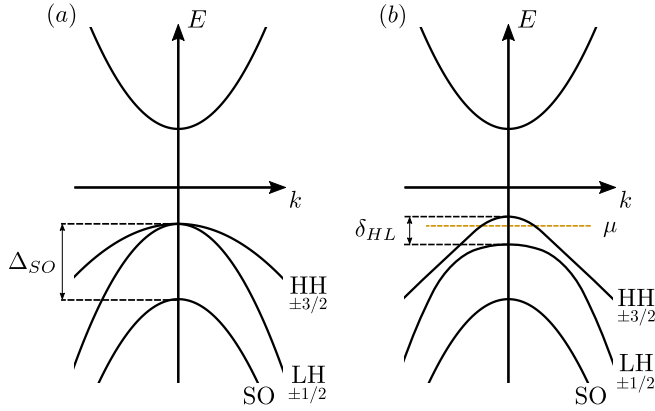


Figure 7.1.: Sketch of the spectrum of a hole gas. We can see the s-orbital conduction band and the p-orbital valence bands, including the split off band and the heavy and light holes. In (a) we see the spectrum in the bulk, while in (b) we see the spectrum of a 2D system. We assume that Δ_{SO} is large and that the chemical potential, μ , is placed close to the top of the HH band.

closes to the gap, called the heavy hole and light hole bands, are mainly what we are interested in. The heavy hole and light hole bands make an effective spin 3/2 system, which is the root of much of the interesting physics which we will see later in this chapter.

The 4×4 Luttinger Hamiltonian describes this effective 3/2 system and is derived from $k \cdot p$ theory, and is obtained by including the effects of the other bands in the full model by perturbation theory. The full Luttinger Hamiltonian (or indeed the full 16 state $k \cdot p$ model, the Kane model), can be looked up in e.g. [125], but we here keep to just writing the 2D Luttinger model, where we have assumed that the sample is heavily confined in the z -direction, in the basis of angular momentum states $\{|+3/2\rangle, |-3/2\rangle, |+1/2\rangle, |-1/2\rangle\}$:

$$H_L = \frac{1}{2m_0} \begin{pmatrix} P+Q & 0 & 0 & M \\ 0 & P+Q & M^* & 0 \\ 0 & M & P-Q & 0 \\ M^* & 0 & 0 & P-Q \end{pmatrix}, \quad (7.1)$$

where

$$P = \gamma_1 (k^2 + \langle k_z^2 \rangle), \quad (7.2a)$$

$$Q = \gamma_2 (k^2 - 2\langle k_z^2 \rangle), \quad (7.2b)$$

$$M = -\frac{1}{2}\sqrt{3} [(\gamma_2 + \gamma_3)k_-^2 + (\gamma_2 - \gamma_3)k_+^2], \quad (7.2c)$$

where $k^2 = k_x^2 + k_y^2$ is the square of the in plane component of the momentum vector, the momentum raising/lowering operators are defined as $k_{\pm} = k_x \pm ik_y$, and γ_i are the so called Luttinger parameters. The Luttinger parameters are material specific; examples of parameters are shown in table 7.1. From this table we can see that for some semiconductors, such as Ge, GaAs, InSb, and InAs (but not Si) the second and third Luttinger parameters are almost equal, $|\gamma_2 - \gamma_3| \ll \gamma_2 + \gamma_3$. When this is the case, the non-spherical symmetric term in equation (7.2c) becomes small. A good approximation for these materials is the spherical approximation, where we drop this non-spherically symmetric term [125]. In the following we assume that we are able to use this approximation. The expectation value of the k_z^2 operator is proportional to the inverse square of the confinement length, $\langle k_z^2 \rangle \sim 1/d^2$, where d is the confinement length in the z -direction.

Spin orbit interaction and the Zeeman effect

We also want to include spin-orbit coupling and the Zeeman effect. We here limit our selves to a Rashba like spin-orbit coupling which could be due to asymmetries created by the interfaces or an externally applied electric field. This coupling can be described by the Hamiltonian:

$$H_R = i\alpha_R(k_+J_- - k_-J_+), \quad (7.3)$$

Table 7.1.: Table over the Luttinger parameters $\gamma_{1,2,3}$ of a few semiconductors of interest [125].

	γ_1	γ_2	γ_3
Ge	13.38	4.24	5.69
GaAs	6.85	2.10	2.90
InAs	20.40	8.30	9.10
InSb	37.10	16.50	17.70
Si	4.285	0.339	1.446

where α_R is the amplitude of the coupling term, and characterizes the strength of the coupling, $J_{\pm} = J_x \pm iJ_y$ are the spin 3/2 raising and lowering operators, which in matrix form can be written in the same basis as the Luttinger Hamiltonian:

$$J_+ = \begin{pmatrix} 0 & 0 & \sqrt{3} & 0 \\ 0 & 0 & 0 & \sqrt{3} \\ 0 & 0 & 0 & 2 \\ 0 & 0 & 0 & 0 \end{pmatrix}, \quad (7.4)$$

$$J_- = \begin{pmatrix} 0 & 0 & 0 & 0 \\ 0 & 0 & 0 & 0 \\ \sqrt{3} & 0 & 0 & 0 \\ 0 & \sqrt{3} & 2 & 0 \end{pmatrix}. \quad (7.5)$$

The Zeeman effect due to an in-plane magnet effect can be described with the Hamiltonian in the effective spin 3/2 system as:

$$H_Z = -2\kappa(B_+J_- + B_-J_+), \quad (7.6)$$

where $B_{\pm} = B_x \pm iB_y$, κ is the g-factor for the holes, and where we are working in units of the Bohr magneton $\mu_B = 1$.

Full Hamiltonian

We now have all the ingredients for writing the full 2DHG Hamiltonian:

$$H_{\text{tot}} = H_0 + H_Z + H_R$$

$$= \begin{pmatrix} k^2/2m_H & 0 & -\sqrt{3}(2\kappa B_- + i\alpha_R k_-) & -k^2/2m_x \\ 0 & k^2/2m_H & -k_+^2/2m_x & \sqrt{3}(-2\kappa B_+ + i\alpha_R k_+) \\ \sqrt{3}(-2\kappa B_+ + i\alpha_R k_+) & -k_-^2/2m_x & \delta_{HL} + k^2/2m_L & -4\kappa B_- - 4i\alpha_R k_- \\ -k_+^2/2m_x & -\sqrt{3}(2\kappa B_- + i\alpha_R k_-) - 4\kappa B_+ + 4i\alpha_R k_+ & \delta_{HL} + k^2/2m_L & \end{pmatrix}, \quad (7.7)$$

where $\delta_{HL} = 2\gamma_2 \langle k_z^2 \rangle / m_0$ is the splitting between the heavy holes and the light holes, $m_H = m_0 / (\gamma_1 + \gamma_2)$ and $m_L = m_0 / (\gamma_1 - \gamma_2)$ are the effective heavy and light hole masses in terms of the Luttinger parameters and the bare electron mass, m_0 . Additionally, we have defined $m_x = 2m_0 / \sqrt{3}(\gamma_2 + \gamma_3)$, to describe the strength of the mixing between the heavy and light holes which comes from the Luttinger Hamiltonian.

Furthermore, assuming that the heavy hole/light (HH-LH) hole splitting, δ_{HL} , is large compared to the other terms of the Hamiltonian allows us to treat the coupling between the heavy hole and the light hole subspace perturbatively. To do this we can use a similar approach as we did in chapter 4, however, keeping track of all terms can again be cumbersome, and instead we here use a Schrieffer-Wolff transformation [128], to decouple the heavy and light hole subspaces perturbatively. The effective heavy hole Hamiltonian to second order in $1/\delta_{HL}$ becomes:

$$H_{HH} = \begin{pmatrix} k^2/2m_H & g \\ g^* & k^2/2m_H \end{pmatrix}, \quad (7.8)$$

$$g = -\frac{\sqrt{3}}{\delta_{HL}} \frac{k_-^2}{m_x} (2\kappa B_- + i\alpha_R k_-) - \frac{12}{\delta_{HL}^2} (2\kappa B_- + i\alpha_R k_-)^2 (\kappa B_- + i\alpha_R k_-). \quad (7.9)$$

7.2. Model

In figure 7.2 we can see a schematic of the system we consider: An SNS junction made up of a zDHG connected to two identical conventional superconductors. As we did in the previous section, we calculate the critical current, the maximal supercurrent which the junction can carry. The approach in this chapter is going to be a bit different. The supercurrent, which is driven by a phase difference, ϕ , between the two superconductors, is in the ground state given by:

$$I(\phi) = \frac{2e}{\hbar} \frac{\partial F}{\partial \phi}, \quad (7.10)$$

where e is the electron charge, \hbar is the reduced Planks constant, and F is the free energy of the junction. Hence, we need a way to calculate the free energy of the junction, and specifically we only care about the part of the free energy which “knows” about the superconductors, i.e. is ϕ -dependent.

For now, we do not assume anything about the Hamiltonian of the normal material, but we do assume that the coupling between

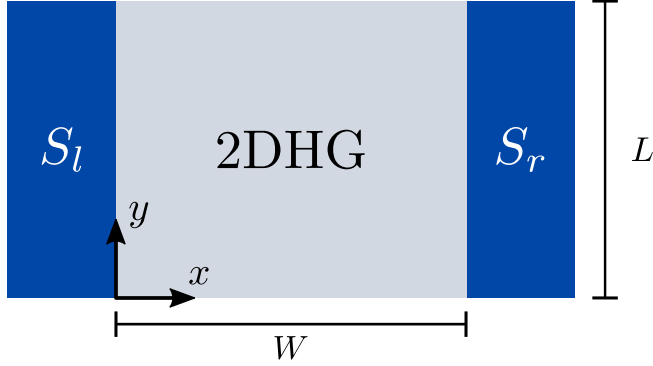


Figure 7.2.: Schematic of the system we consider: An SNS junction of length L and width W , made up of two identical superconductors, S_l and S_r , connected by a 2DHG.

the superconductors and the 2DHG is described by the tunneling Hamiltonian:

$$H_t = \sum_{\sigma} \int dy [t_l \hat{\psi}_{\sigma}^{\dagger}(0, y) \hat{\Psi}_{\sigma, L}(0, y) + t_r \hat{\psi}_{\sigma}^{\dagger}(W, y) \hat{\Psi}_{\sigma, R}(W, y) + \text{H.c.}], \quad (7.11)$$

where $\hat{\psi}_{\sigma}^{\dagger}(\vec{r})$ is the creation operator of an electron from the normal region with spin σ at position \vec{r} , $\hat{\Psi}_{\sigma, L(R)}^{\dagger}(\vec{r})$ is the creation operator of an electron in the left (right) superconductor with spin σ at position \vec{r} , and the superconductor/2DHG interfaces are defined by the lines/planes $x = 0, W$. The coupling is essentially just electrons tunneling between the normal material and the superconductor, with the amplitude $t_{l,r}$.

Furthermore, we assume that the coupling amplitudes $t_{l,r}$ from above are small, so that we can employ a perturbative method in obtaining part of the free energy which “knows” about both superconductors. To do this we employ a Green function formalism.

7.2.1. Green function formalism

To get to the supercurrent we are going to introduce a few concepts. We here only reiterate the key main steps from the supplementary material of Paper [III]. As stated we are going to calculate the free

energy, which is given by:

$$F = -T \ln \text{Tr}[e^{H/T}], \quad (7.12)$$

where, $H = H_{\text{tot}} + H_t$ is the full Hamiltonian of the 2DHG and the tunneling Hamiltonian from above, and T is the temperature (we here use units where $k_B = \hbar = 1$). We here work in the interaction picture, which means that the time dependence is governed by H_{tot} alone. From the definition:

$$S = T_\tau \exp \left[- \int_0^\beta d\tau' H_t(\tau') \right], \quad (7.13)$$

where T_τ is the imaginary-time time-ordering operator, and $\beta = 1/T$ is the inverse temperature, it can be shown that the free energy can be written as:

$$F = F_0 + T \ln \langle S \rangle, \quad (7.14)$$

where $F_0 = -T \ln \text{Tr}[e^{-H_{\text{tot}}/T}]$ and $\langle \dots \rangle$ is the Gibbs statistical average over the unperturbed states. Furthermore, it can be shown that this can be rewritten in terms of only connected diagrams (this can be found in any text book on the topic, e.g. in [129]), that is as a sum over all self-energy diagrams:

$$F = F_0 - T(\langle S \rangle_{\text{con}} - 1), \quad (7.15)$$

where $\langle S \rangle_{\text{con}}$ is the sum over all possible self energy terms contributing to $\langle S \rangle$:

$$\langle S \rangle_{\text{con}} = 1 + \Xi_1 + \Xi_2 + \dots, \quad (7.16)$$

where the self-energy terms are defined as:

$$\Xi_n = \frac{(-1)^n}{n!} \int_0^\beta d\tau_1 \dots d\tau_n \langle T_\tau H_t(\tau_1) \dots H_t(\tau_n) \rangle. \quad (7.17)$$

The self-energy diagrams can be visualized as loops, see figure 7.3. The order of the diagrams is given by the number of tunneling operators, i.e. how many times they cross the boundary between the superconductor and the normal material. It is easy to see that the

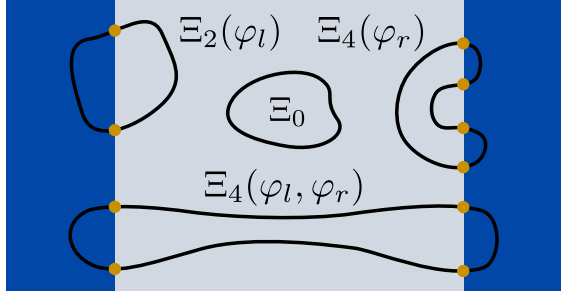


Figure 7.3.: Sketch of self-energy diagrams contributing to the free energy. In the middle is a diagram contributing to the trivial self energy Ξ_0 , to the top left is a diagram contributing to Ξ_2 which only knows about the left superconductor, to the top right is a diagram which contribute to Ξ_4 , but which only knows about the right superconductor. Finally, towards the bottom is a diagram contributing to Ξ_4 which depends on the phase difference between the two superconductors, $\varphi = \varphi_l - \varphi_r$, hence, contributing to the supercurrent.

lowest order diagrams which “know” about both superconductor, and specifically the phase difference $\varphi_l - \varphi_r = \varphi$, has to be fourth order in the tunneling Hamiltonian. For the purposes of calculating the supercurrent, we can throw out lower order diagrams and fourth order diagrams which do not depend on φ , see figure 7.3. Assuming the coupling is weak, we focus on the lowest order correction which is fourth order in the coupling Hamiltonian:

$$\Xi_4 = \frac{1}{4!} \int_0^\beta d\tau_1 d\tau_2 d\tau_3 d\tau_4 \langle T_\tau H_t(\tau_1) H_t(\tau_2) H_t(\tau_3) H_t(\tau_4) \rangle. \quad (7.18)$$

We can now insert the tunneling Hamiltonian from equation (7.11). Assuming that the dimensions of the junction is large compared to the Fermi wavelength, we can assume that the Andreev reflection is local and energy independent. By then applying Wick’s theorem we are able to write the fourth order self-energy as:

$$\Xi_4 = \lambda_l \lambda_r \int dy dy' \text{Re} \left\{ e^{i[\varphi_l(y) - \varphi_r(y')]} \times \sum_k \text{Tr} [\bar{\mathcal{G}}(W, y'; 0, y; i\omega_k) \sigma_y \bar{\mathcal{G}}(W, y'; 0, y; -i\omega_k)^T \sigma_y] \right\},$$

(7.19)

where $\lambda_{r,l} = \pi t_{r,l}^2 v_{\text{eff}}$ is the strength of the coupling between the 2DHG and the right/left superconducting leads, v_{eff} is the local effective one-dimensional tunneling density of states of the superconductor, σ_y is the y Pauli matrix, $\varphi_{r,l}(y)$ is the phase of the right/left superconductor at position (W, y) and $(0, y)$ respectively, and Tr is the trace over the matrix. The \mathcal{G} are matrices in spin space and are defined as:

$$\bar{\mathcal{G}}(x', y'; x, y; i\omega_k) = \begin{pmatrix} \mathcal{G}_{\uparrow\uparrow}(x', y'; x, y; i\omega_k) & \mathcal{G}_{\uparrow\downarrow}(x', y'; x, y; i\omega_k) \\ \mathcal{G}_{\downarrow\uparrow}(x', y'; x, y; i\omega_k) & \mathcal{G}_{\downarrow\downarrow}(x', y'; x, y; i\omega_k) \end{pmatrix}, \quad (7.20)$$

where

$$\mathcal{G}_{\sigma'\sigma}(\vec{r}', \vec{r}; i\omega_k) = - \int_0^\beta d\tau e^{i\omega_k \tau} \langle \hat{T}_\tau \hat{\psi}_{\sigma'}(\vec{r}', \tau) \hat{\psi}_\sigma^\dagger(\vec{r}, 0) \rangle, \quad (7.21)$$

are the so-called Matsubara Green functions with Matsubara frequency $\omega_k = (2k + 1)\pi T$, which describe the propagation in the normal region for an electron with spin σ at location \vec{r} to a location \vec{r}' with spin σ' .

To get to the free energy, which allows us to calculate the supercurrent, we see that the lowest order contribution to the free energy which is dependent on the phase difference between the superconductors, is given by:

$$F^{(4)} = -T\Xi_4. \quad (7.22)$$

What we have obtained is a relatively compact equation for the fourth-order correction to the free energy, which essentially describes the transport of two electrons (or equivalently described by an electron and a hole with negative momentum) from a point, y , at one of the SN surfaces to a different point y' for the other surface. The two electrons emerging from one superconductor and which is reabsorbed by the other superconductor is essentially a Cooper pair. Hence, we write the free energy in terms of a correlation function, $C(\vec{r}'; \vec{r})$, describing cooper pair propagation:

$$F^{(4)} = -\lambda_l \lambda_r \iint dy dy' \text{Re} \left\{ e^{i[\varphi_l(y) - \varphi_r(y')]} C(W, y'; 0, y) \right\}, \quad (7.23)$$

where

$$C(\vec{r}'; \vec{r}) = \frac{T}{2} \sum_k \text{Tr} \left[\bar{\mathcal{G}}(\vec{r}', \vec{r}; i\omega_k) \sigma_y \bar{\mathcal{G}}(\vec{r}', \vec{r}; -i\omega_k)^T \sigma_y \right], \quad (7.24)$$

Out of plane magnetic field

In the presence of an out of plane magnetic field, we get phase differences between electron paths, due to the Aharonov-Bohm effect. Additionally, orbital effects can become important, but we here assume the applied magnetic fields to be small enough to neglect these. The flux penetration effects, on the other hand, can be large even for small fields. To account for this effect we define the phases $\varphi_{r,l}$ from above in such a way that it captures the effects of the flux $\Phi = B_z W L^1$ penetrating the junction:

$$\varphi_l(y) - \varphi_r(y') = \phi + \frac{\pi(y + y')B_z W}{\Phi_0}, \quad (7.25)$$

where the bare phase difference is given by ϕ , and $\Phi_0 = h/2e$ is the flux quantum.

7.3. Linearization of the Hamiltonian and the semi-classical approximation

To obtain analytical results for the critical current we are going to make some approximations. First, we are going to assume that relevant dynamics happen at an energy scale close to the Fermi level, E_F , allowing us to linearize the kinetic energy part of Hamiltonian 7.8, H_{HH} , as well as assuming that the absolute value of the in-plane momentum vector can be approximated by the Fermi momentum, $|\vec{k}| \approx k_F$ for the off-diagonal elements. This gives us the linearized heavy hole Hamiltonian:

$$H_{HH} = v_F(k - k_F) + \vec{\beta}(\theta) \cdot \vec{\sigma}, \quad (7.26)$$

where $v_F = k_F/m_H$ is the Fermi velocity, the field $\vec{\beta}$ describes the effective field the holes experiences and includes all the off-diagonal terms of Hamiltonian 7.8, and θ describes the angle of the in-plane momentum, \vec{k} . This Hamiltonian can easily be diagonalized [130]:

$$H_{HH} = \sum_{\lambda_{\vec{k}} = \pm \vec{k}} \varepsilon_{\vec{k}\lambda} P^{\lambda_{\vec{k}}}, \quad (7.27)$$

-
1. Due to the superconductor expelling the magnetic field, the real flux penetrating the junction would be higher than $\Phi = B_z W L$ from an applied field B_z . We neglect this here, but it could be compensated for by renormalizing B_z .

where the projector

$$P^{\lambda_{\vec{k}}} = |\lambda_{\vec{k}}\rangle\langle\lambda_{\vec{k}}| = \frac{1}{2} (1 + \lambda \hat{\beta}(\theta) \cdot \vec{\sigma}), \quad (7.28)$$

projects onto the two eigenspinors $|\lambda_{\vec{k}}\rangle$, where $\lambda = \pm$. $\hat{\beta}(\theta)$ is the unit vector describing the direction of the effective field, $\hat{\beta}(\theta) = \vec{\beta}(\theta)/|\vec{\beta}(\theta)|$. The energies are given by:

$$\varepsilon_{\vec{k}\lambda}^{\pm} = v_F(k - k_F) + \lambda|\vec{\beta}(\theta)|. \quad (7.29)$$

Assuming that we have full translational invariance in the 2DHG, as well as zero temperature, the correlation function $C(\vec{r}'; \vec{r})$ can be written in terms of the projection operator in the following way, again, see the supplementary material of paper [III] for the details:

$$C(\vec{r}) = \iint_0^{\infty} \frac{d\varepsilon d\varepsilon'}{2(\varepsilon + \varepsilon')} \text{Tr}[\bar{g}(\vec{r}, -\varepsilon)\sigma_y \bar{g}(\vec{r}, -\varepsilon')^T \sigma_y + \bar{g}(\vec{r}, \varepsilon)\sigma_y \bar{g}(\vec{r}, \varepsilon')^T \sigma_y], \quad (7.30)$$

where,

$$\bar{g}(\vec{r}, \varepsilon) = \frac{1}{(2\pi)^2} \sum_{\lambda_{\vec{k}} = \pm} \int d\vec{k} e^{i\vec{k}\cdot\vec{r}} \delta(\varepsilon - \varepsilon_{\vec{k}\lambda}^{\pm}) P^{\lambda_{\vec{k}}}. \quad (7.31)$$

This can be further simplified, if we assume that $k_F r \gg 1$ for all relevant distances, such as the width of the junction W . This is essentially a semi-classical approximation which means we only care about straight electron/hole paths, where the momentum vector is parallel/anti-parallel to \vec{r} . The greatly simplified expression for $C(\vec{r})$ can then be expressed as:

$$C(\vec{r}) = \frac{K}{r^2} \left\{ \cos\left(\frac{|\beta(\theta)|r}{v_F}\right) \cos\left(\frac{|\beta(\bar{\theta})|r}{v_F}\right) - \hat{\beta}(\theta) \cdot \hat{\beta}(\bar{\theta}) \sin\left(\frac{|\beta(\theta)|r}{v_F}\right) \sin\left(\frac{|\beta(\bar{\theta})|r}{v_F}\right) \right\}, \quad (7.32)$$

where $K = k_F/(2\pi)^2 v_F$. The angle θ is now parallel to \vec{r} and the bar signifies that we are talking about anti-parallel angle, $\bar{\theta} = \theta - \pi$.

7.4. Critical current

The expression we derived in the previous section for $C(\vec{r})$ is fairly simple, and could feasibly be integrated analytically, giving us the supercurrent. However, the large number of competing coupling terms seen in equation (7.9) make the effective field $\beta(\theta)$, and hence the supercurrent², look very different depending on parameters such as the exact hole g-factor κ , the Rashba spin orbit strength α_R , the confinement parameterized by the HH-LH splitting δ_{HL} and the Luttinger spin-orbit coupling strength parameterized by $1/m_x$. We will instead focus on the case where a few of these terms are dominating. We look at the case when the HH-LH splitting in a bit of detail, and refer to paper [III], for the details of the remaining limits.

7.4.1. Large HH-LH splitting

When we are in the limit of large HH-LH splitting, the terms which are proportional to $1/\delta_{HL}^2$ are suppressed. Formally, the limit where the terms which are linear in $1/\delta_{HL}$ dominate is when³:

$$\sqrt{\delta_{HL}E_x} \gg E_Z, E_{SO}, \quad (7.33)$$

where we define the energies: $E_Z = \kappa B_{\parallel}$, the Zeeman energy, $E_{SO} = \alpha_R k_F$, the spin orbit energy, and $E_x = k_F^2/2m_x$, which is the energy associated with the orbital coupling of the Luttinger Hamiltonian.

In this limit the effective field, here expressed in terms of $\beta_+ = \beta_x + i\beta_y$:

$$\beta_+(\theta) = \frac{2\sqrt{3}E_x}{\delta_{HL}} \left(iE_{so}e^{3i\theta} - 2E_Ze^{i(2\theta+\phi_B)} \right), \quad (7.34)$$

where θ is the angle of the momentum vector, and ϕ_B is the angle of the in-plane magnetic field. Interestingly the first term makes the effective field rotate 3 times as fast as the momentum vector (or a standard 2DEG

-
2. In the case of zero out of plane magnetic field, which we focus on here, the supercurrent is $\propto \cos \phi$, and so the critical current is found by maximizing this factor, i.e. setting it to 1.
 3. This is assuming that the Luttinger parameters are of order unity. The following discussion is still general, as larger/smaller Luttinger parameters only shifts the ranges where the limits discussed are valid.

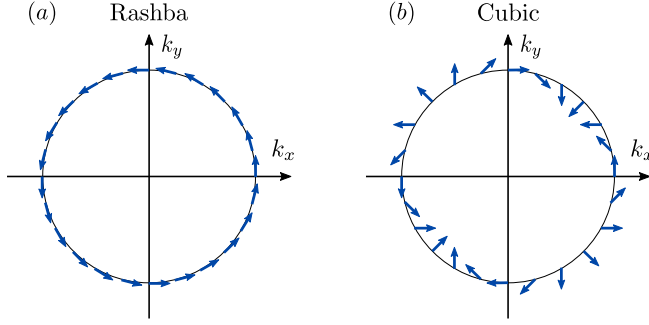


Figure 7.4.: Sketch of the effective field caused by (a) Rashba spin-orbit coupling and (b) the cubic spin orbit term in equation (7.34).

Rashba spin-orbit field) while the second term makes the effective field rotate twice as fast as the momentum vector and at the same rate as the magnetic field (i.e. the same dependence on the angle of the magnetic field as a Zeeman term in a 2DHG), see figure 7.4.

However, as we can see from cooper pair propagator in equation (7.32), the only place where the direction of the effective field comes in is where we take the dot product of the field where the momentum vector points in some direction θ with the effective field where the momentum vector points in the opposite direction $\hat{\theta}$: $\hat{\beta}(\theta) \cdot \hat{\beta}(\hat{\theta})$. What this effectively means is that what matters is the relative orientation of the terms which make up the effective fields. While the terms in the effective field β_+ above might look strange, both of the terms essentially rotate twice as fast as the momentum vector. On top of this the first term rotates at the same rate as the momentum vector (Rashba spin-orbit like) and the second term rotates at the same rate as the in-plane magnetic field (Zeeman like). By dropping the extra rotations we can simplify the cooper pair propagator in the limit where either of the two terms dominate:

$$C(\vec{r}) \approx \frac{K}{r^2} \times \begin{cases} \cos(|\vec{d}|r) & \text{for } E_Z \gg E_{so} \\ \cos([\hat{z} \times \vec{d}] \cdot \vec{r}) & \text{for } E_{so} \gg E_Z \end{cases}, \quad (7.35)$$

where $\vec{d} = \vec{B}_{\parallel} / B_0 W$, where $B_0 = \delta_{HL} v_F / 8\sqrt{3} E_x W \kappa$. This is on the same form as a 2DEG SNS junction with Rashba spin-orbit coupling and Zeeman splitting, see Ref. [130], which is expected since the relative orientation of the effective fields is the same as for the 2DEG SNS

junction. Furthermore, assuming no out-of-plane magnetic field, we are able to calculate the critical current in these limits by evaluating the following integral:

$$I_c(\vec{B}_{\parallel}) = 4 \left| \lambda_l \lambda_r \iint_0^L dy dy' C(W, y' - y) \right|, \quad (7.36)$$

where we have set the electron charge $e = 1$. This integral looks deceptively simple, and even though it is (semi)-analytically solvable, see the supplemental material of paper [III], it is surprisingly complicated. Under the assumption that we are in the long junction limit, i.e. $L \gg W$, the integral simplifies somewhat. For the case of $E_Z \gg E_{so}$ the critical current simplifies to:

$$I_{c1}(\vec{B}_{\parallel}) = I_0 \frac{\pi L}{2W} \left| \pi \alpha [J_0(\alpha)H_1(\alpha) - J_1(\alpha)H_0(\alpha)] + 2[1 - \alpha J_0(\alpha)] \right|, \quad (7.37)$$

where $\alpha = B_{\parallel}/B_0$, $I_0 = 4K|\lambda_l \lambda_r|$ is the scale of the supercurrent, $J_n(x)$ are the Bessel functions of the first kind, and $H_n(x)$ are the Struve functions. For the case of $E_Z \ll E_{so}$, still in the limit of $L \gg W$, it is somewhat easier to show that we can obtain the critical current:

$$I_{c2}(\vec{B}_{\parallel}) \approx I_0 \frac{\pi L}{W} e^{-|B_x/B_0|} |\cos(B_y/B_0)|. \quad (7.38)$$

7.4.2. Numerical calculations

To compare the analytic results from above, and to explore more complicated limits, we can calculate the critical current from the effective field $\beta(\theta)$ numerically. In the following we will look at three different limits: Firstly, the example we looked at above where the HH-LH splitting is large. Secondly, the limit where the HH-LH splitting is not dominating, which opens the possibility of the terms which are quadratic in the HH-LH splitting, $\propto 1/\delta_{HL}^2$ to dominate. And lastly, we look at the limit where there is no Rashba SOI, $\alpha \rightarrow 0$.

Large HH-LH splitting

In figure 7.5 we show the critical current, I_c , as a function of an applied in-plane magnetic field, B_{\parallel} , for different ratios of E_{so}/E_Z . In the figure

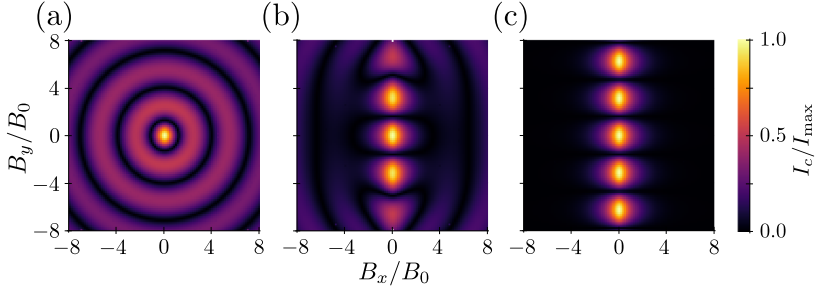


Figure 7.5.: (a-c) Critical current as a function of in-plane magnetic field, $B_{\parallel} = (B_x, B_y)$, $B_z = 0$, in the limit of large HH-LH splitting, $\sqrt{\delta_{HL}E_x} \gg E_z, E_{so}$. The subfigures critical current for different ratios of E_{so}/E_z : (a) $E_{so}/\kappa B_0 = 0.2$, (b) $E_{so}/\kappa B_0 = 2$, and (c) $E_{so}/\kappa B_0 = 20$. Where $B_0 = \delta_{HL}v_F/8\sqrt{3}E_xW\kappa$, and $I_{\max} = I_0\pi L/W$. All plots are calculated for a device with aspect ratio $L/W = 10$.

we have used $E_{so}/\kappa B_0 = 0.2, 2, 20$ respectively. In all the examples we use an aspect ratio of $L/W = 10$.

Comparing these plots with the critical current we derived in equations (7.37) and (7.38) we see that these describe the behavior of the critical current. As expected the plots look similar compared to those of Ref. [130], which describes the critical current of a 2DEG SNS junction.

“Small” HH-LH splitting

When the HH-LH splitting is not quite as large as described in the previously discussed limit, the terms which are inversely quadratic in the HH-LH splitting $\propto 1/\delta_{HL}^2$ can become dominating. Formally we are in this limit when:

$$E_z, E_{so} \gg \sqrt{\delta_{HL}E_x}. \quad (7.39)$$

The total coupling field then becomes:

$$\beta_+(\theta) = \frac{12}{\delta_{HL}^2} \left(-iE_{so}^3 e^{3i\theta} + 5E_{so}^2 E_z e^{i(2\theta+\phi_B)} + 8iE_{so} E_z^2 e^{i(\theta+2\phi_B)} - 4E_z^3 e^{3i\phi_B} \right), \quad (7.40)$$

which is much more involved than the previous limit. In this discussion we only numerically evaluate the critical current, however, similarly

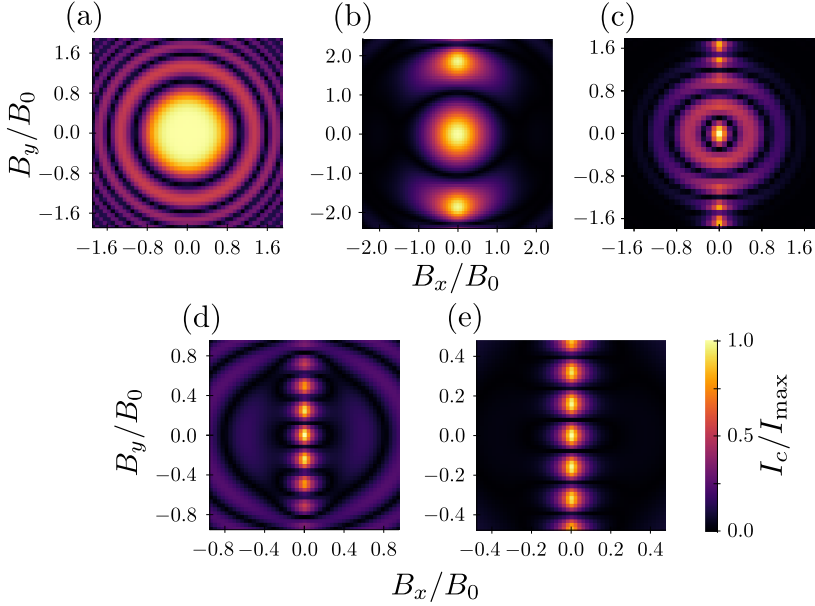


Figure 7.6.: (a-e) Critical current as a function of in-plane magnetic field, $B_{\parallel} = (B_x, B_y)$, $B_z = 0$, in the limit of not so large HH-LH splitting, $E_Z, E_{so} \gg \sqrt{\delta_{HL} E_x}$. The subfigures critical current for different ratios of E_{so}/E_Z : (a) $E_{so}/\kappa B_0 = 0.157$, (b) $E_{so}/\kappa B_0 = 1.19$, (c) $E_{so}/\kappa B_0 = 1.97$, (d) $E_{so}/\kappa B_0 = 3.16$, and (e) $E_{so}/\kappa B_0 = 3.94$. Where $\kappa B_0 = (\delta_{HL}^2 v_F / 96W)^{1/3}$, and $I_{\max} = I_0 \pi L / W$. All plots are calculated for a device with aspect ratio $L/W = 10$.

to the case above we are able to obtain (semi)-analytic results for the critical current when we consider sub-limits where one or two of the terms above dominates, see paper [III].

In figure 7.6 we show the critical current as a function of in-plane magnetic fields, for different ratios of E_{so}/E_Z . In this figure we have used (a) $E_{so}/\kappa B_0 = 0.157$, (b) $E_{so}/\kappa B_0 = 1.19$, (c) $E_{so}/\kappa B_0 = 1.97$, (d) $E_{so}/\kappa B_0 = 3.16$, and (e) $E_{so}/\kappa B_0 = 3.94$, where we now define $\kappa B_0 = (\delta_{HL}^2 v_F / 96W)^{1/3}$. We use the same aspect ratio as before, $L/W = 10$.

We can see that similar patterns from before appear in this limit as well. Some of them are, however, somewhat distorted, which can be explained by some terms having more than one magnetic field operator. e.g. figure 7.6 (a) corresponds to the limit in which the last term of

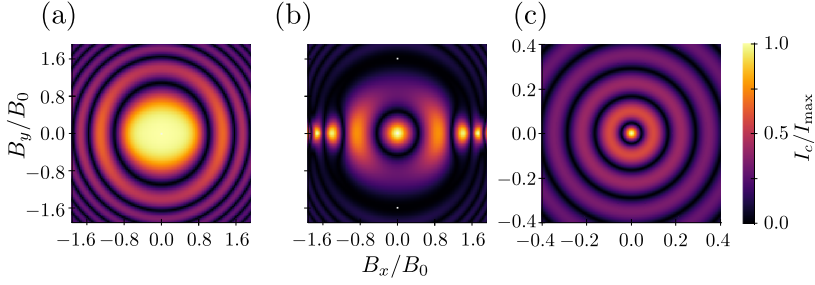


Figure 7.7.: (a-c) Critical current as a function of in-plane magnetic field, $B_{\parallel} = (B_x, B_y)$ and $B_z = 0$, in the limit of weak or no spin-orbit coupling, $\alpha_R \rightarrow 0$. The subfigures show critical current for different ratios of $E_x \delta_{HL} / E_Z^2$: (a) $\sqrt{3} E_x \delta_{HL} / 12(\kappa B_0)^2 = 0.252$, (b) $\sqrt{3} E_x \delta_{HL} / 12(\kappa B_0)^2 = 2.52$, and (c) $\sqrt{3} E_x \delta_{HL} / 12(\kappa B_0)^2 = 25.2$. Where $\kappa B_0 = (\delta_{HL}^2 \nu_F / 96W)^{1/3}$, and $I_{\max} = I_0 \pi L / W$. All plots are calculated for a device with aspect ratio $L/W = 10$.

equation (7.40) dominates, $E_Z \gg E_{so}$, this term looks like a Zeeman term, but is proportional to B^3 , hence the non-linear spacing of the rings. Similar expression as equations (7.37) and (7.38) can be found for the limits we look at in figure 7.6, see paper [III].

Weak spin-orbit coupling

Lastly, we consider the limit where $\alpha_R \rightarrow 0$, i.e. in the case of vanishing Rashba spin-orbit interaction. The effective field in this case is then given by:

$$\beta_+(\theta) = \frac{-4E_Z}{\delta_{HL}} \left(\sqrt{3} E_x e^{i(2\theta + \phi_B)} + \frac{12E_Z^2}{\delta_{HL}} e^{i3\phi_B} \right). \quad (7.41)$$

In figure 7.7 we show the calculated critical current as a function of in-plane magnetic field, for different ratios of $E_x \delta_{HL} / E_Z^2$. We use the parameters: (a) $\sqrt{3} E_x \delta_{HL} / 12(\kappa B_0)^2 = 0.252$, (b) $\sqrt{3} E_x \delta_{HL} / 12(\kappa B_0)^2 = 2.52$, and (c) $\sqrt{3} E_x \delta_{HL} / 12(\kappa B_0)^2 = 25.2$, where $\kappa B_0 = (\delta_{HL}^2 \nu_F / 96W)^{1/3}$ and the aspect ratio of $L/W = 10$.

The only “new” pattern is the intermediary case where the two terms in the effective field is close to being equal in magnitude. We here see islands of high critical current along the x -axis of the plot, as

opposed to the nodes along the y -axis in the previous limits. Similar expression as equations (7.37) and (7.38) can be found for the three limits looked at in figure 7.7, see paper [III].

7.5. Signatures of SOI and Zeeman in critical current

The results in the previous section suggests that the critical current could be useful for characterizing the relative strength of the spin orbit field and the Zeeman field in 2DHG SNS devices.

The simplest possible case is if the patterns we see are unique to a certain limit, e.g. looking at figure 7.7 (b) in which we see islands of high critical current along the x -axis. Seeing this in measurements would indicate that the Rashba SOI of the device is negligible compared to the Zeeman effect, and that Zeeman effect is comparable to the Luttinger orbit coupling.

Another signature, which does not exactly pinpoint the relative strength of the relevant fields, is islands in the critical current along the y -axis, see figure 7.6 (b) and (e), and figure 7.5 (c). The limits which are plotted in these figures have in common that the Rashba spin orbit interaction term is dominating, or a term which contains the Rashba term in the perturbation theory expansion is dominating.

Finally, the most powerful tool in measuring the relative strength of relevant fields, is when we see the transition between patterns. As we can see from figure 7.5 (b), figure 7.6 (c) and figure 7.7 (b), the transition between patterns are fairly sharp, and so observing a transition gives a good estimate of relative strength of the effective fields, as well as the details of the transition giving another signature to pinpoint which limit we are in, e.g. the isotropic rings transitioning to the islands along the y -axis in figure 7.6 (c).

As we can see, much information about the underlying spin mixing in the 2DHG can be extracted from the qualitative patterns in critical current measurements of a 2DHG SNS junction. Even more detailed information can be found by using the analytic results we present in detail in paper [III], information which could be very useful when making complex devices, or when looking for exotic properties in these devices, such as topologically non-trivial phases.

Conclusion

In this thesis we have explored the main concepts of papers [I–III] and the manuscript in preparation [IV], which is the core of this thesis. Along the way we have introduced topics which relate these projects such as the protection of quantum information.

In chapter 3 we showed how it is possible to engineer cat states from coherent states, using a qubit coupled to a microwave cavity by using Landau-Zener-Stückelberg interferometry, based on paper [I]. In chapter 4 we saw how a spin qubit coupled to an anisotropic magnon cavity (ferromagnet) is a physical realization of the quantum Rabi model, based on paper [II]. Furthermore, the anisotropy of the ferromagnet could be used to tune the coupling terms of the model. We also show how this system can be expanded to include three qubits, and that it can be used to creating GHZ states using a single control pulse, which has the advantage of being robust against qubit asymmetries.

In chapter 5 we addressed the theoretical framework needed for working with superconducting hybrid devices, as well as looked at why these systems are currently getting so much attention, and why there still is much to figure out. In chapter 6 we derived an expression for the critical current in a nanowire SNS junction with spin-orbit coupling and an external magnetic field, based on a manuscript in preparation [IV]. The analytic expressions we obtain for the Andreev level are particularly interesting because the positive Andreev levels are separate from the negative. Lastly, in chapter 7 we derived expressions for the critical current for a 2DHG SNS junction for important parameter limits. Showing that the critical current could potentially be used in understanding the spin-dynamics of the 2DHG.

While noisy intermediate-scale quantum (NISQ) computation might be the only option in the following years, the end goal currently is fault-tolerant quantum computation. To achieve this we have to either implement quantum error correction algorithms or look at completely new qubits (or more likely the combination of the two). There are many promising paths both in quantum error correction and in new types of qubits, which could help get us towards this goal.

In this thesis we have explored some of these paths, both looking at quantum error correction made possible by implementing the qubit in

a higher dimensional space, via bosonic cat states and GHZ states, and understanding material properties of parts of hybrid devices which could allow for topological quantum computation.

Bibliography

1. **J.A. Ouassou.**
babathesis.
[https://github.com/jabirali/babathesis.](https://github.com/jabirali/babathesis)
Released under a creative Commons Attribution license [CC BY 4.0.](#)
2. **R.L. Rivest, A. Shamir, L. Adleman.**
A Method for Obtaining Digital Signatures and Public-Key Cryptosystems.
Commun. ACM 21, 120–126 (Feb. 1978).
DOI: [10.1145/359340.359342](https://doi.org/10.1145/359340.359342)
3. **P. Shor.**
Algorithms for Quantum Computation: Discrete Logarithms and Factoring.
in *Proceedings 35th Annual Symposium on Foundations of Computer Science*
(Nov. 1994),
124–134.
DOI: [10.1109/SFCS.1994.365700](https://doi.org/10.1109/SFCS.1994.365700)
4. **P. Shor.**
Polynomial-Time Algorithms for Prime Factorization and Discrete Logarithms on a Quantum Computer.
SIAM Review 41, 303–332 (1999).
DOI: [10.1137/S0036144598347011](https://doi.org/10.1137/S0036144598347011)
5. **R.P. Feynman.**
Simulating Physics with Computers.
Int J Theor Phys 21, 467–488 (June 1982).
DOI: [10.1007/BF02650179](https://doi.org/10.1007/BF02650179)
6. **S. Lloyd.**
Universal Quantum Simulators.
Science 273, 1073–1078 (Aug. 1996).
DOI: [10.1126/science.273.5278.1073](https://doi.org/10.1126/science.273.5278.1073)

7. **D.S. Abrams, S. Lloyd.**
Simulation of Many-Body Fermi Systems on a Universal Quantum Computer.
Phys. Rev. Lett. 79, 2586–2589 (Sept. 1997).
DOI: [10.1103/PhysRevLett.79.2586](https://doi.org/10.1103/PhysRevLett.79.2586)
8. **M.B. Hastings, D. Wecker, B. Bauer, M. Troyer.**
Improving Quantum Algorithms for Quantum Chemistry
(Mar. 2014).
DOI: [10.48550/arXiv.1403.1539](https://doi.org/10.48550/arXiv.1403.1539)
arXiv: [1403.1539](https://arxiv.org/abs/1403.1539) [quant-ph].
9. **S.P. Jordan, K.S.M. Lee, J. Preskill.**
Quantum Algorithms for Quantum Field Theories.
Science 336, 1130–1133 (June 2012).
DOI: [10.1126/science.1217069](https://doi.org/10.1126/science.1217069)
10. **D.P. DiVincenzo.**
The Physical Implementation of Quantum Computation.
Fortschritte der Physik 48, 771–783 (2000).
DOI: [10.1002/1521-3978\(200009\)48:9/11<771::AID-PROP771>3.0.CO;2-E](https://doi.org/10.1002/1521-3978(200009)48:9/11<771::AID-PROP771>3.0.CO;2-E)
11. **F. Arute *et al.***
Quantum Supremacy Using a Programmable Superconducting Processor.
Nature 574, 505–510 (Oct. 2019).
DOI: [10.1038/s41586-019-1666-5](https://doi.org/10.1038/s41586-019-1666-5)
12. **T.I. Andersen *et al.***
Non-Abelian Braiding of Graph Vertices in a Superconducting Processor.
Nature 618, 264–269 (June 2023).
DOI: [10.1038/s41586-023-05954-4](https://doi.org/10.1038/s41586-023-05954-4)
13. **A.F. Kockum, F. Nori.**
in *Fundamentals and Frontiers of the Josephson Effect*
(ed F. Tafuri)
703–741
(Springer International Publishing, Cham, 2019).
ISBN: [978-3-030-20726-7](https://doi.org/10.1007/978-3-030-20726-7)
DOI: [10.1007/978-3-030-20726-7_17](https://doi.org/10.1007/978-3-030-20726-7_17)

14. **J.M. Martinis.**
Superconducting Phase Qubits.
Quantum Inf Process 8, 81–103 (June 2009).
DOI: [10.1007/s11128-009-0105-1](https://doi.org/10.1007/s11128-009-0105-1)
15. **J.E. Mooij *et al.***
Josephson Persistent-Current Qubit.
Science 285, 1036–1039 (Aug. 1999).
DOI: [10.1126/science.285.5430.1036](https://doi.org/10.1126/science.285.5430.1036)
16. **V. Bouchiat, D. Vion, P. Joyez, D. Esteve, M.H. Devoret.**
Quantum Coherence with a Single Cooper Pair.
Phys. Scr. 1998, 165 (Jan. 1998).
DOI: [10.1238/Physica.Topical.076a00165](https://doi.org/10.1238/Physica.Topical.076a00165)
17. **J. Gorman, D.G. Hasko, D.A. Williams.**
Charge-Qubit Operation of an Isolated Double Quantum Dot.
Phys. Rev. Lett. 95, 090502 (Aug. 2005).
DOI: [10.1103/PhysRevLett.95.090502](https://doi.org/10.1103/PhysRevLett.95.090502)
18. **D. Loss, D.P. DiVincenzo.**
Quantum Computation with Quantum Dots.
Phys. Rev. A 57, 120–126 (Jan. 1998).
DOI: [10.1103/PhysRevA.57.120](https://doi.org/10.1103/PhysRevA.57.120)
19. **C.D. Bruzewicz, J. Chiaverini, R. McConnell, J.M. Sage.**
Trapped-Ion Quantum Computing: Progress and Challenges.
Applied Physics Reviews 6, 021314 (May 2019).
DOI: [10.1063/1.5088164](https://doi.org/10.1063/1.5088164)
20. **T. Xia *et al.***
Randomized Benchmarking of Single-Qubit Gates in a 2D Array of Neutral-Atom Qubits.
Phys. Rev. Lett. 114, 100503 (Mar. 2015).
DOI: [10.1103/PhysRevLett.114.100503](https://doi.org/10.1103/PhysRevLett.114.100503)
21. **L. Childress, R. Hanson.**
Diamond NV Centers for Quantum Computing and Quantum Networks.
MRS Bulletin 38, 134–138 (Feb. 2013).
DOI: [10.1557/mrs.2013.20](https://doi.org/10.1557/mrs.2013.20)

22. **J.L. O'Brien.**
Optical Quantum Computing.
Science 318, 1567–1570 (Dec. 2007).
DOI: [10.1126/science.1142892](https://doi.org/10.1126/science.1142892)
23. **M. Mirrahimi *et al.***
Dynamically Protected Cat-Qubits: A New Paradigm for Universal Quantum Computation.
New J. Phys. 16, 045014 (Apr. 2014).
DOI: [10.1088/1367-2630/16/4/045014](https://doi.org/10.1088/1367-2630/16/4/045014)
24. **V. Negîrneac *et al.***
High-Fidelity Controlled-Z Gate with Maximal Intermediate Leakage Operating at the Speed Limit in a Superconducting Quantum Processor.
Phys. Rev. Lett. 126, 220502 (June 2021).
DOI: [10.1103/PhysRevLett.126.220502](https://doi.org/10.1103/PhysRevLett.126.220502)
25. **Y. Sung *et al.***
Realization of High-Fidelity CZ and ZZ-Free iSWAP Gates with a Tunable Coupler.
Phys. Rev. X 11, 021058 (June 2021).
DOI: [10.1103/PhysRevX.11.021058](https://doi.org/10.1103/PhysRevX.11.021058)
26. **A.R. Mills *et al.***
Two-Qubit Silicon Quantum Processor with Operation Fidelity Exceeding 99%.
Science Advances 8, eabn5130 (Apr. 2022).
DOI: [10.1126/sciadv.abn5130](https://doi.org/10.1126/sciadv.abn5130)
27. **A.R. Calderbank, P.W. Shor.**
Good Quantum Error-Correcting Codes Exist.
Phys. Rev. A 54, 1098–1105 (Aug. 1996).
DOI: [10.1103/PhysRevA.54.1098](https://doi.org/10.1103/PhysRevA.54.1098)
28. **A. Peres.**
Reversible Logic and Quantum Computers.
Phys. Rev. A 32, 3266–3276 (Dec. 1985).
DOI: [10.1103/PhysRevA.32.3266](https://doi.org/10.1103/PhysRevA.32.3266)

29. **P.W. Shor.**
Scheme for Reducing Decoherence in Quantum Computer Memory.
Phys. Rev. A 52, R2493–R2496 (Oct. 1995).
DOI: [10.1103/PhysRevA.52.R2493](https://doi.org/10.1103/PhysRevA.52.R2493)
30. **A. Steane.**
Multiple-Particle Interference and Quantum Error Correction.
Proceedings of the Royal Society of London. Series A: Mathematical, Physical and Engineering Sciences 452, 2551–2577 (Jan. 1997).
DOI: [10.1098/rspa.1996.0136](https://doi.org/10.1098/rspa.1996.0136)
31. **T. Aoki *et al.***
Quantum Error Correction beyond Qubits.
Nature Phys 5, 541–546 (Aug. 2009).
DOI: [10.1038/nphys1309](https://doi.org/10.1038/nphys1309)
32. **N.H. Nguyen *et al.***
Demonstration of Shor Encoding on a Trapped-Ion Quantum Computer.
Phys. Rev. Appl. 16, 024057 (Aug. 2021).
DOI: [10.1103/PhysRevApplied.16.024057](https://doi.org/10.1103/PhysRevApplied.16.024057)
33. **D.M. Debroy *et al.***
Optimizing Stabilizer Parities for Improved Logical Qubit Memories.
Phys. Rev. Lett. 127, 240501 (Dec. 2021).
DOI: [10.1103/PhysRevLett.127.240501](https://doi.org/10.1103/PhysRevLett.127.240501)
34. **B.M. Terhal, J. Conrad, C. Vuillot.**
Towards Scalable Bosonic Quantum Error Correction.
Quantum Sci. Technol. 5, 043001 (July 2020).
DOI: [10.1088/2058-9565/ab98a5](https://doi.org/10.1088/2058-9565/ab98a5)
35. **M.H. Michael *et al.***
New Class of Quantum Error-Correcting Codes for a Bosonic Mode.
Phys. Rev. X 6, 031006 (July 2016).
DOI: [10.1103/PhysRevX.6.031006](https://doi.org/10.1103/PhysRevX.6.031006)

36. **V.V. Albert *et al.***
Performance and Structure of Single-Mode Bosonic Codes.
Phys. Rev. A 97, 032346 (Mar. 2018).
DOI: [10.1103/PhysRevA.97.032346](https://doi.org/10.1103/PhysRevA.97.032346)
37. **W. Cai, Y. Ma, W. Wang, C.-L. Zou, L. Sun.**
Bosonic Quantum Error Correction Codes in Superconducting Quantum Circuits.
Fundamental Research 1, 50–67 (Jan. 2021).
DOI: [10.1016/j.fmre.2020.12.006](https://doi.org/10.1016/j.fmre.2020.12.006)
38. **V.V. Albert *et al.***
Pair-Cat Codes: Autonomous Error-Correction with Low-Order Nonlinearity.
Quantum Sci. Technol. 4, 035007 (June 2019).
DOI: [10.1088/2058-9565/ab1e69](https://doi.org/10.1088/2058-9565/ab1e69)
39. **A.Y. Kitaev.**
Fault-Tolerant Quantum Computation by Anyons.
Annals of Physics 303, 2–30 (Jan. 2003).
DOI: [10.1016/S0003-4916\(02\)00018-0](https://doi.org/10.1016/S0003-4916(02)00018-0)
40. **R. Hess, H.F. Legg, D. Loss, J. Klinovaja.**
Trivial Andreev Band Mimicking Topological Bulk Gap Reopening in the Nonlocal Conductance of Long Rashba Nanowires.
Phys. Rev. Lett. 130, 207001 (May 2023).
DOI: [10.1103/PhysRevLett.130.207001](https://doi.org/10.1103/PhysRevLett.130.207001)
41. **M. Aghaee *et al.***
InAs-Al Hybrid Devices Passing the Topological Gap Protocol.
Phys. Rev. B 107, 245423 (June 2023).
DOI: [10.1103/PhysRevB.107.245423](https://doi.org/10.1103/PhysRevB.107.245423)
42. **A.Y. Kitaev.**
Unpaired Majorana Fermions in Quantum Wires.
Phys.-Usp. 44, 131 (Oct. 2001).
DOI: [10.1070/1063-7869/44/10S/S29](https://doi.org/10.1070/1063-7869/44/10S/S29)
43. **M. Freedman, A. Kitaev, M. Larsen, Z. Wang.**
Topological Quantum Computation.
Bull. Amer. Math. Soc. 40, 31–38 (2003).
DOI: [10.1090/S0273-0979-02-00964-3](https://doi.org/10.1090/S0273-0979-02-00964-3)

44. **E. Schrödinger.**
Die Gegenwärtige Situation in Der Quantenmechanik.
Die Naturwissenschaften 23, 844–849 (1935).
DOI: [10.1007/BF01491987](https://doi.org/10.1007/BF01491987)
45. **W.-M. Zhang, D.H. Feng, R. Gilmore.**
Coherent States: Theory and Some Applications.
Rev. Mod. Phys. 62, 867–927 (Oct. 1990).
DOI: [10.1103/RevModPhys.62.867](https://doi.org/10.1103/RevModPhys.62.867)
46. **M. Brune *et al.***
Observing the Progressive Decoherence of the “Meter” in a Quantum Measurement.
Phys. Rev. Lett. 77, 4887–4890 (Dec. 1996).
DOI: [10.1103/PhysRevLett.77.4887](https://doi.org/10.1103/PhysRevLett.77.4887)
47. **W.J. Munro, K. Nemoto, G.J. Milburn, S.L. Braunstein.**
Weak-Force Detection with Superposed Coherent States.
Phys. Rev. A - At. Mol. Opt. Phys. 66, 1–6 (2002).
DOI: [10.1103/PhysRevA.66.023819](https://doi.org/10.1103/PhysRevA.66.023819)
48. **T.C. Ralph.**
Coherent Superposition States as Quantum Rulers.
Phys. Rev. A - At. Mol. Opt. Phys. 65, 5 (2002).
DOI: [10.1103/PhysRevA.65.042313](https://doi.org/10.1103/PhysRevA.65.042313)
49. **J. Joo, W.J. Munro, T.P. Spiller.**
Quantum Metrology with Entangled Coherent States.
Phys. Rev. Lett. 107, 1–4 (2011).
DOI: [10.1103/PhysRevLett.107.083601](https://doi.org/10.1103/PhysRevLett.107.083601)
arXiv: [1101.5044](https://arxiv.org/abs/1101.5044).
50. **T.C. Ralph, A. Gilchrist, G.J. Milburn, W.J. Munro, S. Glancy.**
Quantum Computation with Optical Coherent States.
Phys. Rev. A 68, 042319 (Oct. 2003).
DOI: [10.1103/PhysRevA.68.042319](https://doi.org/10.1103/PhysRevA.68.042319)
51. **A.P. Lund, T.C. Ralph, H.L. Haselgrove.**
Fault-Tolerant Linear Optical Quantum Computing with Small-Amplitude Coherent States.
Phys. Rev. Lett. 100, 1–4 (2008).
DOI: [10.1103/PhysRevLett.100.030503](https://doi.org/10.1103/PhysRevLett.100.030503)
arXiv: [0707.0327](https://arxiv.org/abs/0707.0327).

52. **S. van Enk, O. Hirota.**
Entangled Coherent States: Teleportation and Decoherence.
 Phys. Rev. A 64, 022313 (July 2001).
 DOI: [10.1103/PhysRevA.64.022313](https://doi.org/10.1103/PhysRevA.64.022313)
53. **H. Jeong, M.S. Kim, J. Lee.**
Quantum-Information Processing for a Coherent Superposition State via a Mixedentangled Coherent Channel.
 Phys. Rev. A 64, 052308 (Oct. 2001).
 DOI: [10.1103/PhysRevA.64.052308](https://doi.org/10.1103/PhysRevA.64.052308)
54. **M. Bergmann, P. Van Loock.**
Quantum Error Correction against Photon Loss Using Multicomponent Cat States.
 Phys. Rev. A 94, 42332 (2016).
 DOI: [10.1103/PhysRevA.94.042332](https://doi.org/10.1103/PhysRevA.94.042332)
55. **N. Ofek *et al.***
Extending the Lifetime of a Quantum Bit with Error Correction in Superconducting Circuits.
 Nature 536, 441–445 (2016).
 DOI: [10.1038/nature18949](https://doi.org/10.1038/nature18949)
56. **C. Chamberland *et al.***
Building a Fault-Tolerant Quantum Computer Using Concatenated Cat Codes.
 PRX Quantum 3, 010329 (Feb. 2022).
 DOI: [10.1103/PRXQuantum.3.010329](https://doi.org/10.1103/PRXQuantum.3.010329)
57. **J. Lee, J. Park, J. Heo.**
Rectangular Surface Code under Biased Noise.
 Quantum Inf Process 20, 231 (July 2021).
 DOI: [10.1007/s11128-021-03130-z](https://doi.org/10.1007/s11128-021-03130-z)
58. **E.E. Nikitin, S.Y. Umanskii.**
Theory of Slow Atomic Collisions (eds V.I. Goldanskii, R. Gomer, F.P. Schäfer, J.P. Toennies) (1984).
 ISBN: [978-3-642-82047-2](https://doi.org/10.1007/978-3-642-82047-2) [978-3-642-82045-8](https://doi.org/10.1007/978-3-642-82045-8)
 DOI: [10.1007/978-3-642-82045-8](https://doi.org/10.1007/978-3-642-82045-8)
59. **L.D. Landau.**
Zur Theorie Der Energieübertragung. II.
 Physikalische Zeitschrift der Sowjetunion 2, 46–51 (1932).

60. **C. Zener.**
Non-Adiabatic Crossing of Energy Leves.
Proceedings of the Royal Society of London. Series A, Containing Papers of a Mathematical and Physical Character 137, 696–702 (Sept. 1932).
DOI: [10.1098/rspa.1932.0165](https://doi.org/10.1098/rspa.1932.0165)
61. **E.C.G. Stueckelberg.**
Theorie Der Unelastischen Stösse Zwischen Atomen (1932).
DOI: [10.5169/SEALS-110177](https://doi.org/10.5169/SEALS-110177)
62. **E. Majorana.**
Atomi orientati in campo magnetico variabile.
Nuovo Cim 9, 43–50 (Feb. 1932).
DOI: [10.1007/BF02960953](https://doi.org/10.1007/BF02960953)
63. **B. Damski, W.H. Zurek.**
Adiabatic-Impulse Approximation for Avoided Level Crossings: From Phase-Transition Dynamics to Landau-Zener Evolutions and Back Again.
Phys. Rev. A 73, 063405 (June 2006).
DOI: [10.1103/PhysRevA.73.063405](https://doi.org/10.1103/PhysRevA.73.063405)
64. **S.N. Shevchenko, S. Ashhab, F. Nori.**
Landau-Zener-Stückelberg Interferometry.
Physics Reports 492, 1–30 (2010).
DOI: [10.1016/j.physrep.2010.03.002](https://doi.org/10.1016/j.physrep.2010.03.002)
65. **A. Zenesini *et al.***
Time-Resolved Measurement of Landau-Zener Tunneling in Periodic Potentials.
Phys. Rev. Lett. 103, 090403 (Aug. 2009).
DOI: [10.1103/PhysRevLett.103.090403](https://doi.org/10.1103/PhysRevLett.103.090403)
66. **E. Jaynes, F. Cummings.**
Comparison of Quantum and Semiclassical Radiation Theories with Application to the Beam Maser.
Proceedings of the IEEE 51, 89–109 (Jan. 1963).
DOI: [10.1109/PROC.1963.1664](https://doi.org/10.1109/PROC.1963.1664)

67. **J.R. Johansson, P.D. Nation, F. Nori.**
QuTiP: An Open-Source Python Framework for the Dynamics of Open Quantum Systems.
Comput. Phys. Commun. 183, 1760–1772 (Aug. 2012).
DOI: [10.1016/j.cpc.2012.02.021](https://doi.org/10.1016/j.cpc.2012.02.021)
arXiv: [1110.0573](https://arxiv.org/abs/1110.0573).
68. **J.R. Johansson, P.D. Nation, F. Nori.**
QuTiP 2: A Python Framework for the Dynamics of Open Quantum Systems.
Comput. Phys. Commun. 184, 1234–1240 (Apr. 2013).
DOI: [10.1016/j.cpc.2012.11.019](https://doi.org/10.1016/j.cpc.2012.11.019)
arXiv: [1211.6518](https://arxiv.org/abs/1211.6518).
69. **J. Vaccaro.**
Number-Phase Wigner Function on Fock Space.
Phys. Rev. A 52, 3474–3488 (Nov. 1995).
DOI: [10.1103/PhysRevA.52.3474](https://doi.org/10.1103/PhysRevA.52.3474)
70. **D.M. Greenberger, M.A. Horne, A. Zeilinger.**
Going Beyond Bell's Theorem
(Dec. 2007).
DOI: [10.48550/arXiv.0712.0921](https://doi.org/10.48550/arXiv.0712.0921)
arXiv: [0712.0921](https://arxiv.org/abs/0712.0921) [quant-ph].
71. **J.S. Bell.**
On the Einstein Podolsky Rosen Paradox.
Physics Physique Fizika 1, 195–200 (Nov. 1964).
DOI: [10.1103/PhysicsPhysiqueFizika.1.195](https://doi.org/10.1103/PhysicsPhysiqueFizika.1.195)
72. **M. Hillery, V. Bužek, A. Berthiaume.**
Quantum Secret Sharing.
Phys. Rev. A 59, 1829–1834 (Mar. 1999).
DOI: [10.1103/PhysRevA.59.1829](https://doi.org/10.1103/PhysRevA.59.1829)
73. **X.-R. Jin *et al.***
Three-Party Quantum Secure Direct Communication Based on GHZ States.
Physics Letters A 354, 67–70 (May 2006).
DOI: [10.1016/j.physleta.2006.01.035](https://doi.org/10.1016/j.physleta.2006.01.035)

74. **M. Ben-Or, A. Hassidim.**
Fast Quantum Byzantine Agreement.
in *Proceedings of the Thirty-Seventh Annual ACM Symposium on Theory of Computing*
(Association for Computing Machinery, New York, NY, USA, May 2005),
481–485.
ISBN: 978-1-58113-960-0
DOI: [10.1145/1060590.1060662](https://doi.org/10.1145/1060590.1060662)
75. **I.I. Rabi.**
On the Process of Space Quantization.
Phys. Rev. 49, 324–328 (Feb. 1936).
DOI: [10.1103/PhysRev.49.324](https://doi.org/10.1103/PhysRev.49.324)
76. **I.I. Rabi.**
Space Quantization in a Gyration Magnetic Field.
Phys. Rev. 51, 652–654 (Apr. 1937).
DOI: [10.1103/PhysRev.51.652](https://doi.org/10.1103/PhysRev.51.652)
77. **B.M. Rodríguez-Lara, F. Soto-Eguibar, A.Z. Cárdenas, H.M. Moya-Cessa.**
A Classical Simulation of Nonlinear Jaynes–Cummings and Rabi Models in Photonic Lattices.
Opt. Express, OE 21, 12888–12898 (May 2013).
DOI: [10.1364/OE.21.012888](https://doi.org/10.1364/OE.21.012888)
78. **T. Holstein, H. Primakoff.**
Field Dependence of the Intrinsic Domain Magnetization of a Ferromagnet.
Phys. Rev. 58, 1098–1113 (Dec. 1940).
DOI: [10.1103/PhysRev.58.1098](https://doi.org/10.1103/PhysRev.58.1098)
79. **A.F. Kockum, A. Miranowicz, V. Macrì, S. Savasta, F. Nori.**
Deterministic Quantum Nonlinear Optics with Single Atoms and Virtual Photons.
Phys. Rev. A 95, 063849 (June 2017).
DOI: [10.1103/PhysRevA.95.063849](https://doi.org/10.1103/PhysRevA.95.063849)

80. **W.R. Salzman.**
Diagrammatical Derivation and Representation of Rayleigh–Schrödinger Perturbation Theory.
The Journal of Chemical Physics 49, 3035–3040 (Oct. 1968).
DOI: [10.1063/1.1670546](https://doi.org/10.1063/1.1670546)
81. **J.D. Sau, R.M. Lutchyn, S. Tewari, S. Das Sarma.**
Generic New Platform for Topological Quantum Computation Using Semiconductor Heterostructures.
Phys. Rev. Lett. 104, 040502 (Jan. 2010).
DOI: [10.1103/PhysRevLett.104.040502](https://doi.org/10.1103/PhysRevLett.104.040502)
82. **J. Alicea.**
Majorana Fermions in a Tunable Semiconductor Device.
Phys. Rev. B 81, 125318 (Mar. 2010).
DOI: [10.1103/PhysRevB.81.125318](https://doi.org/10.1103/PhysRevB.81.125318)
83. **Y. Oreg, G. Refael, F. von Oppen.**
Helical Liquids and Majorana Bound States in Quantum Wires.
Phys. Rev. Lett. 105, 177002 (Oct. 2010).
DOI: [10.1103/PhysRevLett.105.177002](https://doi.org/10.1103/PhysRevLett.105.177002)
84. **R.M. Lutchyn, J.D. Sau, S. Das Sarma.**
Majorana Fermions and a Topological Phase Transition in Semiconductor-Superconductor Heterostructures.
Phys. Rev. Lett. 105, 077001 (Aug. 2010).
DOI: [10.1103/PhysRevLett.105.077001](https://doi.org/10.1103/PhysRevLett.105.077001)
85. **P.G.D. Gennes.**
Superconductivity Of Metals And Alloys (May 2019).
ISBN: [978-0-429-49703-2](https://www.isbn-international.org/product/978-0-429-49703-2)
DOI: [10.1201/9780429497032](https://doi.org/10.1201/9780429497032)
86. **J.-X. Zhu.**
Bogoliubov-de Gennes Method and Its Applications (2016).
ISBN: [978-3-319-31312-2](https://www.isbn-international.org/product/978-3-319-31312-2) [978-3-319-31314-6](https://www.isbn-international.org/product/978-3-319-31314-6)
DOI: [10.1007/978-3-319-31314-6](https://doi.org/10.1007/978-3-319-31314-6)
87. **B. Pannetier, H. Courtois.**
Andreev Reflection and Proximity Effect.
Journal of Low Temperature Physics 118, 599–615 (Mar. 2000).
DOI: [10.1023/A:1004635226825](https://doi.org/10.1023/A:1004635226825)

88. **A. Andreev.**
The Thermal Conductivity of the Intermediate State in Superconductors.
Zh. Eksp. Teor. Fiz. 46, 1823–1828 (1964).
89. **C.W.J. Beenakker.**
Universal Limit of Critical-Current Fluctuations in Mesoscopic Josephson Junctions.
Phys. Rev. Lett. 67, 3836–3839 (Dec. 1991).
DOI: [10.1103/PhysRevLett.67.3836](https://doi.org/10.1103/PhysRevLett.67.3836)
90. **P.A.M. Dirac, R.H. Fowler.**
A Theory of Electrons and Protons.
Proceedings of the Royal Society of London. Series A, Containing Papers of a Mathematical and Physical Character 126, 360–365 (Jan. 1997).
DOI: [10.1098/rspa.1930.0013](https://doi.org/10.1098/rspa.1930.0013)
91. **E. Majorana.**
Teoria simmetrica dell'elettrone e del positrone.
Nuovo Cim 14, 171–184 (Apr. 1937).
DOI: [10.1007/BF02961314](https://doi.org/10.1007/BF02961314)
92. **L. Collaboration *et al.***
LEGEND-1000 Preconceptual Design Report
(July 2021).
DOI: [10.48550/arXiv.2107.11462](https://doi.org/10.48550/arXiv.2107.11462)
[arXiv: 2107.11462 \[nucl-ex, physics:physics\]](https://arxiv.org/abs/2107.11462).
93. **Majorana Collaboration *et al.***
Final Result of the Majorana Demonstrator's Search for Neutrinoless Double- β Decay in ^{76}Ge .
Phys. Rev. Lett. 130, 062501 (Feb. 2023).
DOI: [10.1103/PhysRevLett.130.062501](https://doi.org/10.1103/PhysRevLett.130.062501)
94. **C. Beenakker.**
Search for Majorana Fermions in Superconductors.
Annual Review of Condensed Matter Physics 4, 113–136
(2013).
DOI: [10.1146/annurev-conmatphys-030212-184337](https://doi.org/10.1146/annurev-conmatphys-030212-184337)

95. **J. Alicea.**
New Directions in the Pursuit of Majorana Fermions in Solid State Systems.
Rep. Prog. Phys. 75, 076501 (June 2012).
DOI: [10.1088/0034-4885/75/7/076501](https://doi.org/10.1088/0034-4885/75/7/076501)
96. **G.E. Volovik.**
Fermion Zero Modes on Vortices in Chiral Superconductors.
Jep Latt. 70, 609–614 (Nov. 1999).
DOI: [10.1134/1.568223](https://doi.org/10.1134/1.568223)
97. **S. Das Sarma, C. Nayak, S. Tewari.**
Proposal to stabilize and detect half-quantum vortices in strontium ruthenate thin films: Non-Abelian braiding statistics of vortices in a $p_x + ip_y$ superconductor.
Phys. Rev. B 73, 220502 (June 2006).
DOI: [10.1103/PhysRevB.73.220502](https://doi.org/10.1103/PhysRevB.73.220502)
98. **S.D. Sarma, M. Freedman, C. Nayak.**
Majorana Zero Modes and Topological Quantum Computation.
npj Quantum Inf 1, 1–13 (Oct. 2015).
DOI: [10.1038/npjqi.2015.1](https://doi.org/10.1038/npjqi.2015.1)
99. **A.C. Potter, P.A. Lee.**
Engineering a $p + ip$ superconductor: Comparison of topological insulator and Rashba spin-orbit-coupled materials.
Phys. Rev. B 83, 184520 (May 2011).
DOI: [10.1103/PhysRevB.83.184520](https://doi.org/10.1103/PhysRevB.83.184520)
100. **J.D. Sau, S. Tewari, S. Das Sarma.**
Experimental and Materials Considerations for the Topological Superconducting State in Electron- and Hole-Doped Semiconductors: Searching for Non-Abelian Majorana Modes in 1D Nanowires and 2D Heterostructures.
Phys. Rev. B 85, 064512 (Feb. 2012).
DOI: [10.1103/PhysRevB.85.064512](https://doi.org/10.1103/PhysRevB.85.064512)
101. **L. Fu, C.L. Kane.**
Superconducting Proximity Effect and Majorana Fermions at the Surface of a Topological Insulator.
Phys. Rev. Lett. 100, 096407 (Mar. 2008).
DOI: [10.1103/PhysRevLett.100.096407](https://doi.org/10.1103/PhysRevLett.100.096407)

102. **L. Fu, C.L. Kane.**
Josephson Current and Noise at a Superconductor/Quantum-Spin-Hall-insulator/Superconductor Junction.
 Phys. Rev. B 79, 161408 (Apr. 2009).
 DOI: [10.1103/PhysRevB.79.161408](https://doi.org/10.1103/PhysRevB.79.161408)
103. **A. Cook, M. Franz.**
Majorana fermions in a topological-insulator nanowire proximity-coupled to an s-wave superconductor.
 Phys. Rev. B 84, 201105 (Nov. 2011).
 DOI: [10.1103/PhysRevB.84.201105](https://doi.org/10.1103/PhysRevB.84.201105)
104. **J.D. Sau, R.M. Lutchyn, S. Tewari, S. Das Sarma.**
Generic New Platform for Topological Quantum Computation Using Semiconductor Heterostructures.
 Phys. Rev. Lett. 104, 040502 (Jan. 2010).
 DOI: [10.1103/PhysRevLett.104.040502](https://doi.org/10.1103/PhysRevLett.104.040502)
105. **M. Leijnse, K. Flensberg.**
Introduction to Topological Superconductivity and Majorana Fermions.
 Semicond. Sci. Technol. 27, 124003 (Nov. 2012).
 DOI: [10.1088/0268-1242/27/12/124003](https://doi.org/10.1088/0268-1242/27/12/124003)
106. **C. Kallin.**
Chiral P-Wave Order in Sr₂RuO₄.
 Rep. Prog. Phys. 75, 042501 (Mar. 2012).
 DOI: [10.1088/0034-4885/75/4/042501](https://doi.org/10.1088/0034-4885/75/4/042501)
107. **J. Leinaas, J. Myrheim.**
On the Theory of Identical Particles.
 Il nuovo cimento 37, 132 (1977).
108. **J. Fröhlich.**
 in *Nonperturbative Quantum Field Theory*
 (eds G. 't Hooft, A. Jaffe, G. Mack, P.K. Mitter, R. Stora)
 71–100
 (Springer US, New York, NY, 1988).
 ISBN: [978-1-4613-0729-7](https://doi.org/10.1007/978-1-4613-0729-7)
 DOI: [10.1007/978-1-4613-0729-7_4](https://doi.org/10.1007/978-1-4613-0729-7_4)

109. **S. Bravyi.**
Universal quantum computation with the $\nu = 5 / 2$ fractional quantum Hall state.
Phys. Rev. A 73, 042313 (Apr. 2006).
DOI: [10.1103/PhysRevA.73.042313](https://doi.org/10.1103/PhysRevA.73.042313)
110. **S. Plugge, A. Rasmussen, R. Egger, K. Flensberg.**
Majorana Box Qubits.
New J. Phys. 19, 012001 (Jan. 2017).
DOI: [10.1088/1367-2630/aa54e1](https://doi.org/10.1088/1367-2630/aa54e1)
111. **J.D. Sau, S. Tewari, R.M. Lutchyn, T.D. Stanescu, S. Das Sarma.**
Non-Abelian Quantum Order in Spin-Orbit-Coupled Semiconductors: Search for Topological Majorana Particles in Solid-State Systems.
Phys. Rev. B 82, 214509 (Dec. 2010).
DOI: [10.1103/PhysRevB.82.214509](https://doi.org/10.1103/PhysRevB.82.214509)
112. **D.I. Pikulin *et al.***
Protocol to Identify a Topological Superconducting Phase in a Three-Terminal Device
(Mar. 2021).
DOI: [10.48550/arXiv.2103.12217](https://doi.org/10.48550/arXiv.2103.12217)
arXiv: [2103.12217](https://arxiv.org/abs/2103.12217) [[cond-mat](#)].
113. **H. Pan, S. Das Sarma.**
On-Demand Large Conductance in Trivial Zero-Bias Tunneling Peaks in Majorana Nanowires.
Phys. Rev. B 105, 115432 (Mar. 2022).
DOI: [10.1103/PhysRevB.105.115432](https://doi.org/10.1103/PhysRevB.105.115432)
114. **R.S. Souto, M. Leijnse, C. Schrade.**
The Josephson Diode Effect in Supercurrent Interferometers
(May 2022).
DOI: [10.48550/arXiv.2205.04469](https://doi.org/10.48550/arXiv.2205.04469)
arXiv: [2205.04469](https://arxiv.org/abs/2205.04469) [[cond-mat](#), [physics:quant-ph](#)].
115. **R.C. Dynes, T.A. Fulton.**
Supercurrent Density Distribution in Josephson Junctions.
Phys. Rev. B 3, 3015–3023 (May 1971).
DOI: [10.1103/PhysRevB.3.3015](https://doi.org/10.1103/PhysRevB.3.3015)

116. **H. Watzinger *et al.***
A Germanium Hole Spin Qubit.
Nat Commun 9, 3902 (Sept. 2018).
DOI: [10.1038/s41467-018-06418-4](https://doi.org/10.1038/s41467-018-06418-4)
117. **N.W. Hendrickx, D.P. Franke, A. Sammak, G. Scappucci, M. Veldhorst.**
Fast Two-Qubit Logic with Holes in Germanium.
Nature 577, 487–491 (Jan. 2020).
DOI: [10.1038/s41586-019-1919-3](https://doi.org/10.1038/s41586-019-1919-3)
118. **G. Scappucci *et al.***
The Germanium Quantum Information Route.
Nat Rev Mater 6, 926–943 (Oct. 2021).
DOI: [10.1038/s41578-020-00262-z](https://doi.org/10.1038/s41578-020-00262-z)
119. **C. Gradl *et al.***
Asymmetric g Tensor in Low-Symmetry Two-Dimensional Hole Systems.
Phys. Rev. X 8, 021068 (June 2018).
DOI: [10.1103/PhysRevX.8.021068](https://doi.org/10.1103/PhysRevX.8.021068)
120. **S.D. Liles *et al.***
Electrical control of the g tensor of the first hole in a silicon MOS quantum dot.
Phys. Rev. B 104, 235303 (Dec. 2021).
DOI: [10.1103/PhysRevB.104.235303](https://doi.org/10.1103/PhysRevB.104.235303)
121. **E. Marcellina, A.R. Hamilton, R. Winkler, D. Culcer.**
Spin-Orbit Interactions in Inversion-Asymmetric Two-Dimensional Hole Systems: A Variational Analysis.
Phys. Rev. B 95, 075305 (Feb. 2017).
DOI: [10.1103/PhysRevB.95.075305](https://doi.org/10.1103/PhysRevB.95.075305)
122. **P. Philippopoulos, S. Chesi, D. Culcer, W.A. Coish.**
Pseudospin-Electric Coupling for Holes beyond the Envelope-Function Approximation.
Phys. Rev. B 102, 075310 (Aug. 2020).
DOI: [10.1103/PhysRevB.102.075310](https://doi.org/10.1103/PhysRevB.102.075310)

123. **L.A. Terrazos *et al.***
Theory of Hole-Spin Qubits in Strained Germanium Quantum Dots.
Phys. Rev. B 103, 125201 (Mar. 2021).
DOI: [10.1103/PhysRevB.103.125201](https://doi.org/10.1103/PhysRevB.103.125201)
124. **S. Bosco, M. Benito, C. Adelsberger, D. Loss.**
Squeezed Hole Spin Qubits in Ge Quantum Dots with Ultrafast Gates at Low Power.
Phys. Rev. B 104, 115425 (Sept. 2021).
DOI: [10.1103/PhysRevB.104.115425](https://doi.org/10.1103/PhysRevB.104.115425)
125. **R. Winkler.**
Spin–Orbit Coupling Effects in Two-Dimensional Electron and Hole Systems (2003).
ISBN: 978-3-540-01187-3 978-3-540-36616-4
DOI: [10.1007/b13586](https://doi.org/10.1007/b13586)
126. **L. Mao, J. Shi, Q. Niu, C. Zhang.**
Superconducting Phase with a Chiral s -Wave Pairing Symmetry and Majorana Fermions Induced in a Hole-Doped Semiconductor.
Phys. Rev. Lett. 106, 157003 (Apr. 2011).
DOI: [10.1103/PhysRevLett.106.157003](https://doi.org/10.1103/PhysRevLett.106.157003)
127. **M. Luethi, K. Laubscher, S. Bosco, D. Loss, J. Klinovaja.**
Planar Josephson Junctions in Germanium: Effect of Cubic Spin-Orbit Interaction.
Phys. Rev. B 107, 035435 (Jan. 2023).
DOI: [10.1103/PhysRevB.107.035435](https://doi.org/10.1103/PhysRevB.107.035435)
128. **J.R. Schrieffer, P.A. Wolff.**
Relation between the Anderson and Kondo Hamiltonians.
Phys. Rev. 149, 491–492 (Sept. 1966).
DOI: [10.1103/PhysRev.149.491](https://doi.org/10.1103/PhysRev.149.491)
129. **A.A. Abrikosov, L.P. Gorkov, I.E. Dzyaloshinski.**
Methods of Quantum Field Theory in Statistical Physics (May 2012).
ISBN: 978-0-486-14015-5

130. S. Hart *et al.*
*Controlled Finite Momentum Pairing and Spatially Varying
Order Parameter in Proximitized HgTe Quantum Wells.*
Nature Phys 13, 87–93 (Jan. 2017).
DOI: [10.1038/nphys3877](https://doi.org/10.1038/nphys3877)



Paper I

Jonas Lidal and Jeroen Danon

Generation of Schrödinger-cat states through photon-assisted Landau-Zener-Stückelberg interferometry

Physical Review A, **102**, 043717 (2020)

Generation of Schrödinger-cat states through photon-assisted Landau-Zener-Stückelberg interferometry

Jonas Lidal  and Jeroen Danon *Center for Quantum Spintronics, Department of Physics, Norwegian University of Science and Technology, NO-7491 Trondheim, Norway*

(Received 27 August 2020; accepted 12 October 2020; published 28 October 2020)

Schrödinger-cat states are useful for many applications, ranging from quantum-information processing to high-precision measurements. In this paper we propose a method for creating such cat states, based on photon-assisted Landau-Zener-Stückelberg interferometry in a hybrid system consisting of a qubit coupled to a photon cavity. We show that by initializing the qubit in one of its basis states, performing three consecutive sweeps of the qubit energy splitting across the 1-photon resonance, and finally projecting the qubit to the same basis state, the parity of the photon field can be purified to very high degree; when the initial photon state is a coherent state, the final state will then be very close to a Schrödinger-cat state. We present numerical simulations that confirm that our protocol could work with high fidelity (~ 0.99) for coherent states of reasonable size ($|\alpha|^2 \sim 10$). Furthermore, we suggest that our protocol can also be used to transfer quantum information between the qubit and a superposition of orthogonal cat states in the cavity.

DOI: [10.1103/PhysRevA.102.043717](https://doi.org/10.1103/PhysRevA.102.043717)

I. INTRODUCTION

A coherent state is a quantum state of the harmonic oscillator that most closely resembles a classical state, in the sense that it has minimal and equal uncertainty in its two conjugate variables, the expectation values of which follow the classical equations of motion. More explicitly, coherent states are the eigenstates of the oscillator's bosonic annihilation operator, $a|\alpha\rangle = \alpha|\alpha\rangle$, where α is a complex number characterizing the amplitude and phase of the oscillations associated with $|\alpha\rangle$: $|\alpha|^2$ gives the expectation value of the number of excitations in the oscillator.

A superposition of two coherent states, e.g.,

$$|\Psi_{\pm}(\alpha)\rangle = \frac{1}{\mathcal{N}}(|\alpha\rangle \pm |-\alpha\rangle), \quad (1)$$

is, in a way, thus analogous to the cat in Schrödinger's famous thought experiment [1], as it presents a quantum superposition of two different (quasi)classical states. These superpositions are therefore commonly known as Schrödinger-cat states and are interesting for a number of reasons. First, since their behavior is on the border between quantum and classical, they provide a perfect playground for studying decoherence and the quantum-to-classical transition [2], which is of fundamental interest. Further, it has been shown that Schrödinger-cat states can be used as a resource for quantum computation [3,4] and quantum error correction [5–8], quantum teleportation [9,10], and also high-precision measurements [11–14]. For these reasons, reliable generation and manipulation of such cat states has been the focus of a substantial amount of work in the past few decades, both theoretical and experimental.

Most of the cat-based quantum technologies mentioned above, such as high-precision metrology and reliable quantum computation, require the use of coherent states of the freely propagating photon field. Furthermore, these applications work best when the overlap between the coherent states

constituting the cat state is small. For the state (1) this overlap is $|\langle\alpha|-\alpha\rangle| = e^{-2|\alpha|^2}$, and in that case it has been estimated that $|\alpha| > 1.2$ is required for fault-tolerant quantum computing [4].

Over the years, many ways have been put forward on how to produce freely propagating cat states, several of which have successfully been implemented. Yurke and Stoler originally proposed sending a coherent photon state through a strongly nonlinear (Kerr) medium to generate a cat state [15], but all commonly available media are too weakly nonlinear to achieve the required degree of dispersion over reasonable distances. Other proposed methods, some of which have been successfully implemented, include performing conditional measurements on the squeezed vacuum [16–21], mixing a coherent state with a squeezed single-photon beam [22], homodyne detection on a 50:50 split n -photon Fock state [23], and reflecting coherent light pulses from an atom-cavity system [24]. The drawback of these methods is that they become less successful for increasing amplitude $|\alpha|$ of the cat state, the highest amplitudes reached being $|\alpha| \sim 1.5$.

Achieving higher amplitudes is possible via a few different methods. One idea is to combine pairs of small-amplitude cat states into one state with a larger $|\alpha|$ in a process known as “breeding” [22,25]. Another route is to turn to cavity QED, trapping the photons in cavities where they strongly interact with atoms that are shot through the cavity; in that way, the state of the photon field can be manipulated into a cat state [2,26,27]. Advances in qubit technology allowed for replacing the atoms with (superconducting) qubits acting as artificial atoms that are coupled to the cavity mode, which provides an extra level of control over the light-matter interaction. Such hybrid systems can be used to coherently transfer quantum information from a qubit to a superposition of cat states [28] and they allowed for the creation of cat states with amplitudes up to $|\alpha| \sim 10$ [29].

Such cavity-based cat states were used for studying the quantum-to-classical transition [2], but they could also provide a platform for fault-tolerant quantum-information processing [6,28]. Furthermore, for applications where a freely propagating cat state is needed it is possible to “release” a nonclassical photon state from a cavity, which has been demonstrated for single-photon [30] as well as multiphoton states [31].

In this paper, we propose a method of generating Schrödinger-cat states, based on photon-assisted Landau-Zener-Stückelberg interferometry in a hybrid system consisting of a qubit coupled to a photon cavity. Landau-Zener-Stückelberg interferometry has been used before to create entangled states in multipartite few-level systems [32,33], but here we explore the possibility to use it to entangle the *photon field* by manipulating the level structure of the qubit. We show that repeatedly sweeping the level splitting of the qubit through the 1-photon resonance can lead to interference effects which, depending on the details of the level crossing, can selectively amplify and attenuate specific n -photon components in the wave function of the cavity field. Using this principle, we demonstrate how an initial coherent photon state in the cavity can be transformed with high fidelity to a so-called even or odd cat state $|\Psi_{\pm}(\alpha)\rangle$ [see Eq. (1)] by means of three consecutive level crossings. We also speculate that the procedure can be used to transfer quantum information from a qubit state to the photon cavity using an odd cat state and an even state as a basis. We further present numerical simulations of the time evolution of the proposed system which confirm the successful creation of cat states with fidelities up to ~ 0.99 for $|\alpha|^2 \sim 10$.

The rest of this paper is organized as follows. In Sec. II we review the basics of Landau-Zener-Stückelberg interferometry, using the example of two levels that are swept through each other multiple times. In Sec. III we then introduce the system and model Hamiltonian we consider, and we outline the basic working of our cat-state generating protocol; first we do this using the most intuitive picture possible, connecting directly to the example system presented in Sec. II, and then we discuss the main simplifications we made in that picture and estimate the deviations from the ideal situation in a more realistic picture. We end the section suggesting how the same protocol could be used to coherently transfer quantum information from the qubit to a superposition of cat states in the cavity. In Sec. IV we present our numerical simulations, which confirm the working of protocol. Finally, in Sec. V we discuss a few candidate systems that could be used to implement our idea and in Sec. VI we present our conclusions.

II. LANDAU-ZENER-STÜCKELBERG INTERFEROMETRY

The dynamics of a time-dependent level crossing in a two-level system is a well studied problem in quantum mechanics and can be described by the Hamiltonian

$$H_{\text{qub}} = \frac{\Delta(t)}{2} \sigma_z + \delta \sigma_x, \quad (2)$$

written in the diabatic basis $\{|1\rangle, |0\rangle\}$ and using the Pauli matrices $\sigma_{x,z}$. Assuming linear driving of the level splitting, $\Delta(t) = vt$, where t is time and v the sweep speed, the system

will pass a region around $t = 0$ where the coupling term δ mixes the two components of the wave function. In the limit of an infinite linear sweep of the energy splitting, from $t = -\infty$ to $t = \infty$, the probability of a diabatic transition (i.e., the probability for the system to remain in its initial state after the crossing) is given by the famous Landau-Zener formula,

$$P_{\text{LZ}} = e^{-2\pi \frac{\delta^2}{\hbar v}}. \quad (3)$$

This analytic result is valid for an infinite sweep through a single level crossing, and thus needs to be adapted to describe the situation of multiple consecutive level crossings. Assuming that the crossings are far enough apart in time, it is reasonable to assume that all crossings can be treated separately, leading to the adiabatic-impulse model [34]. The general idea is to treat the system as if it evolves adiabatically everywhere except in regions close to the level crossings and the nonadiabatic evolution at all crossings is assumed to be instantaneous. This approximation is considered good if the crossings are locally linear in time and well separated [35].

The time-evolution operator can then be written as a series of adiabatic evolution operators separated by nonadiabatic transfer operators. The adiabatic evolution operator, in the *adiabatic* basis, is

$$U(t_2, t_1) = \begin{pmatrix} e^{-i\theta_+(t_2, t_1)} & 0 \\ 0 & e^{-i\theta_-(t_2, t_1)} \end{pmatrix}, \quad (4)$$

where $\theta_{\pm}(t_2, t_1) = \int_{t_1}^{t_2} dt E_{\pm}(t)$ in terms of the instantaneous eigenenergies $E_{\pm}(t)$. The nonadiabatic evolution at the level crossing reads in the same basis as [35]

$$N = \begin{pmatrix} \sqrt{1 - P_{\text{LZ}}} e^{-i\phi_S} & -\sqrt{P_{\text{LZ}}} \\ \sqrt{P_{\text{LZ}}} & \sqrt{1 - P_{\text{LZ}}} e^{i\phi_S} \end{pmatrix}, \quad (5)$$

where we see that, apart from the (square root) of the Landau-Zener probabilities, all amplitudes pick up a different phase, where ϕ_S in the diagonal elements is [35],

$$\phi_S = -\frac{\pi}{4} + \frac{\delta^2}{\hbar v} \left[\ln \left(\frac{\delta^2}{\hbar v} \right) - 1 \right] + \arg \Gamma \left(1 - i \frac{\delta^2}{\hbar v} \right), \quad (6)$$

with $\Gamma(z)$ being the gamma function.

As an example we consider initializing the system in the state $|0\rangle$ and driving the level splitting through three consecutive crossings, as shown in Fig. 1. The first and last have identical sweep speed v , while the middle crossing is so slow that it is adiabatic. In this limit, the matrix N at the middle crossing becomes $i\sigma_z$ and the final state in the adiabatic-impulse model is thus given by

$$|\psi\rangle_f = iU(t_f, t_3)N\sigma_z U(t_3, t_1)NU(t_1, t_i)|0\rangle, \quad (7)$$

where $t_i < t_1$ is the initial time and $t_f > t_3$ the final time. For the case where $P_{\text{LZ}} = \frac{1}{2}$ for the first and last crossing we can write explicitly in the adiabatic basis

$$|\psi\rangle_f = e^{-i[\theta_+(t_1, t_i) + \frac{1}{2}\theta_+(t_3, t_1) + \frac{1}{2}\theta_-(t_3, t_1)]} \times \begin{pmatrix} i e^{-i[\theta_+(t_f, t_3) + \varphi]} \cos(\frac{1}{2}\phi_d + \varphi) \\ e^{-i\theta_-(t_f, t_3)} \sin(\frac{1}{2}\phi_d + \varphi) \end{pmatrix}, \quad (8)$$

where $\phi_d = \theta_+(t_3, t_1) - \theta_-(t_3, t_1)$ is the phase difference built up during the adiabatic evolution from t_1 to t_3 and $\varphi \approx -1.08$ is the phase ϕ_S that corresponds to the value of $\delta^2/\hbar v$ that

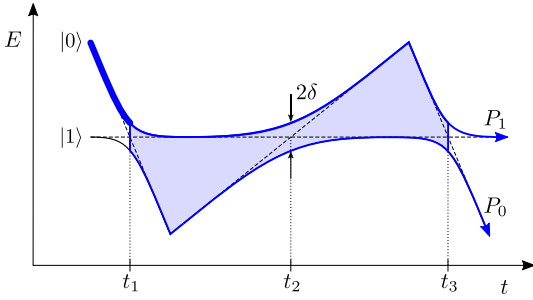


FIG. 1. Time-dependent spectrum of the example sweep protocol discussed in Sec. II. The diabatic energies of $|0\rangle$ and $|1\rangle$ are shown as dashed lines, while the adiabatic (instantaneous) eigenenergies are shown as full lines. Two interfering paths are colored in blue and the dynamic phase difference between them is shown as a blue shaded area.

yields the probability $P_{1,Z} = \frac{1}{2}$. The final occupation probabilities for the two states then follow straightforwardly as

$$P_{1,0} = \frac{1}{2} \pm \frac{1}{2} \cos(\phi_d + 2\varphi). \quad (9)$$

We thus see how this sweep protocol indeed leads to interference effects that depend on the difference in phases acquired along the two possible paths in time (blue lines in Fig. 1). This phase difference has two contributions: (i) the phase φ , given by (6), caused by the first and the last level crossing, and (ii) the dynamical contribution ϕ_d picked up during the adiabatic evolution, which corresponds to the blue shaded area in Fig. 1. As we can see, the total phase and hence the “return” probability is periodically dependent on this area, which we can easily control by tuning the sweep speed or the coupling strength δ at the second crossing.

III. PROPOSAL

The goal is to create even or odd cat states $|\Psi_{\pm}(\alpha)\rangle \propto |\alpha\rangle \pm |-\alpha\rangle$ in the photon field, where the coherent states read explicitly as $|\alpha\rangle = e^{-|\alpha|^2/2} \sum_{n=0}^{\infty} (\alpha^n / \sqrt{n!}) |n\rangle$ in terms of the photon number basis states $|n\rangle$. We see that, due to the factor α^n in the photon number coefficients, an even (odd) cat state only contains even (odd) photon number states, the occupation probabilities of which still have the same Poissonian “envelope” as the coherent states they are constituted of. In short, our cat state generation protocol, which we will explain in detail below, amounts to removing all odd or even components from a coherent photon state, without altering the Poissonian envelope structure of the state too much.

Let us now turn to the hybrid qubit-cavity system with which we would like to perform this protocol. We assume a simplest situation, where a single qubit is coupled to a single mode of the cavity photon field, and we describe the system with the Hamiltonian

$$H = \frac{\Delta(t)}{2} \sigma_z + \hbar\omega a^\dagger a + \hbar A(a + a^\dagger) \sigma_x, \quad (10)$$

where $\Delta(t)$ is the time-dependent qubit splitting, ω the frequency of the cavity mode, and A is the coupling strength

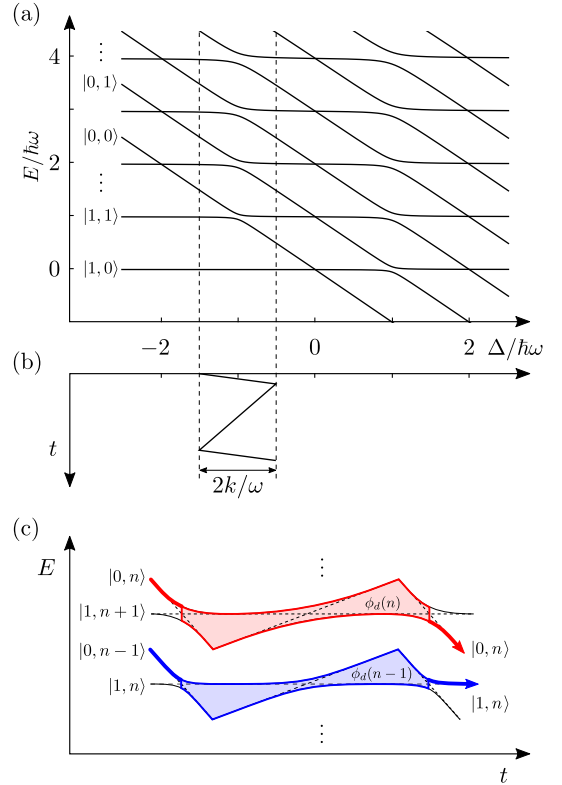


FIG. 2. (a) Schematic plot of the energy spectrum of the Hamiltonian (10) as a function of Δ . Dressed levels $|1\rangle$ and $|0\rangle$ anticross whenever the accompanying number of photons differs by 1. (b) Sketch of the proposed sweep protocol $\Delta(t)$. (c) Zoom-in on neighboring pair of coupled levels that are swept through each other. The n -dependent magnitude of the relative dynamical phases picked up during the sweep is indicated by the shaded red and blue areas.

between the qubit and the photon field. We note that we assumed “transverse” qubit-cavity coupling, i.e., the field in the cavity couples to the σ_x operator in the qubit subspace; comparing with the toy model used in Sec. II we see that $\hbar A(a + a^\dagger)$ now takes the place of δ .

In Fig. 2(a) we sketch the spectrum of H as a function of Δ , where the labels $|i, n\rangle$ indicate the (approximate) basis states $|i\rangle_{\text{qub}} \otimes |n\rangle_{\text{ph}}$. All levels cross, except when the two photon numbers involved differ by 1, in which case the magnitude of the anticrossing is determined by the matrix element

$$\langle 1, n | H | 0, n \pm 1 \rangle = \hbar A \sqrt{n + \frac{1}{2} \pm \frac{1}{2}}, \quad (11)$$

and thus depends on the actual photon numbers involved [36]. The key to our proposal is to use this n dependence of the size of the anticrossings. If we drive the qubit in a zigzag pattern around the 1-photon resonance, as sketched in Fig. 2(b), then we create a “ladder” of time-dependent level crossings between levels $|0, n\rangle$ and $|1, n+1\rangle$; see Fig. 2(c). Each pair of

coupled levels thus undergoes a sweep pattern that is similar to the one discussed in Sec. II and, assuming that we again make sure that the second level crossing is adiabatic, the final state is then given by Eq. (8), where the phase difference ϕ_d now depends on n , as can be seen from the difference in size between the red and blue shaded regions in Fig. 2(c). We note that isolating the dynamics of pairs of levels in such a way is in fact equivalent to applying the usual rotating-wave approximation to the Hamiltonian (10).

The idea is then to initialize in $|0\rangle \otimes |\alpha\rangle$, i.e., the cavity in a coherent state and the qubit in one of its basis states, and perform the sweep protocol sketched in Fig. 2, aiming for the characteristics (i) $P_{LZ} = \frac{1}{2}$ for all first and last crossings, (ii) all middle crossings are adiabatic, and (iii) $\phi_d(n+1) - \phi_d(n) = \pi$ as closely as possible for all relevant n . Of course, in reality the n dependence of the dynamical phase difference is not linear over larger ranges of n and P_{LZ} is also n dependent. Below we will investigate how well the desired characteristics can be satisfied at the same time, but let us for now assume the ideal (hypothetical) situation where $P_{LZ} = \frac{1}{2}$ and $\phi_d(n) = \phi_d(0) + n\pi$.

The phase $\phi_d(0)$ can be tuned by changing parts of the time-dependent level structure that are the same for all n , such as the minimum and maximum value of $\Delta(t)$ or the coupling strength A . Tuning $\phi_d(0) = -2\varphi$ is thus in principle possible, independently from trying to approach $\phi_d(n+1) - \phi_d(n) = \pi$. Then we see from Eq. (8) that the initial component $|0, n\rangle$ will evolve as

$$|0, n\rangle \rightarrow e^{-i\omega T} \left[\sin\left(\frac{n}{2}\pi\right) |0, n\rangle + ie^{-i\varphi} \cos\left(\frac{n}{2}\pi\right) |1, n+1\rangle \right], \quad (12)$$

where we introduced the total sweep time $T = t_f - t_i$, setting $t_f = t_3$ and $t_i = t_1$ for simplicity [37]. We see that all components $|0, n\rangle$ evolve (up to a phase factor) into $|0, n\rangle$ for odd n and into $|1, n+1\rangle$ for even n , thereby yielding zero weight in all even- n components of the final state of the photon field [38].

We thus end up with a photon field with a perfect odd parity. Since the weight of each even- n component that was removed was transferred to a neighboring n , one could expect that the envelope of the resulting cavity state is still relatively close to that of the coherent state, thus yielding (almost) a cat state. Even better, however, would be to end the protocol with a selective measurement of the qubit state: only accepting the outcome $|0\rangle$ will project the photon field to the state

$$\frac{-ie^{-\frac{1}{2}|\beta|^2}}{\mathcal{N}} \sum_{n=0}^{\infty} \left[\frac{\beta^n}{\sqrt{n!}} - \frac{(-\beta)^n}{\sqrt{n!}} \right] |n\rangle = -i |\Psi_-(\beta)\rangle, \quad (13)$$

with $\beta = ie^{-i\omega T} \alpha$, which is a perfect odd cat state.

Let us now investigate how closely our idealized assumptions about P_{LZ} and the dynamical phase differences can actually be met by a system described by the Hamiltonian (10). First of all, we write the full final state for the pair of levels $\{|0, n\rangle, |1, n+1\rangle\}$ after the sweep protocol, now allowing for deviations from our assumptions. From Eqs. (4)–(7) we

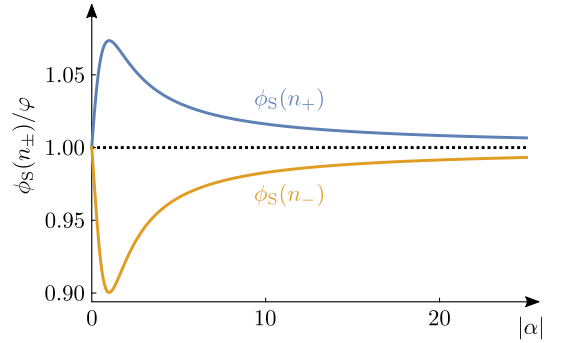


FIG. 3. The deviation of the phase $\phi_S(n)$ at $n = |\alpha|^2 \pm |\alpha|$ from the assumption $\phi_S(n) = \varphi \approx -1.08$. The sweep speed is tuned such that $P_{LZ}(|\alpha|^2) = \frac{1}{2}$ and thus $\phi_S(|\alpha|^2) = \varphi$.

find the explicit expression

$$|0, n\rangle \rightarrow e^{-i\omega T} \left\{ 2 \sin\left(\frac{1}{2}\phi_d + \phi_S\right) \sqrt{P_{LZ}(1 - P_{LZ})} |0, n\rangle + e^{-i\phi_S} \left[(1 - 2P_{LZ}) \sin\left(\frac{1}{2}\phi_d + \phi_S\right) + i \cos\left(\frac{1}{2}\phi_d + \phi_S\right) \right] |1, n+1\rangle \right\}, \quad (14)$$

where now ϕ_d, ϕ_S , as well as P_{LZ} are n dependent. As is well known, the relative width of the photon number distribution of a coherent state decreases for increasing $|\alpha|$, suggesting that this n dependence might become less important for large $|\alpha|$.

We first focus on the n dependence of the Landau-Zener probability for the first and last crossing, which simply reads as

$$P_{LZ}(n) = \exp\left(-\frac{2\pi \hbar A^2 [n+1]}{v_f}\right), \quad (15)$$

where v_f is the “fast” sweep speed at those two crossings. For any particular α we can tune this speed such that $P_{LZ}(|\alpha|^2) = \frac{1}{2}$. We then estimate the decrease in fidelity of creating the desired state due to the n dependence of P_{LZ} by calculating the modulo square of the weight of the final component $|0, n\rangle$ at $n_{\pm} = |\alpha|^2 \pm |\alpha|$, using the fact that the photon distribution will have a Poissonian envelope with both mean and variance equal to $|\alpha|^2$. We then find that for $|\alpha|^2 \gtrsim 1$

$$4P_{LZ}(n_{\pm})[1 - P_{LZ}(n_{\pm})] \approx 1 - \frac{\ln 2}{|\alpha|^2}; \quad (16)$$

i.e., the deviation from 1 is suppressed for increasing $|\alpha|^2$.

Next we investigate in a similar way the n dependence of ϕ_S which we above also assumed to be constant, $\phi_S(n) = \varphi \approx -1.08$. Using the same sweep speed v_f such that $P_{LZ}(|\alpha|^2) = \frac{1}{2}$ we calculate the phases $\phi_S(n_{\pm})$ using Eq. (6). In Fig. 3 we show the result, where we normalized the two phases with φ . We see again that the deviation from the ideal condition decreases monotonically for $|\alpha|^2 \gtrsim 1$.

Finally, we investigate the dynamical phases $\phi_d(n)$, for which we assumed $d(n) \equiv \phi_d(n+1) - \phi_d(n) = \pi$. Assuming that the sweep is performed using the detuning extrema

$-\hbar\omega \pm \hbar k$ (with $k < \omega$; see Fig. 2) we find

$$d(n) \approx \frac{2\hbar A^2}{v^*} \left[\ln \left(\frac{k^2}{A^2[n+1]} \right) - \frac{1}{2[n+1]} \right], \quad (17)$$

valid in the limit $A^2 n \ll k^2$ and at $n \gtrsim 1$, where $v^* = v_f v_s / (v_f + v_s)$ is an average of the two different sweep speeds, with v_s the “slow” adiabatic sweep speed. The derivative with respect to n of this phase difference,

$$d'(n) \approx \frac{2\hbar A^2}{v^*} \left(-\frac{1}{n+1} + \frac{1}{2[n+1]^2} \right), \quad (18)$$

decreases faster than $1/\sqrt{n}$ for increasing n , but the total error in $d(n)$ at $n_{\pm} = |\alpha|^2 \pm |\alpha|$ is a cumulative error, contributed to by all n between $|\alpha|^2$ and n_{\pm} . To arrive at an estimate for the typical error in $d(n)$ we thus need to sum over all contributing phase differences from $|\alpha|^2$ to n_{\pm} , yielding approximately

$$\begin{aligned} & \pm \frac{2\hbar A^2}{v^*} \left(-\frac{1}{|\alpha|^2+1} + \frac{1}{2[|\alpha|^2+1]^2} \right) \sum_{l=1}^{|\alpha|} l \\ & = \pm \frac{\hbar A^2}{v^*} \left(-\frac{1}{|\alpha|^2+1} + \frac{1}{2[|\alpha|^2+1]^2} \right) (|\alpha|^2 + |\alpha|). \end{aligned} \quad (19)$$

We see that this contribution to the infidelity of our protocol does not decrease as a function of increasing $|\alpha|^2$: for large $|\alpha|$ it approaches $\hbar A^2/v^*$. In principle one could tune $\hbar A^2/v^*$ as small as desired, but, due to the conditions (i) $d(|\alpha|^2) = \pi$ and (ii) $\hbar A^2|\alpha|^2/v_s \gg 1$, that would require an exponential increase of $k/A|\alpha|$, see Eq. (17), and a very large ratio $\hbar k^2/v_s$. These requirements are not in contradiction with any of our other assumptions, but might be inconvenient from a practical point of view.

We thus showed how our proposed protocol conceptually works, and we demonstrated that the most important intrinsic inaccuracies can in principle be tuned to be of arbitrarily small importance, e.g., by going to large $|\alpha|^2$ and small $\hbar A^2/v^*$. However, deviations from the other assumptions we made, such as the validity of the adiabatic-impulse model, will also contribute to the infidelity of the protocol. In order to investigate their importance quantitatively, we will present numerical simulations of the protocol in Sec. IV, showing that fidelities of ~ 0.99 are theoretically indeed achievable.

So far, we used the qubit mainly as a tool to tune the spectrum and sweep the system through multiple level crossings. As an example, we showed how initialization of the system in $|0\rangle \otimes |\alpha\rangle$ can produce an odd cat state of the photon field after projecting the final qubit state to $|0\rangle$. We could, however, also assume a more general initial state of the qubit, $|\chi\rangle_{\text{qub}} = a|0\rangle + b|1\rangle$, and investigate to what extent and in what way the quantum information in this initial qubit state is transferred to the photon field during the sweep protocol.

It is straightforward to focus on the same pair of levels $\{|0, n\rangle, |1, n+1\rangle\}$ as before and use Eq. (8) to write down the final state after initializing in $|1, n+1\rangle$, assuming the same ideal conditions as in (12),

$$\begin{aligned} |1, n+1\rangle \rightarrow & -e^{-i\omega T} \left[\sin \left(\frac{n}{2}\pi \right) |1, n+1\rangle \right. \\ & \left. + i e^{i\varphi} \cos \left(\frac{n}{2}\pi \right) |0, n\rangle \right]. \end{aligned} \quad (20)$$

We see that now for even n the population is fully transferred to $|0, n\rangle$ and for odd n to $|1, n+1\rangle$. This means that initialization in $|1\rangle \otimes |\alpha\rangle$ would produce a final photon state with a perfect *even* parity, whereas initialization in $|0\rangle \otimes |\alpha\rangle$ yielded a perfect *odd* state. Initializing in $|\chi\rangle_{\text{qub}} \otimes |\alpha\rangle$ will thus yield a photonic state that is in a superposition of a perfectly odd state (with an amplitude proportional to a) and an even state (with amplitude proportional to b). Since the even and odd cat states $|\Psi_{\pm}(\alpha)\rangle$ form a good orthogonal basis for cat-based quantum-information applications [3,4], where $|\chi\rangle_{\text{cat}} = a|\Psi_{-}(\alpha)\rangle + b|\Psi_{+}(\alpha)\rangle$ encodes the same quantum information as $|\chi\rangle_{\text{qub}}$, this suggests that our protocol might provide a way to transfer the quantum information coherently from the qubit to the photon field.

We thus initialize in $|\chi\rangle_{\text{qub}} \otimes |\alpha\rangle$ and perform the same sweep protocol as before, assuming the same hypothetical ideal conditions. If we again selectively measure the final state of the qubit, only accepting the outcome $|0\rangle$, we will project the photon field to the state

$$\begin{aligned} & -ia|\Psi_{-}(\beta)\rangle \\ & -ibe^{i\varphi} \frac{e^{-\frac{1}{2}|\beta|^2}}{\mathcal{N}} \sum_{n=0}^{\infty} \frac{\alpha}{\sqrt{n+1}} \left[\frac{\beta^n}{\sqrt{n!}} + \frac{(-\beta)^n}{\sqrt{n!}} \right] |n\rangle. \end{aligned} \quad (21)$$

We see that the even part of the field is nearly a cat state, the weight of each n -photon component being slightly off since it originated from the component $|n+1\rangle$ in the initial coherent state $|\alpha\rangle$ of the field. The modulo square of the overlap of the part of the photon field proportional to b with the state $-ie^{i\varphi}|\Psi_{+}(\beta)\rangle$ can be evaluated numerically: we find that it is 0.99 for $|\alpha| \approx 5$ and approaches 1 monotonically for increasing $|\alpha|$. Therefore we conclude that with high fidelity the final photon state approaches

$$-i[a|\Psi_{-}(\beta)\rangle + e^{i\varphi}b|\Psi_{+}(\beta)\rangle]. \quad (22)$$

The phase $\varphi \approx -1.08$ is known and can thus be compensated for, meaning that our sweep protocol indeed provides a means to coherently transfer quantum information from an actual two-level system to a superposition of even and odd cat states in a photon field. Of course, the final state (21) was derived under the same assumptions concerning $P_{LZ}(n)$, $\phi_S(n)$, and $\phi_d(n)$ as (12); i.e., the deviations from these ideal conditions investigated before will affect the fidelity of this transfer protocol in a way that should be quantitatively similar.

IV. NUMERICAL SIMULATIONS

We solved the time-dependent Schrödinger equation using the function “solve” from the Quantum Toolbox in Python (QuTiP) package [39,40]. We initialize the system in a direct product state of one of the two qubit basis states and a coherent state of the photon field $|\alpha\rangle$, using the basis states $|0, n\rangle$ and $|1, n\rangle$, where we cut off the Hilbert space for $n \geq 2|\alpha|^2 + 10$, and work in units where $\hbar = 1$. Then we evolve the system using the Hamiltonian as given in (10) with

$$\Delta(t) = \begin{cases} -\omega - k + v_f t, & \text{for } 0 \leq t \leq \tau_1, \\ -\omega + k - v_s(t - \tau_1), & \text{for } \tau_1 \leq t \leq \tau_2, \\ -\omega - k + v_f(t - \tau_2), & \text{for } \tau_2 \leq t \leq \tau_3, \end{cases} \quad (23)$$

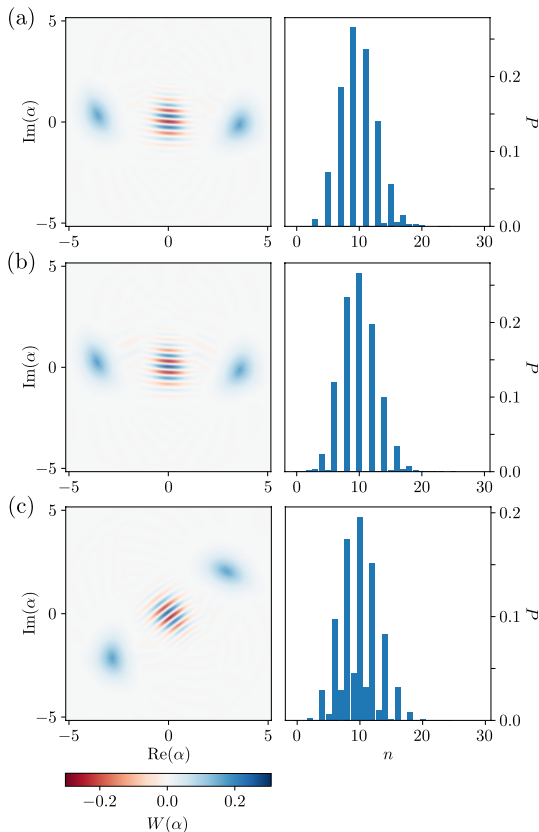


FIG. 4. Numerically calculated final photon states after performing the sweep protocol (23) and projecting the qubit to the state $|0\rangle$. In the left panels we show their Wigner distribution function $W(\alpha)$ and in the right panels their photon number distribution function P_n . In all simulations we used $|\alpha|^2 = 10$ and $A = 0.003$. The sweep speeds $v_{s,f}$ were chosen such that $P_{LZ}(10) = \frac{1}{2}$ and $d(10) = \pi$. (a), (b) Fine-tuning the parameter k to $k = 0.50017$ yields (a) an odd cat state with fidelity 0.986 if the qubit was initialized in $|0\rangle$ and (b) an even cat state with fidelity 0.989 if it was in $|1\rangle$. (c) Not fine-tuning k yields a cat state of a more general form; see Eq. (24). In this case $k = 0.49$ resulted in $\theta = 0.713\pi$ with fidelity 0.988.

with $\tau_1 = 2k/v_f$, $\tau_2 = \tau_1 + 2k/v_s$, and $\tau_3 = \tau_2 + 2k/v_f$. This results in the sweep pattern as shown in Fig. 2(b), with the detuning extrema $-\omega \pm k$.

We will first present numerical results for $|\alpha|^2 = 10$. We set $A = 0.003$ (in units of ω), which will allow for large $k/A|\alpha|$ while still satisfying the condition $k \leq \omega$. Then we set the other simulation parameters as follows: v_f is calculated using Eq. (15), demanding that $P_{LZ}(10) = \frac{1}{2}$, and v_s and k are tuned together to satisfy $d(10) = \pi$, see Eq. (17), and $\phi_d(10) = -2\phi_S(10)$ as closely as possible, which corresponds to fixing the “offset” phase $\phi_d(0) = -2\varphi$ in the ideal picture presented above. This yielded $v_f \approx 8.9741 \times 10^{-4}$, $v_s \approx 4.6965 \times 10^{-5}$, and $k = 0.50017$. In Fig. 4 we show final

photon states after the sweep protocol, assuming the qubit to have been projected to $|0\rangle$. The left panels show the Wigner distribution function $W(\alpha)$ of the state, all of them showing the characteristics of a cat state, including the typical fringes around $\alpha = 0$ signaling quantum-mechanical interference between the state’s two main components. The right panels show the photon number distribution P_n of the final state.

Figure 4(a) presents the final photon state that results after initializing the qubit in $|0\rangle$. In the right panel we see that state has almost perfect odd parity, suggesting that it is indeed close to an odd cat state, as predicted above. We can calculate numerically the overlap of this final state with the desired odd cat state, as a measure of the fidelity of our protocol, yielding $F_- = |\langle \Psi_f | \Psi_- \rangle|^2 \approx 0.986$, where $|\beta| = \sqrt{10}$. In Fig. 4(b) we show the resulting final photon state after the same sweep procedure, but now having initialized the qubit in $|1\rangle$. The parity of this state is indeed almost exactly opposite, and as fidelity of the thusly created even cat state we find $F_+ \approx 0.989$. As expected, the Wigner distribution functions of the two states shown in Figs. 4(a) and 4(b) look very similar. The main difference is in the phase of the interference fringes appearing around $\alpha = 0$, which is set by the relative sign of the two components constituting the cat state. Finally, in Fig. 4(c) we show the resulting state if the parameter k is not fine-tuned but simply fixed to some value, we set $k = 0.49$, after which only $v_f \approx 8.9741 \times 10^{-4}$ and $v_s \approx 4.6705$ are adjusted to satisfy $P_{LZ}(10) = \frac{1}{2}$ and $d(10) = \pi$, following Eqs. (15) and (17). This means we no longer ensure that $\phi_d(10) = -2\phi_S(10)$, which introduces an extra phase shift in the n -dependent oscillations of all final amplitudes; see Eq. (14). This phase shift results in a final state that is still close to a cat state, but now of the more general form

$$|\Psi_\theta(\beta)\rangle = \frac{1}{\mathcal{N}}(|\beta\rangle + e^{i\theta} |-\beta\rangle), \quad (24)$$

where θ is no longer necessarily π or 0. For our particular choice of k we found a maximum overlap with the cat state with $\theta = 0.713\pi$, yielding a fidelity of $F_\theta \approx 0.988$.

We thus see that our protocol is in principle indeed able to produce Schrödinger-cat states with fidelities up to ~ 0.99 , already at moderate $|\alpha|$. Next, we investigate how the fidelity of the protocol depends on $|\alpha|$ by varying $|\alpha|^2$ from 3 to 25. We initialize the qubit in $|0\rangle$ and perform the sweep procedure using the same parameters $A = 0.003$ and $k = 0.50017$ as before, while adjusting v_f and v_s such that $P_{LZ}(|\alpha|^2) = \frac{1}{2}$ and $d(|\alpha|^2) = \pi$ for each $|\alpha|^2$. After projecting the qubit to $|0\rangle$ we find the cat state $|\Psi_\theta(\beta)\rangle$ that has largest overlap with the final photon state and calculate the modulo square of that overlap to determine the fidelity F . In Fig. 5 we plot F as a function of $|\alpha|^2$, and we see that the fidelity is around 0.98 for all $|\alpha|^2$ in the range plotted, with a slight decrease for larger $|\alpha|^2$. This is a sign that the assumption of $A|\alpha|/k \ll 1$, which is one of the conditions for the adiabatic-impulse model to be a good approximation, is starting to become questionable.

V. DISCUSSION

We demonstrated that our protocol can generate cat states in a photon cavity with fidelities up to ~ 0.99 and could possibly also be used to coherently transfer quantum information

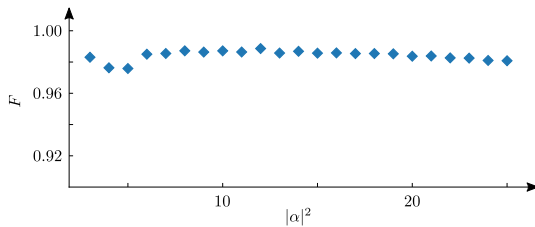


FIG. 5. Fidelity of the resulting final cat state as a function of $|\alpha|^2$ using the same parameters $A = 0.003$ and $k = 0.50017$ throughout, while adjusting v_f and v_s such that the conditions $P_{LZ}(|\alpha|^2) = \frac{1}{2}$ and $d(|\alpha|^2) = \pi$ remain fulfilled.

between a qubit and a superposition of different, orthogonal cat states in the cavity. However, so far we assumed both the cavity and the qubit to be lossless and coherent at all times. In reality, both subsystems are coupled to many environmental degrees of freedom, leading to photon loss from the cavity, typically characterized with the decay rate κ , and qubit decoherence characterized with the rate γ . Roughly speaking, good coherence during the full protocol will thus be guaranteed if the total time of the procedure $T \sim 2\hbar k/v_s \ll \kappa^{-1}, \gamma^{-1}$, where v_s should be small enough to ensure that the second crossing is adiabatic. It is therefore straightforward to investigate the typical coherence properties of a few obvious candidate systems for implementing our protocol and compare them in the context of this requirement.

The paradigmatic system providing a well-controllable qubit coupled to a single mode of the photon field is the circuit-QED setup of a superconducting qubit coupled to a transmission line resonator [41,42]. In such hybrid systems coupling strengths of $A/2\pi \sim 100$ MHz can easily be reached [43], which, assuming $|\alpha|^2 \sim 10$, leads to the constraint $v_s \lesssim 25 \mu\text{eV/ns}$. Typical resonator frequencies are of the order $\omega/2\pi \sim 10$ GHz and picking $2k \approx \omega$, as we did in our numerical examples, then yields a lower limit $T \gtrsim 2$ ns, which is well below typical decay and dephasing times $\kappa^{-1}, \gamma^{-1} \sim 0.1\text{--}1 \mu\text{s}$. In fact, depending on the choice of qubit (transmon, flux, phase, or charge), having such a strong coupling parameter A might make it challenging to implement a sweep speed v_f high enough to yield a Landau-Zener probability of $\frac{1}{2}$. But since the minimum and maximum T estimated above are still several orders of magnitude apart, there is enough room to work with significantly smaller coupling A .

Another, more recently developed class of hybrid systems that could be used to implement our idea is that of gate-defined semiconductor quantum dots coupled to a superconducting cavity [44]. This would allow us to perform the protocol using a spin-based qubit instead of a superconducting qubit, which provides potentially superior qubit coherence properties. Direct spin-photon coupling is weak, typically on the peV scale, but the effective coupling strength can be significantly enhanced by using multielectron spin qubits instead, where the basis states are spin-charge mixtures that couple much more efficiently to the photon field [44]. The most advanced example in this field is the triple-dot three-electron exchange-only qubit [45–47], which provides fast all-electric control and potentially strong coupling to the cavity mode [48]. Recently the coherent coupling between such a qubit and a microwave cavity has been demonstrated experimentally [49], yielding the device parameters $\omega/2\pi \approx 4.5$ GHz, $\kappa^{-1} \approx 20$ ns, and $\gamma^{-1} \approx 0.1 \mu\text{s}$, while providing coupling strengths up to $A/2\pi \approx 31$ MHz. The same rough estimate as above then yields the constraint $v_s \lesssim 2 \mu\text{eV/ns}$ and thus a lower limit $T \gtrsim 9$ ns, which is within the reported decoherence times.

VI. CONCLUSION

We presented a way to create Schrödinger-cat states in a photonic cavity using Landau-Zener-Stückelberg interferometry, by coupling the cavity to a qubit and manipulating the qubit splitting as a function of time. We show how our protocol can create cat states with a fidelity up to ~ 0.99 for $|\alpha|^2 \sim 10$, and how it could also be used to coherently transfer quantum information between the qubit and the photon field, where it can be stored in the form of coherent superpositions of orthogonal cat states. We corroborated our presentation of the protocol with numerical simulations and finally discussed a few candidate hybrid systems that could be used to implement our idea.

ACKNOWLEDGMENTS

We gratefully acknowledge financial support from NTNU's Onsager Fellowship Program, as well as partial support through the Centers of Excellence funding scheme of the Research Council of Norway, 262633, QuSpin. We thank A. Kamra for giving useful feedback on our manuscript in preparation.

-
- [1] E. Schrödinger, *Naturwissenschaften* **23**, 844 (1935).
 - [2] M. Brune, E. Hagley, J. Dreyer, X. Maître, A. Maali, C. Wunderlich, J. M. Raimond, and S. Haroche, *Phys. Rev. Lett.* **77**, 4887 (1996).
 - [3] T. C. Ralph, A. Gilchrist, G. J. Milburn, W. J. Munro, and S. Glancy, *Phys. Rev. A* **68**, 042319 (2003).
 - [4] A. P. Lund, T. C. Ralph, and H. L. Haselgrove, *Phys. Rev. Lett.* **100**, 030503 (2008).
 - [5] P. T. Cochrane, G. J. Milburn, and W. J. Munro, *Phys. Rev. A* **59**, 2631 (1999).
 - [6] D. Gottesman, A. Kitaev, and J. Preskill, *Phys. Rev. A* **64**, 012310 (2001).
 - [7] M. Bergmann and P. van Loock, *Phys. Rev. A* **94**, 042332 (2016).
 - [8] N. Ofek, A. Petrenko, R. Heeres, P. Reinhold, Z. Leghtas, B. Vlastakis, Y. Liu, L. Frunzio, S. M. Girvin, L. Jiang, M. Mirrahimi, M. H. Devoret, and R. J. Schoelkopf, *Nature (London)* **536**, 441 (2016).
 - [9] S. J. van Enk and O. Hirota, *Phys. Rev. A* **64**, 022313 (2001).

- [10] H. Jeong, M. S. Kim, and J. Lee, *Phys. Rev. A* **64**, 052308 (2001).
- [11] W. J. Munro, K. Nemoto, G. J. Milburn, and S. L. Braunstein, *Phys. Rev. A* **66**, 023819 (2002).
- [12] T. C. Ralph, *Phys. Rev. A* **65**, 042313 (2002).
- [13] A. Gilchrist, K. Nemoto, W. J. Munro, T. C. Ralph, S. Glancy, S. L. Braunstein, and G. J. Milburn, *J. Opt. B: Quantum Semiclass. Opt.* **6**, S828 (2004).
- [14] J. Joo, W. J. Munro, and T. P. Spiller, *Phys. Rev. Lett.* **107**, 083601 (2011).
- [15] B. Yurke and D. Stoler, *Phys. Rev. Lett.* **57**, 13 (1986).
- [16] M. Dakna, T. Anhut, T. Opatrny, L. Knöll, and D.-G. Welsch, *Phys. Rev. A* **55**, 3184 (1997).
- [17] A. Ourjoumtsev, R. Tualle-Brouiri, J. Laurat, and P. Grangier, *Science* **312**, 83 (2006).
- [18] J. S. Neergaard-Nielsen, B. M. Nielsen, C. Hettich, K. Mølmer, and E. S. Polzik, *Phys. Rev. Lett.* **97**, 083604 (2006).
- [19] H. Takahashi, K. Wakui, S. Suzuki, M. Takeoka, K. Hayasaka, A. Furusawa, and M. Sasaki, *Phys. Rev. Lett.* **101**, 233605 (2008).
- [20] A. Ourjoumtsev, F. Ferreyrol, R. Tualle-Brouiri, and P. Grangier, *Nat. Phys.* **5**, 189 (2009).
- [21] T. Gerrits, S. Glancy, T. S. Clement, B. Calkins, A. E. Lita, A. J. Miller, A. L. Migdall, S. W. Nam, R. P. Mirin, and E. Knill, *Phys. Rev. A* **82**, 031802(R) (2010).
- [22] A. P. Lund, H. Jeong, T. C. Ralph, and M. S. Kim, *Phys. Rev. A* **70**, 020101(R) (2004).
- [23] A. Ourjoumtsev, H. Jeong, R. Tualle-Brouiri, and P. Grangier, *Nature (London)* **448**, 784 (2007).
- [24] B. Hacker, S. Welte, S. Daiss, A. Shaikat, S. Ritter, L. Li, and G. Rempe, *Nat. Photon.* **13**, 110 (2019).
- [25] D. V. Sychev, A. E. Ulanov, A. A. Pushkina, M. W. Richards, I. A. Fedorov, and A. I. Lvovsky, *Nat. Photon.* **11**, 379 (2017).
- [26] M. Brune, S. Haroche, J. M. Raimond, L. Davidovich, and N. Zagury, *Phys. Rev. A* **45**, 5193 (1992).
- [27] S. Deléglise, I. Dotsenko, C. Sayrin, J. Bernu, M. Brune, J. M. Raimond, and S. Haroche, *Nature (London)* **455**, 510 (2008).
- [28] Z. Leghtas, G. Kirchmair, B. Vlastakis, R. J. Schoelkopf, M. H. Devoret, and M. Mirrahimi, *Phys. Rev. Lett.* **111**, 120501 (2013).
- [29] B. Vlastakis, G. Kirchmair, Z. Leghtas, S. E. Nigg, L. Frunzio, S. M. Girvin, M. Mirrahimi, M. H. Devoret, and R. J. Schoelkopf, *Science* **342**, 607 (2013).
- [30] J. i. Yoshikawa, K. Makino, S. Kurata, P. van Loock, and A. Furusawa, *Phys. Rev. X* **3**, 041028 (2013).
- [31] W. Pfaff, C. J. Axline, L. D. Burkhardt, U. Vool, P. Reinhold, L. Frunzio, L. Jiang, M. H. Devoret, and R. J. Schoelkopf, *Nat. Phys.* **13**, 882 (2017).
- [32] G. Sun, X. Wen, B. Mao, J. Chen, Y. Yu, P. Wu, and S. Han, *Nat. Commun.* **1**, 51 (2010).
- [33] G. Sun, X. Wen, B. Mao, Y. Yu, J. Chen, W. Xu, L. Kang, P. Wu, and S. Han, *Phys. Rev. B* **83**, 180507(R) (2011).
- [34] B. Damski and W. H. Zurek, *Phys. Rev. A* **73**, 063405 (2006).
- [35] S. N. Shevchenko, S. Ashhab, and F. Nori, *Phys. Rep.* **492**, 1 (2010).
- [36] One can also assume “longitudinal” coupling, using the Hamiltonian $H = \frac{1}{2}\Delta(t)\sigma_z + \delta\sigma_x + \hbar\omega a^\dagger a + \hbar A(a + a^\dagger)\sigma_z$. In that case, the protocol will work in a qualitatively similar but slightly less efficient way, the relevant matrix elements reading $\langle 1, n|H|0, n \pm 1\rangle = (A\delta/\omega)\sqrt{n + \frac{1}{2} \pm \frac{1}{2}}$ to leading order in A/ω .
- [37] Making the time intervals $[t_i, t_1]$ and $[t_3, t_f]$ finite will add extra phase factors in (12) that are again absorbed into T in the final state of the photon field after projection.
- [38] Tuning to $\phi_d(0) = -2\varphi + \pi$ will result in only *even* states surviving.
- [39] J. R. Johansson, P. D. Nation, and F. Nori, *Comput. Phys. Commun.* **183**, 1760 (2011).
- [40] J. R. Johansson, P. D. Nation, and F. Nori, *Comput. Phys. Commun.* **184**, 1234 (2013).
- [41] A. Blais, R.-S. Huang, A. Wallraff, S. M. Girvin, and R. J. Schoelkopf, *Phys. Rev. A* **69**, 062320 (2004).
- [42] A. Wallraff, D. I. Schuster, A. Blais, L. Frunzio, R. S. Huang, J. Majer, S. Kumar, S. M. Girvin, and R. J. Schoelkopf, *Nature (London)* **431**, 162 (2004).
- [43] A. Blais, A. L. Grimsmo, S. M. Girvin, and A. Wallraff, [arXiv:2005.12667](https://arxiv.org/abs/2005.12667).
- [44] G. Burkard, M. J. Gullans, X. Mi, and J. R. Petta, *Nat. Rev. Phys.* **2**, 149 (2020).
- [45] D. P. DiVincenzo, D. Bacon, J. Kempe, G. Burkard, and K. B. Whaley, *Nature (London)* **408**, 339 (2000).
- [46] J. M. Taylor, V. Srinivasa, and J. Medford, *Phys. Rev. Lett.* **111**, 050502 (2013).
- [47] M. Russ and G. Burkard, *J. Phys.: Condens. Matter* **29**, 393001 (2017).
- [48] V. Srinivasa, J. M. Taylor, and C. Tahan, *Phys. Rev. B* **94**, 205421 (2016).
- [49] A. J. Landig, J. V. Koski, P. Scarlino, U. C. Mendes, A. Blais, C. Reichl, W. Wegscheider, A. Wallraff, K. Ensslin, and T. Ihn, *Nature (London)* **560**, 179 (2018).

Paper II

Ida C. Skogvoll, Jonas Lidal, Jeroen Danon, and Akashdeep Kamra

*Tunable Anisotropic Quantum Rabi Model
via a Magnon–Spin-Qubit Ensemble*


Physical Review Applied, **16**, 064008 (2021)

Tunable Anisotropic Quantum Rabi Model via a Magnon–Spin-Qubit Ensemble

Ida C. Skogvoll,¹ Jonas Lidal¹,,¹ Jeroen Danon¹,,¹ and Akashdeep Kamra^{2,1,*}

¹*Center for Quantum Spintronics, Department of Physics, Norwegian University of Science and Technology, Trondheim NO-7491, Norway*

²*Condensed Matter Physics Center (IFIMAC) and Departamento de Física Teórica de la Materia Condensada, Universidad Autónoma de Madrid, Madrid E-28049, Spain*

 (Received 19 May 2021; revised 16 August 2021; accepted 15 November 2021; published 2 December 2021)

The ongoing rapid progress towards quantum technologies relies on new hybrid platforms optimized for specific quantum computation and communication tasks, and researchers are striving to achieve such platforms. We study theoretically a spin qubit exchange-coupled to an anisotropic ferromagnet that hosts magnons with a controllable degree of intrinsic squeezing. We find this system to physically realize the quantum Rabi model from the isotropic to the Jaynes-Cummings limit with coupling strengths that can reach the deep-strong regime. We demonstrate that the composite nature of the squeezed magnon enables concurrent excitation of three spin qubits coupled to the same magnet. Thus, three-qubit Greenberger-Horne-Zeilinger and related states needed for implementing Shor’s quantum error-correction code can be robustly generated. Our analysis highlights some unique advantages offered by this hybrid platform, and we hope that it will motivate corresponding experimental efforts.

DOI: [10.1103/PhysRevApplied.16.064008](https://doi.org/10.1103/PhysRevApplied.16.064008)

I. INTRODUCTION

A bosonic mode interacting with a two-level system constitutes the paradigmatic quantum Rabi model (QRM) employed in understanding light-matter interactions [1,2]. The recent theoretical discovery of its integrability [3] and the increasing coupling strengths realized in experiments have brought the QRM into sharp focus [4,5]. The QRM also models a qubit interacting with an electromagnetic mode, a key ingredient for quantum communication and distant qubit-qubit coupling [6–9]. Thus, the ongoing quantum information revolution [6,10] capitalizes heavily on the advancements in physically realizing and theoretically understanding the QRM. In particular, larger coupling strengths are advantageous for faster gate operations on qubits, racing against imminent decoherence. Generating squeezed states of the bosonic mode [11,12], typically light, via parametric amplification has emerged as a nonequilibrium means of strengthening this coupling and achieving various entangled states [13–18]. Other related methods [19,20] that exploit drives to control, for example, the QRM anisotropy [4] have also been proposed.

Contemporary digital electronics relies heavily on very large-scale integration of silicon-based circuits. In sharp contrast, the emerging quantum information technologies benefit from the availability of multiple physical realizations of qubits and their interconnects in order for one to

be able to choose the best platform for implementing a specific task or computation [6,8,21–24]. Fault-tolerant quantum computing, either via less error-prone qubits [25] or via implementation of quantum error correction [26–28], is widely seen as the path forward. A paradigmatic error-correction code [26] put forth by Shor requires encoding one logical qubit into nine physical qubits and generating three-qubit Greenberger-Horne-Zeilinger (GHZ) [29] and related states. A continuous-variable analog of this code employing squeezed states of light has been experimentally demonstrated [30]. This has spurred fresh hopes of fault-tolerant quantum computing and demonstrated the use of bosonic modes as more than just interconnects for qubits.

In our discussion above, we encounter squeezed states of light in multiple contexts. These nonequilibrium states, which have widespread applications from metrology [31] to quantum teleportation [32,33], decay with time. In contrast, the bosonic normal modes—magnons—in anisotropic ferromagnets have recently been shown to be squeezed [34] and to embody various quantum features inherent in such squeezed states [11,35–37]. Being equilibrium in nature, these modes are also somewhat different from light and require care when making comparisons. This calls for examining ways in which we can exploit the robust equilibrium-squeezed nature of magnons in addressing the challenges facing emerging quantum technologies [24,38,39]. The spin qubit [22,23,40] becomes the perfect partner because of its potential silicon-based

*akashdeep.kamra@uam.es

nature, the feasibility of strong exchange coupling to the magnet, its reliance on a mature fabrication technology, and so on.

Here, we study theoretically a ferromagnet exchange-coupled to a spin qubit. We find that the ensuing magnon-qubit ensemble combines the various complementary advantages mentioned above into one promising platform. We show that this system realizes an ideal Jaynes-Cummings model, enabled by spin conservation in a system that forbids counter-rotating terms (CRTs) by symmetry. If we allow anisotropy in the magnet, the squeezed magnon [34,35] becomes the normal mode, giving rise to nonzero and controllable CRTs. The squeezed nature of the magnon leads further to an enhancement in the coupling strength, without the need for a nonequilibrium drive. Considering three spin qubits coupled to the same ferromagnet, we demonstrate theoretically the simultaneous resonant excitation of the three qubits via a single squeezed magnon. Thus, the system enables a robust means to generate the entangled three-qubit GHZ and related states that underlie Shor's error-correction code [26]. The magnon–spin-qubit ensemble offers an optimal platform for realizing the QRM with large coupling strengths and implementing fault-tolerant quantum computing protocols.

II. ONE MAGNONIC MODE COUPLED TO ONE QUBIT

We consider a thin film of an insulating ferromagnet that acts as a magnonic cavity. Considering an applied magnetic field $H_0\hat{z}$, the ferromagnetic Hamiltonian is expressed as [41]

$$\tilde{H}_F = -J \sum_{\langle i,j \rangle} \tilde{\mathbf{S}}_i \cdot \tilde{\mathbf{S}}_j + |\gamma| \mu_0 H_0 \sum_i \tilde{S}_{iz}, \quad (1)$$

where J (> 0) parameterizes the ferromagnetic exchange between nearest neighbors, γ (< 0) is the gyromagnetic ratio, and $\tilde{\mathbf{S}}_i$ denotes the spin operator at position i . We set $\hbar = 1$ throughout and identify operators with an overhead tilde. A detailed derivation of the system Hamiltonian is presented in Appendix A. We discuss the key steps and their physical implications here in the main text. Because of the Zeeman energy, the ferromagnet has all its spins pointing along $-\hat{z}$ in its ground state. Employing Holstein-Primakoff transformations [42] and switching to Fourier space, the ferromagnetic Hamiltonian is written in terms of spin-1 magnons [43] as follows:

$$\tilde{H}_F = \text{const} + \sum_{\mathbf{k}} (\omega_0 + c_l J S a^2 k^2) \tilde{a}_{\mathbf{k}}^\dagger \tilde{a}_{\mathbf{k}}, \quad (2)$$

where $\omega_0 \equiv |\gamma| \mu_0 H_0$ is the ferromagnetic resonance frequency (on the order of a gigahertz) corresponding to the

uniform ($\mathbf{k} = \mathbf{0}$) magnon mode, a is the lattice constant, S is the spin, c_l is a factor that depends on the lattice considered, and $\tilde{a}_{\mathbf{k}}$ denotes the annihilation operator for a magnon with wave vector \mathbf{k} . The magnons here have unit spin, as each of them reduces the total spin in the ferromagnet by that amount [43]. The boundary conditions for small magnets result in a discrete magnon spectrum [44]. This leads to discrete allowed values of the wave vector \mathbf{k} , leaving the Hamiltonian unchanged otherwise. Furthermore, \mathbf{k} then labels standing waves instead of traveling waves. For typical values of J , spatial dimensions in the micrometer range result in magnon energies differing by a few gigahertz. Hence, we consider only the $\mathbf{k} = \mathbf{0}$ mode henceforth, denoting \tilde{a}_0 simply as \tilde{a} . We may disregard the higher modes, as we exploit coherent resonant interactions in this study.

As depicted in Fig. 1(a), the confined electron gas that becomes a spin qubit is interfaced directly with the ferromagnet to enable exchange coupling [45–48]:

$$\tilde{H}_{\text{int}} = J_{\text{int}} \sum_l \tilde{\mathbf{S}}_l \cdot \tilde{\mathbf{s}}_l, \quad (3)$$

where J_{int} parameterizes the interfacial exchange interaction, $\tilde{\mathbf{s}}_l$ denotes the spin operator of the spin-qubit electronic state at site l , and l runs over the interfacial sites. In terms of the relevant eigenmodes, the interfacial interaction is simplified to

$$\tilde{H}_{\text{int}} = g (\tilde{a}^\dagger \tilde{\sigma}_- + \tilde{a} \tilde{\sigma}_+), \quad (4)$$

where $g = J_{\text{int}} N_{\text{int}} |\psi|^2 \sqrt{S/(2N_F)}$, with N_{int} being the number of interfacial sites, $|\psi|^2$ the spin-qubit electron probability averaged over the interface, and N_F the total number of sites in the ferromagnet. The operators

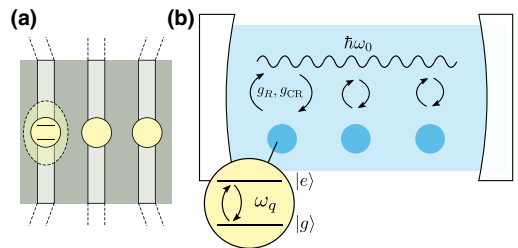


FIG. 1. Schematic depiction of three spin qubits exchange-coupled to one magnon mode. (a) Semiconducting wires hosting the localized electronic states that constitute the spin qubit are deposited on top of a thin insulating ferromagnet layer. A direct contact enables strong interfacial exchange coupling. (b) The corresponding anisotropic QRM. Three qubits interact with a single magnonic mode via controllably strong rotating (g_R) and counter-rotating (g_{CR}) terms [Eq. (9)].

$\tilde{\sigma}_{+,-} = (\tilde{\sigma}_x \pm i\tilde{\sigma}_y)/2$ excite or relax the spin qubit, which is further described via

$$\tilde{H}_q = \frac{\omega_q}{2} \tilde{\sigma}_z. \quad (5)$$

Thus, our total Hamiltonian becomes

$$\tilde{H}_1 = \tilde{H}_F + \tilde{H}_q + \tilde{H}_{\text{int}}, \quad (6)$$

where $\tilde{H}_F = \omega_0 \tilde{a}^\dagger \tilde{a}$, and the other contributions are given by Eqs. (4) and (5).

Our system thus realizes the Jaynes-Cummings Hamiltonian [Eq. (6)], which conserves the total number of excitations. This is a direct consequence of spin conservation, afforded by the exchange coupling in our system. A spin-1 magnon can be absorbed by a spin qubit, flipping the latter from its spin-(-1/2) to its spin-(+1/2) state. The same transition in the spin qubit, however, cannot emit a magnon. This is in contrast to the case of dipolar coupling between a spin qubit and a ferromagnet [7,41,48–50], which does not necessarily conserve spin. Further, as numerically estimated below, on account of exchange being a much stronger interaction, the effective coupling g in our system can exceed the magnon frequency ω_0 , thereby covering the full coupling range from weak to deep-strong [51–53]. Nonclassical behavior is typically manifested when one starts with ultrastrong couplings $g/\omega_0 > 0.1$ [51,54,55].

We consider the ferromagnet to be isotropic thus far. However, such films manifest a strong shape anisotropy, in addition to potential magnetocrystalline anisotropies [41]. We now account for these effects by including the single-ion anisotropy contribution, parameterized via $K_{x,y,z}$:

$$\tilde{H}_{\text{an}} = \sum_i K_x (\tilde{S}_{ix})^2 + K_y (\tilde{S}_{iy})^2 + K_z (\tilde{S}_{iz})^2.$$

Our assumed general form for the anisotropy allows us to capture all possible contributions to the uniform magnon-mode Hamiltonian and provides design principles for choosing the right material. The specific cases of shape anisotropy [34,47] and magnetocrystalline anisotropy in specific materials [56] are adequately captured by our general considerations, and have been detailed elsewhere [34,47,56]. If we retain only the uniform mode, the anisotropy contribution above results in the following magnon Hamiltonian:

$$\tilde{H}_F = A \tilde{a}^\dagger \tilde{a} + B (\tilde{a}^2 + \tilde{a}^{\dagger 2}), \quad (7)$$

where $A \equiv |\gamma| \mu_0 H_0 + K_x S + K_y S - 2K_z S$ and $B \equiv S(K_x - K_y)/2$. For typical physical systems, both A and B are in the gigahertz regime and are determined via the applied field and the anisotropies as delineated by the

expressions presented above. The ensuing Hamiltonian, Eq. (7), possesses squeezing terms proportional to B , which, unlike in the case of light, result from the magnet trying to minimize its ground-state energy while respecting the Heisenberg uncertainty principle [35]. The new eigenmode, dubbed a squeezed magnon [34], is obtained via a Bogoliubov transform $\tilde{a} = \cosh r \tilde{\alpha} + \sinh r \tilde{\alpha}^\dagger$, resulting in

$$\tilde{H}_F = \omega_0 \tilde{\alpha}^\dagger \tilde{\alpha}, \quad (8)$$

where we continue to denote the eigenmode energy as ω_0 , and we now have $\omega_0 = \sqrt{A^2 - 4B^2}$. Further, the squeeze parameter r is governed by the relation $\sinh r = -2B/\sqrt{(A + \omega_0)^2 - 4B^2}$. The stability of the ground state requires $\omega_0 > 0$ and $(A + \omega_0)^2 > 4B^2$. Thus, while the physical system in question allows values of A and B outside this domain, our assumption of a uniformly ordered ground state becomes invalid in that case. We confine our analysis to the case of a sufficiently large applied field H_0 such that the system harbors a uniformly ordered ground state. The limit of a divergent squeezing r is nevertheless within the domain of applicability. A detailed analysis of squeezing resulting from shape anisotropy shows it to be a strong effect [34,47], with $\sinh r$ being of the order of unity for typical experiments. It can be much larger for small applied fields, or when the magnet is close to a ground-state instability, or when a magnet with strong magnetocrystalline anisotropy is chosen. Further, the analysis above shows that breaking the symmetry in the plane transverse to the equilibrium spin order yields a squeezing effect, while a uniaxial anisotropy does not contribute to it. In the new eigenbasis, we obtain

$$\tilde{H}_{\text{int}} = g_R (\tilde{\alpha}^\dagger \tilde{\sigma}_- + \tilde{\alpha} \tilde{\sigma}_+) + g_{\text{CR}} (\tilde{\alpha}^\dagger \tilde{\sigma}_+ + \tilde{\alpha} \tilde{\sigma}_-), \quad (9)$$

where $g_R = g \cosh r$ and $g_{\text{CR}} = g \sinh r$. The interaction now has both rotating (proportional to g_R) and counter-rotating (proportional to g_{CR}) terms [Fig. 1(b)].

Our system can be analyzed in terms of two different bases: using a spin-1 magnon (represented by \tilde{a}) or a squeezed magnon ($\tilde{\alpha}$). The latter is the eigenmode and comprises a superposition of odd-magnon-number states [Fig. 2(a)] [34,35,57,58]. Since a spin-1 magnon is associated with a physical spin flip in the magnet [42], the interaction in Eq. (4) still comprises absorption and emission of magnons (\tilde{a}) accompanied by transitions in the qubit. On the other hand, in the eigenbasis, the qubit is now interacting with a new bosonic eigenmode, the squeezed magnon ($\tilde{\alpha}$), via an interaction that includes rotating and counter-rotating terms [Eq. (9)]. Therefore, in the eigenbasis, our system accomplishes an anisotropic QRM [4,5] [Fig. 1(b) and Eqs. (5), (6), (8), and (9)]. The squeeze parameter r , tunable via the applied field and the anisotropies [59], further enhances the coupling strength and controls the relative importance of the rotating and counter-rotating terms: $g_R = g \cosh r$ and $g_{\text{CR}} = g \sinh r$.

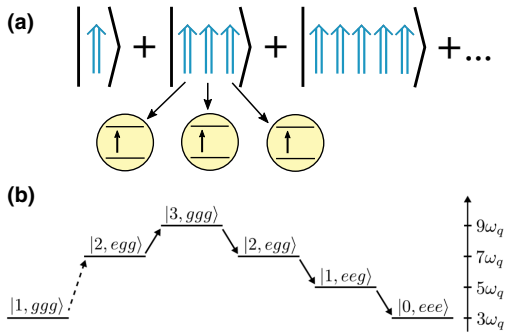


FIG. 2. Schematic depiction of the transition $|1, ggg\rangle \rightarrow |0, eee\rangle$. (a) The squeezed magnon comprises a superposition of odd-magnon-number states. This composite nature enables its absorption by an odd number of qubits. We focus on the case of three qubits. (b) An example pathway that takes the system from containing one squeezed magnon and three ground-state qubits ($|1, ggg\rangle$) to zero squeezed magnons and three excited qubits ($|0, eee\rangle$) via a series of virtual states. The first transition is effected by a CRT and is indicated by a dashed arrow. The right scale indicates the state energy, assuming $\omega_0 = 3\omega_q$.

III. ONE MAGNONIC MODE COUPLED TO THREE QUBITS

We now exploit the squeezed and composite nature of the magnonic eigenmode to generate useful entangled states [35]. As depicted in Fig. 2(a), the composite nature of the squeezed magnon should enable joint excitation of an odd number of qubits. Considering the paramount importance of generating such three-qubit GHZ states [29] for Shor’s error-correction code [26], we consider three qubits coupled to the same squeezed-magnon eigenmode:

$$\tilde{H}_3 = \tilde{H}_F + \sum_{n=1,2,3} \left(\tilde{H}_q^n + \tilde{H}_{\text{int}}^n \right), \quad (10)$$

with the individual contributions expressed via Eqs. (5), (8), and (9). For simplicity, we assume the three qubits and their couplings with the magnet to be identical. The qualitative physics is unaffected by asymmetries among the three qubits, which are detailed in Appendix B. Henceforth, we analyze the problem in its eigenbasis, employing a methodology consistent with a previous investigation of joint photon absorption [60].

We are interested in jointly exciting the three qubits using a single squeezed-magnon eigenmode, a transition denoted as $|1, ggg\rangle \rightarrow |0, eee\rangle$. To gain physical insight, we first analyze this transition within the perturbation-theory framework detailed in Appendix B. While the transition is not possible via a direct process [first order in the interaction Eq. (9)], it can be accomplished via a series of virtual states. As the transition requires an increase in

the total excitation number by 2, at least one of the virtual processes needs to be effected via CRTs, thus requiring a nonzero squeezing r in our system. The shortest path to effecting the transition consists of three virtual processes, but its amplitude is canceled exactly by a complementary path, as detailed in Appendix B. Hence, the lowest nonvanishing order for accomplishing this transition is 5, with an example pathway being depicted in Fig. 2(b) [61]. As detailed in Appendix B, several such paths contribute to the overall transition amplitude. The energy-conservation requirement on the initial and final states necessitates $\omega_0 \approx 3\omega_q$.

Guided by intuition from the perturbative analysis, we now study the system [Eq. (10)] numerically using the QuTiP package [62,63]. Unless stated otherwise, and for simplicity, we employ $g_R = g_{CR} = 0.1\omega_q$ in our analysis. A numerical diagonalization of the total Hamiltonian in Eq. (10) yields the energy spectrum, as depicted in Fig. 3(a). To understand it, let us first consider the simpler case of zero qubit-magnon coupling. In that case, the spectrum should contain eight (2^3) flat curves, corresponding to the different excited qubits and zero squeezed-magnon occupation. Two triplets of these overlap, resulting in four visually distinct flat curves. The same three-qubit spectrum combined with N squeezed magnons yields the same four visually distinct curves, now with a slope of N . Let us turn on the qubit-magnon coupling now. For the small but finite coupling considered in Fig. 3(a), we see the typical one-excitation Rabi splitting around $\omega_0 \approx \omega_q$ that results from a direct process. Around $\omega_0 \approx 2\omega_q$, we see crossings between different levels [64]. A coupling here is forbidden, as only an odd number of qubits can be excited by one squeezed magnon [Fig. 2(a)]. The apparent crossing around $\omega_0 \approx 3\omega_q$ is in fact an anticrossing, manifesting a small Rabi splitting between the states $|1, ggg\rangle$ and $|0, eee\rangle$ [see Fig. 3(b)]. This is the transition of interest, and the effective coupling responsible for it can be expressed as

$$\tilde{H}_{\text{eff}} = g_{\text{eff}} (|1, ggg\rangle \langle 0, eee| + |0, eee\rangle \langle 1, ggg|), \quad (11)$$

where $g_{\text{eff}} = (g_{CR}g_R^4 - 0.3g_{CR}^3g_R^2)/\omega_q^4$ is obtained by fitting (almost perfectly) its $g_{R,CR}$ dependence predicted by the perturbative analysis to the Rabi splittings obtained via numerical diagonalization. In carrying out this analysis, we numerically find the resonance condition, which occurs around $\omega_0 \approx 3\omega_q$, and evaluate the Rabi splitting. Hence, the expression for g_{eff} above is valid for $\omega_0 \approx 3\omega_q$. The comparison between the squeezed-magnon occupation, the single-qubit excitation, and the three-qubit correlations plotted in Fig. 3(c) for Rabi oscillations around $\omega_0 \approx 3\omega_q$ confirms the joint nature of the three-qubit excitation.

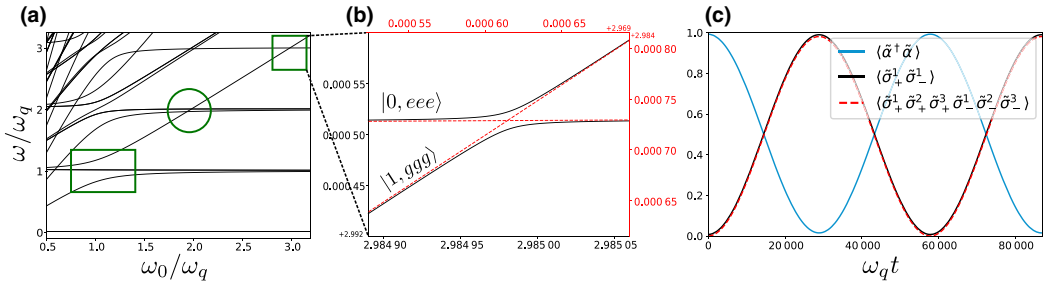


FIG. 3. Numerically evaluated spectrum and dynamics of three qubits coupled to one magnonic mode [Eq. (10)]. (a) Energy spectrum evaluated assuming $g_R = g_{CR} = 0.1\omega_q$. The green rectangle encloses the typical one-excitation anticrossing ($\omega_0 \approx \omega_q$). The circle highlights crossings around $\omega_0 \approx 2\omega_q$, as only an odd number of qubits can be excited [Fig. 2(a)]. The square emphasizes the weaker three-excitation anticrossing around $\omega_0 \approx 3\omega_q$, which results from finite squeezing and the resulting CRTs. (b) Enlargement of the three-excitation anticrossing that stems from the transition depicted in Fig. 2. The red dashed lines depict the spectrum evaluated assuming $g_{CR} = 0$, leaving the rest unchanged. (c) Zero-detuning system dynamics around $\omega_0 \approx 3\omega_q$ with the initial state $|1, ggg\rangle$. The squeezed-magnon occupation (blue solid line) and single-qubit excitation (black solid line) manifest typical Rabi oscillations. The nearly perfect overlap between the single-qubit and three-qubit (red dashed line) correlations confirms the joint nature of the three-qubit excitation in these Rabi oscillations.

IV. DISCUSSION

Our system enables the transition $|1, ggg\rangle \rightarrow |0, eee\rangle$ with an effective coupling strength g_{eff} [Eq. (11)], or equivalently the Rabi frequency, that is tunable via the magnon squeezing: $g_{CR} = g \sinh r$. Bringing the system into resonance to enable a Rabi oscillation for a fraction of a cycle can be exploited to robustly generate three-qubit GHZ and related entangled states, $(|ggg\rangle \pm |eee\rangle)/\sqrt{2}$. Convenient generation of these states is central to Shor's error-correction code [26] and thus of great value in achieving fault-tolerant quantum computing. Such three-qubit entangled states can be generated on contemporary quantum computers via sequential one- and two-qubit gate operations [65–67]. In theory, and for ideal gate operations, our suggested method appears not to offer any advantage over such sequential gate operations executed on state-of-the-art quantum computers. However, each two-qubit gate operation entails applying an exact pulse that, in turn, depends on the qubit frequencies and their coupling to the bosonic mode. Further, such sequential operations necessarily create an asymmetry between the three qubits, since one of them needs to be addressed in the end. In the presence of decoherence, this can compromise the quality of the GHZ states achieved in practice. Finally, sequential operations are bound to take a longer time to generate the desired GHZ state, which reduces the time available for other computations, given that decoherence limits the total time available. In contrast, capitalizing on energy and spin conservation, our proposed single-pulse method is intrinsically robust against any qubit asymmetries and perfectly synchronizes the excitation of the three qubits. This resilience of our suggested method comes because there is a unique resonance condition around

$\omega_0 \approx \omega_{q1} + \omega_{q2} + \omega_{q3}$ for the single pulse needed. Since the three qubits need to absorb the energy of one squeezed magnon together, their GHZ-state generation is automatically synchronized.

Being a fifth-order process, g_{eff} is evaluated to be small for the parameters employed in our analysis above ($g_R = g_{CR} = 0.1\omega_q$). However, notwithstanding our choice of parameters, which is motivated by a comparison with perturbation theory, the proposed system can achieve very high bare couplings g [Eq. (9)], $g_R, g_{CR} > \omega_q$, such that the higher-order processes are not diminished and g_{eff} becomes large. An increase in the coupling strength and the relevance of higher-order processes, however, has its trade-offs. While some of these higher-order processes merely renormalize the qubit and magnon frequencies, thereby not affecting the phenomena discussed here, others can bring the independent existence of the magnon and qubit subsystems into question. Thus, depending on the desired application, an optimal value for g_{eff} needs to be chosen. The key benefit of the proposed system is the wide range of g_{eff} that it admits. Spin-pumping experiments yield interfacial exchange couplings [Eq. (3)] $J_{\text{int}} \approx 10$ meV between various (insulating) magnets and adjacent metals [68–70]. Assuming the qubit wave function to be localized in five monolayers below an equally thin ferromagnet and an interface comprising 100 sites, we obtain a bare coupling rate [Eq. (4)] $g \approx 0.005J_{\text{int}} \approx 80$ GHz, significantly larger than typical spin-qubit and uniform-magnon-mode frequencies.

In general, one can design a system (e.g., by choosing the ferromagnet thickness) to have a desired bare coupling, and exploit the squeezing-mediated tunability *in situ*. The latter effect, although an interesting and useful property of

the system, may not be needed in a specific application, given that deep-strong coupling could be achieved without this enhancement. In particular, our example of choice, the generation of GHZ states, need not exploit this enhancement effect.

Our proposal for leveraging intrinsic magnon squeezing in generating entanglement via a coherent process is complementary to previous incoherent interaction-based proposals [36,48,71,72]. The latter typically necessitate diabatic decoupling of qubits from the magnet after achieving an entangled state. Our proposal thus uncovers an unexplored and experimentally favorable avenue for exploiting the squeezing intrinsic to magnets.

V. SUMMARY

We demonstrate that a magnon–spin-qubit ensemble can realize an anisotropic quantum Rabi model with coupling strengths that make it feasible to reach the deep-strong regime. This system is shown to capitalize on various unique features of squeezed magnons hosted by magnets. These include squeezing-mediated coupling enhancement, tunable anisotropy of the Rabi model, and convenient synchronous entanglement of three qubits. Thus, the magnon–spin-qubit ensemble provides a promising platform for investigating phenomena beyond the ultrastrong regime and implementing error-correction codes.

ACKNOWLEDGMENTS

We thank Wolfgang Belzig, Tim Ludwig, and Rembert Duine for valuable discussions. We acknowledge financial support from the Research Council of Norway through its Centers of Excellence funding scheme, Project 262633, “QuSpin,” and the Spanish Ministry for Science and Innovation, AEI Grant No. CEX2018-000805-M (through the “Maria de Maeztu” Program for Units of Excellence in R&D).

APPENDIX A: SYSTEM HAMILTONIAN

In this section, we derive the Hamiltonian describing our magnon–spin-qubit ensemble. First, starting with the ferromagnetic spin Hamiltonian, we obtain a description of the magnonic mode. Then, we specify the spin qubit. Finally, we derive the interfacial exchange-mediated interaction between the two subsystems.

1. Magnonic mode

Taking into account the Zeeman energy, ferromagnetic exchange, and a general anisotropy, the ferromagnet is

described via the spin Hamiltonian

$$\begin{aligned} \tilde{H}_F = & |\gamma| \mu_0 H_0 \sum_i \tilde{S}_{iz} - J \sum_{(i,j)} \tilde{\mathbf{S}}_i \cdot \tilde{\mathbf{S}}_j \\ & + \sum_i \left[K_x \left(\tilde{S}_{ix} \right)^2 + K_y \left(\tilde{S}_{iy} \right)^2 + K_z \left(\tilde{S}_{iz} \right)^2 \right], \end{aligned} \quad (\text{A1})$$

where the applied magnetic field is $H_0 \hat{\mathbf{z}}$, γ (< 0) is the gyromagnetic ratio, J (> 0) is the exchange energy, (i, j) denotes a sum over nearest neighbors, and $K_{x,y,z}$ parameterize the magnetic anisotropy. While the anisotropy may arise due to dipolar interactions or magnetocrystalline single-ion anisotropies, our assumed general form encompasses all such symmetry-allowed contributions that can contribute to determining the uniform $\mathbf{k} = \mathbf{0}$ magnon mode [47].

Assuming the Zeeman energy to dominate over the anisotropy, we consider all spins to point along $-\hat{\mathbf{z}}$ in the magnetic ground state. We may express the spin Hamiltonian in Eq. (A1) in terms of bosonic magnons via the Holstein-Primakoff transformation [42] corresponding to our spin ground state,

$$\tilde{S}_{j+} = \sqrt{2S} \tilde{a}_j^\dagger, \quad (\text{A2})$$

$$\tilde{S}_{j-} = \sqrt{2S} \tilde{a}_j, \quad (\text{A3})$$

$$\tilde{S}_{jz} = -S + \tilde{a}_j^\dagger \tilde{a}_j, \quad (\text{A4})$$

where $\tilde{S}_{j\pm} \equiv \tilde{S}_{jx} \pm i\tilde{S}_{jy}$, \tilde{a}_j is the magnon annihilation operator at position j , and S is the spin magnitude. In addition, we need the Fourier relations

$$\tilde{a}_j = \frac{1}{\sqrt{N_F}} \sum_{\mathbf{k}} \tilde{a}_{\mathbf{k}} e^{-i\mathbf{k}\cdot\mathbf{r}_j}, \quad (\text{A5})$$

$$\tilde{a}_{\mathbf{k}} = \frac{1}{\sqrt{N_F}} \sum_j \tilde{a}_j e^{i\mathbf{k}\cdot\mathbf{r}_j}, \quad (\text{A6})$$

where N_F is the total number of sites in the ferromagnet and $\tilde{a}_{\mathbf{k}}$ is the annihilation operator for the magnon mode with wave vector \mathbf{k} . Employing these Holstein-Primakoff and Fourier transformations in Eq. (A1), we obtain the magnonic Hamiltonian

$$\tilde{H}_F = \text{const} + \sum_{\mathbf{k}} \left[A_{\mathbf{k}} \tilde{a}_{\mathbf{k}}^\dagger \tilde{a}_{\mathbf{k}} + B_{\mathbf{k}} \left(\tilde{a}_{\mathbf{k}}^\dagger \tilde{a}_{-\mathbf{k}}^\dagger + \tilde{a}_{\mathbf{k}} \tilde{a}_{-\mathbf{k}} \right) \right], \quad (\text{A7})$$

where $A_{\mathbf{k}} \equiv |\gamma| \mu_0 H_0 + K_x S + K_y S - 2K_z S + 4JS [3 - (\cos k_x a + \cos k_y a + \cos k_z a)]$ and $B_{\mathbf{k}} \equiv S(K_x - K_y)/2$. In obtaining the exchange contribution to $A_{\mathbf{k}}$, we assume

a simple cubic lattice with lattice constant a . In the long-wavelength limit, i.e., $ak_{x,y,z} \ll 1$, the cosines can be approximated by parabolas.

As discussed in the main text, we retain only the uniform mode corresponding to $\mathbf{k} = \mathbf{0}$ in our consideration of the magnon–spin–qubit system. This is justifiable because, for small dimensions of the magnet considered here, the allowed wave vectors \mathbf{k} correspond to magnon energies separated from the lowest uniform mode (with an energy of a few gigahertz) by at least several gigahertz. Thus, we may disregard such high-energy modes when considering coherent resonant interactions, as we do in this paper. Further diagonalization of Eq. (A7), considering only the uniform mode, via a Bogoliubov transformation is described in the main text.

2. The spin qubit

We consider our spin qubit to comprise a confined electronic orbital that admits spin-up and spin-down states. Considering a lifting of the spin degeneracy by, for example, an applied magnetic field, the spin-qubit Hamiltonian may be expressed as

$$\tilde{H}_q = \text{const} + \frac{\omega_q}{2} (\tilde{c}_\uparrow^\dagger \tilde{c}_\uparrow - \tilde{c}_\downarrow^\dagger \tilde{c}_\downarrow), \quad (\text{A8})$$

where, considering a negative gyromagnetic ratio and an applied magnetic field along $\hat{\mathbf{z}}$, ω_q (> 0) is the qubit splitting. We further introduce the notation

$$\tilde{\sigma}_z \equiv \begin{pmatrix} \tilde{c}_\uparrow^\dagger & \tilde{c}_\downarrow^\dagger \\ 0 & -1 \end{pmatrix} \begin{pmatrix} \tilde{c}_\uparrow \\ \tilde{c}_\downarrow \end{pmatrix} \equiv \underline{\tilde{c}}^\dagger \underline{\sigma}_z \underline{\tilde{c}}, \quad (\text{A9})$$

where an underline identifies a matrix. With this notation, and dropping the spin-independent constant, the spin-qubit Hamiltonian is expressed as

$$\tilde{H}_q = \frac{\omega_q}{2} \underline{\tilde{\sigma}}_z. \quad (\text{A10})$$

With the notation defined in Eq. (A9), $\tilde{\sigma}_+ \equiv (\tilde{\sigma}_x + i\tilde{\sigma}_y)/2$ becomes the qubit excitation operator, while $\tilde{\sigma}_- \equiv (\tilde{\sigma}_x - i\tilde{\sigma}_y)/2$ is the qubit relaxation operator.

3. Exchange coupling

The magnon and spin qubit are considered to be coupled via an interfacial exchange interaction parameterized via J_{int} [45–47],

$$\tilde{H}_{\text{int}} = J_{\text{int}} \sum_l \tilde{\mathbf{S}}_l \cdot \tilde{\mathbf{s}}_l, \quad (\text{A11})$$

where l labels the interfacial sites, $\tilde{\mathbf{S}}$ denotes the ferromagnetic spin operator, and $\tilde{\mathbf{s}}$ represents the spin of the electronic states that comprise the qubit. We wish to

express the interfacial Hamiltonian in Eq. (A11) in terms of the magnon and qubit operators. To this end, $\tilde{\mathbf{S}}_l$ can be expressed via magnon operators using the Holstein-Primakoff and Fourier transforms [Eqs. (A2)–(A6)] already described above. We now discuss the representation of $\tilde{\mathbf{s}}_l$ in terms of the qubit operators $\tilde{\sigma}_{x,y,z}$ [Eq. (A9)].

Following quantum-field-theory notation for discrete sites, the spin operator at a given position \mathbf{r} can be expressed in terms of ladder operators at the same position:

$$\tilde{\mathbf{s}}(\mathbf{r}) = \frac{1}{2} \sum_{s,s'=\uparrow,\downarrow} \tilde{\Psi}_s^\dagger(\mathbf{r}) \underline{\sigma}_{ss'} \tilde{\Psi}_{s'}(\mathbf{r}), \quad (\text{A12})$$

where $\underline{\sigma} = \sigma_x \hat{\mathbf{x}} + \sigma_y \hat{\mathbf{y}} + \sigma_z \hat{\mathbf{z}}$, with $\sigma_{x,y,z}$ being the Pauli matrices. The local ladder operators can be represented further in terms of the complete set of eigenstates labeled via an orbital index t :

$$\tilde{\Psi}_s(\mathbf{r}) = \sum_t \psi_t(\mathbf{r}) \tilde{c}_{ts}, \quad (\text{A13})$$

where $\psi(\mathbf{r})$ is the spatial wave function of the orbital and \tilde{c}_{ts} are the ladder operators for each spin-resolved orbital. Employing this relation, Eq. (A12) becomes

$$\tilde{\mathbf{s}}(\mathbf{r}) = \frac{1}{2} \sum_{s,s',t,t'} \psi_t^*(\mathbf{r}) \psi_{t'}(\mathbf{r}) \underline{\sigma}_{ss'} \tilde{c}_{ts}^\dagger \tilde{c}_{t's'}. \quad (\text{A14})$$

Since, for our spin qubit, we are interested in only one orbital out of the complete set, we allow only one value of t and thus drop the index t in accordance with our previous considerations in Eq. (A8):

$$\tilde{\mathbf{s}}(\mathbf{r}) = \frac{1}{2} \sum_{s,s'} |\psi(\mathbf{r})|^2 \underline{\sigma}_{ss'} \tilde{c}_s^\dagger \tilde{c}_{s'}, \quad (\text{A15})$$

$$= \frac{|\psi(\mathbf{r})|^2}{2} \underline{\tilde{c}}^\dagger \underline{\sigma} \underline{\tilde{c}}, \quad (\text{A16})$$

$$\Rightarrow \tilde{\mathbf{s}}_l = \frac{|\psi_l|^2}{2} \underline{\tilde{c}}^\dagger \underline{\sigma} \underline{\tilde{c}}, \quad (\text{A17})$$

where ψ_l is the wave-function amplitude of the qubit orbital at position l .

The interfacial interaction in Eq. (A11) is now simplified to

$$\tilde{H}_{\text{int}S} = J_{\text{int}} \sum_l \left[\tilde{S}_{lz} \tilde{s}_{lz} + \frac{1}{2} (\tilde{S}_{l+} \tilde{s}_{l-} + \tilde{S}_{l-} \tilde{s}_{l+}) \right], \quad (\text{A18})$$

where $\tilde{S}_{l\pm} \equiv \tilde{S}_{lx} \pm i\tilde{S}_{ly}$ and $\tilde{s}_{l\pm} \equiv \tilde{s}_{lx} \pm i\tilde{s}_{ly}$. Employing Eq. (A17) together with Eqs. (A2)–(A6) and retaining only

the uniform magnon mode, the interfacial Hamiltonian is simplified to include two contributions:

$$\tilde{H}_{\text{int}} = \tilde{H}_{\text{int}1} + \tilde{H}_{\text{int}2}. \quad (\text{A19})$$

The first contribution is our desired magnon–spin-qubit exchange coupling,

$$\tilde{H}_{\text{int}1} = J_{\text{int}} N_{\text{int}} |\psi|^2 \sqrt{\frac{S}{2N_F}} (\tilde{\alpha}^\dagger \tilde{\sigma}_- + \tilde{\alpha} \tilde{\sigma}_+), \quad (\text{A20})$$

where N_{int} is the number of interfacial sites and $|\psi|^2 \equiv (\sum_l |\psi_l|^2) / N_{\text{int}}$ is the qubit electronic state wave function averaged over the interface. The second contribution,

$$\tilde{H}_{\text{int}2} = -\frac{S J_{\text{int}} N_{\text{int}} |\psi|^2}{2} \tilde{\sigma}_z, \quad (\text{A21})$$

renormalizes the spin-qubit energy and can be absorbed into ω_q [Eq. (A10)].

APPENDIX B: DERIVING AN EXPRESSION FOR THE EFFECTIVE COUPLING WITH PERTURBATION THEORY

Here we look at the Hamiltonian describing three qubits coupled to the same squeezed-magnon eigenmode, as described in the main text. We assume the interaction terms, \tilde{H}_{int}^n , to be small compared with the rest of the Hamiltonian, $\tilde{H}_0 = \omega_0 \tilde{\alpha}^\dagger \tilde{\alpha} + \sum_{n=1,2,3} (\omega_{qn}/2) \tilde{\sigma}_z^n$, and calculate the effective coupling g_{eff}^n between the two states $|1, ggg\rangle$ and $|0, eee\rangle$ using perturbation theory. The interaction term, \tilde{H}_{int}^n , is given by

$$\tilde{H}_{\text{int}}^n = g_{Rn} (\tilde{\alpha}^\dagger \tilde{\sigma}_-^n + \tilde{\alpha} \tilde{\sigma}_+^n) + g_{CRn} (\tilde{\alpha}^\dagger \tilde{\sigma}_+^n + \tilde{\alpha} \tilde{\sigma}_-^n). \quad (\text{B1})$$

The relevant virtual processes can be shown as paths from $|1, ggg\rangle$ (blue) to $|0, eee\rangle$ (red) on a grid of “number of magnon excitations” and “number of qubit excitations.” The rotating term (drawn as a full line) keeps the total number of excitations constant, while the counter-rotating term (drawn as a dotted line) changes the total number of excitations by two. The detailed expressions for each diagram are calculated using a diagrammatic approach presented in Ref. [73].

1. Third-order perturbation theory

We start by applying perturbation theory to third order. The two third-order diagrams are shown in Fig. 4. For general qubits, these two diagrams result in the effective coupling

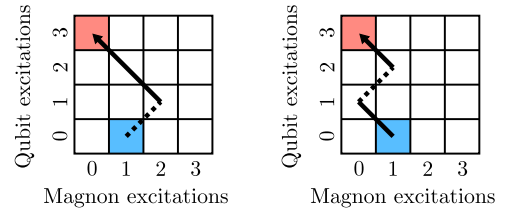


FIG. 4. Diagrams connecting $|1, ggg\rangle$ (blue) and $|0, eee\rangle$ (red) via virtual transitions to third order. Counter-rotating processes are represented by dashed lines.

$$g_{\text{eff}}^{(3)} = \sum_{\substack{i,j,k \\ i \neq j \neq k \neq i}} \left[\frac{2g_{CRi} g_{Rj} g_{Rk}}{(-\omega_0 - \omega_{qi})(-\omega_{qi} - \omega_{qj})} + \frac{g_{Ri} g_{CRj} g_{Rk}}{(\omega_0 - \omega_{qi})(-\omega_{qi} - \omega_{qj})} \right], \quad (\text{B2})$$

where the sum is over all qubit permutations.

If we assume that the qubits are identical ($g_{CRi} = g_{CR}$, $g_{Ri} = g_R$, $\omega_{qi} = \omega_q$), all qubit permutations are equivalent, and the sum can be carried out by counting qubit permutations:

$$g_{\text{eff}}^{(3)} = 3g_R^2 g_{CR} \frac{3\omega_q - \omega_0}{\omega_q (\omega_0^2 - \omega_q^2)}. \quad (\text{B3})$$

As we can see, the two paths cancel at resonance, i.e., $\omega_0 = 3\omega_q$. Moreover, it can be shown from Eq. (B2) that the third-order term cancels when $\omega_0 = \sum_i \omega_{qi}$. The result of pure third-order perturbation theory is therefore zero.

2. Fifth-order perturbation theory

Since the third-order result is zero and there are no fourth-order paths, we move on to fifth order by drawing all fifth-order paths from the initial state $|1, ggg\rangle$ (blue) to the state $|0, eee\rangle$ (red). We use the result that the third-order term cancels at resonance to note that pairs of diagrams

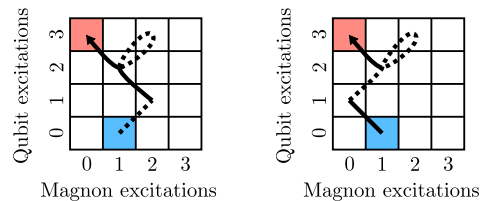


FIG. 5. Example of fifth-order diagrams that cancel if $\omega_0 = 3\omega_q$. Pairs of two third-order diagrams with an additional loop on a shared vertex that is not the initial vertex fully cancel at resonance. Counter-rotating terms are represented by dashed lines.

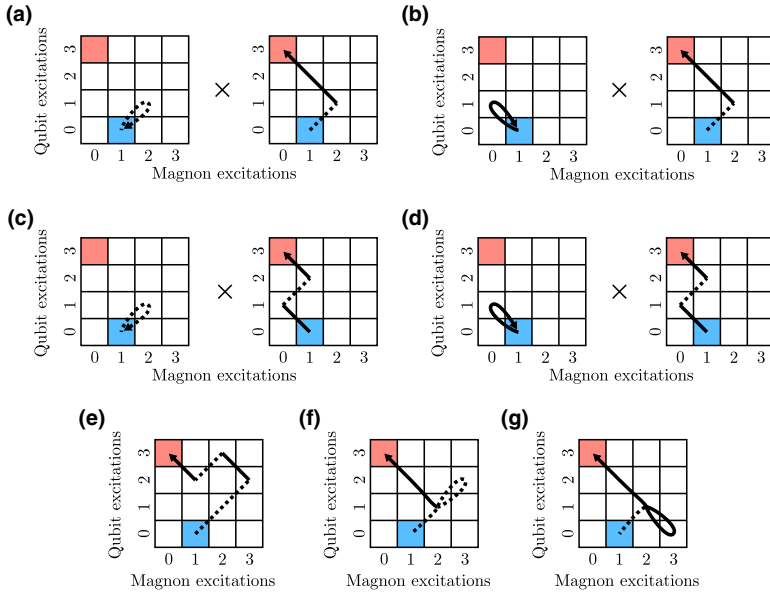


FIG. 6. Relevant diagrams that connect $|1, ggg\rangle$ (blue) and $|0, eee\rangle$ (red) via virtual transitions to fifth order. Counter-rotating terms are represented by dashed lines.

such as the ones in Fig. 5, i.e., the two third-order diagrams with an additional loop on a shared vertex that is not the initial vertex, also fully cancel at resonance.

All remaining diagrams are shown in Fig. 6. Diagrams (a) and (c) cancel partially but not fully, and give the contribution

$$g_{\text{eff}}^{(5a)} + g_{\text{eff}}^{(5c)} = \sum_{\substack{i,j,k,l \\ j \neq k \neq l \neq j}} \left[\left(\frac{2g_{\text{CR}i}^2}{(-\omega_0 - \omega_{qi})} \right) \left(\frac{2g_{\text{CR}j}g_{\text{R}k}g_{\text{R}l}}{(-\omega_0 - \omega_{qi})^2(-\omega_{qi} - \omega_{qj})} + \frac{g_{\text{R}j}g_{\text{CR}k}g_{\text{R}l}}{(\omega_0 - \omega_{qi})^2(-\omega_{qi} - \omega_{qj})} \right) \right]. \quad (\text{B4})$$

Similarly, for (b) and (d),

$$g_{\text{eff}}^{(5b)} + g_{\text{eff}}^{(5d)} = \sum_{\substack{i,j,k,l \\ j \neq k \neq l \neq j}} \left[\left(\frac{g_{\text{R}i}^2}{(\omega_0 - \omega_{qi})} \right) \left(\frac{2g_{\text{CR}j}g_{\text{R}k}g_{\text{R}l}}{(-\omega_0 - \omega_{qi})^2(-\omega_{qi} - \omega_{qj})} + \frac{g_{\text{R}j}g_{\text{CR}k}g_{\text{R}l}}{(\omega_0 - \omega_{qi})^2(-\omega_{qi} - \omega_{qj})} \right) \right]. \quad (\text{B5})$$

The contributions from diagrams (e), (f), and (g) are

$$g_{\text{eff}}^{(5e)} = \sum_{\substack{i,j,k,l \\ i \neq j \neq k \neq l}} \frac{6g_{\text{CR}i}g_{\text{CR}j}g_{\text{R}k}g_{\text{CR}l}g_{\text{R}l}}{(-\omega_0 - \omega_{qi})(-2\omega_0 - \omega_{qi} - \omega_{qj})(-\omega_0 - \sum_n \omega_{qn})(\omega_{ql} - \sum_n \omega_{qn})} \quad (\text{B6})$$

$$g_{\text{eff}}^{(5f)} = \sum_{\substack{i,j,k,l,m,n \\ i \neq j \neq k \neq l \\ l=i,j \\ m=l,k \\ n \neq m \quad n=l,k}} \frac{6g_{\text{CR}i}g_{\text{CR}j}g_{\text{CR}l}g_{\text{R}m}g_{\text{R}n}}{(-\omega_0 - \omega_{qi})(-2\omega_0 - \omega_{qi} - \omega_{qj})(-\omega_0 + \omega_{ql} + \omega_{qk} - \sum_p \omega_{qp})(\omega_{qn} - \sum_p \omega_{qp})}, \quad (\text{B7})$$

$$g_{\text{eff}}^{(5g)} = \sum_{\substack{i,j,k,l \\ j \neq k \neq l \neq j}} \frac{6g_{\text{CR}i}g_{\text{R}i}g_{\text{R}j}g_{\text{R}k}g_{\text{R}l}}{(-\omega_0 - \omega_{qi})(-2\omega_0)(-\omega_0 - \omega_{qj})(-\omega_{qj} - \omega_{qk})}. \quad (\text{B8})$$

If we now assume that we are at resonance and that the qubits are identical ($g_{CRi} = g_{CR}$, $g_{Ri} = g_R$, $\omega_{qi} = \omega_q$, and $\omega_0 = 3\omega_q$), the sums can again be carried out by counting qubit permutations. The total effective coupling to fifth order is then

$$g_{\text{eff}}^{(5)} = -\frac{9(3g_{CR}^3 g_R^2 - 8g_{CR} g_R^4)}{32\omega_q^4}. \quad (\text{B9})$$

3. Additional corrections

As we have seen, the third-order contribution to the effective coupling is zero when $\omega_0 = 3\omega_q$. However, if we are interested in the details of the (anti)crossing, there is an additional detail we need to consider. The perturbation causes the energy levels to shift, which causes the (anti)crossing to take place at a small shift away from $\omega_0 = 3\omega_q$.

By applying second-order perturbation theory (at $\omega_0 = 3\omega_q$) to the energies of the two relevant states, we find that the crossing takes place at

$$\omega_0 = 3\omega_q + \frac{3g_{CR}^2}{2\omega_q} - \frac{3g_R^2}{\omega_q}. \quad (\text{B10})$$

Inserting this into the third-order effective coupling, Eq. (B3), and keeping terms of up to fifth order in $g_{CR/R}$ leaves us with [74]

$$g_{\text{eff}}^{(3)'} = \frac{9(g_{CR}^3 g_R^2 - 2g_{CR} g_R^4)}{16\omega_q^4}, \quad (\text{B11})$$

where the prime indicates that the effective coupling is evaluated at the (anti)crossing.

- [1] I. I. Rabi, On the process of space quantization, *Phys. Rev.* **49**, 324 (1936).
- [2] I. I. Rabi, Space quantization in a gyrating magnetic field, *Phys. Rev.* **51**, 652 (1937).
- [3] D. Braak, Integrability of the Rabi Model, *Phys. Rev. Lett.* **107**, 100401 (2011).
- [4] Q.-T. Xie, S. Cui, J.-P. Cao, L. Amico, and H. Fan, Anisotropic Rabi Model, *Phys. Rev. X* **4**, 021046 (2014).
- [5] Q. Xie, H. Zhong, M. T. Batchelor, and C. Lee, The quantum Rabi model: Solution and dynamics, *J. Phys. A: Math. Theor.* **50**, 113001 (2017).
- [6] S. Wehner, D. Elkouss, and R. Hanson, Quantum internet: A vision for the road ahead, *Science* **362**, eaam9288 (2018).
- [7] M. Fukami, D. R. Candido, D. D. Awschalom, and M. E. Flatté, Opportunities for Long-Range Magnon-Mediated Entanglement of Spin Qubits via On- and Off-Resonant Coupling, *PRX Quantum* **2**, 040314 (2021).
- [8] D. D. Awschalom *et al.*, Quantum engineering with hybrid magnonics systems and materials, *IEEE Trans. Quantum Eng.* **2**, 1 (2021).
- [9] G. Burkard, M. J. Gullans, X. Mi, and J. R. Petta, Superconductor–semiconductor hybrid-circuit quantum electrodynamics, *Nat. Rev. Phys.* **2**, 129 (2020), arXiv:1905.01155.
- [10] A. Laucht *et al.*, Roadmap on quantum nanotechnologies, *Nanotechnology* **32**, 162003 (2021), arXiv:2101.07882.
- [11] C. Gerry and P. Knight, *Introductory Quantum Optics* (Cambridge University Press, New York, 2004).
- [12] D. F. Walls, Squeezed states of light, *Nature* **306**, 141 (1983).
- [13] W. Qin, A. Miranowicz, P.-B. Li, X.-Y. Lü, J. Q. You, and F. Nori, Exponentially Enhanced Light-Matter Interaction, Cooperativities, and Steady-State Entanglement Using Parametric Amplification, *Phys. Rev. Lett.* **120**, 093601 (2018).
- [14] C. Leroux, L. C. G. Govia, and A. A. Clerk, Enhancing Cavity Quantum Electrodynamics via Antisqueezing: Synthetic Ultrastrong Coupling, *Phys. Rev. Lett.* **120**, 093602 (2018).
- [15] X.-Y. Lü, Y. Wu, J. R. Johansson, H. Jing, J. Zhang, and F. Nori, Squeezed Optomechanics with Phase-Matched Amplification and Dissipation, *Phys. Rev. Lett.* **114**, 093602 (2015).
- [16] Y.-H. Chen, W. Qin, and F. Nori, Fast and high-fidelity generation of steady-state entanglement using pulse modulation and parametric amplification, *Phys. Rev. A* **100**, 012339 (2019).
- [17] Y.-H. Chen, W. Qin, X. Wang, A. Miranowicz, and F. Nori, Shortcuts to Adiabaticity for the Quantum Rabi Model: Efficient Generation of Giant Entangled Cat States via Parametric Amplification, *Phys. Rev. Lett.* **126**, 023602 (2021).
- [18] S. C. Burd, R. Srinivas, H. M. Knaack, W. Ge, A. C. Wilson, D. J. Wineland, D. Leibfried, J. J. Bollinger, D. T. C. Allcock, and D. H. Slichter, Quantum amplification of boson-mediated interactions, *Nat. Phys.* **17**, 898 (2021).
- [19] G. Wang, R. Xiao, H. Z. Shen, C. Sun, and K. Xue, Simulating anisotropic quantum Rabi model via frequency modulation, *Sci. Rep.* **9**, 4569 (2019).
- [20] C. Sánchez Muñoz, A. Frisk Kockum, A. Miranowicz, and F. Nori, Simulating ultrastrong-coupling processes breaking parity conservation in Jaynes-Cummings systems, *Phys. Rev. A* **102**, 033716 (2020).
- [21] M. Russ and G. Burkard, Three-electron spin qubits, *J. Phys.: Condens. Matter* **29**, 393001 (2017).
- [22] A. Chatterjee, P. Stevenson, S. D. Franceschi, A. Morello, N. P. d. Leon, and F. Kuemmeth, Semiconductor qubits in practice, *Nat. Rev. Phys.* **3**, 157 (2021), arXiv:2005.06564.
- [23] L. M. K. Vandersypen and M. A. Eriksson, Quantum computing with semiconductor spins, *Phys. Today* **72**, 38 (2019).
- [24] D. Lachance-Quirion, Y. Tabuchi, A. Gloppe, K. Usami, and Y. Nakamura, Hybrid quantum systems based on magnonics, *Appl. Phys. Express* **12**, 070101 (2019).
- [25] C. Nayak, S. H. Simon, A. Stern, M. Freedman, and S. Das Sarma, Non-abelian anyons and topological quantum computation, *Rev. Mod. Phys.* **80**, 1083 (2008).
- [26] P. W. Shor, Scheme for reducing decoherence in quantum computer memory, *Phys. Rev. A* **52**, R2493 (1995).
- [27] B. M. Terhal, J. Conrad, and C. Vuillot, Towards scalable bosonic quantum error correction, *Quantum Sci. Technol.* **5**, 043001 (2020).

- [28] D. Gottesman, A. Kitaev, and J. Preskill, Encoding a qubit in an oscillator, *Phys. Rev. A* **64**, 012310 (2001).
- [29] D. M. Greenberger, M. A. Horne, and A. Zeilinger, Going beyond bell's theorem, [arXiv:0712.0921](https://arxiv.org/abs/0712.0921) [quant-ph] (2007).
- [30] T. Aoki, G. Takahashi, T. Kajiyu, J.-i. Yoshikawa, S. L. Braunstein, P. van Loock, and A. Furusawa, Quantum error correction beyond qubits, *Nat. Phys.* **5**, 541 (2009).
- [31] R. Schnabel, Squeezed states of light and their applications in laser interferometers, *Phys. Rep.* **684**, 1 (2017).
- [32] Z. Y. Ou, S. F. Pereira, H. J. Kimble, and K. C. Peng, Realization of the Einstein-Podolsky-Rosen Paradox for Continuous Variables, *Phys. Rev. Lett.* **68**, 3663 (1992).
- [33] G. J. Milburn and S. L. Braunstein, Quantum teleportation with squeezed vacuum states, *Phys. Rev. A* **60**, 937 (1999).
- [34] A. Kamra and W. Belzig, Super-Poissonian Shot Noise of Squeezed-Magnon Mediated Spin Transport, *Phys. Rev. Lett.* **116**, 146601 (2016).
- [35] A. Kamra, W. Belzig, and A. Brataas, Magnon-squeezing as a niche of quantum magnonics, *Appl. Phys. Lett.* **117**, 090501 (2020).
- [36] J. Zou, S. K. Kim, and Y. Tserkovnyak, Tuning entanglement by squeezing magnons in anisotropic magnets, *Phys. Rev. B* **101**, 014416 (2020).
- [37] S. Sharma, V. A. S. V. Bittencourt, A. D. Karenowska, and S. V. Kusminskiy, Spin cat states in ferromagnetic insulators, *Phys. Rev. B* **103**, L100403 (2021).
- [38] Y.-P. Wang and C.-M. Hu, Dissipative couplings in cavity magnonics, *J. Appl. Phys.* **127**, 130901 (2020).
- [39] Y. Tabuchi, S. Ishino, A. Noguchi, T. Ishikawa, R. Yamazaki, K. Usami, and Y. Nakamura, Coherent coupling between a ferromagnetic magnon and a superconducting qubit, *Science* **349**, 405 (2015).
- [40] D. Loss and D. P. DiVincenzo, Quantum computation with quantum dots, *Phys. Rev. A* **57**, 120 (1998).
- [41] A. Akhiezer, V. Bar'iakhtar, and S. Peletminski, *Spin Waves* (North-Holland Publishing Company, Amsterdam, 1968).
- [42] T. Holstein and H. Primakoff, Field dependence of the intrinsic domain magnetization of a ferromagnet, *Phys. Rev.* **58**, 1098 (1940).
- [43] C. Kittel, *Quantum Theory of Solids* (Wiley, New York, 1963).
- [44] D. D. Stancil and A. Prabhakar, *Spin Waves: Theory and Applications* (Springer US, New York, 2009).
- [45] S. Takahashi, E. Saitoh, and S. Maekawa, Spin current through a normal-metal/insulating-ferromagnet junction, *J. Phys.: Conference Ser.* **200**, 062030 (2010).
- [46] S. A. Bender and Y. Tserkovnyak, Interfacial spin and heat transfer between metals and magnetic insulators, *Phys. Rev. B* **91**, 140402 (2015).
- [47] A. Kamra and W. Belzig, Magnon-mediated spin current noise in ferromagnet | nonmagnetic conductor hybrids, *Phys. Rev. B* **94**, 014419 (2016).
- [48] L. Trifunovic, F. L. Pedrocchi, and D. Loss, Long-Distance Entanglement of Spin Qubits via Ferromagnet, *Phys. Rev. X* **3**, 041023 (2013).
- [49] B. Flebus and Y. Tserkovnyak, Quantum-Impurity Relaxometry of Magnetization Dynamics, *Phys. Rev. Lett.* **121**, 187204 (2018).
- [50] C. Du, T. van der Sar, T. X. Zhou, P. Upadhyaya, F. Casola, H. Zhang, M. C. Onbasli, C. A. Ross, R. L. Walsworth, Y. Tserkovnyak, and A. Yacoby, Control and local measurement of the spin chemical potential in a magnetic insulator, *Science* **357**, 195 (2017).
- [51] A. Frisk Kockum, A. Miranowicz, S. De Liberato, S. Savasta, and F. Nori, Ultrastrong coupling between light and matter, *Nat. Rev. Phys.* **1**, 19 (2019).
- [52] J. Casanova, G. Romero, I. Lizuain, J. J. García-Ripoll, and E. Solano, Deep Strong Coupling Regime of the Jaynes-Cummings Model, *Phys. Rev. Lett.* **105**, 263603 (2010).
- [53] T. Niemczyk, F. Deppe, H. Huebl, E. P. Menzel, F. Hocke, M. J. Schwarz, J. J. Garcia-Ripoll, D. Zueco, T. Hümmer, E. Solano, A. Marx, and R. Gross, Circuit quantum electrodynamics in the ultrastrong-coupling regime, *Nat. Phys.* **6**, 772 (2010).
- [54] P. Forn-Díaz, L. Lamata, E. Rico, J. Kono, and E. Solano, Ultrastrong coupling regimes of light-matter interaction, *Rev. Mod. Phys.* **91**, 025005 (2019).
- [55] S. Ashhab and F. Nori, Qubit-oscillator systems in the ultrastrong-coupling regime and their potential for preparing nonclassical states, *Phys. Rev. A* **81**, 042311 (2010).
- [56] G. Q. Zhang, Y. P. Wang, and J. Q. You, Theory of the magnon Kerr effect in cavity magnonics, *Sci. China: Phys. Mech. Astron.* **62**, 987511 (2019), [arXiv:1903.03754](https://arxiv.org/abs/1903.03754).
- [57] M. M. Nieto, Displaced and squeezed number states, *Phys. Lett. A* **229**, 135 (1997).
- [58] P. Král, Displaced and squeezed Fock states, *J. Mod. Opt.* **37**, 889 (1990).
- [59] The magnetocrystalline anisotropies can be tuned via strain, for example.
- [60] L. Garziano, V. Macri, R. Stassi, O. Di Stefano, F. Nori, and S. Savasta, One Photon Can Simultaneously Excite Two or More Atoms, *Phys. Rev. Lett.* **117**, 043601 (2016).
- [61] Since this path involves four rotating processes and one counter-rotating one, its amplitude scales as approximately $\frac{g_{CR}g_A^4}{\hbar}$.
- [62] J. Johansson, P. Nation, and F. Nori, Qutip: An open-source python framework for the dynamics of open quantum systems, *Comput. Phys. Commun.* **183**, 1760 (2012).
- [63] J. Johansson, P. Nation, and F. Nori, Qutip 2: A python framework for the dynamics of open quantum systems, *Comput. Phys. Commun.* **184**, 1234 (2013).
- [64] The "crossing," as opposed to anticrossing, nature of these intersections has been verified carefully by evaluating the energy spectra around them to very high precision.
- [65] M. Neeley, R. C. Bialczak, M. Lenander, E. Lucero, M. Mariantoni, A. D. O'Connell, D. Sank, H. Wang, M. Weides, J. Wenner, Y. Yin, T. Yamamoto, A. N. Cleland, and J. M. Martinis, Generation of three-qubit entangled states using superconducting phase qubits, *Nature* **467**, 570 (2010).
- [66] L. DiCarlo, M. D. Reed, L. Sun, B. R. Johnson, J. M. Chow, J. M. Gambetta, L. Frunzio, S. M. Girvin, M. H. Devoret, and R. J. Schoelkopf, Preparation and measurement of three-qubit entanglement in a superconducting circuit, *Nature* **467**, 574 (2010).
- [67] M. D. Reed, L. DiCarlo, S. E. Nigg, L. Sun, L. Frunzio, S. M. Girvin, and R. J. Schoelkopf, Realization of three-qubit quantum error correction with superconducting circuits, *Nature* **482**, 382 (2012).
- [68] Y. Kajiwara, K. Harii, S. Takahashi, J. Ohe, K. Uchida, M. Mizuguchi, H. Umezawa, H. Kawai, K. Ando,

- K. Takanashi, S. Maekawa, and E. Saitoh, Transmission of electrical signals by spin-wave interconversion in a magnetic insulator, *Nature* **464**, 262 (2010).
- [69] F. D. Czeschka, L. Dreher, M. S. Brandt, M. Weiler, M. Althammer, I.-M. Imort, G. Reiss, A. Thomas, W. Schoch, W. Limmer, H. Huebl, R. Gross, and S. T. B. Goennenwein, Scaling Behavior of the Spin Pumping Effect in Ferromagnet-Platinum Bilayers, *Phys. Rev. Lett.* **107**, 046601 (2011).
- [70] M. Weiler, M. Althammer, M. Schreier, J. Lotze, M. Pernpeintner, S. Meyer, H. Huebl, R. Gross, A. Kamra, J. Xiao, Y.-T. Chen, H. Jiao, G. E. W. Bauer, and S. T. B. Goennenwein, Experimental Test of the Spin Mixing Interface Conductivity Concept, *Phys. Rev. Lett.* **111**, 176601 (2013).
- [71] A. Kamra, E. Thingstad, G. Rastelli, R. A. Duine, A. Brataas, W. Belzig, and A. Sudbø, Antiferromagnetic magnons as highly squeezed Fock states underlying quantum correlations, *Phys. Rev. B* **100**, 174407 (2019).
- [72] H. Y. Yuan, A. Kamra, D. M. F. Hartmann, and R. A. Duine, Electrically Switchable Entanglement Channel in van der Waals Magnets, *Phys. Rev. Appl.* **16**, 024047 (2021).
- [73] W. R. Salzman, Diagrammatical derivation and representation of Rayleigh–Schrödinger perturbation theory, *J. Chem. Phys.* **49**, 3035 (1968).
- [74] The effective coupling obtained from Eqs. (B9) and (B11) can be tuned to zero, both separately (at $g_{\text{CR}} = \pm\sqrt{(8/3)}g_R$ and $g_{\text{CR}} = \pm\sqrt{2}g_R$, respectively) and for the sum of the two ($g_{\text{CR}} = \pm 2g_R$).



Paper III

Jonas Lidal and Jeroen Danon


*Effects of spin-orbit coupling and in-plane Zeeman fields on
the critical current in two-dimensional hole gas SNS junctions*

Physical Review B, **107**, 085303 (2023)

Effects of spin-orbit coupling and in-plane Zeeman fields on the critical current in two-dimensional hole gas SNS junctions

Jonas Lidal  and Jeroen Danon 

Center for Quantum Spintronics, Department of Physics, Norwegian University of Science and Technology, NO-7491 Trondheim, Norway

 (Received 24 October 2022; revised 30 January 2023; accepted 31 January 2023; published 10 February 2023)

Superconductor-semiconductor hybrid devices are currently attracting much attention, fueled by the fact that strong spin-orbit interaction in combination with induced superconductivity can lead to exotic physics with potential applications in fault-tolerant quantum computation. The detailed nature of the spin dynamics in such systems is, however, often strongly dependent on device details and hard to access in experiment. In this paper we theoretically investigate a superconductor-normal-superconductor junction based on a two-dimensional hole gas with additional Rashba spin-orbit coupling, and we focus on the dependence of the critical current on the direction and magnitude of an applied in-plane magnetic field. We present a simple model, which allows us to systematically investigate different parameter regimes and obtain both numerical results and analytical expressions for all limiting cases. Our results could serve as a tool for extracting more information about the detailed spin physics in a two-dimensional hole gas based on a measured pattern of critical currents.

DOI: [10.1103/PhysRevB.107.085303](https://doi.org/10.1103/PhysRevB.107.085303)

I. INTRODUCTION

Hybrid devices made of superconductors and semiconductors have gained much interest in recent years due to their rich and complex behavior. Spin-orbit coupling in combination with superconducting correlations induced via the proximity effect can give rise to exotic spin physics inside the semiconductor, which could be exploited to engineer topological superconductivity [1–7]. Since such topological superconductors are expected to host low-energy Majorana modes that obey non-Abelian anyonic statistics, they could provide a platform for implementing fault-tolerant quantum computation with topologically protected qubit operations [8–10].

Arguably the simplest hybrid device one can create using superconducting and normal elements is the superconductor-normal-superconductor (SNS) junction, which finds applications in a wide range of directions, including superconducting qubits [11–15] and electronic and magnetic measuring devices [16–20]. In addition to being an essential component of superconducting circuits, an SNS junction can also be used for studying the underlying properties of the constituent elements of the hybrid structure. For the case of a semiconducting normal region, an SNS setup allows to probe details of the spin-orbit interaction in the semiconductor and its interplay with the Zeeman effect [21–23], as well as to study phase transitions into and out of topological phases [24–26].

One quantity that encodes several details of the underlying physics of the system is the critical current through the SNS junction, i.e., the maximal supercurrent the junction can support. By applying a magnetic field perpendicular to a two-dimensional junction, information about the current density distribution can be extracted from the measured critical current [27]. For a uniform current distribution, the

critical current as a function of the out-of-plane magnetic field emerges as a so-called Fraunhofer pattern, which reflects the flux enclosed by the junction. A deviation from a Fraunhofer pattern is a sign of a nonuniform current distribution and the pattern of critical current can be directly related to the actual current distribution profile in the junction [28–34].

The field-dependent behavior of an SNS junction is heavily influenced by the properties of the normal part, and junctions based on a wide range of materials have been explored in the past [35–38]. In this paper we focus on SNS junctions comprised of a two-dimensional hole gas (2DHG) contacted by two conventional superconductors. Our choice is motivated by the recent surge in interest for lower-dimensional quantum devices hosted in 2DHGs [39–46], which was sparked by their interesting properties including strong inherent and tunable spin-orbit interaction [47–51] and highly anisotropic and tunable g tensors [52–55], all caused by the underlying p -type orbital structure of the valence band states [56]. Additionally, germanium-based hole gases have recently shown great promise for straightforward integration with superconducting elements [57–60].

The effective spin-orbit interaction and Zeeman coupling that together can give rise to its useful properties depend strongly on many details of the 2DHG, including its exact out-of-plane confining potential, the carrier density, strain, and the local electrostatic landscape. For this reason it is not always straightforward to access the relevant underlying spin-orbit and g -tensor parameters in experiment for a given system. Here, we theoretically study the dependence of the critical current through a 2DHG-based SNS junction on the direction and magnitude of an applied *in-plane* magnetic field. We show how to derive an elegant expression for the field-dependent critical current in a semiclassical limit (where the

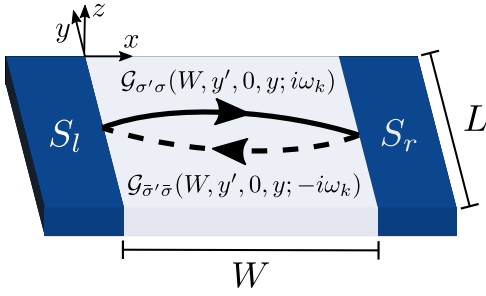


FIG. 1. Schematic of the SNS junction: two identical conventional superconductors S_l and S_r , connected by a 2D hole gas. The junction has a length of L and a width of W , as indicated. An example of a diagram contributing to the Cooper-pair propagator is drawn in the normal region, where the electron (hole) propagator is depicted with a solid (dashed) line.

system is large compared to its Fermi wavelength), which allows for straightforward numerical evaluation of the current. Assuming that we can describe the dynamics of the holes in the normal region with a simple 4×4 Luttinger Hamiltonian and that the carrier density is low enough that only the lowest (heavy-hole) subband is occupied, we identify several different parameter regimes where different spin-mixing mechanisms could be dominating and we calculate the field-dependent critical current in all these regimes. We are able to connect each mechanism to clear qualitative features in the pattern of critical current that emerges and we present analytical expressions for the current in most limiting cases. Our results could thus help distinguishing the dominating spin-mixing process at play in an experiment, and as such give insight in the strength and nature of the underlying spin-orbit and Zeeman couplings in the system.

The rest of the paper is organized as follows. In Sec. II we will introduce the setup we consider and the model we use to describe it. We outline our method of calculating the critical current through the junction and explain how we tailor it to the situation where all transport in the normal region is carried by the heavy holes. In Sec. III we present both our numerical and analytical results, systematically going through the different parameter regimes that could be reached. Finally, in Sec. IV we present a short conclusion.

II. MODEL

Figure 1 shows a cartoon of the system we consider: A 2DHG is contacted from two sides by two identical conventional superconductors to create an SNS junction, where we assume the coupling between the superconductors and the normal region to be weak. We define the length L and width W of the junction as indicated in the figure and choose the coordinate system such that the average flow of supercurrent is in the x direction and the out-of-plane direction is denoted by z . We assume the clean junction limit, as the width of experimentally viable devices is typically of the order 100 nm to 1 μm [58,59,61], while the mean-free path of, e.g., Ge 2DHGs has been measured to be up to $\sim 6 \mu\text{m}$ [58,59].

We will first introduce the method we chose for calculating the supercurrent through the junction. In the ground state, the current is given by

$$I(\phi) = \frac{2e}{\hbar} \frac{\partial F}{\partial \phi}, \quad (1)$$

where F is the free energy of the junction and ϕ is the difference in phase between the two superconductors.

We describe the coupling between the hole gas and the superconducting leads with a tunneling Hamiltonian

$$H_t = \sum_{\sigma} \int dy \int dx [t_l \hat{\psi}_{\sigma}^{\dagger}(0, y) \hat{\Psi}_{\sigma,L}(0, y) + t_r \hat{\psi}_{\sigma}^{\dagger}(W, y) \hat{\Psi}_{\sigma,R}(W, y) + \text{H.c.}], \quad (2)$$

where $\hat{\psi}_{\sigma}^{\dagger}(\mathbf{r})$ is the creation operator for an electron with spin σ at position \mathbf{r} in the normal region, and $\hat{\Psi}_{\sigma,L(R)}^{\dagger}(\mathbf{r})$ for an electron with spin σ at position \mathbf{r} in the left (right) superconductor. The lines $x = 0, W$ define the interfaces between the superconductors and the normal region.

We assume the coupling amplitudes $t_{l,r}$ to be small enough to justify a perturbative treatment of H_t . Weak coupling can result from, e.g., interfacial disorder, but could also be a consequence of the difference in underlying orbital structure of the electronic wave functions in the superconductors' conduction band and the semiconductor's valence band. The leading-order correction to F that depends on ϕ is second order in the self-energy due to the proximity of the superconductors, or fourth order in the coupling Hamiltonian H_t [62]:

$$F^{(4)} = -\frac{1}{4! \beta} \int_0^{\beta} d\tau_{1\dots 4} \langle \hat{T}_{\tau} H_t(\tau_1) H_t(\tau_2) H_t(\tau_3) H_t(\tau_4) \rangle, \quad (3)$$

where $\beta = 1/T$ is the inverse temperature, \hat{T}_{τ} is the (imaginary) time-ordering operator, and $\hbar = k_B = 1$. In the evaluation of (3) we focus on the fully connected diagrams only since those are the ones that can probe the phase difference between the two superconductors.

Anticipating that we will make a semiclassical approximation later, assuming that the dimensions of the junction are much larger than the Fermi wavelength λ_F , we will take the Andreev reflection at the NS interface to be local and energy independent. After applying Wick's theorem to the correlator in (3) this allows us to simplify the correction to

$$F^{(4)} = -\lambda_l \lambda_r \iint dy dy' \text{Re} \{ e^{i[\varphi_l(y) - \varphi_r(y')] } C(W, y'; 0, y) \}, \quad (4)$$

where $\lambda_{l,r} = \pi t_{l,r}^2 \nu_{\text{eff}}$ parametrize the strength of the coupling to the superconducting leads, with ν_{eff} the local effective one-dimensional tunneling density of states of the superconductors (giving the λ 's dimensions energy \times meters). The phase difference

$$\varphi_l(y) - \varphi_r(y') = \phi + \frac{\pi(y + y') B_z W}{\Phi_0}, \quad (5)$$

with $\Phi_0 = h/2e$ the flux quantum, depends on the two y coordinates in such a way that it captures the coupling to an out-of-plane magnetic field [63], due to the flux $\Phi = B_z W L$ penetrating the junction. We assume that the magnetic field

B_z is small enough that it does not significantly affect the trajectories of the charges.¹ We used the function

$$C(\mathbf{r}', \mathbf{r}) = \frac{T}{2} \sum_k \text{Tr}[\bar{\mathcal{G}}(\mathbf{r}', \mathbf{r}; i\omega_k) \sigma_y \bar{\mathcal{G}}(\mathbf{r}, \mathbf{r}; -i\omega_k)^T \sigma_y], \quad (6)$$

were the $\bar{\mathcal{G}}$ are 2×2 matrices in spin space,

$$\bar{\mathcal{G}}(\mathbf{r}', \mathbf{r}; i\omega_k) = \begin{pmatrix} \mathcal{G}_{\uparrow\uparrow}(\mathbf{r}', \mathbf{r}; i\omega_k) & \mathcal{G}_{\uparrow\downarrow}(\mathbf{r}', \mathbf{r}; i\omega_k) \\ \mathcal{G}_{\downarrow\uparrow}(\mathbf{r}', \mathbf{r}; i\omega_k) & \mathcal{G}_{\downarrow\downarrow}(\mathbf{r}', \mathbf{r}; i\omega_k) \end{pmatrix}, \quad (7)$$

with $\mathcal{G}_{\sigma'\sigma}(\mathbf{r}', \mathbf{r}; i\omega_k) = -\int_0^\beta d\tau e^{i\omega_k\tau} \langle \hat{T}_\tau \hat{\psi}_{\sigma'}(\mathbf{r}', \tau) \hat{\psi}_\sigma^\dagger(\mathbf{r}, 0) \rangle$ the thermal Green function at Matsubara frequency $\omega_k = (2k + 1)\pi T$ for (spin-dependent) electronic propagation in the normal region. The correlation function $C(W, y'; 0, y)$ as used in (4) can thus be interpreted as the probability amplitude for a Cooper pair to cross the junction, from the point $(0, y)$ to the point (W, y') , as illustrated by the simple diagram shown in Fig. 1. In writing Eq. (4) we further assumed the pairing in the superconductors to be conventional s type, described by pairing terms like $H_{\text{pair}}^{(S)} = -\sum_{\mathbf{k}} \{\Delta_0 \hat{\Psi}_{\mathbf{k}\uparrow}^\dagger \hat{\Psi}_{-\mathbf{k}\downarrow}^\dagger + \Delta_0^* \hat{\Psi}_{-\mathbf{k}\downarrow} \hat{\Psi}_{\mathbf{k}\uparrow}\}$. Within all approximations made, other details of the dynamics inside the superconductors will only affect the magnitude of the two coupling parameters $\lambda_{l,r}$.

We assume that the carriers in the normal region can be described by a 4×4 Luttinger Hamiltonian [56]

$$H_0 = \frac{1}{2m_0} \begin{pmatrix} P+Q & 0 & 0 & M \\ 0 & P+Q & M^* & 0 \\ 0 & M & P-Q & 0 \\ M^* & 0 & 0 & P-Q \end{pmatrix}, \quad (8)$$

where

$$P = \gamma_1(k^2 + \langle k_z^2 \rangle), \quad (9a)$$

$$Q = \gamma_2(k^2 - 2\langle k_z^2 \rangle), \quad (9b)$$

$$M = -\frac{1}{2}\sqrt{3}[(\gamma_2 + \gamma_3)k_-^2 + (\gamma_2 - \gamma_3)k_+^2], \quad (9c)$$

using $k_\pm = k_x \pm ik_y$ and $k^2 = k_x^2 + k_y^2$, and with m_0 being the bare electron mass and $\gamma_{1,2,3}$ the three-dimensionless

¹The total magnetic flux penetrating the junction area is in reality often enhanced by flux focusing due to the Meissner effect, which we will neglect here for simplicity. Including this effect can be done simply by renormalizing B_z .

material-specific Luttinger parameters. This Hamiltonian is written in the basis of the angular-momentum states $\{|+\frac{3}{2}\rangle, |-\frac{3}{2}\rangle, |+\frac{1}{2}\rangle, |-\frac{1}{2}\rangle\}$ with total angular momentum $\frac{3}{2}$ and it includes an extra minus sign, i.e., it describes the dynamics from a hole perspective. The z coordinate (along which the holes are strongly confined) has already been integrated out, $\langle k_z^2 \rangle \sim 1/d^2$, with d the transverse confinement length, and we neglect the effects of strain for simplicity.

We now assume that transverse confinement is strong enough to make the splitting $\delta_{HL} = 2\gamma_2 \langle k_z^2 \rangle / m_0$ the largest energy scale involved, on the order of ~ 100 meV in planar Ge [49,57,64], which allows us to focus on the so-called heavy-hole (HH) subspace $\{|+\frac{3}{2}\rangle, |-\frac{3}{2}\rangle\}$ and treat the coupling to the light-hole (LH) states $\{|+\frac{1}{2}\rangle, |-\frac{1}{2}\rangle\}$ perturbatively. We will further assume that the Andreev reflection at the interfaces with the superconductors pairs hole states with opposite orbital and spin angular momentum, such as $|\pm\frac{3}{2}\rangle$. This allows us to treat the low-energy HH subspace $\{|+\frac{3}{2}\rangle, |-\frac{3}{2}\rangle\}$ as an effective spin- $\frac{1}{2}$ system that can host a supercurrent that can be described with the formalism presented above.²

Furthermore, we want to include the Zeeman effect due to an in-plane magnetic field \mathbf{B}_\parallel as well as Rashba-type spin-orbit coupling. We describe the in-plane Zeeman effect with the Hamiltonian

$$H_Z = -2\kappa(B_+J_- + B_-J_+), \quad (10)$$

where $J_\pm = J_x \pm iJ_y$ are the spin- $\frac{3}{2}$ raising and lowering operators, $B_\pm = B_x \pm iB_y$, the hole g factor is κ , and we set $\mu_B = 1$. The spin-orbit coupling, which can be due to asymmetries in the confining potential or to an externally applied out-of-plane electric field, is described with

$$H_R = i\alpha_R(k_+J_- - k_-J_+), \quad (11)$$

where α_R characterizes the strength of the coupling.

We add these two ingredients to the projected two-dimensional Luttinger Hamiltonian introduced above and we make the so-called spherical approximation, amounting to the assumption $|\gamma_2 - \gamma_3| \ll \gamma_2 + \gamma_3$, which allows to drop the last term in (9c). For many commonly used semiconductors, such as Ge, GaAs, InSb, and InAs (but not for Si), this is a valid approximation [56]. Otherwise, we impose no constraints on the Luttinger parameters. Then the total Hamiltonian for the hole gas is

$$H_{\text{tot}} = H_0 + H_Z + H_R = \begin{pmatrix} k^2/2m_H & 0 & -\sqrt{3}(2\kappa B_- + i\alpha_R k_-) & -k_-^2/2m_x \\ 0 & k^2/2m_H & -k_+^2/2m_x & \sqrt{3}(-2\kappa B_+ + i\alpha_R k_+) \\ \sqrt{3}(-2\kappa B_+ + i\alpha_R k_+) & -k_-^2/2m_x & \delta_{HL} + k^2/2m_L & -4\kappa B_- - 4i\alpha_R k_- \\ -k_+^2/2m_x & -\sqrt{3}(2\kappa B_- + i\alpha_R k_-) & -4\kappa B_+ + 4i\alpha_R k_+ & \delta_{HL} + k^2/2m_L \end{pmatrix}, \quad (12)$$

where we introduced the effective HH and LH masses $m_H = m_0/(\gamma_1 + \gamma_2)$ and $m_L = m_0/(\gamma_1 - \gamma_2)$. We further used $m_x = 2m_0/\sqrt{3}(\gamma_2 + \gamma_3)$, which governs the strength of the momentum-dependent HH-LH mixing. A sketch of Hamiltonian (12) can be seen in Fig. 2.

²Treating the holes as electrons results in an overall minus sign for the supercurrent, which is irrelevant in the context of this work.

Our assumption that δ_{HL} is the largest energy scale involved allows us to treat the HH-LH coupling perturbatively. We first diagonalize the LH subspace in (12), after which we perform a Schrieffer-Wolff transformation to decouple the HH and LH subspaces. To second order in $1/\delta_{HL}$ we find the effective HH Hamiltonian

$$H_{HH} = \begin{pmatrix} k^2/2m_H & -\delta_{HL}^{-1}(k_-^2/m_x)\beta_1 - 4\delta_{HL}^{-2}\beta_1^2\beta_2 \\ -\delta_{HL}^{-1}(k_+^2/m_x)\beta_1^* - 4\delta_{HL}^{-2}(\beta_1^*)^2\beta_2^* & k^2/2m_H \end{pmatrix}, \quad (13)$$

where we ignored the shift of the diagonal elements, and we used $\beta_1 = \sqrt{3}(2\kappa B_- + i\alpha_R k_-)$ and $\beta_2 = \kappa B_- + i\alpha_R k_-$. We see that, depending on the magnitude of δ_{HL} , the typical in-plane (Fermi) momentum k_F of the current-carrying holes, the strength of the spin-orbit coupling α_R , and the magnitude of the applied in-plane magnetic field, different terms can dominate the effective coupling of the two HH states. We used that in the perturbative limit we consider here one always has $(\delta_{HL}^{-1}k_{\pm}^2/m_x)^2 \ll \delta_{HL}^{-1}k_{\pm}^2/m_x$, and we thus ignore the contribution $-4\delta_{HL}^{-2}(k_{\pm}^2/m_x)^2(\beta_2^*\sigma_+ + \beta_2\sigma_-)$ to Eq. (13).

We can now consider different cases. First, for a very thin 2DHG we can assume that the term $\propto\delta_{HL}^{-1}$ will dominate, which leaves two qualitatively different coupling terms in H_{HH} ,

$$H_{0,3}^{(1)} = \frac{-i\sqrt{3}\alpha_R}{m_x\delta_{HL}}(k_-^3\sigma_+ - k_+^3\sigma_-), \quad (14)$$

$$H_{1,2}^{(1)} = \frac{-2\sqrt{3}\kappa}{m_x\delta_{HL}}(B_-k_-^2\sigma_+ + B_+k_+^2\sigma_-), \quad (15)$$

where the subscripts of H refer to the powers of B and k appearing in the term, respectively, and the superscript indicates the power of δ_{HL}^{-1} . If the 2DHG is less thin, then the term $\propto\delta_{HL}^{-2}$ in (13) could also contribute, which allows for four additional coupling terms:

$$H_{0,3}^{(2)} = 12\frac{i\alpha_R^3}{\delta_{HL}^2}(k_-^3\sigma_+ - k_+^3\sigma_-), \quad (16)$$

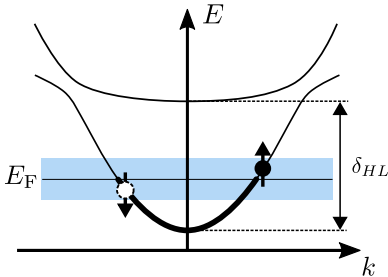


FIG. 2. A sketch of the spectrum of the Hamiltonian (12), where we assumed the perturbations H_Z and H_R to be small enough to be neglected. We see the heavy-hole and light-hole bands being split by the HH-LH splitting δ_{HL} and anticross where they are mixed by the off-diagonal terms $k_{\pm}^2/2m_x$. The blue shaded region around the Fermi energy E_F indicates the energy window within which all relevant dynamics are assumed to happen, its width being of the order of $|\Delta_0|$. Superconducting pairing in the 2DHG is induced between holes in the HH band with opposite spin and momentum, as illustrated in the figure.

$$H_{1,2}^{(2)} = 60\frac{\alpha_R^2\kappa}{\delta_{HL}^2}(B_-k_-^2\sigma_+ + B_+k_+^2\sigma_-), \quad (17)$$

$$H_{2,1}^{(2)} = -96\frac{i\alpha_R\kappa^2}{\delta_{HL}^2}(B_-^2k_-^2\sigma_+ - B_+^2k_+^2\sigma_-), \quad (18)$$

$$H_{3,0}^{(2)} = -48\frac{\kappa^3}{\delta_{HL}^2}(B_-^3\sigma_+ + B_+^3\sigma_-). \quad (19)$$

We now make the assumption that all relevant dynamics happen on an energy scale very close to the Fermi level E_F . This allows us to linearize the kinetic energy in H_{HH} in \mathbf{k} and to assume that the magnitude of the in-plane momentum $k \approx k_F$ in the off-diagonal terms. This leaves us with a general 2×2 Hamiltonian effectively describing the HH subsystem (up to a constant)

$$H_{HH} = v_F(k - k_F) + \boldsymbol{\beta}(\theta) \cdot \boldsymbol{\sigma}, \quad (20)$$

where $v_F = k_F/m_H$ is the Fermi velocity and the field $\boldsymbol{\beta}$ includes the off-diagonal terms of H_{HH} , depending only on the angle θ , the in-plane direction of \mathbf{k} . The vector $\boldsymbol{\sigma} = \{\sigma_x, \sigma_y, \sigma_z\}$ consists of the three Pauli matrices.

Following the approach of Ref. [63], we recognize that H_{HH} in (20) can be diagonalized in spin space and we denote the two \mathbf{k} -dependent eigenspinors with $|\lambda_{\mathbf{k}}\rangle$, where $\lambda = \pm$. This allows to rewrite Eq. (20) as

$$H_{HH} = \sum_{\lambda_{\mathbf{k}}=\pm\mathbf{k}} \epsilon_{\mathbf{k}\lambda} P^{\lambda_{\mathbf{k}}}, \quad (21)$$

in terms of the energies $\epsilon_{\mathbf{k}\lambda} = v_F(k - k_F) + \lambda|\boldsymbol{\beta}(\theta)|$ and the projectors $P^{\lambda_{\mathbf{k}}} = |\lambda_{\mathbf{k}}\rangle\langle\lambda_{\mathbf{k}}| = \frac{1}{2}[1 + \lambda\hat{\boldsymbol{\beta}}(\theta) \cdot \boldsymbol{\sigma}]$, where the dimensionless vector $\hat{\boldsymbol{\beta}}(\theta) = \boldsymbol{\beta}(\theta)/|\boldsymbol{\beta}(\theta)|$ points along the direction of the field $\boldsymbol{\beta}(\theta)$.

Assuming for simplicity translational invariance inside the 2DHG, the correlation function $C(\mathbf{r}'; \mathbf{r})$ is only a function of the difference in coordinates and reduces at zero temperature to (see the Supplemental Material [65] for a more detailed derivation)

$$C(\mathbf{r}) = \iint_0^\infty \frac{d\epsilon d\epsilon'}{2(\epsilon + \epsilon')} \text{Tr}[\bar{\mathbf{g}}(\mathbf{r}, -\epsilon)\sigma_y\bar{\mathbf{g}}(\mathbf{r}, -\epsilon')^T\sigma_y + \bar{\mathbf{g}}(\mathbf{r}, \epsilon)\sigma_y\bar{\mathbf{g}}(\mathbf{r}, \epsilon')^T\sigma_y], \quad (22)$$

using the propagator

$$\bar{\mathbf{g}}(\mathbf{r}, \epsilon) = \frac{1}{(2\pi)^2} \sum_{\lambda_{\mathbf{k}}=\pm\mathbf{k}} \int d\mathbf{k} e^{i\mathbf{k}\cdot\mathbf{r}} \delta(\epsilon - \epsilon_{\mathbf{k}\lambda}) P^{\lambda_{\mathbf{k}}}. \quad (23)$$

We then additionally assume that $k_{FR} \gg 1$ for all distances $r = |\mathbf{r}|$ of interest (such as W), which amounts to employing a semiclassical approximation. In that case one finds that the only momenta that contribute significantly in the propagators $\bar{\mathbf{g}}(\mathbf{r}, \epsilon)$ have a wave vector \mathbf{k} parallel or antiparallel to \mathbf{r} (see

the Supplemental Material [65] for a formal derivation). In this limit we find a greatly simplified approximation for the Cooper-pair propagator

$$C(\mathbf{r}) = \frac{K}{r^2} \left\{ \cos\left(\frac{|\boldsymbol{\beta}(\theta)|r}{v_F}\right) \cos\left(\frac{|\boldsymbol{\beta}(\bar{\theta})|r}{v_F}\right) - \hat{\boldsymbol{\beta}}(\theta) \cdot \hat{\boldsymbol{\beta}}(\bar{\theta}) \sin\left(\frac{|\boldsymbol{\beta}(\theta)|r}{v_F}\right) \sin\left(\frac{|\boldsymbol{\beta}(\bar{\theta})|r}{v_F}\right) \right\}, \quad (24)$$

where the constant $K = k_F/(2\pi)^2 v_F$, and $\theta(\bar{\theta})$ is now the in-plane direction parallel (antiparallel) to \mathbf{r} , which means $\mathbf{r} = \{r \cos \theta, r \sin \theta\}$ and $\bar{\theta} = \theta - \pi$.

We note that by inserting this propagator in Eq. (4) to evaluate the supercurrent we only account for the contribution of straight trajectories between the two superconducting contacts, i.e., we neglect trajectories that involve scattering off the edges of the 2DHG. This approximation becomes better with increasing aspect ratio L/W of the junction.

III. RESULTS

We now have all ingredients needed to calculate the supercurrent through the junction, to leading order in the SN coupling strength and within a semiclassical approximation. In this section we will present our results.

Due to the large number of competing coupling terms we consider [Eqs. (14)–(19)], the field $\boldsymbol{\beta}(\theta)$, and thus the current, can look very different depending on the parameters one assumes. However, in the limiting case where only one of the six terms dominates, the Cooper-pair propagator immediately simplifies further: Assuming that one term $H_{n,m}$ is by far the largest (where, again, n and m refer to the powers of B and k in the coupling term), one finds

$$\hat{\boldsymbol{\beta}}(\theta) \cdot \hat{\boldsymbol{\beta}}(\bar{\theta}) = \cos(m\pi), \quad (25)$$

and in that case the expression given in (24) reduces to

$$C(\mathbf{r}) = \frac{K}{r^2} \times \begin{cases} \cos(2r|\boldsymbol{\beta}|/v_F) & \text{for } m \text{ even,} \\ 1 & \text{for } m \text{ odd,} \end{cases} \quad (26)$$

where we used that all coupling terms listed above correspond to fields for which $|\boldsymbol{\beta}(\theta)|$ is independent of θ .

In this case the supercurrent through the junction will thus not depend on the direction of the applied in-plane field, only on its magnitude if the coupling term has an even power of k . This is indeed what one expects: When the field $\boldsymbol{\beta}$ is even in momentum, a pairing of opposite spins at the Fermi level introduces a finite average Cooper-pair momentum which is to first approximation linear in the magnitude of the field. For fields that are odd in momentum, the sign change of $\boldsymbol{\beta}$ upon inversion of \mathbf{k} guarantees that there are always eigenstates with opposite spin and momentum available at the Fermi level, independent of the magnitude of the total field.

A more interesting dependence on the magnitude and direction of the in-plane field can arise when two or more coupling terms with different dependence on B and k compete [63]. Calculating the supercurrent numerically for an arbitrary combination of coupling mechanisms is straightforward. However, to structure our discussion and to gain qualitative insight in the significance of all terms, we will mostly consider limiting cases below, where only a few terms play a role.

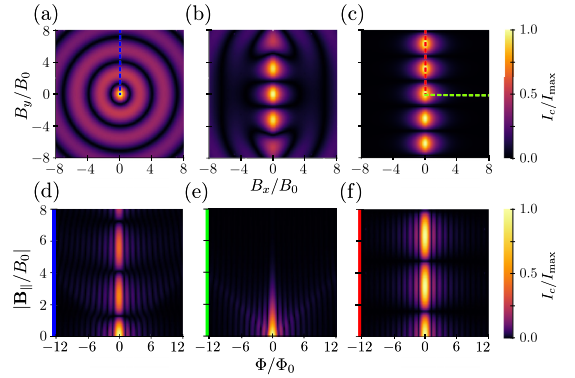


FIG. 3. (a)–(c) Numerically calculated critical current as a function of in-plane magnetic field $B_{\parallel} = (B_x, B_y)$ and $B_z = 0$, expressed in units of $B_0 = \delta_{HL} v_F / 8\sqrt{3} \kappa E_x W$. We work in the limit of large HH-LH splitting everywhere, using a field $\boldsymbol{\beta}(\theta)$ as defined by (28). We show results for different values of E_{SO} : (a) $E_{SO}/\kappa B_0 = 0.2$, (b) $E_{SO}/\kappa B_0 = 2$, and (c) $E_{SO}/\kappa B_0 = 20$. (d)–(f) Critical current as a function of in-plane magnetic field (vertical axis) along given directions, and an additional out-of-plane magnetic field (horizontal axis), quantified by the total flux trough the junction Φ . The colors at the vertical axes correspond to the colored dashed lines in (a)–(c), which indicate the direction of the in-plane field. For all plots the aspect ratio is set at $L/W = 10$, the scale of the critical current is described by $I_{\max} = I_0 \pi L/W$, and $\Phi_0 = h/2e$ is the flux quantum.

A. Large HH-LH splitting

The first case we will investigate is when we have a large HH-LH splitting δ_{HL} (corresponding to tight out-of-plane confinement). In that case, the terms (16)–(19), which are proportional to δ_{HL}^{-2} , are suppressed and the dominating coupling terms are $H_{0,3}^{(1)}$ and $H_{1,2}^{(1)}$. More quantitatively, we see that this regime is reached when

$$\sqrt{\delta_{HL} E_x} \gg E_Z, E_{SO}, \quad (27)$$

where we introduced the Zeeman energy $E_Z = \kappa B_{\parallel}$, the spin-orbit energy $E_{SO} = \alpha_R k_F$, and the orbital coupling energy $E_x = k_F^2 / 2m_x$. (Assuming that the Luttinger parameters are of order unity,³ this last energy scale is of the order of the Fermi energy in the valence band and can thus be tuned by varying the carrier density.) In this case, the total coupling field is defined by

$$\boldsymbol{\beta}_{\pm}(\theta) = \frac{2\sqrt{3}E_x}{\delta_{HL}} (iE_{SO}e^{3i\theta} - 2E_Z e^{i(2\theta + \phi_B)}), \quad (28)$$

where ϕ_B is the direction of the in-plane magnetic field.

As mentioned, this effective field allows us to calculate the supercurrent and hence the critical current through the junction. In Fig. 3 we show the dependence of the resulting

³The actual values of the Luttinger parameters only affect the magnitude of parameters like δ_{HL} and E_x and can thus only lead to a shift of the ranges of validity of the limits discussed, not to a change of the phenomenology of the patterns observed in the critical current.

critical current on the applied magnetic field, for different ratios of E_{SO}/E_Z : In the top row of panels we plot the critical current as a function of the the magnitude and direction of a purely in-plane field. In Figs. 3(a)–3(c) we used $E_{SO}/\kappa B_0 = 0.2, 2,$ and 20 , respectively, where $\kappa B_0 = \delta_{HL} v_F / 8\sqrt{3} E_x W$ and we used an aspect ratio of $L/W = 10$. For reference, and to compare with Ref. [63], we show in the bottom row the Fraunhofer-type patterns of critical current that emerge when, in addition to an in-plane field (vertical axes), a small perpendicular magnetic field B_z is applied (horizontal axes). The direction of each \mathbf{B}_{\parallel} is indicated with a dashed line in the plots in the top row: In Fig. 3(d) we have $E_{SO}/\kappa B_0 = 0.2$, as in Fig. 3(a), while the in-plane field is oriented along \hat{y} (blue dashed line). In Figs. 3(e) and 3(f) we used $E_{SO}/\kappa B_0 = 20$ with 3(e) the in-plane field along \hat{x} [green dashed line in 3(c)] and 3(f) the field along \hat{y} [red dashed line in 3(c)].

We see that these results are similar to those of Ref. [63] for the case where the competition between Zeeman and Rashba coupling is investigated (cf. Fig. 3 in Ref. [63]). This can be easily understood from the structure of the semiclassical Cooper-pair propagator (24), which only depends on the relative orientation and the magnitude of the fields acting on the “electrons” and “holes” that propagate with opposite momentum. The main difference in our coupling terms as compared to the electronic case studied in Ref. [63] is an extra factor k_{\pm}^2 due to the intrinsic HH-LH mixing in the valence band. This additional factor only serves to rotate all effective fields by the same amount, thereby not affecting the direction dependence of the Cooper-pair propagator.

As expected, in the limit of dominating Zeeman coupling [Fig. 3(a)] the period of the oscillations is independent of the direction of propagation of the Cooper pair since spin rotations are in this case not related to the direction of propagation of Cooper pairs. In the spin-orbit-dominated case the oscillations in $C(\mathbf{r})$ occur always in a direction perpendicular to \mathbf{B}_{\parallel} for the case of the Rashba-type spin-orbit coupling assumed here.

As was pointed out in Ref. [63], in the two limiting cases of strongly dominating E_{SO} or E_Z the propagator simplifies considerably:

$$C(\mathbf{r}) \approx \frac{K}{r^2} \times \begin{cases} \cos(|\mathbf{d}|r) & \text{for } E_Z \gg E_{SO}, \\ \cos([\hat{z} \times \mathbf{d}] \cdot \mathbf{r}) & \text{for } E_{SO} \gg E_Z \end{cases} \quad (29)$$

with $\mathbf{d} = \mathbf{B}_{\parallel}/B_0 W$ being a vector that characterizes the spatial oscillations of the propagator.

The dependence of the supercurrent on the in-plane field as plotted in Figs. 3(a)–3(c) follows from evaluating the following integral (setting the electron charge $e = 1$):

$$I_c(\mathbf{B}_{\parallel}) = 4 \left| \lambda_l \lambda_r \right| \iint_0^L dy dy' C(W, y' - y), \quad (30)$$

which can be performed (semi)analytically in the two limits discussed above. For the case of $E_Z \gg E_{SO}$ we rewrite (30) as

$$I_c(\mathbf{B}_{\parallel}) = 2I_0 \int_1^q d\rho \frac{\cos(\alpha\rho)}{\rho} \left(\frac{L}{W\sqrt{\rho^2 - 1}} - 1 \right), \quad (31)$$

where $I_0 = 4K|\lambda_l \lambda_r|$ sets the scale of the supercurrent, we introduced the parameter $q = \sqrt{1 + (L/W)^2}$, and we used $\alpha = B_{\parallel}/B_0$. In the limit of a long junction, i.e., $L \gg W$, we

can approximate $q \rightarrow \infty$, yielding

$$I_{c1}(\mathbf{B}_{\parallel}) = I_0 \frac{\pi L}{2W} \left[\pi \alpha [J_0(\alpha)H_1(\alpha) - J_1(\alpha)H_0(\alpha)] + 2[1 - \alpha J_0(\alpha)] \right], \quad (32)$$

where $J_n(x)$ are Bessel functions of the first kind and $H_n(x)$ are Struve functions. We note that we neglected the second term in (31), which implies the assumption that α is not exponentially small, i.e., $\alpha \gg e^{-L/W}$. An approximate analytic solution of (31) for general L/W is presented in the Supplemental Material [65]. For the second case, $E_{SO} \gg E_Z$, we find in the same limit of $L \gg W$

$$I_{c2}(\mathbf{B}_{\parallel}) \approx I_0 \frac{\pi L}{W} e^{-|B_{\parallel}/B_0|} |\cos(B_y/B_0)|. \quad (33)$$

Comparing to Figs. 3(a) and 3(c) we see that the analytic expressions (32) and (33) indeed capture the behavior of the critical current as a function of \mathbf{B}_{\parallel} in the two limiting cases: For large Zeeman fields the current shows “damped” oscillations as a function of B_{\parallel} and for dominating spin-orbit coupling the behavior becomes direction dependent, showing oscillations for \mathbf{B}_{\parallel} being perpendicular to the mean direction of current flow and rapid decay for \mathbf{B}_{\parallel} parallel to the current.

B. Smaller HH-LH splitting

The second situation we will consider is when we have a smaller HH-LH splitting and/or orbital coupling E_x . In this case the second-order terms (16)–(19), which are proportional to δ_{HL}^2 , can be dominating. Formally, this will be the case when

$$E_Z, E_{SO} \gg \sqrt{\delta_{HL} E_x}, \quad (34)$$

and the total coupling field then becomes

$$\beta_+(\theta) = \frac{12}{\delta_{HL}^2} \left(-iE_{SO}^3 e^{3i\theta} + 5E_{SO}^2 E_Z e^{i(2\theta + \phi_B)} + 8iE_{SO} E_Z^2 e^{i(\theta + 2\phi_B)} - 4E_Z^3 e^{3i\phi_B} \right). \quad (35)$$

If we do not assume anything about the ratio E_{SO}/E_Z , then all four terms could contribute significantly.

We thus assume throughout this section that the inequality (34) holds so that the total field β can be approximated by (35), and we start by numerically exploring the behavior of the critical current as a function of in-plane field, over a range of E_{SO}/E_Z . In Fig. 4 we show the calculated critical current, where we used (a) $E_{SO}/\kappa B_0 = 0.157$, (b) $E_{SO}/\kappa B_0 = 1.19$, (c) $E_{SO}/\kappa B_0 = 1.97$, (d) $E_{SO}/\kappa B_0 = 3.16$, and (e) $E_{SO}/\kappa B_0 = 3.94$, where now $\kappa B_0 = (\delta_{HL}^2 v_F / 96W)^{1/3}$ and in all cases we again used an aspect ratio of $L/W = 10$. In the limits of small or large $E_{SO}/\kappa B_0$ [Figs. 4(a) and 4(e)] we see qualitatively similar behavior as for the case of large HH-LH splitting [cf. Figs. 3(a) and 3(c)], whereas the intermediate regime shows several new features. With this in mind we now discuss the different parameter regimes, which will provide some understanding of the critical-current patterns we observe.

We first consider the case where the g factor κ is relatively large, so that for most fields of interest one has

$$E_Z \gg E_{SO} \gg \sqrt{\delta_{HL} E_x}. \quad (36)$$

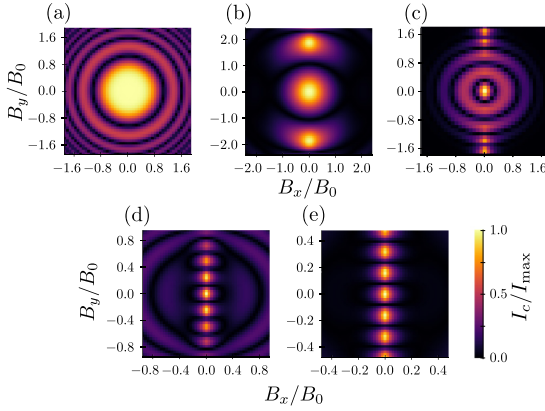


FIG. 4. Numerically calculated critical current as a function of in-plane magnetic field, $B_{\parallel} = (B_x, B_y)$, assuming small HH-LH splitting δ_{HL} . We explore (a) $E_{SO}/\kappa B_0 = 0.157$, (b) $E_{SO}/\kappa B_0 = 1.19$, (c) $E_{SO}/\kappa B_0 = 1.97$, (d) $E_{SO}/\kappa B_0 = 3.16$, and (e) $E_{SO}/\kappa B_0 = 3.94$, where now $\kappa B_0 = (\delta_{HL}^2 v_F / 96W)^{1/3}$. For all plots the aspect ratio is set at $L/W = 10$, the scale of the critical current is described by $I_{\max} = I_0 \pi L/W$.

In that case we can approximate

$$\beta_+(\theta) \approx \frac{48E_Z^2}{\delta_{HL}^2} (2iE_{SO}e^{i(\theta+2\phi_B)} - E_Z e^{3i\phi_B}), \quad (37)$$

i.e., the behavior of β is dominated by the two terms $H_{2,1}^{(2)}$ and $H_{3,0}^{(2)}$. Comparing this expression with Eq. (28) we see that the effective coupling field is similar to that in the case of large δ_{HL} , the main difference being an additional factor that is quadratic in E_Z . This means that, within the range of validity of (37), limiting expressions for the Cooper-pair propagator can be derived that look very similar to Eq. (29). We thus find

$$C(\mathbf{r}) \approx \frac{K}{r^2} \cos(|\mathbf{d}|r) \quad \text{for } E_Z \gg E_{SO}, \quad (38)$$

where now $\mathbf{d} = (B_{\parallel}/B_0)^3 (\hat{b}_{\parallel}/W)$, with \hat{b}_{\parallel} being the unit vector pointing in the direction of \mathbf{B}_{\parallel} and B_0 still being defined by $\kappa B_0 = (\delta_{HL}^2 v_F / 96W)^{1/3}$. The only difference with the corresponding limit in Eq. (28) is indeed a cubic versus linear dependence on B_{\parallel} , which explains the main difference in appearance between Figs. 4(a) and 3(a). In the limit of a large aspect ratio $L \gg W$ we thus obtain the same approximate analytic expression $I_{c1}(\mathbf{B}_{\parallel})$ as presented in Eq. (32), the only difference being that one now needs to insert $\alpha = (B_{\parallel}/B_0)^3$.

When E_{SO} is increased, as is done in Figs. 4(b)–4(e), the opposite limit of $E_{SO} \gg E_Z$ will of course not be reached while still satisfying (36). However, in that hypothetical limit one would find from (37) that $C(\mathbf{r}) \approx (K/r^2) \cos([\hat{z} \times \mathbf{d}] \cdot \mathbf{r})$, analogously to the case of large δ_{HL} , again with $\mathbf{d} = (B_{\parallel}/B_0)^3 (\hat{b}_{\parallel}/W)$. This would ultimately yield the same approximate expression for the critical current in the limit of $L \gg W$ as before,

$$I_{c2}(\mathbf{B}_{\parallel}) \approx I_0 \frac{\pi L}{W} e^{-|B_x^2/B_0^3|} |\cos(B_{\parallel}^2 B_y / B_0^3)|, \quad (39)$$

again with a cubic instead of linear dependence on the fields. Although this limit will obviously never be reached, the change in behavior of the critical current from Fig. 4(a) to 4(b) can be understood as a first step into the intermediate regime between the two limits, similar to the difference between Figs. 3(a) and 3(b) but now with a cubic dependence on the in-plane field.

We now turn our attention to the opposite case of a relatively small g factor κ , so that

$$E_{SO} \gg E_Z \gg \sqrt{\delta_{HL} E_x} \quad (40)$$

for most fields of interest. In that case the main competing coupling terms will be $H_{0,3}^{(2)}$ and $H_{1,2}^{(2)}$, yielding approximately

$$\beta_+(\theta) \approx \frac{12E_{SO}^2}{\delta_{HL}^2} (-iE_{SO}e^{3i\theta} + 5E_Z e^{i(2\theta+\phi_B)}). \quad (41)$$

This is qualitatively the same as the coupling field in (28), where the energy scale E_x is replaced by E_{SO}^2/δ_{HL} . The Cooper-pair propagator thus becomes

$$C(\mathbf{r}) \approx \frac{K}{r^2} \cos([\hat{z} \times \mathbf{d}] \cdot \mathbf{r}) \quad \text{for } E_{SO} \gg E_Z, \quad (42)$$

with $\mathbf{d} = (5E_{SO}^2/4\kappa^2 B_0^2)(B_{\parallel}/B_0 W)$, still using the same $\kappa B_0 = (\delta_{HL}^2 v_F / 96W)^{1/3}$, and in the limit $L \gg W$ the critical current takes again the form

$$I_{c2}(\mathbf{B}_{\parallel}) \approx I_0 \frac{\pi L}{W} e^{-\gamma|B_x/B_0|} |\cos(\gamma B_y/B_0)|, \quad (43)$$

with $\gamma = 5E_{SO}^2/4\kappa^2 B_0^2$. We indeed see that the numerical results presented in Figs. 4(e) and 3(c) coincide, up to scaling factors.

We can again qualitatively understand the phenomenology of the change in the pattern of critical current when moving toward the intermediate regime by decreasing E_{SO} : When the Zeeman term becomes more important, the competition between the two terms in (41) will start a transition from a periodic critical-current pattern along B_y [Figs. 4(e) and 3(c)] toward a circularly symmetric pattern with a linear dependence on B_{\parallel} as described by (32) with $\alpha = \gamma B_{\parallel}/B_0$ [compare Fig. 4(d) with 3(b)]. The true limit yielding such a circular pattern will again not be reached since (41) will break down already when $E_{SO} \lesssim E_Z$.

The remaining “intermediate” plot shown in Fig. 4(c) can be roughly interpreted as a hybrid result between the two regimes discussed above: At small fields, a circularly symmetric linear-in-field limiting pattern emerges that is expected from using (41) for small E_{SO} (the large-field limit for the case of dominating spin-orbit interaction), which transitions at larger fields into the oscillating pattern along B_y described by (39) resulting from assuming small E_Z in (37) (the small-field limit for dominating Zeeman coupling).

C. Weak spin-orbit coupling

The final limit we can consider is that of vanishing spin-orbit coupling $\alpha_R \rightarrow 0$. In this case the surviving coupling

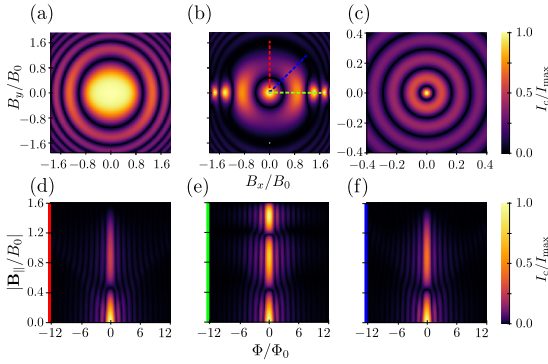


FIG. 5. Numerically calculated critical current in the absence of spin-orbit coupling. (a)–(c) The dependence of the current on an in-plane field, where (a) $\sqrt{3}E_x\delta_{HL}/12(\kappa B_0)^2 = 0.252$, (b) $\sqrt{3}E_x\delta_{HL}/12(\kappa B_0)^2 = 2.52$, and (c) $\sqrt{3}E_x\delta_{HL}/12(\kappa B_0)^2 = 25.2$, with $\kappa B_0 = (\delta_{HL}^2 v_F/96W)^{1/3}$. (d)–(f) Fraunhofer-type patterns of critical current as a function of a small additional out-of-plane magnetic field B_z , giving the total flux Φ through the junction, using $\sqrt{3}E_x\delta_{HL}/12(\kappa B_0)^2 = 2.52$ [see (b)]. The directions of the in-plane fields are indicated in (b): (d) along \hat{x} , (e) along \hat{y} , and (f) diagonally along $(\hat{x} + \hat{y})/\sqrt{2}$. For all plots the aspect ratio is set to $L/W = 10$, the scale of the critical current is described by $I_{\max} = I_0\pi L/W$, and $\Phi_0 = h/2e$ is the flux quantum.

terms are $H_{1,2}^{(2)}$ and $H_{3,0}^{(3)}$, yielding the total field

$$\beta_{\pm}(\theta) = \frac{-4E_Z}{\delta_{HL}} \left(\sqrt{3}E_x e^{i(2\theta + \phi_B)} + \frac{12E_Z^2}{\delta_{HL}} e^{i3\phi_B} \right). \quad (44)$$

In Fig. 5 we show the dependence of the resulting critical current on the applied magnetic field, for different ratios of $E_x\delta_{HL}/E_Z^2$. In the top row of panels we plot the critical current as a function of the in-plane field, where we have used (a) $\sqrt{3}E_x\delta_{HL}/12(\kappa B_0)^2 = 0.252$, (b) $\sqrt{3}E_x\delta_{HL}/12(\kappa B_0)^2 = 2.52$, and (c) $\sqrt{3}E_x\delta_{HL}/12(\kappa B_0)^2 = 25.2$. We defined again $\kappa B_0 = (\delta_{HL}^2 v_F/96W)^{1/3}$ and used an aspect ratio of $L/W = 10$ for the junction. In the bottom row we added for reference the Fraunhofer-type patterns of critical current that emerge when a small perpendicular magnetic field B_z is added in the intermediate case of Fig. 5(b). The direction of each \mathbf{B}_{\parallel} is indicated with a dashed line in Fig. 5(b): the in-plane magnetic field in 5(d) points along \hat{y} (red dashed line), 5(e) along \hat{x} (green dashed line), and 5(f) along $(\hat{x} + \hat{y})/\sqrt{2}$ (blue dashed line).

In the two limiting cases, for small and large $E_x\delta_{HL}/(\kappa B_0)^2$ [Figs. 5(a) and 5(c), respectively], we see, as expected, patterns that are similar to those for the Zeeman-dominated cases investigated above, showing the same circularly symmetric patterns with a “linear” dependence on B_{\parallel} in the former case and the “cubic” dependence in the latter [cf. Figs. 3(a) and 4(a)]. In the intermediate case Fig. 5(b), where $\sqrt{3}E_x\delta_{HL} = 12(\kappa B_0)^2$, we expect a crossover from the pattern seen in Fig. 5(c) at small fields (where E_x dominates) to the pattern of Fig. 5(a) for large fields (where E_Z dominates). Closer inspection of Fig. 5(b) seems to confirm this behavior, also

for increasing field; when we plot for even larger $B_{\parallel} \gtrsim 5B_0$ the pattern indeed becomes circularly symmetric again.

Deriving approximate expressions for the Cooper-pair propagator in the two limits again,

$$C(\mathbf{r}) \approx \frac{K}{r^2} \times \begin{cases} \cos(ar) & \text{for } E_x\delta_{HL} \gg E_Z^2, \\ \cos(br) & \text{for } E_x\delta_{HL} \ll E_Z^2 \end{cases} \quad (45)$$

with $a = (\sqrt{3}E_x\delta_{HL}/12\kappa^2 B_0^2)(B_{\parallel}/B_0W)$ and $b = (B_{\parallel}/B_0)^3(1/W)$, we can again arrive at approximate analytic expressions in the limit $L \gg W$. In both cases one finds again the functional form of Eq. (32), where one now has to use $\alpha_a = (\sqrt{3}E_x\delta_{HL}/12\kappa^2 B_0^2)(B_{\parallel}/B_0)$ and $\alpha_b = (B_{\parallel}/B_0)^3$, respectively, as expected.

The additional structure observed in Fig. 5(b) around $B_{\parallel} \approx B_0$ can be understood from considering the propagator exactly at the point where $\sqrt{3}E_x\delta_{HL} = 12(\kappa B_{\parallel})^2$, where one finds

$$C(\mathbf{r}) = \frac{K}{r^2} \cos(\mathbf{c} \cdot \mathbf{r}), \quad (46)$$

with $\mathbf{c} = 4(3)^{1/4} \sqrt{E_x^3/\delta_{HL}v_F^2} \hat{b}_{\parallel}$. This leads straightforwardly to an analytic expression for the critical current in the limit $L \gg W$,

$$I_c \approx I_0 \frac{\pi L}{W} e^{-|\gamma \sin \phi_B|} |\cos(\gamma \cos \phi_B)|, \quad (47)$$

with $\gamma = 4(3)^{1/4} \sqrt{E_x^3 W^2/\delta_{HL}v_F^2}$, where we again emphasize that this expression is derived for the specific field strength where $\sqrt{3}E_x\delta_{HL} = 12(\kappa B_{\parallel})^2$. This indicates that there can be an intermediate regime, where the pattern of $I_c(\mathbf{B}_{\parallel})$ does not look like a set of concentric high-current rings but only has significant supercurrent flowing when \mathbf{B}_{\parallel} is oriented along $\pm \hat{x}$. This is indeed consistent with the features we observe in Fig. 5(b) around $B_{\parallel} \approx 1.5B_0$. This behavior can be qualitatively understood from considering Eq. (44) again: When $\sqrt{3}E_x\delta_{HL} = 12(\kappa B_{\parallel})^2$ the two competing terms have exactly the same magnitude. Most carriers that contribute to the current will propagate approximately in the x direction where $\theta = 0, \pi$. For those carriers, the total coupling thus becomes $\alpha e^{i\phi_B} + e^{i3\phi_B}$, which indeed vanishes for fields along $\pm \hat{y}$: in those directions the coupling terms $H_{1,2}^{(1)}$ and $H_{3,0}^{(2)}$ interfere destructively.

D. Discussion

The results presented above could be useful for characterizing the effective spin physics within the heavy-hole subspace in a two-dimensional hole gas in experiment. Comparing a measured pattern of critical current as a function of in-plane field qualitatively with the patterns for the limiting and intermediate cases we present above could give an indication of the dominating spin-mixing mechanism in the heavy-hole subspace.

First and foremost, the largest amount of information can be gained if one observes a transition from one pattern to another upon increasing the magnitude of the field, e.g., from “lobes” to rings, as this can yield quantitative information about the ratio of the relevant terms in the Hamiltonian. Most of the intermediate patterns we show above, Fig. 3(b) ($E_Z \sim E_{SO}$ for large $\sqrt{\delta_{HL}E_x}$), Figs. 4(b)–4(d) ($E_Z \sim E_{SO}$ for small

$\sqrt{\delta_{HL}E_x}$), and Fig. 5(b) ($E_Z \sim \sqrt{\delta_{HL}E_x}$ for $E_{SO} = 0$), look qualitatively different in terms of the direction along which the lobes appear, the periodicity of the lobes, and the order of the transitions from lobes to rings. A critical-current pattern measured in a system that happens to be in one of the intermediate regimes can thus often be unambiguously connected to a parameter regime in our theory. For instance, lobes appearing along the x direction [Fig. 5(b)] are always an indication of negligible spin-orbit coupling and the intermediate regime $E_Z \sim \sqrt{\delta_{HL}E_x}$.

In general, the more information about the system is available, the more precise conclusions one can potentially draw from a comparison to our theory. For instance, if it is known that the spin-orbit coupling is non-negligible and that the Zeeman coupling dominates over the SOI, then the periodicity of the oscillations as a function of in-plane field can reveal information about the HH-LH splitting: Linearly spaced isotropic oscillations [Fig. 3(a)] show that one is in the large HH-LH splitting limit, where Eq. (27) holds, while “cubicly” spaced isotropic oscillations [Fig. 4(a)] suggest relatively small HH-LH splitting, where Eq. (34) holds. The same holds if the system has negligible spin orbit; a linear pattern [Fig. 5(c)] signals large HH-LH splitting and a cubic pattern [Fig. 5(a)] the opposite. Equally spaced lobes for magnetic fields along the junction [Figs. 3(c) and 4(e)] are always a sign of strong Rashba-type spin-orbit coupling, similar to the electronic case [63].

Comparing the regimes we consider above with realistic experimental parameters, we see that often one will be in a situation where $\sqrt{E_x\delta_{HL}} \gg E_Z, E_{SO}$, i.e., the one considered in Secs. III A and III C: Focusing for example on Ge-based 2DHGs, one typically has a HH-LH splitting of $\delta_{HL} \sim 20\text{--}80$ meV and an “off-diagonal Fermi energy” of $E_x \sim 1\text{--}10$ meV, whereas the Zeeman and spin-orbit energies E_Z and E_{SO} are significantly smaller. We thus believe that currently the results presented in Secs. III A and III C are the most relevant ones for experiment. However, since all energy scales depend in a different way on $\gamma_{1,2,3}$ and the “bare” g

factor in the valence band (all material parameters) as well as the thickness and asymmetry of the quantum well (device parameters), the opposite limit considered in Sec. III B can become relevant for other materials and/or less conventionally designed quantum wells.

IV. CONCLUSION

In this paper we studied an SNS junction where the normal part consists of a two-dimensional hole gas in which only the lowest (heavy-hole) subband is populated. We investigated the dependence of the critical current through the junction on the direction and magnitude of an applied in-plane magnetic field. Due to the underlying p -type nature of the valence band, the manifestation of the in-plane Zeeman effect as well as the spin-orbit coupling inside the heavy-hole subband has an intricate structure, yielding many qualitatively different spin-mixing mechanisms that could be at play. We present a systematic analysis of the different regimes that potentially could be reached by varying the g factor, the strength of a Rashba-type spin-orbit coupling, the out-of-plane confinement length, and the heavy-hole carrier density. Applying a semiclassical approximation for the normal region (assuming the Fermi wavelength to be the smallest relevant length scale) we present a straightforward numerical method for calculating the critical current in the junction. The simplicity of the resulting expressions allows us to derive (approximate) analytic expressions for the critical current in all limiting cases, which show good agreement with the numerical results. These results could therefore potentially serve as a tool for investigating the detailed effective spin physics within the heavy-hole subspace of a two-dimensional hole gas.

ACKNOWLEDGMENT

We gratefully acknowledge financial support via NTNU’s Onsager Fellowship Program.

- [1] J. D. Sau, R. M. Lutchyn, S. Tewari, and S. Das Sarma, Generic New Platform for Topological Quantum Computation Using Semiconductor Heterostructures, *Phys. Rev. Lett.* **104**, 040502 (2010).
- [2] J. Alicea, Majorana fermions in a tunable semiconductor device, *Phys. Rev. B* **81**, 125318 (2010).
- [3] Y. Oreg, G. Refael, and F. von Oppen, Helical Liquids and Majorana Bound States in Quantum Wires, *Phys. Rev. Lett.* **105**, 177002 (2010).
- [4] R. M. Lutchyn, J. D. Sau, and S. Das Sarma, Majorana Fermions and a Topological Phase Transition in Semiconductor-Superconductor Heterostructures, *Phys. Rev. Lett.* **105**, 077001 (2010).
- [5] S. D. Sarma, M. Freedman, and C. Nayak, Majorana zero modes and topological quantum computation, *npj Quantum Inf.* **1**, 15001 (2015).
- [6] M. Hell, M. Leijnse, and K. Flensberg, Two-Dimensional Platform for Networks of Majorana Bound States, *Phys. Rev. Lett.* **118**, 107701 (2017).
- [7] R. M. Lutchyn, E. P. A. M. Bakkers, L. P. Kouwenhoven, P. Krogstrup, C. M. Marcus, and Y. Oreg, Majorana zero modes in superconductor–semiconductor heterostructures, *Nat. Rev. Mater.* **3**, 52 (2018).
- [8] C. Nayak, S. H. Simon, A. Stern, M. Freedman, and S. Das Sarma, Non-abelian anyons and topological quantum computation, *Rev. Mod. Phys.* **80**, 1083 (2008).
- [9] J. K. Pachos, *Introduction to Topological Quantum Computation* (Cambridge University Press, Cambridge, 2012).
- [10] T. D. Stanescu, *Introduction to Topological Quantum Matter & Quantum Computation* (CRC Press, Boca Raton, FL, 2020).
- [11] Y. Nakamura, Y. A. Pashkin, and J. S. Tsai, Coherent control of macroscopic quantum states in a single-Cooper-pair box, *Nature (London)* **398**, 786 (1999).
- [12] J. R. Friedman, V. Patel, W. Chen, S. K. Tolpygo, and J. E. Lukens, Quantum superposition of distinct macroscopic states, *Nature (London)* **406**, 43 (2000).

- [13] J. M. Martinis, S. Nam, J. Aumentado, and C. Urbina, Rabi Oscillations in a Large Josephson-Junction Qubit, *Phys. Rev. Lett.* **89**, 117901 (2002).
- [14] J. Koch, T. M. Yu, J. Gambetta, A. A. Houck, D. I. Schuster, J. Majer, A. Blais, M. H. Devoret, S. M. Girvin, and R. J. Schoelkopf, Charge-insensitive qubit design derived from the Cooper pair box, *Phys. Rev. A* **76**, 042319 (2007).
- [15] L. Casparis, M. R. Connolly, M. Kjaergaard, N. J. Pearson, A. Kringhøj, T. W. Larsen, F. Kuummeth, T. Wang, C. Thomas, S. Gronin, G. C. Gardner, M. J. Manfra, C. M. Marcus, and K. D. Petersson, Superconducting gatemon qubit based on a proximitized two-dimensional electron gas, *Nat. Nanotechnol.* **13**, 915 (2018).
- [16] R. C. Jaklevic, J. Lambe, A. H. Silver, and J. E. Mercereau, Quantum Interference Effects in Josephson Tunneling, *Phys. Rev. Lett.* **12**, 159 (1964).
- [17] A. H. Silver and J. E. Zimmerman, Quantum states and transitions in weakly connected superconducting rings, *Phys. Rev.* **157**, 317 (1967).
- [18] C. D. Tesche and J. Clarke, Dc SQUID: Noise and optimization, *J. Low Temp. Phys.* **29**, 301 (1977).
- [19] R. L. Kautz, Noise, chaos, and the Josephson voltage standard, *Rep. Prog. Phys.* **59**, 935 (1996).
- [20] R. Kleiner, D. Koelle, F. Ludwig, and J. Clarke, Superconducting quantum interference devices: State of the art and applications, *Proc. IEEE* **92**, 1534 (2004).
- [21] E. V. Bezuglyi, A. S. Rozhavsky, I. D. Vagner, and P. Wyder, Combined effect of Zeeman splitting and spin-orbit interaction on the Josephson current in a superconductor–two-dimensional electron gas–superconductor structure, *Phys. Rev. B* **66**, 052508 (2002).
- [22] T. Yokoyama, M. Eto, and Y. V. Nazarov, Anomalous Josephson effect induced by spin-orbit interaction and Zeeman effect in semiconductor nanowires, *Phys. Rev. B* **89**, 195407 (2014).
- [23] A. Rasmussen, J. Danon, H. Suominen, F. Nichele, M. Kjaergaard, and K. Flensberg, Effects of spin-orbit coupling and spatial symmetries on the Josephson current in SNS junctions, *Phys. Rev. B* **93**, 155406 (2016).
- [24] P. San-Jose, J. Cayao, E. Prada, and R. Aguado, Multiple Andreev reflection and critical current in topological superconducting nanowire junctions, *New J. Phys.* **15**, 075019 (2013).
- [25] P. San-Jose, E. Prada, and R. Aguado, Mapping the Topological Phase Diagram of Multiband Semiconductors with Supercurrents, *Phys. Rev. Lett.* **112**, 137001 (2014).
- [26] F. Dominguez, E. G. Novik, and P. Recher, Fraunhofer pattern in the presence of Majorana zero modes, [arXiv:2210.02065](https://arxiv.org/abs/2210.02065).
- [27] R. C. Dynes and T. A. Fulton, Supercurrent density distribution in Josephson junctions, *Phys. Rev. B* **3**, 3015 (1971).
- [28] H. H. Zappe, Determination of the current density distribution in Josephson tunnel junctions, *Phys. Rev. B* **11**, 2535 (1975).
- [29] H.-Y. Hui, A. M. Lobos, J. D. Sau, and S. Das Sarma, Proximity-induced superconductivity and Josephson critical current in quantum spin Hall systems, *Phys. Rev. B* **90**, 224517 (2014).
- [30] S. Hart, H. Ren, T. Wagner, P. Leubner, M. Mühlbauer, C. Brüne, H. Buhmann, L. W. Molenkamp, and A. Yacoby, Induced superconductivity in the quantum spin Hall edge, *Nat. Phys.* **10**, 638 (2014).
- [31] V. S. Pribiag, A. J. A. Beukman, F. Qu, M. C. Cassidy, C. Charpentier, W. Wegscheider, and L. P. Kouwenhoven, Edge-mode superconductivity in a two-dimensional topological insulator, *Nat. Nanotechnol.* **10**, 593 (2015).
- [32] M. T. Allen, O. Shtanko, I. C. Fulga, A. R. Akhmerov, K. Watanabe, T. Taniguchi, P. Jarillo-Herrero, L. S. Levitov, and A. Yacoby, Spatially resolved edge currents and guided-wave electronic states in graphene, *Nat. Phys.* **12**, 128 (2016).
- [33] H. J. Suominen, J. Danon, M. Kjaergaard, K. Flensberg, J. Shabani, C. J. Palmström, F. Nichele, and C. M. Marcus, Anomalous Fraunhofer interference in epitaxial superconductor-semiconductor Josephson junctions, *Phys. Rev. B* **95**, 035307 (2017).
- [34] A. Kononov, G. Abulizi, K. Qu, J. Yan, D. Mandrus, K. Watanabe, T. Taniguchi, and C. Schönenberger, One-dimensional edge transport in few-layer WTe₂, *Nano Lett.* **20**, 4228 (2020).
- [35] T. Kontos, M. Aprili, J. Lesueur, F. Genêt, B. Stephanidis, and R. Boursier, Josephson Junction through a Thin Ferromagnetic Layer: Negative Coupling, *Phys. Rev. Lett.* **89**, 137007 (2002).
- [36] B. M. Andersen, I. V. Bobkova, P. J. Hirschfeld, and Y. S. Barash, $0-\pi$ Transitions in Josephson Junctions with Antiferromagnetic Interlayers, *Phys. Rev. Lett.* **96**, 117005 (2006).
- [37] C. Kurter, A. D. K. Finck, Y. S. Hor, and D. J. Van Harlingen, Evidence for an anomalous current–phase relation in topological insulator Josephson junctions, *Nat. Commun.* **6**, 7130 (2015).
- [38] V. E. Calado, S. Goswami, G. Nanda, M. Diez, A. R. Akhmerov, K. Watanabe, T. Taniguchi, T. M. Klapwijk, and L. M. K. Vandersypen, Ballistic Josephson junctions in edge-contacted graphene, *Nat. Nanotechnol.* **10**, 761 (2015).
- [39] H. Watzinger, J. Kukučka, L. Vukušić, F. Gao, T. Wang, F. Schäffler, J.-J. Zhang, and G. Katsaros, A germanium hole spin qubit, *Nat. Commun.* **9**, 3902 (2018).
- [40] J. Ridderbos, M. Brauns, A. Li, E. P. A. M. Bakkers, A. Brinkman, W. G. van der Wiel, and F. A. Zwanenburg, Multiple Andreev reflections and Shapiro steps in a Ge-Si nanowire Josephson junction, *Phys. Rev. Mater.* **3**, 084803 (2019).
- [41] N. W. Hendrickx, D. P. Franke, A. Sammak, G. Scappucci, and M. Veldhorst, Fast two-qubit logic with holes in germanium, *Nature (London)* **577**, 487 (2020).
- [42] F. N. M. Froning, L. C. Camenzind, O. A. H. van der Molen, A. L. E. P. A. M. Bakkers, D. M. Zumbühl, and F. R. Braakman, Ultrafast hole spin qubit with gate-tunable spin–orbit switch functionality, *Nat. Nanotechnol.* **16**, 308 (2021).
- [43] G. Scappucci, C. Kloeffel, F. A. Zwanenburg, D. Loss, M. Myronov, J.-J. Zhang, S. De Franceschi, G. Katsaros, and M. Veldhorst, The germanium quantum information route, *Nat. Rev. Mater.* **6**, 926 (2021).
- [44] D. Jirovec, A. Hofmann, A. Ballabio, P. M. Mutter, G. Tavani, M. Botifoll, A. Crippa, J. Kukučka, O. Sagi, F. Martins, J. Saez-Mollejo, I. Prieto, M. Borovkov, J. Arbiol, D. Chrastina, G. Isella, and G. Katsaros, A singlet-triplet hole spin qubit in planar ge, *Nat. Mater.* **20**, 1106 (2021).
- [45] N. Piot, B. Brun, V. Schmitt, S. Zihlmann, V. P. Michal, A. Apra, J. C. Abadillo-Uriel, X. Jehl, B. Bertrand, H. Niebojewski, L. Hutin, M. Vinet, M. Urdampilleta, T. Meunier, Y.-M. Niquet, R. Maurand, and S. D. Franceschi, A single hole spin with enhanced coherence in natural silicon, *Nat. Nanotechnol.* **17**, 1072 (2022).
- [46] F. Borsoi, N. W. Hendrickx, V. John, S. Motz, F. van Riggelen, A. Sammak, S. L. de Snoo, G. Scappucci, and M. Veldhorst,

- Shared control of a 16 semiconductor quantum dot crossbar array, [arXiv:2209.06609](https://arxiv.org/abs/2209.06609).
- [47] E. Marcellina, A. R. Hamilton, R. Winkler, and D. Culcer, Spin-orbit interactions in inversion-asymmetric two-dimensional hole systems: A variational analysis, *Phys. Rev. B* **95**, 075305 (2017).
- [48] P. Philippopoulos, S. Chesi, D. Culcer, and W. A. Coish, Pseudospin-electric coupling for holes beyond the envelope-function approximation, *Phys. Rev. B* **102**, 075310 (2020).
- [49] L. A. Terrazos, E. Marcellina, Z. Wang, S. N. Coppersmith, M. Friesen, A. R. Hamilton, X. Hu, B. Koiller, A. L. Saraiva, D. Culcer, and R. B. Capaz, Theory of hole-spin qubits in strained germanium quantum dots, *Phys. Rev. B* **103**, 125201 (2021).
- [50] S. Bosco, B. Hetényi, and D. Loss, Hole spin qubits in Si finfets with fully tunable spin-orbit coupling and sweet spots for charge noise, *PRX Quantum* **2**, 010348 (2021).
- [51] S. Bosco, M. Benito, C. Adelsberger, and D. Loss, Squeezed hole spin qubits in Ge quantum dots with ultrafast gates at low power, *Phys. Rev. B* **104**, 115425 (2021).
- [52] A. Crippa, R. Maurand, L. Bourdet, D. Kotekar-Patil, A. Amisse, X. Jehl, M. Sanquer, R. Laviéville, H. Bohuslavskiy, L. Hutin, S. Barraud, M. Vinet, Y.-M. Niquet, and S. De Franceschi, Electrical Spin Driving by g -Matrix Modulation in Spin-Orbit Qubits, *Phys. Rev. Lett.* **120**, 137702 (2018).
- [53] C. Gradl, R. Winkler, M. Kempf, J. Holler, D. Schuh, D. Bougeard, A. Hernández-Mínguez, K. Biermann, P. V. Santos, C. Schüller, and T. Korn, Asymmetric g Tensor in Low-Symmetry Two-Dimensional Hole Systems, *Phys. Rev. X* **8**, 021068 (2018).
- [54] S. D. Liles, F. Martins, D. S. Miserev, A. A. Kiselev, I. D. Thorvaldson, M. J. Rendell, I. K. Jin, F. E. Hudson, M. Veldhorst, K. M. Itoh, O. P. Sushkov, T. D. Ladd, A. S. Dzurak, and A. R. Hamilton, Electrical control of the g tensor of the first hole in a silicon mos quantum dot, *Phys. Rev. B* **104**, 235303 (2021).
- [55] J. H. Qvist and J. Danon, Anisotropic g -tensors in hole quantum dots: Role of transverse confinement direction, *Phys. Rev. B* **105**, 075303 (2022).
- [56] R. Winkler, *Spin-Orbit Coupling Effects in Two-Dimensional Electron and Hole Systems* (Springer, Berlin, 2003).
- [57] N. W. Hendrickx, D. P. Franke, A. Sammak, M. Kouwenhoven, D. Sabbagh, L. Yeoh, R. Li, M. L. V. Tagliaferri, M. Virgilio, G. Capellini, G. Scappucci, and M. Veldhorst, Gate-controlled quantum dots and superconductivity in planar germanium, *Nat. Commun.* **9**, 2835 (2018).
- [58] N. W. Hendrickx, M. L. V. Tagliaferri, M. Kouwenhoven, R. Li, D. P. Franke, A. Sammak, A. Brinkman, G. Scappucci, and M. Veldhorst, Ballistic supercurrent discretization and micrometer-long Josephson coupling in germanium, *Phys. Rev. B* **99**, 075435 (2019).
- [59] K. Aggarwal, A. Hofmann, D. Jirovec, I. Prieto, A. Sammak, M. Botifoll, S. Martí-Sánchez, M. Veldhorst, J. Arbiol, G. Scappucci, J. Danon, and G. Katsaros, Enhancement of proximity-induced superconductivity in a planar Ge hole gas, *Phys. Rev. Res.* **3**, L022005 (2021).
- [60] A. Tosato, V. Levajac, J.-Y. Wang, C. J. Boor, F. Borsoi, M. Botifoll, C. N. Borja, S. Martí-Sánchez, J. Arbiol, A. Sammak, M. Veldhorst, and G. Scappucci, Hard superconducting gap in a high-mobility semiconductor, [arXiv:2206.00569](https://arxiv.org/abs/2206.00569).
- [61] F. Vigneau, R. Mizokuchi, D. C. Zanuz, X. Huang, S. Tan, R. Maurand, S. Frolov, A. Sammak, G. Scappucci, F. Lefloch, and S. De Franceschi, Germanium Quantum-Well Josephson Field-Effect Transistors and Interferometers, *Nano Lett.* **19**, 1023 (2019).
- [62] G. D. Mahan, *Many-Particle Physics, Third Edition* (Plenum, New York, 2000).
- [63] S. Hart, H. Ren, M. Kosowsky, G. Ben-Shach, P. Leubner, C. Brüne, H. Buhmann, L. W. Molenkamp, B. I. Halperin, and A. Yacoby, Controlled finite momentum pairing and spatially varying order parameter in proximitized HgTe quantum wells, *Nat. Phys.* **13**, 87 (2017).
- [64] A. Sammak, D. Sabbagh, N. W. Hendrickx, M. Lodari, B. Paquelet Wuetz, A. Tosato, L. Yeoh, M. Bollani, M. Virgilio, M. A. Schubert, P. Zaumseil, G. Capellini, M. Veldhorst, and G. Scappucci, Shallow and undoped germanium quantum wells: A playground for spin and hybrid quantum technology, *Adv. Funct. Mater.* **29**, 1807613 (2019).
- [65] See Supplemental Material at <http://link.aps.org/supplemental/10.1103/PhysRevB.107.085303> for detailed derivations of equations used in the main text.

Supplemental material: Effects of spin-orbit coupling and in-plane Zeeman fields on the critical current in two-dimensional hole gas SNS junctions

Jonas Lidal and Jeroen Danon
*Center for Quantum Spintronics, Department of Physics,
Norwegian University of Science and Technology, NO-7491 Trondheim, Norway*
(Dated: October 24, 2022)

I. DERIVATION OF EQ. (4) IN THE MAIN TEXT

The current in the ground state is given by

$$I(\phi) = \frac{2e}{\hbar} \frac{\partial F}{\partial \phi}, \quad (1)$$

where ϕ is the phase difference between the two superconductors and F is the free energy, $F = -T \ln \text{Tr}\{e^{-H/T}\}$, where T is the temperature (using $k_B = \hbar = 1$).

Working in an interaction picture, we split the full Hamiltonian, $H = H_0 + H_t$, into the tunnel coupling term H_t [see Eq. (2) of the main text], which we will treat perturbatively, and an unperturbed part H_0 . In this picture all operators gain time dependence governed by H_0 only, and we can define a so-called S-matrix as

$$\mathcal{S} = T_\tau \exp \left\{ - \int_0^\beta d\tau' H_t(\tau') \right\}, \quad (2)$$

where T_τ is the imaginary-time time-ordering operator and $\beta = 1/T$. From this definition it follows that

$$F = F_0 - T \ln \langle \mathcal{S} \rangle_0, \quad (3)$$

where $\langle \dots \rangle_0$ is the Gibbs statistical average over the unperturbed ground state (below we will drop the subscript 0, which is implied from now on).

It is straightforward to show (see, e.g., Chapter 15 in Ref. [1]) that

$$F = F_0 - T (\langle \mathcal{S} \rangle_{\text{con}} - 1), \quad (4)$$

where

$$\langle \mathcal{S} \rangle_{\text{con}} = 1 + \Xi_1 + \Xi_2 + \dots, \quad (5)$$

is the sum over all fully connected diagrams contributing to $\langle \mathcal{S} \rangle$,

$$\Xi_n = \frac{(-1)^n}{n!} \int_0^\beta d\tau_1 \dots d\tau_n \langle T_\tau H_t(\tau_1) \dots H_t(\tau_n) \rangle_{\text{con}}. \quad (6)$$

We are interested in the lowest-order correction that depends on the phase difference of the two superconductors, which is fourth order in the coupling Hamiltonian H_t ,

$$\Xi_4 = \frac{1}{4!} \int_0^\beta d\tau_1 \dots d\tau_4 \langle \hat{T}_\tau \hat{H}_t(\tau_1) \hat{H}_t(\tau_2) \hat{H}_t(\tau_3) \hat{H}_t(\tau_4) \rangle. \quad (7)$$

We thus insert the coupling Hamiltonian, written as

$$\hat{H}_t = \sum_\sigma \int dy \left[\sqrt{\frac{\lambda_l}{\pi \nu_{\text{eff}}}} e^{2\pi i \varphi_l(y)} \hat{\psi}_\sigma^\dagger(0, y) \hat{\Psi}_{\sigma,L}(0, y) + \sqrt{\frac{\lambda_r}{\pi \nu_{\text{eff}}}} e^{2\pi i \varphi_r(y)} \hat{\psi}_\sigma^\dagger(W, y) \hat{\Psi}_{\sigma,R}(W, y) + \text{H.c.} \right], \quad (8)$$

in terms of the coupling parameters $\lambda_{l,r}$ introduced in the main text. Here, ν_{eff} is the effective one-dimensional tunneling density of states of the superconducting contacts (assumed to be equal in the two superconductors, for

simplicity), $\hat{\psi}_\sigma^\dagger(\mathbf{r})$ and $\hat{\Psi}_{\sigma,L(R)}^\dagger(\mathbf{r})$ are the creation operators for an electron with spin σ at position \mathbf{r} in the normal region and the left(right) superconducting contact, respectively, and the phases $\varphi_{l,r}(y)$ are defined through

$$\varphi_l(y) - \varphi_r(y') = \phi + \frac{\pi(y+y')B_z W}{\Phi_0}, \quad (9)$$

with $\Phi_0 = h/2e$ the flux quantum. These phases thus incorporate the phase difference of the two superconductors as well as the orbital effect of an out-of-plane magnetic field. We note that with this gauge choice the field operators $\hat{\Psi}^{(\dagger)}(\mathbf{r})$ for the electrons in the superconductors are no longer dependent on the superconducting phases.

We collect the contributions to Ξ_4 that depend on ϕ and apply Wick's theorem to separate them into single-particle Green functions, yielding

$$\begin{aligned} \Xi_4 = T^4 \frac{\lambda_l \lambda_r}{2\pi^2 \nu_{\text{eff}}^2} \sum_{k_{1..4}} \int dy_{1..4} \int_0^\beta d\tau_{1..4} \\ \times \left[-e^{\frac{i}{2}\Delta\varphi(y_1, y_2, y_3, y_4)} e^{-i\omega_{k_1}(\tau_1 - \tau_2)} \mathcal{G}_{eh}^{\text{sc}}(0, y_1, \sigma_1; 0, y_2, \sigma_2; i\omega_{k_1}) e^{-i\omega_{k_2}(\tau_3 - \tau_4)} \mathcal{G}_{he}^{\text{sc}}(W, y_3, \sigma_3; W, y_4, \sigma_4; i\omega_{k_2}) \right. \\ \times e^{-i\omega_{k_3}(\tau_3 - \tau_1)} \mathcal{G}(W, y_3, \sigma_3; 0, y_1, \sigma_1; i\omega_{k_3}) e^{-i\omega_{k_4}(\tau_4 - \tau_2)} \mathcal{G}(W, y_4, \sigma_4; 0, y_2, \sigma_2; i\omega_{k_4}) \\ \left. - e^{-\frac{i}{2}\Delta\varphi(y_1, y_2, y_3, y_4)} e^{-i\omega_{k_1}(\tau_1 - \tau_2)} \mathcal{G}_{eh}^{\text{sc}}(W, y_1, \sigma_1; W, y_2, \sigma_2; i\omega_{k_1}) e^{-i\omega_{k_2}(\tau_3 - \tau_4)} \mathcal{G}_{he}^{\text{sc}}(0, y_3, \sigma_3; 0, y_4, \sigma_4; i\omega_{k_2}) \right. \\ \left. \times e^{-i\omega_{k_3}(\tau_3 - \tau_1)} \mathcal{G}(0, y_3, \sigma_3; W, y_1, \sigma_1; i\omega_{k_3}) e^{-i\omega_{k_4}(\tau_4 - \tau_2)} \mathcal{G}(0, y_4, \sigma_4; W, y_2, \sigma_2; i\omega_{k_4}) \right], \quad (10) \end{aligned}$$

where $\Delta\varphi(y_1, y_2, y_3, y_4) = \frac{1}{2}[\varphi_l(y_1) + \varphi_l(y_2) - \varphi_r(y_3) - \varphi_r(y_4)]$, there are sums over fermionic Matsubara frequencies $\omega_k = (2k+1)\pi T$, and we used the standard definitions

$$-\langle T_\tau \hat{\Psi}_{\sigma_1}(x_1, y_1; \tau_1) \hat{\Psi}_{\sigma_2}(x_2, y_2; \tau_2) \rangle = T \sum_k e^{-i\omega_k(\tau_1 - \tau_2)} \mathcal{G}_{eh}^{\text{sc}}(x_1, y_1, \sigma_1; x_2, y_2, \sigma_2; i\omega_k), \quad (11)$$

$$-\langle T_\tau \hat{\Psi}_{\sigma_1}^\dagger(x_1, y_1; \tau_1) \hat{\Psi}_{\sigma_2}^\dagger(x_2, y_2; \tau_2) \rangle = T \sum_k e^{-i\omega_k(\tau_1 - \tau_2)} \mathcal{G}_{he}^{\text{sc}}(x_1, y_1, \sigma_1; x_2, y_2, \sigma_2; i\omega_k), \quad (12)$$

$$-\langle T_\tau \hat{\psi}_{\sigma_1}(x_1, y_1; \tau_1) \hat{\psi}_{\sigma_2}^\dagger(x_2, y_2; \tau_2) \rangle = T \sum_k e^{-i\omega_k(\tau_1 - \tau_2)} \mathcal{G}(x_1, y_1, \sigma_1; x_2, y_2, \sigma_2; i\omega_k), \quad (13)$$

where we dropped the subscripts L, R [2]. We then assume that the Andreev reflection processes described by $\mathcal{G}_{eh}^{\text{sc}}$ and $\mathcal{G}_{he}^{\text{sc}}$ in Eq. (10) are local and energy-independent, which we do via the substitutions

$$\mathcal{G}_{eh}^{\text{sc}}(0, y_1, \sigma_1; 0, y_2, \sigma_2; i\omega_k) = \pi \nu_{\text{eff}} \sigma_1 \delta(y_1 - y_2) \delta_{\sigma_2, \bar{\sigma}_1}, \quad (14)$$

$$\mathcal{G}_{eh}^{\text{sc}}(W, y_1, \sigma_1; W, y_2, \sigma_2; i\omega_k) = \pi \nu_{\text{eff}} \sigma_1 \delta(y_1 - y_2) \delta_{\sigma_2, \bar{\sigma}_1}, \quad (15)$$

$$\mathcal{G}_{he}^{\text{sc}}(0, y_1, \sigma_1; 0, y_2, \sigma_2; i\omega_k) = -\pi \nu_{\text{eff}} \sigma_1 \delta(y_1 - y_2) \delta_{\sigma_2, \bar{\sigma}_1}, \quad (16)$$

$$\mathcal{G}_{he}^{\text{sc}}(W, y_1, \sigma_1; W, y_2, \sigma_2; i\omega_k) = -\pi \nu_{\text{eff}} \sigma_1 \delta(y_1 - y_2) \delta_{\sigma_2, \bar{\sigma}_1}. \quad (17)$$

After some rearrangements and using the relation $\mathcal{G}(W, y', \sigma'; 0, y, \sigma; i\omega_k) = \mathcal{G}(0, y, \sigma; W, y', \sigma'; -i\omega_k)^*$ this yields the expression

$$\Xi_4 = \lambda_l \lambda_r \int dy dy' \text{Re} \left\{ e^{i[\varphi_l(y) - \varphi_r(y')]} \sum_k \text{Tr} [\bar{\mathcal{G}}(W, y'; 0, y; i\omega_k) \sigma_y \bar{\mathcal{G}}(W, y'; 0, y; -i\omega_k)^T \sigma_y] \right\}, \quad (18)$$

where we introduced the matrix notation

$$\bar{\mathcal{G}}(x', y'; x, y; i\omega_k) = \begin{pmatrix} \mathcal{G}_{\uparrow\uparrow}(x', y'; x, y; i\omega_k) & \mathcal{G}_{\uparrow\downarrow}(x', y'; x, y; i\omega_k) \\ \mathcal{G}_{\downarrow\uparrow}(x', y'; x, y; i\omega_k) & \mathcal{G}_{\downarrow\downarrow}(x', y'; x, y; i\omega_k) \end{pmatrix}. \quad (19)$$

Using the fact that $F^{(4)} = -T\Xi_4$, we arrive at Eq. (4) of the main text.

II. DERIVATION OF EQ. (22) IN THE MAIN TEXT

In this Section we will show how we derive Eq. (22) from Eq. (4) in the main text; the derivation follows the same approach as the one outlined in Ref. [4]. We start by assuming translational invariance within the normal region of

the junction, which means that we can write the correlation function (6) in the main text as

$$C(\mathbf{r}) = \frac{T}{2} \sum_k \text{Tr} [\bar{G}(\mathbf{r}; i\omega_k) \sigma_y \bar{G}(\mathbf{r}; -i\omega_k)^T \sigma_y], \quad (20)$$

where \mathbf{r} is now the distance vector $\mathbf{r}' - \mathbf{r}$ in terms of the coordinates used above. We then convert the sum over Matsubara frequencies to an integral in the complex plane, which yields (assuming zero temperature for simplicity)

$$C(\mathbf{r}) = \frac{1}{4\pi i} \int_0^\infty d\omega \text{Tr} [\bar{G}^R(\mathbf{r}; \omega) \sigma_y \bar{G}^A(\mathbf{r}; -\omega)^T \sigma_y - \bar{G}^A(\mathbf{r}; \omega) \sigma_y \bar{G}^R(\mathbf{r}; -\omega)^T \sigma_y], \quad (21)$$

in terms of the retarded and advanced Green function matrices $\bar{G}^{A,R}$. We rewrite these matrices using the two \mathbf{k} -dependent spin eigenstates $|\lambda_{\mathbf{k}}\rangle$,

$$\bar{G}^{R,A}(\mathbf{r}; \omega) = \frac{1}{(2\pi)^2} \int d\mathbf{k} e^{i\mathbf{k}\cdot\mathbf{r}} \sum_{\lambda_{\mathbf{k}}} \frac{|\lambda_{\mathbf{k}}\rangle \langle \lambda_{\mathbf{k}}|}{\omega - \epsilon_{\mathbf{k}\lambda} \pm i\eta}, \quad (22)$$

with $\eta = 0^+$ and $\epsilon_{\mathbf{k}\lambda}$ the eigenenergy of the state $|\lambda_{\mathbf{k}}\rangle$. After some manipulation this yields

$$C(\mathbf{r}) = \frac{1}{2(2\pi)^4} \int d\mathbf{k} d\mathbf{k}' \sum_{\lambda_{\mathbf{k}}, \lambda_{\mathbf{k}'}} e^{i(\mathbf{k}+\mathbf{k}')\cdot\mathbf{r}} \left(\frac{\theta(-\epsilon_{\mathbf{k}'\lambda})}{-\epsilon_{\mathbf{k}'\lambda} - \epsilon_{\mathbf{k}\lambda}} + \frac{\theta(\epsilon_{\mathbf{k}\lambda})}{\epsilon_{\mathbf{k}\lambda} + \epsilon_{\mathbf{k}'\lambda}} \right) \text{Tr} [|\lambda_{\mathbf{k}}\rangle \langle \lambda_{\mathbf{k}}| \sigma_y |\lambda_{\mathbf{k}'}\rangle \langle \lambda_{\mathbf{k}'}|^T \sigma_y], \quad (23)$$

where $\theta(x)$ is the Heaviside step function. We rewrite this expression in terms of an integral over two variables ϵ and ϵ' , the limits of which incorporate the effect of the step functions,

$$C(\mathbf{r}) = \frac{1}{2(2\pi)^4} \int d\mathbf{k} d\mathbf{k}' \sum_{\lambda_{\mathbf{k}}, \lambda_{\mathbf{k}'}} e^{i(\mathbf{k}+\mathbf{k}')\cdot\mathbf{r}} \text{Tr} [|\lambda_{\mathbf{k}}\rangle \langle \lambda_{\mathbf{k}}| \sigma_y |\lambda_{\mathbf{k}'}\rangle \langle \lambda_{\mathbf{k}'}|^T \sigma_y] \\ \times \left(\int_0^\infty d\epsilon \int d\epsilon' \frac{\delta(\epsilon' - \epsilon_{\mathbf{k}'\lambda}) \delta(\epsilon - \epsilon_{\mathbf{k}\lambda})}{\epsilon' + \epsilon} - \int d\epsilon \int_{-\infty}^0 d\epsilon' \frac{\delta(\epsilon' - \epsilon_{\mathbf{k}'\lambda}) \delta(\epsilon - \epsilon_{\mathbf{k}\lambda})}{\epsilon' + \epsilon} \right). \quad (24)$$

We see that when $\epsilon > 0$ and $\epsilon' < 0$ the two terms on the second line cancel, so

$$C(\mathbf{r}) = \frac{1}{2(2\pi)^4} \int_0^\infty d\epsilon \int_0^\infty d\epsilon' \int d\mathbf{k} d\mathbf{k}' \sum_{\lambda_{\mathbf{k}}, \lambda_{\mathbf{k}'}} e^{i(\mathbf{k}+\mathbf{k}')\cdot\mathbf{r}} \text{Tr} [|\lambda_{\mathbf{k}}\rangle \langle \lambda_{\mathbf{k}}| \sigma_y |\lambda_{\mathbf{k}'}\rangle \langle \lambda_{\mathbf{k}'}|^T \sigma_y] \\ \times \left(\frac{\delta(\epsilon' - \epsilon_{\mathbf{k}'\lambda}) \delta(\epsilon - \epsilon_{\mathbf{k}\lambda})}{\epsilon' + \epsilon} + \frac{\delta(-\epsilon' - \epsilon_{\mathbf{k}'\lambda}) \delta(-\epsilon - \epsilon_{\mathbf{k}\lambda})}{\epsilon' + \epsilon} \right). \quad (25)$$

We now define a propagator

$$\bar{g}(\mathbf{r}, \epsilon) = \frac{1}{(2\pi)^2} \int d\mathbf{k} \sum_{\lambda_{\mathbf{k}}} e^{i\mathbf{k}\cdot\mathbf{r}} \delta(\epsilon - \epsilon_{\mathbf{k}\lambda}) |\lambda_{\mathbf{k}}\rangle \langle \lambda_{\mathbf{k}}|, \quad (26)$$

which finally yields the expression

$$C(\mathbf{r}) = \int_0^\infty d\epsilon \int_0^\infty d\epsilon' \frac{\text{Tr} [\bar{g}(\mathbf{r}, \epsilon) \sigma_y \bar{g}(\mathbf{r}, \epsilon')^T \sigma_y + \bar{g}(\mathbf{r}, -\epsilon) \sigma_y \bar{g}(\mathbf{r}, -\epsilon')^T \sigma_y]}{2(\epsilon + \epsilon')}, \quad (27)$$

which is Eq. (22) of the main text.

III. SEMI-CLASSICAL APPROXIMATION

We now specify the Hamiltonian for the normal region [see Eq. (20) of the main text],

$$H_{\mathbf{k}} = v_F(k - k_F) + \beta(\theta) \cdot \boldsymbol{\sigma}, \quad (28)$$

where v_F is the Fermi velocity, k_F is the Fermi momentum, $\boldsymbol{\sigma}$ is the vector of the three Pauli spin matrices, θ is the in-plane angle of the wave vector \mathbf{k} , and $\boldsymbol{\beta}$ is the momentum-dependent effective field acting on the spin of the propagating carriers. Introducing the projection operator $P^{\lambda\mathbf{k}} = |\lambda_{\mathbf{k}}\rangle\langle\lambda_{\mathbf{k}}| = \frac{1}{2}[\mathbb{1} + \lambda\hat{\boldsymbol{\beta}}(\theta) \cdot \boldsymbol{\sigma}]$, where $\hat{\boldsymbol{\beta}}(\theta) = \boldsymbol{\beta}(\theta)/|\boldsymbol{\beta}(\theta)|$, and using that $\epsilon_{\mathbf{k}\lambda} = v_F(k - k_F) + \lambda|\boldsymbol{\beta}(\theta)|$, we can write

$$\bar{g}(\mathbf{r}, \epsilon) \approx \frac{k_F}{(2\pi)^2 v_F} \int_0^{2\pi} d\theta \sum_{\lambda_{\mathbf{k}}} e^{i[(\epsilon - \lambda|\boldsymbol{\beta}(\theta)|)/v_F + k_F]r \cos\theta} P^{\lambda\mathbf{k}}, \quad (29)$$

where $r = |\mathbf{r}|$ and we have assumed that $(\epsilon - \lambda|\boldsymbol{\beta}(\theta)|)/v_F \ll k_F$, which amounts to implying that all the relevant dynamics happen close to the Fermi energy. The in-plane angle θ in (29) is now defined to be $\theta = 0$ in the direction of \mathbf{r} . Using these approximations, \mathbf{k} in $\lambda_{\mathbf{k}}$ is approximated as $|\mathbf{k}| \approx k_F$, so $\lambda_{\mathbf{k}}$ is only a function of the direction of \mathbf{k} .

We thus denote the projector from now on as $P^{\lambda\theta}$ and write

$$\bar{g}(\mathbf{r}, \epsilon) = \frac{k_F}{(2\pi)^2 v_F} \int_0^{2\pi} d\theta \sum_{\lambda_{\mathbf{k}}} e^{if(\theta)r \cos\theta} P^{\lambda\theta}, \quad (30)$$

with the shorthand notation $f(\theta) = (\epsilon - \lambda|\boldsymbol{\beta}(\theta)|)/v_F + k_F$. We now use that

$$e^{iz \cos(\theta)} = \sum_n i^n J_n(z) e^{in\theta}, \quad (31)$$

where $J_n(z)$ are Bessel functions of the first kind. This allows us to write

$$\bar{g}(\mathbf{r}, \epsilon) = \frac{k_F}{(2\pi)^2 v_F} \int_0^{2\pi} d\theta \sum_{\lambda_{\mathbf{k}}} \sum_n i^n J_n[f(\theta)r] e^{in\theta} P^{\lambda\theta}. \quad (32)$$

Using again that $(\epsilon - \lambda|\boldsymbol{\beta}(\theta)|)/v_F \ll k_F$ and the semi-classical limit $k_F r \gg 1$, we use the asymptotic limit of the Bessel functions $J_n(z) \approx \sqrt{2/\pi z} \cos(-z + \frac{1}{4}\pi + \frac{1}{2}n\pi)$ for large z ,

$$\begin{aligned} \bar{g}(\mathbf{r}, \epsilon) &\approx \frac{k_F}{(2\pi)^2 v_F} \int_0^{2\pi} d\theta \sum_{\lambda_{\mathbf{k}}} \sum_n \sqrt{\frac{2}{\pi k_F r}} \cos\left(-f(\theta)r + \frac{\pi}{4} + \frac{n\pi}{2}\right) e^{in(\theta+\pi/2)} P^{\lambda\theta} \\ &= \frac{k_F}{(2\pi)^2 v_F} \int_0^{2\pi} d\theta \sum_{\lambda_{\mathbf{k}}} \sum_l \sqrt{\frac{1}{2\pi k_F r}} \left[e^{i(f(\theta)r - \frac{\pi}{4})} e^{in\theta} + e^{i(-f(\theta)r + \frac{\pi}{4})} e^{in(\theta+\pi)} \right] P^{\lambda\theta}. \end{aligned} \quad (33)$$

We then make use of the fact that $\sum_n e^{inx} = 2\pi\delta(x)$, yielding

$$\begin{aligned} \bar{g}(\mathbf{r}, \epsilon) &= \frac{\sqrt{k_F}}{(2\pi)^{3/2} v_F \sqrt{r}} \sum_{\lambda} \left[e^{i(f(0)r - \frac{\pi}{4})} P^{\lambda_0} + e^{i(-f(\pi)r + \frac{\pi}{4})} P^{\lambda_\pi} \right] \\ &= \frac{\sqrt{k_F}}{(2\pi)^{3/2} v_F \sqrt{r}} \sum_{\lambda} \left[e^{i[(\epsilon - \lambda|\boldsymbol{\beta}(0)|)/v_F + k_F]r - i\pi/4} P^{\lambda_0} + e^{-i[(\epsilon - \lambda|\boldsymbol{\beta}(\pi)|)/v_F + k_F]r + i\pi/4} P^{\lambda_\pi} \right], \end{aligned} \quad (34)$$

where $\lambda_{0,\pi}$ with $\lambda = \pm$ thus label the eigenstates parallel and antiparallel to \mathbf{r} , respectively.

We now insert this semi-classical result into the expression for the Cooper-pair propagator $C(\mathbf{r})$ and use that

$$\int_0^\infty d\epsilon \int_0^\infty d\epsilon' \frac{e^{\pm i(\epsilon - \epsilon')a}}{\epsilon + \epsilon'} = \frac{\pi}{2a}, \quad (35)$$

which yields

$$C(\mathbf{r}) = \frac{k_F}{(4\pi)^2 v_F r^2} \text{Tr} \left\{ \sum_{\lambda, \lambda'} \left[P^{\lambda_0} \sigma_y (P^{\lambda_\pi})^T \sigma_y + P^{\lambda'_\pi} \sigma_y (P^{\lambda'_0})^T \sigma_y \right] \right\} e^{-i(\lambda|\boldsymbol{\beta}(0)| - \lambda'|\boldsymbol{\beta}(\pi)|)r/v_F}. \quad (36)$$

We now use that $P^{\lambda\mathbf{k}} = \frac{1}{2}[\mathbb{1} + \lambda\hat{\boldsymbol{\beta}}(\theta) \cdot \boldsymbol{\sigma}]$ and $\sigma_y (P^{\lambda\mathbf{k}})^T \sigma_y = \frac{1}{2}[\mathbb{1} - \lambda\hat{\boldsymbol{\beta}}(\theta) \cdot \boldsymbol{\sigma}]$ which finally yields

$$C(\mathbf{r}) = \frac{k_F}{(4\pi)^2 v_F r^2} \sum_{\lambda, \lambda'} \left[1 - \lambda\lambda' \hat{\boldsymbol{\beta}}(0) \cdot \hat{\boldsymbol{\beta}}(\pi) \right] e^{-i(\lambda|\boldsymbol{\beta}(0)| - \lambda'|\boldsymbol{\beta}(\pi)|)r/v_F}, \quad (37)$$

which reduces to Eq. (24) in the main text after summing over $\lambda, \lambda' = \pm$. In the main text we denoted the directions parallel and antiparallel to \mathbf{r} with θ and $\bar{\theta}$, respectively.

IV. APPROXIMATE ANALYTIC SOLUTIONS OF EQ. (30)

$$\text{A. } C(\mathbf{r}) = K \cos(|\mathbf{d}|r)/r^2$$

We first consider the integral (30) in the limit where

$$C(\mathbf{r}) = K \cos(|\mathbf{d}|r)/r^2, \quad (38)$$

which is first discussed in Sec. III.A. After switching to sum and difference coordinates, $\sigma = \frac{1}{2}(y + y')$ and $\tau = y - y'$, the integral over σ can be easily performed. Substituting $\rho = \sqrt{(\tau/W)^2 + 1}$ then yields

$$I_c(\mathbf{B}_{\parallel}) = 2I_0 \int_1^q d\rho \frac{\cos(\alpha\rho)}{\rho} \left(\frac{L}{W\sqrt{\rho^2 - 1}} - 1 \right), \quad (39)$$

where $I_0 = 4K|\lambda_t\lambda_r|$ and $\alpha = B_{\parallel}/B_0$. A solution in the limit $q = \sqrt{1 + (L/W)^2} \rightarrow \infty$ is presented in the main text, but for general L/W the first term in (39) is not analytically solvable. To arrive at an approximate solution we substitute

$$\frac{1}{\rho\sqrt{\rho^2 - 1}} \rightarrow \frac{\rho^2 - \sqrt{2\rho - 2}}{\rho^2\sqrt{2\rho - 2}} e^{5(1-\rho)/2} + \frac{1}{\rho^2}, \quad (40)$$

which is accurate within a few percent for all $\rho > 1$. This yields the approximate result

$$I_c(\mathbf{B}_{\parallel}) \approx I_0 \frac{2L}{W} \left(\alpha [\text{Si}(\alpha) - \text{Si}(q\alpha)] + \frac{e^{5(1-q)/2} - 1}{q} \cos(q\alpha) + e^{5/2} \text{Re} \left[e^{\zeta} \sqrt{\frac{\pi}{-2\zeta}} \text{erf}(\sqrt{(1-q)\zeta}) + \zeta (\text{Ei}[\zeta] - \text{Ei}[q\zeta]) \right] \right) + 2I_0 [\text{Ci}(\alpha) - \text{Ci}(q\alpha)], \quad (41)$$

where $\text{Si}(x)$ and $\text{Ci}(x)$ are the sine and cosine integral, respectively, $\text{Ei}(x)$ is the exponential integral function, $\text{erf}(x)$ is the error function, and we introduced the parameter $\zeta = -\frac{5}{2} + i\alpha$ for concise notation.

$$\text{B. } C(\mathbf{r}) = K \cos(\boldsymbol{\kappa} \cdot \mathbf{r})/r^2$$

The other limiting form the Cooper pair propagator takes is

$$C(\mathbf{r}) = K \frac{\cos(\boldsymbol{\kappa} \cdot \mathbf{r})}{r^2}, \quad (42)$$

where $\boldsymbol{\kappa}$ can be $\boldsymbol{\kappa} \propto \hat{z} \times \mathbf{B}_{\parallel}$ (as in Sec. III.A and III.B) or $\boldsymbol{\kappa} \propto \mathbf{B}_{\parallel}$ (as in Sec. III.C). In the limit of large L/W one can approximate

$$I_c(\mathbf{B}_{\parallel}) \approx I_0 \int_0^L dy' \int_{-\infty}^{\infty} dy \frac{\cos[\kappa_x L + \kappa_y(y - y')]}{L^2 + (y - y')^2} = I_0 \frac{\pi L}{W} e^{-|\kappa_y|W} \cos(\kappa_x W). \quad (43)$$

For general L/W the original integral (i.e., without setting the limits of the second integral to $\pm\infty$) can be (quasi)analytically solved, resulting in

$$I_c(\mathbf{B}_{\parallel}) = I_0 \cos(\kappa_x W) \text{Re} \left[e^{|\kappa_y W|} (\pi\omega + \text{Ei}[-|\kappa_y W|] - (1 + i\omega)\text{Ei}[-(1 + i\omega)|\kappa_y W|]) + e^{-|\kappa_y W|} (\pi\omega + \text{Ei}[|\kappa_y W|] - (1 + i\omega)\text{Ei}[(1 + i\omega)|\kappa_y W|]) \right], \quad (44)$$

where $\omega = L/W$ is the aspect ratio of the junction and $\text{Ei}(x)$ is again the exponential integral function.

- [1] A. A. Abrikosov, I. E. Dzyaloshinski, and L. P. Gorkov, *Methods of Quantum Field Theory in Statistical Physics*, Prentice-Hall (1965).
- [2] The prefactor of Eq. (10) is 1/4 for the linked cluster expansion we are doing here instead of 1, when all imaginary times τ_n can be permuted (see, e.g., Chapter 3 in Ref. [3]). An additional factor 2 arises from the fact that the two superconductors are not equivalent, which yields two choices for which superconductor interacts with the normal region at τ_1 .
- [3] G. D. Mahan, *Many-Particle Physics*, Plenum (2000).
- [4] S. Hart, H. Ren, M. Kosowsky, G. Ben-Shach, P. Leubner, C. Brüne, H. Buhmann, L. W. Molenkamp, B. I. Halperin, and A. Yacoby, *Nat. Phys.* **13**, 87 (2017).

ISBN 978-82-326-7220-2 (printed ver.)
ISBN 978-82-326-7219-6 (electronic ver.)
ISSN 1503-8181 (printed ver.)
ISSN 2703-8084 (online ver.)



NTNU

Norwegian University of
Science and Technology